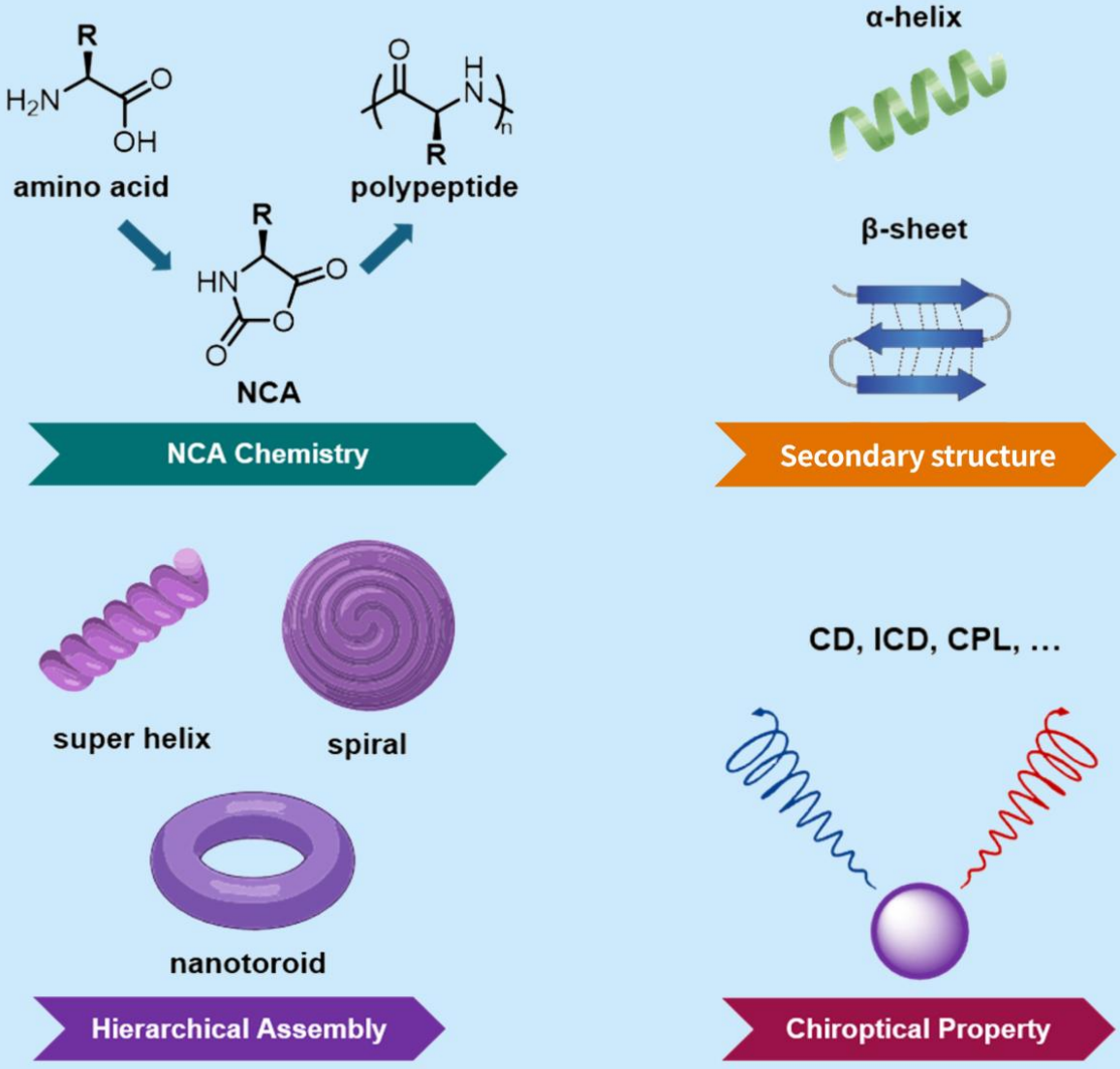
https://www.sciltp.com/journals/mi
Online ISSN: 2982-2394
Volume 3, Issue 3, 2026

Materials and Interfaces



Cover image @2026 Zhiqun Lin etc.

N-Carboxyanhydride-Derived Polypeptides as Programmable Platforms for Hierarchical Chiral Assembly and Chiroptical Materials

Scilight

Contents

Vol. 3 No. 3, September 2026

Imaging of Brain Tissue Using CdSe/CdS Core/Shell Quantum Dots for Correlative Fluorescence and Electron Microscopy 227

Hawi N. Nyiera, Janeth Pérez-Garza, Linnaea Ostroff, and Jing Zhao *

Semiconductor SERS Platform Enables Rapid Discrimination of Structurally Similar Flavonoids in Multicomponent Systems 233

Haisu Wang, Siqi Li, Yuting Song, Yanguo Guo, Junbo Li, Lei Sun *, Yunfei Xie *, and Wei Ji *

Hybrid SERS Platforms for Enhanced Biochemical Sensing 245

Jiazheng Bao, Bin Lian, Hyungmok Joh, Alan Xiaolong Wang *, and Donglei Emma Fan *

Effect of Electropolishing on Morphology and Adhesion of Nanostructured Anodic Tantalum Oxide Thin Films 287

Sarah E. Pooley, Cyrus Koroni, Shinthia Binte Eskender, Jacob Olson, Joshua A. Russell, Max Bork, Timothy Merrell, Gage Cook, Scarlet Fields, Kaden Kunz, Kiev Dixon, Pete Barnes, Brian Jaques, and Hui Xiong *

Structurally Modulated AuPd Alloy Nanorods for Plasmon-Promoted Methanol Electrooxidation 298

Zixu Wang, Guoxin Cao, Guizeng Yang, Lichao Sun *, Vladimir Bochenkov *, and Qingfeng Zhang *

***N*-Carboxyanhydride-Derived Polypeptides as Programmable Platforms for Hierarchical Chiral Assembly and Chiroptical Materials** 313

Shuo Wang, Mingyue Zhang, Minju Kim, Wenxuan Wu, and Zhiqun Lin *

Injectable Fiber-Hydrogel Hybrid Scaffolds for Localized Growth Factor Delivery and Modulation of Vascular and Neuronal Cell Responses 333

Li Ruan, Kaiqin Mo, Wenzhe Du, Kang Huo, Jianfeng Han, Jichuan Qiu, Feng Tian *, and Jiajia Xue *

Materials and Interfaces

Scilight

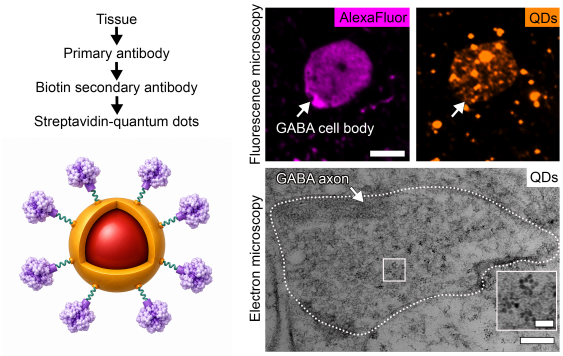
Communication

Imaging of Brain Tissue Using CdSe/CdS Core/Shell Quantum Dots for Correlative Fluorescence and Electron Microscopy

Hawi N. Nyiera [1,†], Janeth Pérez-Garza [2,†], Linnaea Ostroff [2,3,4], and Jing Zhao [1,3,*]

[1] Department of Chemistry, University of Connecticut, Storrs, CT 06269, USA
[2] Department of Physiology and Neurobiology, University of Connecticut, Storrs, CT 06269, USA
[3] Institute of Materials Science, University of Connecticut, Storrs, CT, 06269, USA
[4] Institute for the Brain and Cognitive Sciences, University of Connecticut, Storrs, CT, 06269, USA
* Correspondence: jing.zhao@uconn.edu
† These authors contributed equally to this work.
Received: 15 May 2026; Revised: 5 July 2026; Accepted: 25 July 2026; Published: 14 August 2026

Abstract: Detecting molecules across different spatial scales remains a major challenge in biological samples, particularly in complex tissues such as brain, where linking molecular identification and nanoscale structural detail is essential for understanding function. Fluorescence microscopy provides selective labeling of specific molecules but cannot fully resolve many cellular and subcellular features, whereas electron microscopy reveals ultrastructure without molecular specificity. Bridging these modalities is difficult because commonly used fluorescent probes such as dyes and proteins cannot provide electron contrast. Quantum dots are particularly useful as they retain fluorescence while providing sufficient electron density for ultrastructural visualization. Here, we show that streptavidin-functionalized CdSe/CdS core/shell quantum dots can function as dual-modal probes for labeling γ-aminobutyric acid (GABA) neurons in brain tissue. The quantum dots produce bright and stable fluorescence signals for optical detection while their inorganic composition generates strong electron contrast in ultrathin sections examined by transmission electron microscopy. This work demonstrates that functionalized CdSe/CdS quantum dots can serve as stable dual-modal probes for fluorescence and electron microscopy in complex tissues, highlighting the potential of semiconductor nanocrystals for multifunctional imaging applications.



Keywords: quantum dots; tissue labeling; fluorescence microscopy; electron microscopy

1. Introduction

Understanding the molecular architecture of complex tissues is challenging due to the high-resolution imaging needed to localize molecules at the subcellular level. Fluorescence microscopy (FM) has been the primary tool to specifically label and identify molecular and structural features of brain cells such as a cell body, dendrites and axons as seen in neurons [1,2]. However, it lacks the spatial resolution needed to resolve subcellular structures. In contrast, electron microscopy (EM) provides ultrastructural detail but does not inherently convey molecular specificity. To integrate molecular information with ultrastructural context, we focused on the use of CdSe/CdS quantum dots (QDs) as correlative probes for FM and EM visualization.

EM approaches to molecular localization come with certain limitations. Normally, one must balance the ultrastructural and molecular preservation of a determined target, followed later by immunoelectron microscopy techniques (immuno-EM) [3]. Immunolabeling on ultrathin EM sections is detected by direct or indirect visualization of antibodies by colloidal gold particles, which are electron dense for EM imaging but cannot be imaged by light microscopy [4,5]. Additionally, the size of gold-antibody complexes provides a challenge since labeling efficiency

Copyright: © 2026 by the authors. This is an open access article under the terms and conditions of the Creative Commons Attribution (CC BY) license (https://creativecommons.org/licenses/by/4.0/).
Publisher's Note: Scilight stays neutral with regard to jurisdictional claims in published maps and institutional affiliations.

decreases with larger gold particles (5–15 nm) [6,7]. Although ultra-small gold particles (0.8–1.4 nm) can improve labeling and imaging resolution, detection requires silver enhancement which is subject to background and may not reflect individual gold particles. These features therefore increase detection inaccuracies, potentially obscuring ultrastructural details and increasing background due to heterogenous particle sizes. Accordingly, probes that are reliably visualized and support dual FM and EM imaging are needed for immuno-EM applications [6–9].

Semiconductor QDs offer a promising platform to address these limitations. QDs exhibit high brightness, photostability, and size-tunable emission [10–12], making them well suited as fluorescent probes in biological systems [13–16]. In addition, their inorganic composition provides intrinsic electron density, suggesting their potential as contrast agents for EM [17–19]. These properties make QDs attractive candidates for dual-modal imaging. The ability to synthesize and functionalize QDs *de novo* provides flexibility to optimize particle size, emission, and surface properties for specific research needs. Although functionalized QDs have shown efficient correlative labeling in pre-embedding approaches [20–23], their use for post-embedding correlative FM and EM on ultrathin sections has not been developed.

Because commercially available QDs may not always provide optimal surface functionalization, labeling performance, and EM visibility, requiring signal enhancement in some cases [21], we describe in detail the synthesis and functionalization of CdSe/CdS core/shell QDs for use as dual-modal labels in brain tissue post-embedding immuno-EM. By functionalizing the QDs with streptavidin, biotinylated γ-aminobutyric acid (GABA) cells are successfully labeled and visualized in ultrathin brain tissue sections for both FM and EM imaging. Ultrathin sections permit visualization of cells and subcellular structures that can be followed through consecutive series of sections [24]. Immunolabeling using two consecutive serial sections demonstrates that the functionalized streptavidin-QDs enable correlative FM and EM imaging in brain tissue, maintaining functionality across both imaging workflows.

2. Results and Discussion

CdSe/CdS QDs were synthesized using the hot injection method [25]. The QDs exhibit a broad absorption spectrum and a sharp photoluminescence (PL) maximum at 620 nm, as shown in Figure 1A. To further evaluate their optical properties, the photoluminescence quantum yield (PLQY) was measured before and after aqueous transfer. The as-synthesized QDs in hexane exhibited a PLQY of 44.5%, while the MUA-capped QDs after ligand exchange and aqueous dispersion exhibited a PLQY of 16.2%. Although the PLQY decreased after ligand exchange, the QDs retained detectable fluorescence in water (Figure S1), supporting their use as fluorescent probes. Transmission electron microscopy (TEM) revealed that the QDs have a spherical morphology with an average size of 9.0 ± 0.9 nm shown in Figure 1B. To make the QDs water soluble and thus biocompatible, ligand exchange with mercaptoundecanoic acid (MUA) was performed on the as-synthesized QDs. Following ligand exchange, the QDs were functionalized with streptavidin to allow for targeted biological labeling through biotin-streptavidin interactions [26–28]. Details of the functionalization method are available in the Supporting Information, Section 4.

To confirm that streptavidin has been successfully introduced on the QDs, Förster resonance energy transfer (FRET) measurements were conducted using the streptavidin-functionalized QDs as an energy donor and Cy5 biotin as an acceptor fluorophore. The FRET measurement takes advantage of the spectral overlap between QD emission and Cy5 dye absorption (Figure S2) and the strong distance dependence of FRET, which is most effective over donor-acceptor separations of approximately 1–10 nm [29–31]. Therefore, Cy5 dye emission is only detectable when Cy5 biotin binds to streptavidin on the QD surface and brings the acceptor fluorophore into close proximity with the QD donor. For FRET measurements, streptavidin-functionalized QDs dispersed in PBS/BSA were reacted directly with Cy5 biotin in solution and allowed to react for 30 min. Following the addition of Cy5 biotin to the streptavidin-functionalized QDs, the reaction mixture was excited at 400 nm to selectively excite the QDs only and PL emission spectra were collected. Under these conditions, Cy5 emission was observed at 670 nm (Figure 1C), indicating that FRET occurred due to successful binding of Cy5 biotin to streptavidin. Furthermore, PL decay measurements were performed under the same experimental conditions using a 405 nm pulsed laser excitation and the decay curves were fit using a tri-exponential function (Figure S3 and Table S1). A decrease in the QD donor PL lifetime from 17.90 ns to 11.42 ns was observed in the presence of Cy5 biotin (Figure 1D). The faster PL decay observed of the conjugated biotin-streptavidin pair indicates nonradiative energy transfer from QDs to Cy5 which further confirms binding between streptavidin-functionalized QDs and Cy5 biotin [32–34]. These results demonstrate successful streptavidin functionalization at the QD surface.

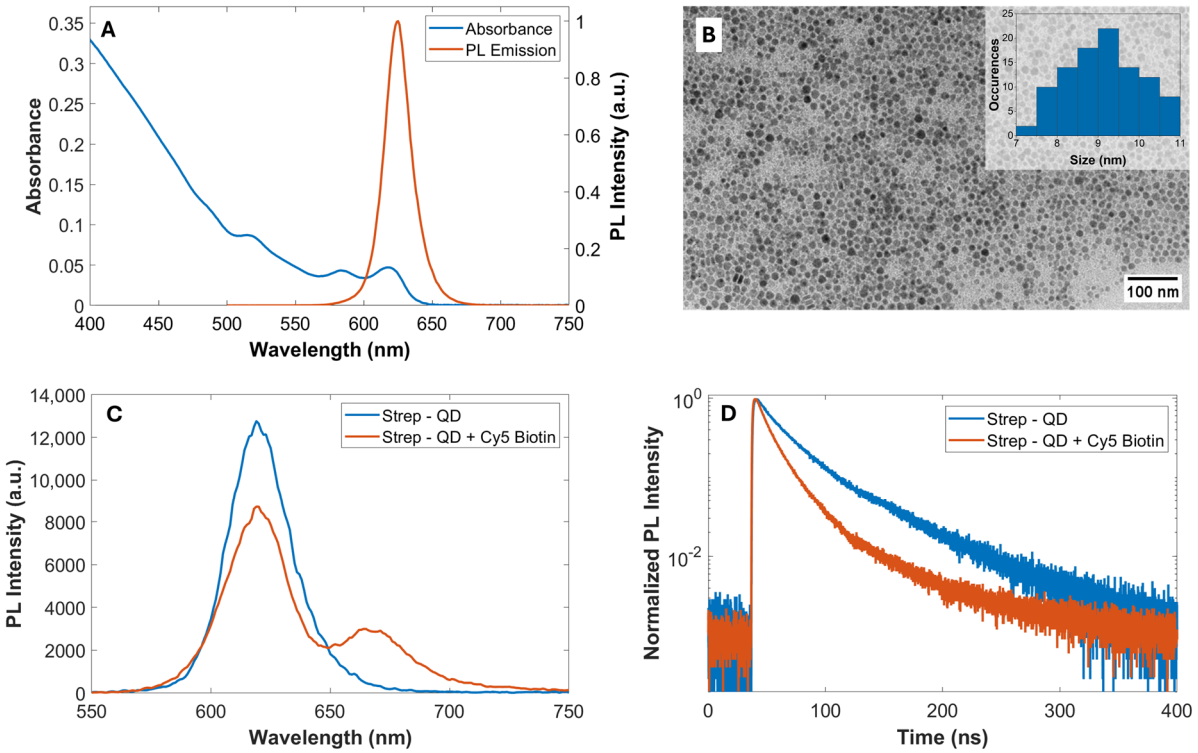


Figure 1. (**A**) UV-vis absorption spectrum (left axis) and photoluminescence (PL) emission spectrum (right axis) of CdSe/CdS QDs in hexane. (**B**) Representative TEM image of the QDs. The inset shows a histogram of the QD size distribution. (**C**) PL spectra of streptavidin-conjugated QDs before and after addition of Cy5 biotin, excited at 400 nm. (**D**) Time-resolved PL decays of streptavidin-conjugated QDs before and after addition of Cy5 biotin.

While successful conjugation of streptavidin was confirmed *in vitro*, removal of unbound streptavidin is critical to ensure effective labeling of the targets in the tissue sections by QDs rather than free streptavidin. A 100 kDa molecular weight cut off filter was applied to purify the streptavidin-functionalized QDs to remove unbound streptavidin. The QDs were evaluated for specific labeling in ultrathin brain tissue sections using an antibody-based approach as illustrated in Figure 2A. The QDs were then used to visualize GABA, one of the main neurotransmitters to identify inhibitory cell types in the brain, on ultrathin (70 nm) sections of rat brain [35,36]. Perfusion-fixed rat brains were sectioned on a vibratome and the amygdala region was dissected out and embedded in resin following the procedure in Section 6 in the Supporting Information. Embedded tissue blocks were sectioned at 70 nm using an ultramicrotome and sections placed on coverslips or gold pioloform grids were used for immuno-EM labeling. The tissue sections were then treated with the primary antibody to GABA followed by a biotinylated secondary antibody. Lastly, the tissue sections were incubated with streptavidin-QDs or AlexaFluor 647 as a control, as detailed in Section 7 in the Supporting Information. The tissues were examined under fluorescence or transmission electron microscopes. Ultrathin tissue sections ensure that adjacent sections contain nearly identical structural information, allowing reliable comparison across sections.

In the brain, GABA is found in the neuron cell body, as well as in dendrites and axons [36,37]. Labeling of GABA cells using streptavidin-AlexaFluor 647 is seen with a strong labeled cell body (arrow in Figure 2B). A consecutive section labeled with streptavidin-QDs show the same pattern of staining of the same cell (arrow in Figure 2C), although some non-specific puncta were observed in the tissue (arrowheads in Figure 2C). Fluorescence microscopy images of QDs were excited at 385 nm and emission was collected with an ET605/52 nm filter. Fluorescence imaging indicates that streptavidin-functionalized QDs preferentially bind in the presence of biotin in tissue, with minimal QD signal observed in the absence of the primary antibody (Figure 2D). GABA is widely distributed in the brain making it difficult to confirm non-specific QDs puncta in neuropil (the dense space between neuronal cell bodies primarily composed of axons, dendrites and glial cells), so EM is needed to confirm the specificity of the QD labels. Axons and dendrites can be followed through series of consecutive ultrathin sections [24]. To test streptavidin-QDs labeling at EM resolution, two consecutive ultrathin 70 nm sections were labeled with GABA, using one section with streptavidin AlexaFluor 647 as a validation of the labeled structures (magenta signal in Figure 2E), and the following one with QDs directly to tissue on EM gold pioloform grids (Figure 2F,G). Imaging at high resolution showed individual QDs on tissue structures (arrows in Figure 2G). GABA positive puncta was aligned to specific neuronal processes using the AlexaFluor 647 signal (Figure 2E),

and QDs were distributed within these processes (white arrows in Figure 2F,G). However, non-specific binding of QDs was also present in some GABA-negative processes (arrowheads in Figure 2F), and not all GABA-positive processes exhibited QD labeling (black arrow in Figure 2F). The presence of streptavidin-functionalized QDs on some GABA-positive processes supports target-associated labeling; however, nonspecific binding in GABA-negative structures and incomplete labeling of GABA-positive processes indicate that labeling efficiency and specificity remain limited. These observations may reflect inefficient binding of the QD probes to the secondary antibody due to incomplete removal of unbound streptavidin, as excess free streptavidin could occupy the biotinylated secondary antibody sites. Although size exclusion filters have previously been used for QD purification [38–40], as well as to remove excess free streptavidin [41], more precise purification methods, such as high-performance size exclusion chromatography (HPSEC) may further reduce unbound streptavidin and QD aggregates [42] potentially improving labeling specificity. Together, these factors highlight the importance of optimizing purification and surface functionalization to improve labeling specificity in tissue sections.

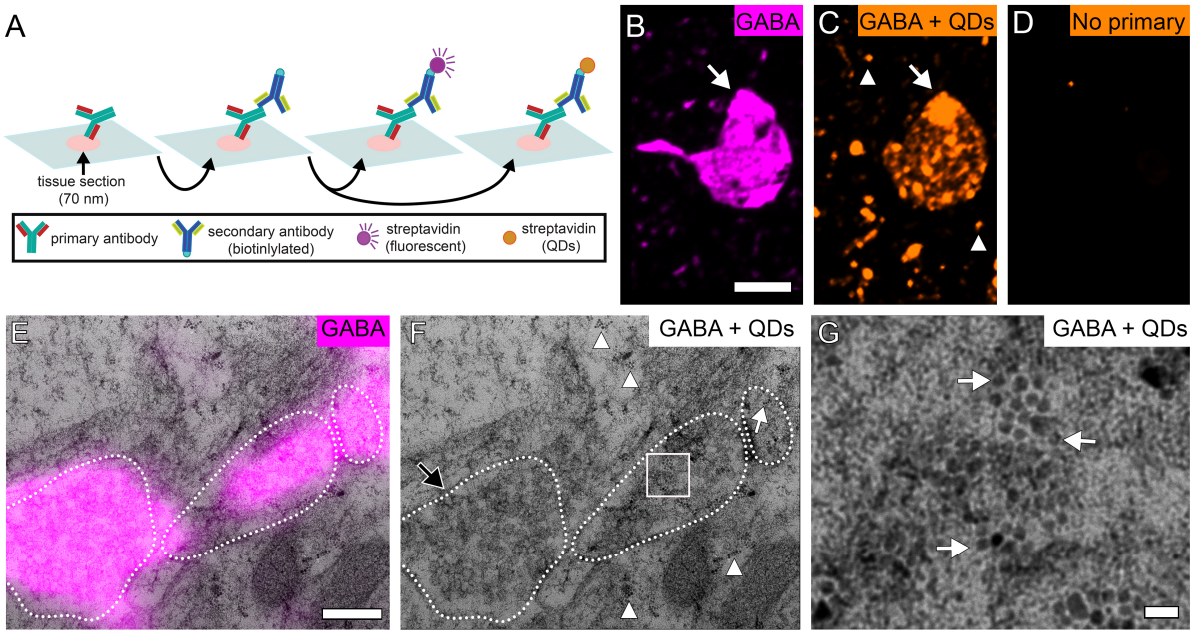


Figure 2. (**A**) Schematic of immunolabeling on 70 nm ultrathin sections. Signal from primary antibody is detected by biotin and streptavidin interaction. Streptavidin is either fluorescent or functionalized with QDs. A GABA positive cell is detected by fluorescent streptavidin (arrow in **B**) and streptavidin-QDs (arrow in **C**) after immunolabeling is performed on ultrathin sections. A no primary antibody control shows less or no signal of streptavidin-QDs (**D**). GABA positive processes are visualized at EM level after immunolabeling is performed on EM gold pioloform grids. Fluorescence microscopy in a consecutive 70 nm section validates labeled structures (magenta signal in **E**). Streptavidin-QDs are seen in positive (white arrows in **F** and **G**) and non-positive (arrowheads in **F**) GABA processes. A positive GABA axon (black arrow in **F**) is shown with no QDs. (**G**) is an inset magnification of the boxed region in (**F**). Scale bars: 10 µm in (**B**), 200 nm in (**E**), and 10 nm in (**G**).

In conclusion, streptavidin functionalized CdSe/CdS QDs function as dual-modal probes that retain fluorescence and electron contrast, enabling correlative imaging in ultrathin brain tissue sections. While specific labeling of GABA neuronal processes was achieved, nonspecific binding and incomplete labeling indicates that further optimization of purification and surface functionalization is needed. These results demonstrate the feasibility of using semiconductor QDs for integrated fluorescence and electron microscopy and support their continued development as multifunctional imaging probes.

Supplementary Materials: The following supporting information can be downloaded at: https://media.sciltp.com/articles/others/2608141007326916/MI-26050111-SI.pdf, Chemicals, instrumentation, QD synthesis and surface functionalization procedures, tissue embedding, sectioning and labeling procedures, and additional experimental data.

Author Contributions: J.Z. and L.O. conceived the project. H.N.N. and J.P.-G. carried out all the experiments and performed data analysis under the supervision of J.Z. and L.O. The manuscript was written through contributions of all authors. All authors have read and agreed to the published version of the manuscript.

Funding: This research was funded by NIH MH123994 and NIH MH5674790.

Institutional Review Board Statement: All animal procedures were approved by the University of Connecticut Institutional Animal Care and Use Committee (protocol # A22-038).

Data Availability Statement: All data generated in this study, such as the raw and processed data from spectral characterizations and microscopy images will be shared upon request. The data will be deposited in the open-access repository Figshare and made available after the publication of this work.

Conflicts of Interest: The authors declare no conflict of interest.

Use of AI and AI-Assisted Technologies: No AI tools were utilized for this paper.

References

1. Rah, J.C.; Choi, J.H. Finding Needles in a Haystack with Light: Resolving the Microcircuitry of the Brain with Fluorescence Microscopy. *Mol. Cells* **2022**, *45*, 84–92.
2. Yin, C.; Li, J.; Meng, K.; Zhang, J.; Chen, M.; Chen, R.; Hu, Y.; Wang, S.; Xie, S. Fluorescent Labeling Methods for Brain Structure Research. *Molecules* **2026**, *31*, 817.
3. Luján, R.; Rubio, M.E. Editorial: Immunoelectron Microscopy: Placing Molecular Functions within a Neuronal Context. *Front. Neuroanat.* **2022**, *16*, 1043371.
4. Jones, J.C.R. Pre- and Post-Embedding Immunogold Labeling of Tissue Sections. *Methods Mol. Bio.* **2016**, *1474*, 291–307.
5. Lucocq, J. Particulate Markers for Immunoelectron Microscopy. In *Fine Structure Immunocytochemistry*; Griffiths, G., Ed.; Springer: Berlin/Heidelberg, Germany, 1993; pp. 279–306.
6. Humbel, B.M.; Sibon, O.C.; Stierhof, Y.D.; Schwarz, H. Ultra-Small Gold Particles and Silver Enhancement as a Detection System in Immunolabeling and in Situ Hybridization Experiments. *J. Histochem. Cytochem.* **1995**, *43*, 735–737.
7. Stierhof, Y.-D.; Humbel, B.M.; Hermann, R.; Otten, M.T.; Schwarz, H. Direct Visualization and Silver Enhancement of Ultra-Small Antibody-Bound Gold Particles on Immunolabeled Ultrathin Resin Sections. *Scanning Microsc.* **1992**, *6*, 12.
8. Petralia, R.S.; Wang, Y.X. Review of Post-Embedding Immunogold Methods for the Study of Neuronal Structures. *Front. Neuroanat.* **2021**, *15*, 763427.
9. Mayer, G.; Leone, R.D.; Hainfeld, J.F.; Bendayan, M. Introduction of a Novel HRP Substrate-Nanogold Probe for Signal Amplification in Immunocytochemistry. *J. Histochem. Cytochem.* **2000**, *48*, 461–469.
10. Greytak, A.B.; Allen, P.M.; Liu, W.; Zhao, J.; Young, E.R.; Popović, Z.; Walker, B.J.; Nocera, D.G.; Bawendi, M.G. Alternating Layer Addition Approach to CdSe/CdS Core/Shell Quantum Dots with near-Unity Quantum Yield and High on-Time Fractions. *Chem. Sci.* **2012**, *3*, 2028–2034.
11. Chen, O.; Zhao, J.; Chauhan, V.P.; Cui, J.; Wong, C.; Harris, D.K.; Wei, H.; Han, H.S.; Fukumura, D.; Jain, R.K.; et al. Compact High-Quality CdSe-CdS Core-Shell Nanocrystals with Narrow Emission Linewidths and Suppressed Blinking. *Nat. Mater.* **2013**, *12*, 445–451.
12. Murray, C.B.; Norris, D.J.; Bawendi, M.G. Synthesis and Characterization of Nearly Monodisperse CdE (E = S, Se, Te) Semiconductor Nanocrystallites. *J. Am. Chem. Soc.* **1993**, *115*, 8706–8715.
13. Nisman, R.; Dellaire, G.; Ren, Y.; Li, R.; Bazett-Jones, D.P. Application of Quantum Dots as Probes for Correlative Fluorescence, Conventional, and Energy-Filtered Transmission Electron Microscopy. *J. Histochem. Cytochem.* **2004**, *52*, 13–18.
14. Smith, A.M.; Nie, S. Chemical Analysis and Cellular Imaging with Quantum Dots. *Analyst* **2004**, *129*, 672–677.
15. Cotta, M.A. Quantum Dots and Their Applications: What Lies Ahead? *Appl. Nano Mater.* **2020**, *3*, 4920–4924.
16. Susumu, K.; Uyeda, H.T.; Medintz, I.L.; Pons, T.; Delehanty, J.B.; Mattoussi, H. Enhancing the Stability and Biological Functionalities of Quantum Dots via Compact Multifunctional Ligands. *J. Am. Chem. Soc.* **2007**, *129*, 13987–13996.
17. Walther, T. Electron Microscopy of Quantum Dots. *J. Microsc.* **2015**, *257*, 171–178.
18. Ogunkoya, Y.; Nickel, B.M.; Gay, V.L.; Murray, S.A. Using Quantum Dots to Visualize Clathrin Associations. *Biotech. Histochem.* **2009**, *84*, 109–115.
19. Bera, D.; Qian, L.; Tseng, T.K.; Holloway, P.H. Quantum Dots and Their Multimodal Applications: A Review. *Materials* **2010**, *3*, 2260–2345.
20. Killingsworth, M.C.; Bobryshev, Y.V. Correlative Light- and Electron Microscopy Using Quantum Dot Nanoparticles. *J. Vis. Exp.* **2016**, *114*, e54307.
21. Uematsu, M.; Mikami, K.; Nakamura, A.; Takahashi, R.; Yokota, T.; Hirokawa, K.; Uchihara, T. Parallel Gold Enhancement of Quantum Dots 565/655 for Double-Labelling Correlative Light and Electron Microscopy on Human Autopsied Samples. *Sci. Rep.* **2022**, *12*, 6113.
22. Deerinck, T.J. The Application of Fluorescent Quantum Dots to Confocal, Multiphoton, and Electron Microscopic Imaging. *Toxicol. Pathol.* **2008**, *36*, 112–116.
23. Giepmans, B.N.G.; Adams, S.R.; Ellisman, M.H.; Tsien, R.Y. The Fluorescent Toolbox for Assessing Protein Location and Function. *Science* **2006**, *312*, 217–224.

24. Pérez-Garza, J.; Orea, J.; Deane, Z.; Raimondi, G.; Tripp, R.; Charles, I.; Ostroff, L. Ultraplex Microscopy: Versatile Highly-Multiplexed Molecular Labeling and Imaging across Scale and Resolution. *bioRxiv* **2024**. https://doi.org/10.1101/2024.08.17.605585.
25. Wang, X.; Chen, S.; Thota, S.; Wang, Y.; Tan, H.; Tang, M.; Quan, Z.; Zhao, J. Anisotropic Arm Growth in Unconventional Semiconductor CdSe/CdS Nanotetrapod Synthesis Using Core/Shell CdSe/CdS as Seeds. *J. Phys. Chem. C* **2019**, *123*, 19238–19245.
26. Bayer, E.A.; Wilchek, M. Application of Avidin—Biotin Technology to Affinity-Based Separations. *J. Chromatogr. A* **1990**, *510*, 3–11.
27. Michael Green, N. Avidin and Streptavidin. *Methods Enzymol.* **1990**, *184*, 51–67.
28. Chen, Y.; Ren, H.L.; Liu, N.; Sai, N.; Liu, X.; Liu, Z.; Gao, Z.; Ning, A.N. A Fluoroimmunoassay Based on Quantum Dot−Streptavidin Conjugate for the Detection of Chlorpyrifos. *J. Agric. Food Chem.* **2010**, *58*, 8895–8903.
29. Cardoso Dos Santos, M.; Algar, W.R.; Medintz, I.L.; Hildebrandt, N. Quantum Dots for Förster Resonance Energy Transfer (FRET). *Trends Anal. Chem* **2020**, *125*, 115819.
30. Clegg, R.M. Fluorescence Resonance Energy Transfer. *Curr. Opin. Biotechnol.* **1995**, *6*, 103–110.
31. Medintz, I.L.; Clapp, A.R.; Mattoussi, H.; Goldman, E.R.; Fisher, B.; Mauro, J.M. Self-Assembled Nanoscale Biosensors Based on Quantum Dot FRET Donors. *Nat. Mater.* **2003**, *2*, 630–638.
32. Lu, X.; Hou, X.; Tang, H.; Yi, X.; Wang, J. A High-Quality CdSe/CdS/ZnS Quantum-Dot-Based FRET Aptasensor for the Simultaneous Detection of Two Different Alzheimer's Disease Core Biomarkers. *Nanomaterials* **2022**, *12*, 4031.
33. Medintz, I.L.; Mattoussi, H. Quantum Dot-Based Resonance Energy Transfer and Its Growing Application in Biology. *Phys. Chem. Chem. Phys.* **2008**, *11*, 17–45.
34. Clapp, A.R.; Medintz, I.L.; Mauro, J.M.; Fisher, B.R.; Bawendi, M.G.; Mattoussi, H. Fluorescence Resonance Energy Transfer Between Quantum Dot Donors and Dye-Labeled Protein Acceptors. *J. Am. Chem. Soc.* **2003**, *126*, 301–310.
35. McDonald, A.J. Functional Neuroanatomy of the Basolateral Amygdala: Neurons, Neurotransmitters, and Circuits. In *Handbook of Behavioral Neuroscience*; Elsevier: Amsterdam, The Netherlands, 2020; Volume 26, pp. 1–38.
36. McDonald, A.J. Immunohistochemical Identification of γ-Aminobutyric Acid-Containing Neurons in the Rat Basolateral Amygdala. *Neurosci. Lett.* **1985**, *53*, 203–207.
37. Jiang, C.; Chen, Y.; Sun, T. From the Gut to the Brain, Mechanisms and Clinical Applications of γ-Aminobutyric Acid (GABA) on the Treatment of Anxiety and Insomnia. *Front. Neurosci.* **2025**, *19*, 1570173.
38. Shamirian, A.; Samareh Afsari, H.; Hassan, A.; Miller, L.W.; Snee, P.T. In Vitro Detection of Hypoxia Using a Ratiometric Quantum Dot-Based Oxygen Sensor. *ACS Sens.* **2016**, *1*, 1244–1250.
39. Tosat-Bitrián, C.; Avis-Bodas, A.; Porras, G.; Borrego-Hernández, D.; García-Redondo, A.; Martín-Requero, A.; Palomo, V. CdSe Quantum Dots in Human Models Derived from ALS Patients: Characterization, Nuclear Penetration Studies and Multiplexing. *Nanomaterials* **2021**, *11*, 671.
40. Le, P.; Lim, S.J.; Baculis, B.C.; Chung, H.J.; Kilian, K.A.; Smith, A.M. Counting Growth Factors in Single Cells with Infrared Quantum Dots to Measure Discrete Stimulation Distributions. *Nat. Commun.* **2019**, *10*, 909.
41. Zrazhevskiy, P.; Gao, X. Quantum Dot Imaging Platform for Single-Cell Molecular Profiling. *Nat. Commun.***2013**, *4*, 1619.
42. Wu, J.K.; Tian, Z.Q.; Zhang, Z.L.; Liu, A.A.; Tang, B.; Zhang, L.J.; Chen, Z.L.; Pang, D.W. Purification of Quantum Dot-Based Bioprobes via High-Performance Size Exclusion Chromatography. *Talanta* **2016**, *159*, 64–73.

Materials and Interfaces

Scilight

Article

Check for updates

Semiconductor SERS Platform Enables Rapid Discrimination of Structurally Similar Flavonoids in Multicomponent Systems

Haisu Wang [1], Siqi Li [1], Yuting Song [1], Yanguo Guo [1], Junbo Li [1], Lei Sun [1,*], Yunfei Xie [2,*], and Wei Ji [1,*]

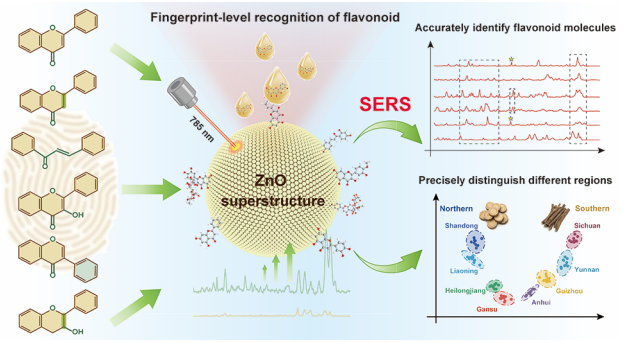
[1] College of Chemistry, Chemical Engineering and Resource Utilization, Northeast Forestry University, Harbin 150040, China

[2] State Key Laboratory of Food Science and Resources, School of Food Science and Technology, Jiangnan University, Wuxi 214122, China

* Correspondence: slei@nefu.edu.cn (L.S.); xieyunfei@jiangnan.edu.cn (Y.X.); jiwei@nefu.edu.cn (W.J.)

Received: 14 June 2026; Revised: 29 July 2026; Accepted: 14 August 2026; Published: 26 August 2026

Abstract: Rapid and reliable discrimination of structurally similar small molecules in complex systems remains a significant challenge for chemical sensing, particularly when subtle structural variations lead to highly overlapping spectral features. Herein, we develop a semiconductor surface-enhanced Raman scattering (SERS) platform based on ZnO superstructures for the reliable discrimination of structurally similar flavonoids in both single-component and multicomponent systems. The ZnO-based SERS platform enables the generation of molecule-specific spectral fingerprints, with characteristic variations in both skeletal vibration and functional group regions, allowing effective differentiation of closely related flavonoids. By integrating multivariate statistical analysis, robust classification, and discrimination of flavonoids with highly similar structures were achieved, including in mixed-component systems. The practical applicability of the platform is further validated using real plant-derived samples, where distinct spectral signatures enable effective discrimination of samples with different compositional profiles, thereby demonstrating its capability for botanical origin authentication. Notably, the proposed approach allows rapid analysis with minimal sample pretreatment and without the need for chromatographic separation. These results demonstrate that ZnO-based semiconductor SERS sensing provides a robust and scalable strategy for the detection and discrimination of structurally similar flavonoids in complex systems, highlighting its practical applicability for quality control and authenticity assessment in food and plant-derived materials.



Keywords: SERS; ZnO superstructures; flavonoids; multicomponent analysis; semiconductor sensing

1. Introduction

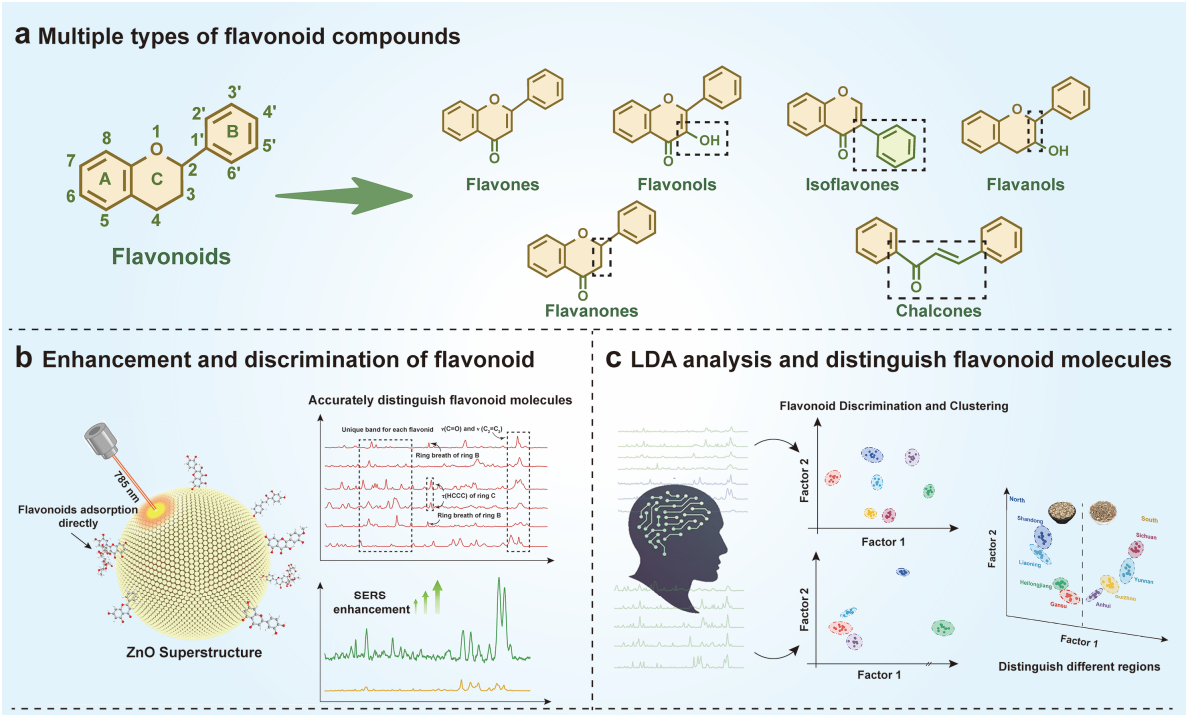
Rapid and reliable discrimination of structurally similar small molecules in complex systems remains a significant challenge in chemical sensing, particularly when subtle variations in molecular structure led to highly overlapping spectral features [1,2]. Such challenges are frequently encountered in plant-derived systems, where structurally related compounds coexist and exhibit minor differences in functional groups and substitution patterns [3,4]. Flavonoids, which are widely distributed in plant-derived systems and are known for their antioxidant and bioactive properties, are a representative class of such compounds, characterized by a common C6–C3–C6 framework with diverse substitution patterns and oxidation states [5–7] (Scheme 1a). These structural variations result in highly similar molecular backbones but subtle differences in functional groups, making their rapid identification and discrimination in complex matrices particularly challenging. Due to their structural diversity

Copyright: © 2026 by the authors. This is an open access article under the terms and conditions of the Creative Commons Attribution (CC BY) license (https://creativecommons.org/licenses/by/4.0/).
Publisher's Note: Scilight stays neutral with regard to jurisdictional claims in published maps and institutional affiliations.

and abundance, flavonoids are often used as characteristic markers for compositional evaluation of plant-derived materials. Therefore, developing effective analytical strategies for distinguishing structurally similar flavonoids is of considerable importance for compositional analysis and quality evaluation of plant-derived materials.

Surface-enhanced Raman scattering (SERS) provides molecular fingerprint specificity, rapid detection, minimal sample pretreatment, and low sample consumption, making it a promising tool for chemical sensing applications [8–17]. While noble-metal substrates can deliver high sensitivity, their practical use is often limited by cost, oxidation instability, and the need for surface modification [18–21]. In contrast, semiconductor-based SERS substrates offer improved chemical stability and can facilitate molecule-specific interactions through charge-transfer mechanisms [22–24]. In particular, ZnO is capable of interacting with hydroxyl-rich flavonoids via surface Zn^{2+} sites and hydroxyl groups, enabling adsorption-dependent signal modulation and enhancing sensitivity to subtle structural differences [25]. These interactions further modulate charge-transfer processes between ZnO and adsorbed molecules, providing a basis for selective enhancement of vibrational modes.

In this work, we develop a ZnO superstructure-based SERS platform for the discrimination of structurally similar flavonoids (Scheme 1b). The platform enables the generation of distinct spectral fingerprints while preserving intrinsic molecular vibrational features. By integrating chemometric analysis, reliable classification of flavonoids is achieved in both single-component and multicomponent systems. To demonstrate practical applicability, Isatis Root (Banlangen), a plant-derived material with known compositional variability, was selected as a representative system (Scheme 1c). Notably, northern and southern Isatis Root in China originate from different botanical sources and exhibit distinct chemical profiles, particularly in flavonoid composition [26]. These differences provide a suitable model system for evaluating the capability of the proposed SERS platform in discriminating complex samples with subtle compositional variations [27,28]. This approach provides a rapid and practical strategy for the analysis of structurally similar compounds in complex systems.



Scheme 1. Conceptual illustration of SERS-based flavonoid discrimination and application workflow. (**a**) Representative structural classes of flavonoids. (**b**) Schematic illustration of SERS-based molecular fingerprinting of flavonoids on ZnO superstructure substrates. (**c**) Taking northern and southern Isatis Roots as examples, distinguished and classified flavonoids from different plant sources.

2. Experimental Section

2.1. Chemicals

Zinc acetate dihydrate, diethylene glycol, absolute ethanol, chromatographic-grade methanol, luteolin, chrysin, rutin, quercetin, and kaempferol were purchased from Aladdin Chemistry Co., Ltd. (Shanghai, China). Isorhamnetin, naringenin, liquiritigenin, L-epicatechin, genistein, isoliquiritigenin, linarin, and neohesperidin were obtained from Rhawn Chemical Technology Co., Ltd. (Shanghai, China). Traditional Chinese medicinal samples

were collected from Shandong, Gansu, Liaoning, Heilongjiang, Sichuan, Yunnan, Guizhou, and Anhui provinces, China. All solutions were prepared using analytical-grade reagents and Milli-Q water.

2.2. Characterization Methods

Scanning electron microscopy (SEM) images were acquired using a JSM-7500F field-emission scanning electron microscope (JEOL Ltd., Tokyo, Japan). X-ray diffraction (XRD) patterns were recorded on a Shimadzu XRD-6100 diffractometer with Cu Kα radiation (λ = 1.5406 Å) at room temperature (Shimadzu Corporation, Kyoto, Japan). Raman and SERS spectra were measured using a Raman spectrometer (Zolix Finder Insight FI785-Pro) equipped with a 785 nm excitation laser (Zolix Instruments Co., Ltd., Beijing, China). The instrument was calibrated using the 520.7 cm^{-1} vibrational band of a silicon wafer.

2.3. Synthesis of ZnO Superstructures

ZnO superstructures were synthesized via a solvothermal method. Briefly, 0.01 mol of zinc acetate dihydrate was dissolved in 100 mL of diethylene glycol and heated slowly to 160 °C under magnetic stirring for 1 h, forming a turbid colloidal suspension. After cooling to room temperature, the suspension was centrifuged, and the supernatant was collected as the seed solution. Subsequently, another 0.01 mol of zinc acetate dihydrate was dissolved in 100 mL of diethylene glycol and heated to 130 °C. Then, 0.3 mL of the seed solution was introduced into the hot solution, and the temperature was rapidly increased to 160 °C and maintained for 1 h to obtain spherical ZnO particles. The resulting nanoparticles were collected by centrifugation, washed three times with distilled water and absolute ethanol, and finally dried in a vacuum oven at 60 °C for 12 h before use.

2.4. Preparation of Chinese Medicine Samples and SERS Measurements

Chinese medicinal samples from different geographical origins were ground into fine powders using a grinder. Approximately 0.5 g of powder was dispersed in chromatographic-grade methanol and ultrasonically extracted for 90 min. The organic phase was collected and concentrated to dryness under reduced pressure using a rotary evaporator. Prior to LC–MS/MS analysis, the extract was re-dissolved in 10 mL of methanol and filtered through a 0.45 μm nylon membrane. For SERS measurements, 10 μL of the crude extract was dropped onto a ZnO superstructure substrate dispersed in ethanol and allowed to dry naturally. The flavonoid signals were directly recorded using a 785 nm Raman spectrometer with a laser power of 20 mW and an acquisition time of 3 s. The obtained spectra were baseline-corrected and smoothed using LabSpec 5 software (Version) prior to further analysis.

2.5. LDA Analysis of SERS Spectra

Linear discriminant analysis (LDA) was performed using the SERS spectra of crude Chinese medicinal samples extracts collected over the range of 200–2000 cm^{-1}. All spectra were preprocessed by baseline correction and smoothing before analysis in SPSS Statistics 25.0. The processed data were subsequently visualized and further analyzed using Origin 2023 to generate two-dimensional LDA score plots, enabling effective discrimination among different flavonoids and TCM samples from various geographical origins.

3. Result and Discussion

3.1. Analytical Performance of ZnO Superstructure-Based SERS Platform

The ZnO superstructure substrate was designed and evaluated with a focus on its analytical suitability for SERS-based flavonoid analysis. The near-field scattering efficiency (Q_{NF}) of spherical ZnO particles was theoretically calculated based on Mie theory (Figure 1a,b), indicating that particles with a diameter around 400 nm led to enhanced local electric-fields under 785 nm excitation. This size-dependent optical response provides a rational basis for optimizing SERS performance. Based on this consideration, ZnO superstructures were synthesized via a polyol-mediated precipitation method, forming uniform spherical architectures assembled from nanoscale primary particles [8]. As shown in Figure 1c,d, the structures exhibit good morphological uniformity with an average diameter of approximately 492.62 ± 2.02 nm, which is beneficial for achieving reproduceable SERS responses. X-ray diffraction analysis (Figure 1e) confirms the formation of phase-pure hexagonal wurtzite ZnO, ensuring structural reliability of the sensing substrate.

The SERS performance of the ZnO superstructures was evaluated using rutin as a model analyte (Figure 1f). The obtained SERS spectrum shows peak positions highly consistent with its intrinsic Raman spectrum, indicating that the platform preserves characteristic molecular vibrational features. In contrast, Ag substrate yields weak and

limited signals due to the lack of adsorption sites for rutin molecules. The superior performance of ZnO is attributed to its ability to facilitate direct interaction with hydroxyl-rich flavonoid molecules, enabling efficient signal transduction without additional surface modification. To further evaluate the generality of the platform, the SERS spectra of multiple representative flavonoids were collected and compared with their intrinsic Raman spectra (Figures S1–S7). The results show that ZnO superstructures not only provide significant signal enhancement but also largely preserve intrinsic vibrational features, demonstrating their suitability for fingerprint-based discrimination of structurally similar compounds. To evaluate the reproducibility of the ZnO superstructure-based SERS platform, repeated measurements were performed for representative flavonoid molecules, and the corresponding relative standard deviation (RSD) values were calculated (Figure S8). The obtained RSD values ranged from 2.76% to 4.86% among the 13 investigated flavonoids, demonstrating high spectral reproducibility of the substrate. The low variation among repeated measurements can be attributed to the uniform morphology of ZnO superstructures and the stable molecule substrate interactions, confirming their suitability for reliable flavonoid sensing and discrimination.

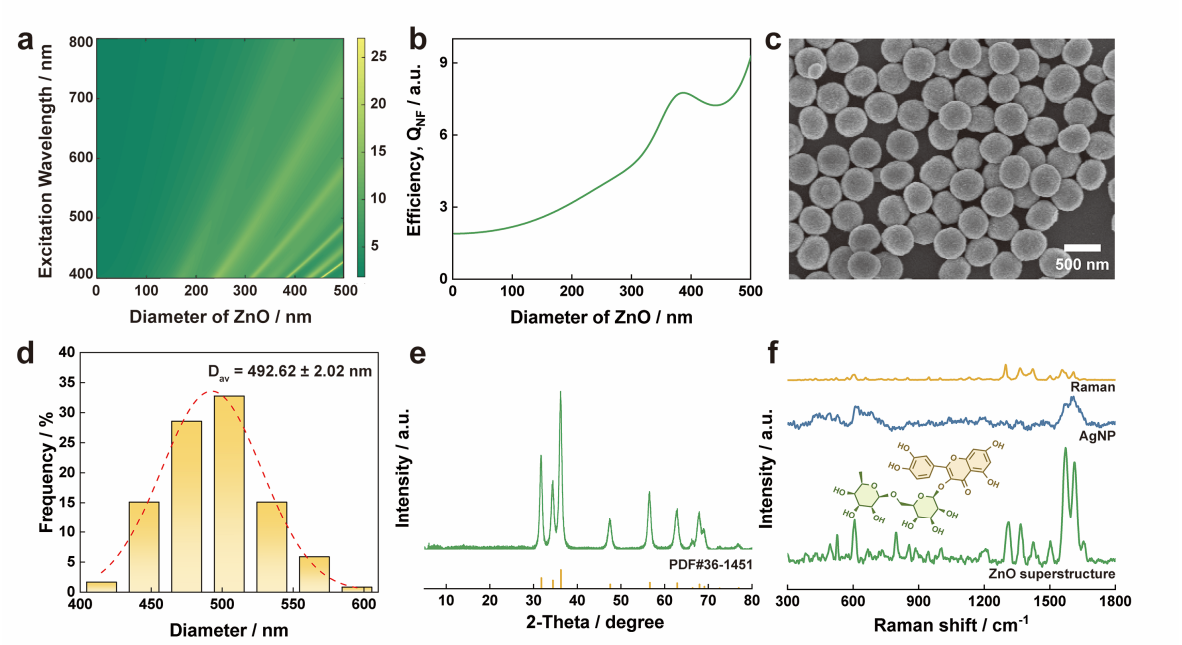


Figure 1. Structural characterization and SERS performance of ZnO superstructures. (**a**) Calculated near-field scattering efficiency of ZnO microspheres as a function of incident wavelength and particle diameter. (**b**) Near-field scattering efficiency of ZnO particles as a function of particle diameter under 785 nm excitation. (**c**) SEM image of ZnO superstructures. (**d**) Particle size distribution of ZnO superstructures. (**e**) XRD pattern of ZnO superstructures. (**f**) SERS spectra of rutin obtained on ZnO superstructures (green) and Ag nanoparticle (AgNP) substrates (blue), together with the intrinsic Raman spectrum of rutin powder (yellow).

The enhanced SERS activity of ZnO superstructures can be attributed to the synergistic effect of adsorption-dependent interactions, charge-transfer (CT) enhancement, and size-induced electric field enhancement. Flavonoid molecules containing hydroxyl and carbonyl groups can strongly interact with surface Zn^{2+} sites and hydroxyl groups, leading to favorable adsorption configurations and enhanced electronic coupling. These interactions facilitate charge-transfer transitions between ZnO and the adsorbed molecules, which selectively enhance specific vibrational modes. In addition, the optimized particle size contributes to Mie resonance-induced local field enhancement, further improving the overall SERS response. The synergistic effect of these factors enables sensitive and discriminative detection of structurally similar flavonoids.

3.2. Spectral Fingerprints and Discrimination of Individual Flavonoids

To evaluate the capability of the ZnO-based SERS platform for discriminating structurally similar molecules, representative flavonoids with different substitution patterns and structural types were systematically investigated (Figure 2). Despite sharing a common C6–C3–C6 backbone, variations in the type, position, and number of substituents on the A, B, and C rings underpin the structural diversity of flavonoid molecules. According to their structural characteristics, six representative flavonoids from distinct structural subclasses, including chrysin

(flavone), quercetin (flavonol), naringenin (flavanone), epicatechin (flavanol), genistein (isoflavone), and isoliquiritigenin (chalcone), were selected to be systematically investigated (Figure 2). To systematically evaluate the discrimination capability of the proposed SERS platform, structurally similar flavonoids within the same subclass were first selected to assess its sensitivity to subtle molecular variations, followed by representative flavonoids from different subclasses to evaluate its ability to distinguish broader structural differences.

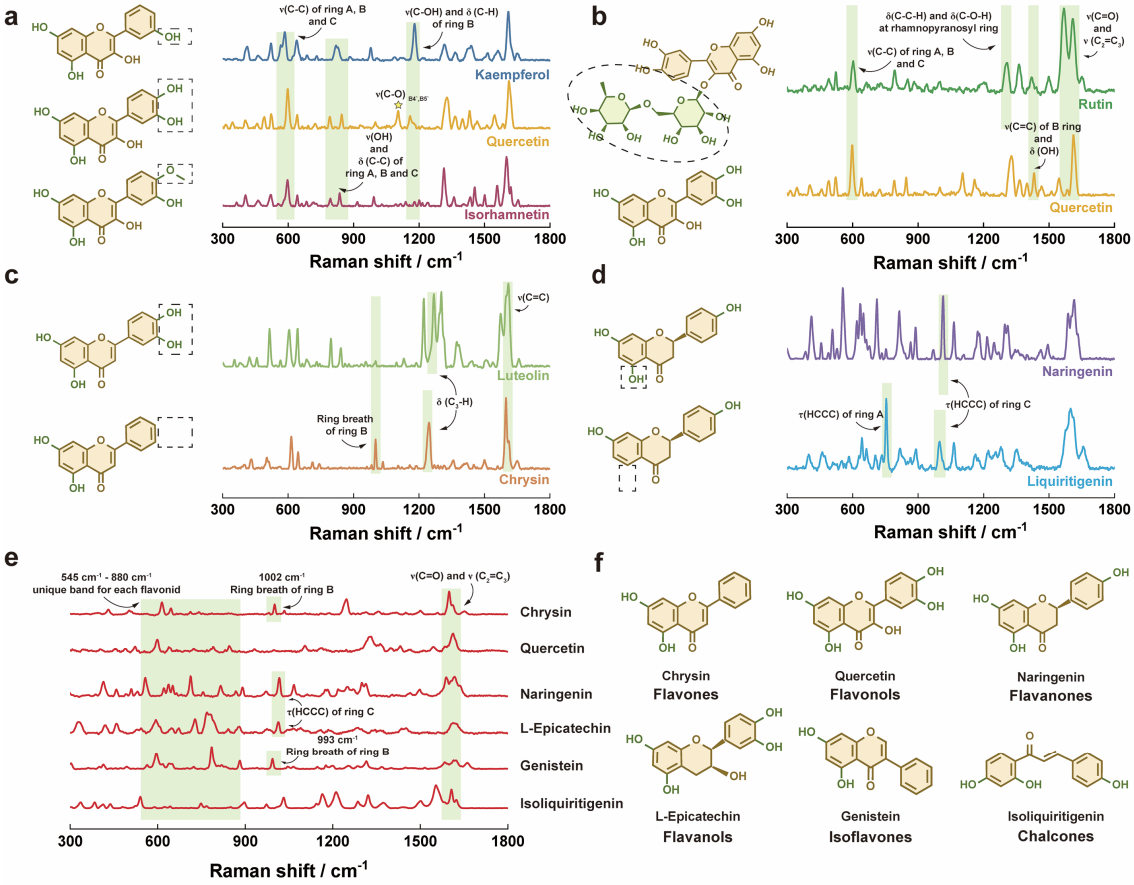


Figure 2. SERS spectral fingerprints of representative flavonoids. (**a**) Chemical structures and SERS spectra of three flavonols: kaempferol, quercetin, and isorhamnetin. (**b**) Chemical structures and SERS spectra of rutin and quercetin. (**c**) Chemical structures and SERS spectra of luteolin and chrysin. (**d**) Chemical structures and SERS spectra of naringenin and liquiritigenin. (**e**) SERS spectra of six representative flavonoid subclasses: chrysin (flavone), quercetin (flavonol), naringenin (flavanone), epicatechin (flavanol), genistein (isoflavone), and isoliquiritigenin (chalcone). (**f**) Corresponding chemical structures of the six flavonoids shown in (**e**).

Kaempferol, quercetin, and isorhamnetin are representative flavonols (Figure 2a). Specifically, kaempferol contains a single hydroxyl group at the 5′ position of the B ring; quercetin possesses two hydroxyl groups at the 4′ and 5′ positions; and isorhamnetin is derived from quercetin via substitution of the 4′-hydroxyl group with a methoxy group. Although these structural differences are subtle, their SERS spectra exhibit clear and reproducible distinctions. For kaempferol, the C–C stretching vibrations of the A, B, and C rings split into two characteristic peaks at 567 and 581 cm^{-1} whereas the corresponding vibrations of quercetin and isorhamnetin appear as a single peak at 595 cm^{-1}. Quercetin and isorhamnetin both exhibit two peaks at 787 and 848 cm^{-1}, attributed to ring vibrations involving O–H and C–C modes, while kaempferol shows only one peak at 820 cm^{-1} [29]. In addition, kaempferol presents a strong peak at 1178 cm^{-1} assigned to C–OH stretching and C–H bending vibrations of the B ring, whereas quercetin displays two overlapping peaks at 1161 and 1176 cm^{-1}, and no prominent peak is observed for isorhamnetin in this region. Notably, quercetin exhibits a unique peak at 1102 cm^{-1}, which is absent in kaempferol and isorhamnetin, providing a useful diagnostic feature associated with the presence of adjacent hydroxyl groups on the B ring.

Quercetin and rutin belong to different subclasses of flavonoids. Quercetin is a flavonol, whereas rutin is a flavonol glycoside formed by linking the 3-hydroxyl group of the aglycone to a rutinose moiety via a glycosidic bond. Compared with quercetin, rutin contains additional hydroxyl groups and exhibits a more complex molecular

structure (Figure 2b). Their SERS spectra are highly similar below 900 cm^{-1}; however, at approximately 600 cm^{-1}, the C–C stretching vibration shows markedly higher intensity for quercetin than that for rutin. Rutin exhibits a broad band spanning 1390–1490cm^{-1} with a sharp peak at 1419 cm^{-1}, corresponding to the peak at 1430 cm^{-1} for quercetin, both assigned to C=C stretching and O–H bending vibrations of the B ring [30]. Furthermore, rutin displays two peaks of comparable intensity at 1567 and 1607 cm^{-1}, which are attributed to C=O stretching and C_2=C_3 stretching vibrations, whereas quercetin shows only a single peak at 1612 cm^{-1}. These differences provide effective spectral markers for distinguishing glycosylated and non-glycosylated flavonoids.

Luteolin and chrysin are both flavones, differing from flavonols by the absence of a hydroxyl group at the 3′ position. The key structural difference lies in the presence of two adjacent hydroxyl groups on the B ring of luteolin, whereas chrysin lacks substituents on its B ring (Figure 2c). In the SERS spectra, chrysin exhibits a distinct peak at 1002 cm^{-1} that is absent in luteolin, attributable to an undisturbed ring-breathing vibration enabled by the unsubstituted B ring [31–33]. In the range of 1200–1320 cm^{-1}, chrysin displays a single strong peak at 1244 cm^{-1} assigned to C_3–H bending vibration, while luteolin shows three distinct peaks, among which the peak at 1269 cm^{-1} shares the same vibrational assignment as the 1244 cm^{-1} peak of chrysin. Additionally, luteolin presents two characteristic peaks at 1574 and 1609 cm^{-1}, whereas chrysin exhibits a single, relatively broad peak at 1598 cm^{-1} corresponding to C=C stretching vibration. These features enable reliable differentiation between substituted and unsubstituted B-ring structures.

Naringenin and liquiritigenin are flavanones characterized by fully saturated C-ring positions at C_2 and C_3. Compared with liquiritigenin (Figure 2d), naringenin contains an additional hydroxyl group at the 5 position of the A ring, which enhances its interaction with the ZnO surface and results in stronger SERS signals. In addition to intensity differences, distinct spectral features are observed: liquiritigenin exhibits a sharp peak at 752 cm^{-1} attributed to A-ring torsional vibration, while peaks associated C-ring torsional vibration appear at 1022 cm^{-1} for naringenin and 995 cm^{-1} for liquiritigenin, with the latter showing substantially lower intensity [34,35].

These spectral differences can be attributed to structure-dependent adsorption configurations and interfacial electronic interactions between flavonoids and the ZnO surface. Hydroxyl and carbonyl groups in flavonoids can interact with surface Zn^{2+} sites and hydroxyl groups, leading to different adsorption geometries. Variations in adsorption configuration affect the degree of orbital overlap and electronic coupling, thereby modulating charge-transfer processes between ZnO and the adsorbed molecules. As a result, specific vibrational modes are selectively enhanced, and small peak shifts are observed in the SERS spectra. These differences further demonstrate the sensitivity of the ZnO-based SERS platform to subtle structural variations.

Accordingly, systematic spectral assignment and comparison were conducted for representative flavonoids across multiple subclasses. All flavonoids exhibit distinct fingerprint features, particularly within the 545–880 cm^{-1} region (Figure 2e), which serves as a key spectral window for classification [32]. For molecules lacking B-ring substituents, such as chrysin and genistein, display characteristic B-ring breathing vibrations near 1000 cm^{-1}, whereas flavanones and flavanols with saturated C rings show characteristic torsional modes near 1015 cm^{-1}. In addition, variations in peak position, intensity, and line shape within the 1580–1630 cm^{-1} region, corresponding to C=O and C_2=C_3 stretching vibrations, further contribute to molecular differentiation. These results collectively establish a set of diagnostic spectral features for flavonoid identification and provide a robust analytical basis for resolving structurally similar compounds. Importantly, the well-defined and reproducible spectral differences observed here lay the foundation for extending this approach to the analysis of multicomponent systems, as discussed in the following section.

3.3. Discrimination of Flavonoids in Multicomponent Systems

The capability of the ZnO-based SERS platform for resolving structurally similar flavonoids was further evaluated in multicomponent systems. Mixed detection of structurally related molecules provides a direct assessment of analytical applicability and further validates the diagnostic spectral features identified for individual compounds. To this end, representative flavonoid subclasses, including flavones and flavonols, were selected for binary and multicomponent mixture analysis.

For flavones, binary mixtures of chrysin and luteolin were prepared at different ratios (Figure S9a–c). As the proportion of chrysin decreased, the characteristic peak at 1002 cm^{-1}, assigned to B-ring breathing vibration, shows a pronounced reduction in intensity. In the 1150–1350 cm^{-1} region, the gradual shift of the in-plane C–H bending vibration from 1244 cm^{-1} toward 1269 cm^{-1} was observed with increasing luteolin content, consistent with the spectral features of the pure components (Figure S9d). These results demonstrate that both intensity variation and peak position shifts can serve as effective indicators for resolving structurally similar flavonoids in binary systems.

Similar mixture experiments were conducted for two flavonols, including kaempferol and quercetin (Figure 3a–c). Samples 1–4 corresponded to kaempferol/quercetin molar ratios of 4:1, 3:2, 2:3, and 1:4, respectively. As shown in Figure 3d, in the 555–620 cm^{-1} region, when quercetin predominated in sample 4, the C–C stretching vibration of the A, B, and C rings was dominated by a strong peak at 597 cm^{-1}, with the 585 cm^{-1} peak appearing as a shoulder. As the quercetin content decreased, this dominant peak gradually shifted toward 585 cm^{-1}, while the characteristic kaempferol peak at 567 cm^{-1} increased markedly with increasing kaempferol proportion. Meanwhile, in the 750–900 cm^{-1} region, the evolution from a single peak (820 cm^{-1}, kaempferol) to two distinct peaks (787 and 848 cm^{-1}, quercetin) further confirms the composition-dependent spectral response. In addition, the intensity of the kaempferol-specific peak at 1178 cm^{-1} decreased systematically with decreasing kaempferol proportion. These results indicate that the SERS spectra provide consistent and composition-sensitive features for distinguishing flavonol mixtures.

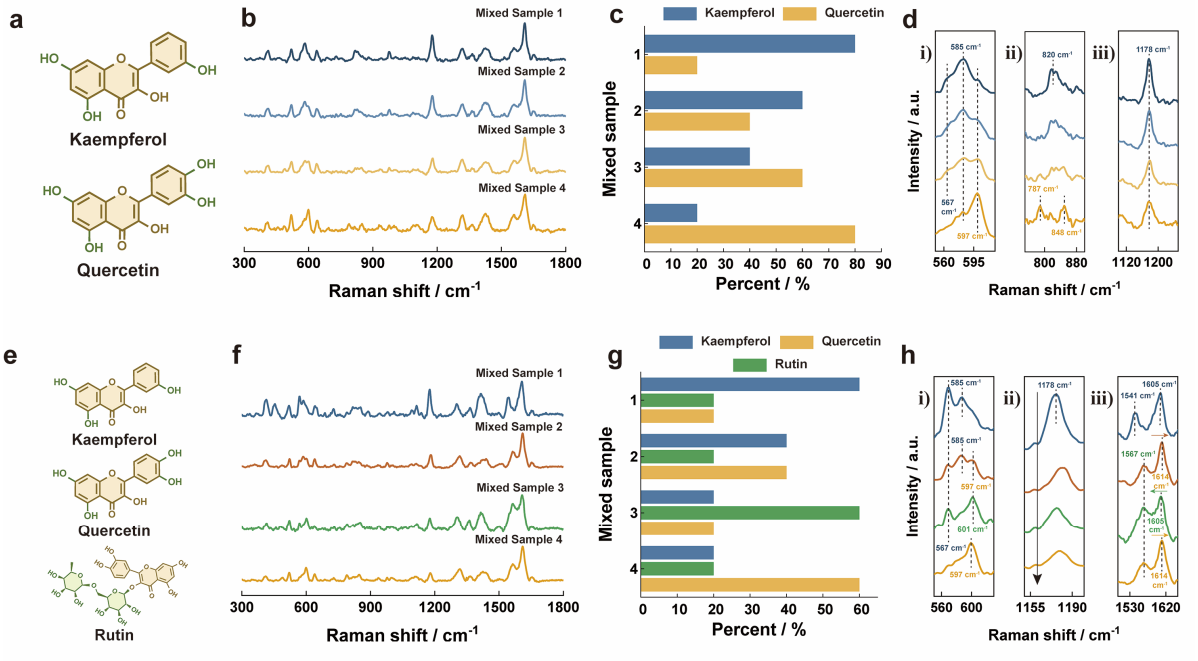


Figure 3. SERS analysis of binary and ternary flavonoid mixtures. (**a**–**d**) Binary mixtures of kaempferol and quercetin: (**a**) chemical structures; (**b**) SERS spectra; (**c**) composition ratios; (**d**) expanded spectral regions (555–620, 750–900, and 1110–1250 cm^{-1}). (**e**–**h**) Ternary mixtures of kaempferol, quercetin, and rutin: (**e**) chemical structures; (**f**) SERS spectra; (**g**) composition ratios; (**h**) expanded spectral regions (550–630, 1150–1200, and 1500–1650 cm^{-1}). Binary mixtures were prepared at molar ratios of 4:1, 3:2, 2:3, and 1:4, while ternary mixtures were prepared at molar ratios of 3:1:1, 2:1:2, 1:3:1, and 1:1:3. For all binary and ternary mixtures, the total flavonoid concentration was fixed at 10^{-3} M, and the concentration of each component was calculated according to its stated molar fraction. For the binary ratios of 4:1, 3:2, 2:3, and 1:4, the corresponding component concentrations were 8.0/2.0, 6.0/4.0, 4.0/6.0, and 2.0/8.0 × 10^{-4} M, respectively. For the ternary ratios of 3:1:1, 2:1:2, 1:3:1, and 1:1:3, the corresponding concentrations were 6.0/2.0/2.0, 4.0/2.0/4.0, 2.0/6.0/2.0, and 2.0/2.0/6.0 × 10^{-4} M, respectively.

To further evaluate the discrimination of glycosylated and non-glycosylated species, mixtures of rutin and quercetin were analyzed (Figure S9a–c). With increasing quercetin content, the intensity of the C–C stretching vibration near 597 cm^{-1} increased correspondingly. In the 1380–1470 cm^{-1} region, the spectral profile of the mixtures gradually evolved from the broad band characteristic of rutin toward that of quercetin, reflecting differences in molecular structure and hydrogen-bonding interactions. In the high-wavenumber region, the peak near 1607 cm^{-1} gradually shifted toward 1612 cm^{-1} with increasing quercetin proportion, accompanied by an increase in intensity (Figure S10d). These composition-dependent spectral changes enable effective differentiation between glycoside and aglycone forms.

Furthermore, ternary mixture experiments involving kaempferol, quercetin, and rutin were performed to evaluate the performance of the platform in more complex systems (Figure 3e–g). Across all samples, the SERS spectra retained characteristic features of the individual components, particularly in the regions of 550–630 cm^{-1} and 1500–1650 cm^{-1}. The intensity variation of characteristic peaks, such as the kaempferol-specific band at 1178 cm^{-1}, closely followed the changes in composition, while minor peak shifts further reflected differences in molecular

interactions (Figure 3h). Collectively, these results demonstrate that the ZnO-based SERS platform provides composition-dependent and reproducible spectral responses, enabling reliable discrimination of structurally similar flavonoids in both binary and multicomponent systems without chromatographic separation.

3.4. Application to Real Samples: Authentication of Isatis Root

Isatis Root is one of the most widely used traditional Chinese medicinal materials and is rich in flavonoid bioactive components, including quercetin, liquiritigenin, and isorhamnetin [6,32]. Notably, northern Isatis Root (derived from *Isatis indigotica* Fort., Brassicaceae) and southern Isatis Root (derived from *Baphicacanthus cusia* (Nees) Bremek., Acanthaceae) differ significantly in botanical origin, chemical composition, and pharmacological activity [27,28,36,37]. Accurate discrimination between northern and southern Isatis Root is therefore important for compositional analysis and quality evaluation.

Flavonoid components were extracted from commercially available samples using ultrasonic extraction. LC–MS/MS analysis was first employed as a reference method (Figures 4a,b and S11–S13), confirming distinct compositional profiles between northern and southern Isatis Root. Northern samples were found to predominantly contain kaempferol, rutin, neohesperidin, linarin, liquiritigenin, quercetin, and isorhamnetin, whereas southern samples were enriched in quercetin, kaempferol, isorhamnetin, epicatechin, and luteolin [38,39]. These compositional differences provide a chemical basis for subsequent SERS-based discrimination. The ZnO superstructures were subsequently used as SERS substrates to analyze the extracted samples, and linear discriminant analysis (LDA) was applied for classification (Figure 4c,f). The results demonstrate that distinct SERS spectral signatures corresponding to different flavonoid compositions were observed, and LDA yielded well-separated clusters, demonstrating the capability of the method for reliable discrimination of samples with different botanical origins. To further elucidate the spectral variables responsible for sample discrimination, principal component loading analysis was performed as a variable contribution assessment (Figure S14). The loading plots of PC1 and PC2 illustrate the contribution of individual Raman shift variables to the corresponding principal components. Raman variables with higher absolute loading coefficients represent spectral regions that contribute more significantly to the differentiation of samples. Several characteristic Raman regions exhibited relatively large loading coefficients, suggesting that these vibrational features play important roles in describing the spectral differences among Isatis Root samples. These discriminative regions are mainly associated with molecular skeletal vibrations and functional group vibrations of flavonoid-related components.

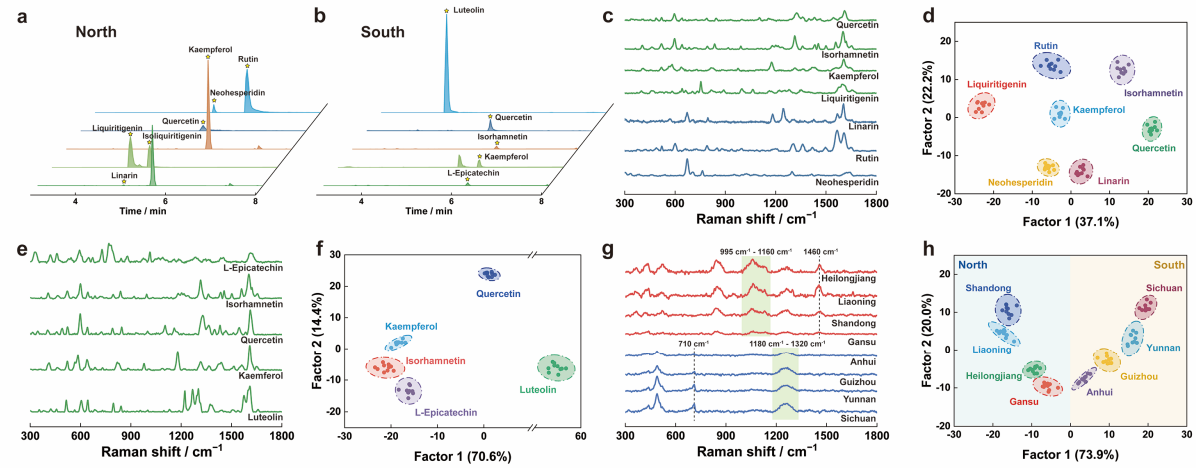


Figure 4. Application of the ZnO-based SERS platform for discrimination of plant-derived samples. (**a**,**b**) LC–MS/MS analysis of flavonoid composition in crude extracts of northern (Heilongjiang) and southern (Sichuan) Isatis Root. (**c**,**d**) Representative flavonoids in northern Isatis Root: (**c**) SERS spectra (10^{-3} M) of quercetin, isorhamnetin, kaempferol, liquiritigenin, linarin, rutin, and neohesperidin; (**d**) corresponding LDA score plot. (**e**,**f**) Representative flavonoids in southern Isatis Root: (**e**) SERS spectra (10^{-3} M) of epicatechin, isorhamnetin, quercetin, kaempferol, and luteolin; (**f**) corresponding LDA score plot. (**g**,**h**) Analysis of crude extracts from multiple regions: (**g**) SERS spectra of ultrasonic extracts from northern (red) and southern (blue) Isatis Root samples; (**h**) LDA score plot of samples collected from eight different regions.

To further evaluate practical applicability, Isatis Root samples collected from eight provinces across northern and southern China were analyzed (Figure 4g–h). Although the overall spectral profiles are similar due to shared

flavonoid components, clear differences in characteristic peak intensities were observed, enabling discrimination of geographical origin (Figure 4g). Northern samples exhibit prominent peaks in the 995–1160 cm^{-1} region, associated with C-ring torsional vibrations in liquiritigenin, along with a distinct peak at 1460 cm^{-1} attributed to C_3–H bending vibration of rutin. In contrast, southern samples display a characteristic peak at 710 cm^{-1} related to C–C stretching vibrations of rings A, B, and C in epicatechin, as well as a broad band in the 1180–1320 cm^{-1} region corresponding to C_3–H bending vibration of luteolin. These spectral differences enabled effective discrimination of geographical origin.

The LDA results exhibit clear clustering of samples from different provinces, with all samples falling within their respective 95% confidence ellipses, and more importantly, northern and southern samples symmetrically separated on opposite sides of the zero axis (Figure 4h). Notably, this differentiation was achieved without chromatographic separation and with minimal sample pretreatment. These findings demonstrate that ZnO-based SERS combined with multivariate statistical analysis offers a powerful and reliable strategy for the classification and identification of traditional Chinese medicine samples, highlighting its potential for quality control and origin discrimination in complex plant-derived systems.

4. Conclusions

In conclusion, we developed a ZnO superstructure-based semiconductor SERS platform for the rapid discrimination of structurally similar flavonoids. The optimized ZnO architectures provide effective molecule substrate interactions and enhanced charge transfer processes, enabling the acquisition of characteristic Raman fingerprints with high spectral reproducibility. By combining SERS with multivariate statistical analysis, the proposed platform successfully differentiated individual flavonoids, multicomponent mixtures, and plant-derived samples with subtle compositional differences. Furthermore, the analysis of real Isatis Root samples demonstrates the potential of this strategy for rapid quality evaluation and authenticity assessment of complex botanical materials. This work highlights the capability of semiconductor SERS platforms for resolving challenging molecular discrimination problems beyond conventional sensitivity-oriented detection, providing a practical approach for chemical sensing and natural product analysis.

Supplementary Materials: The following supporting information can be downloaded at: https://media.sciltp.com/articles/others/2608261533227573/MI-26060131-SM.pdf. Figure S1: Comparison of the SERS spectra (green) and powder Raman spectra (yellow) of chrysin (a) and luteolin (b); Figure S2: Comparison of the SERS spectra (green) and powder Raman spectra (yellow) of kaempferol (a), quercetin (b) and isorhamnetin (c); Figure S3: Comparison of the SERS spectra (green) and powder Raman spectra (yellow) of naringenin (a) and liquiritigenin (b); Figure S4: Comparison of the SERS spectra (green) and powder Raman spectra (yellow) of neohesperidin (a) and linarin (b); Figure S5: Comparison of the SERS spectra (green) and powder Raman spectra (yellow) of isoliquiritigenin; Figure S6: Comparison of the SERS spectra (green) and powder Raman spectra (yellow) of L-epicatechin; Figure S7: Comparison of the SERS spectra (green) and powder Raman spectra (yellow) of genistein; Figure S8: Reproducibility evaluation of ZnO superstructure-based SERS measurements. (a–m) Repeated SERS spectra and corresponding RSD values of 13 representative flavonoids, including chrysin, luteolin, kaempferol, quercetin, isorhamnetin, naringenin, liquiritigenin, neohesperidin, linarin, rutin, isoliquiritigenin, L-epicatechin, and genistein; Figure S9: (a–d) Binary mixtures of chrysin and luteolin: (a) chemical structures; (b) SERS spectra (10^{-3} M); (c) composition ratios; (d) expanded spectral regions (950–1050, 1150–1350, and 1550–1650 cm^{-1}). Binary mixtures were prepared at molar ratios of 4:1, 3:2, 2:3, and 1:4, corresponding to individual concentrations of 8.0×10^{-4} and 2.0×10^{-4} M, 6.0×10^{-4} and 4.0×10^{-4} M, 4.0×10^{-4} and 6.0×10^{-4} M, and 2.0×10^{-4} and 8.0×10^{-4} M, respectively; Figure S10: (a–d) Binary mixtures of rutin and quercetin: (a) chemical structures; (b) SERS spectra; (c) composition ratios; (d) expanded spectral regions (550–650, 1380–1470, and 1500–1650 cm^{-1}). Binary mixtures were prepared at molar ratios of 4:1, 3:2, 2:3, and 1:4, corresponding to individual concentrations of 8.0×10^{-4} and 2.0×10^{-4} M, 6.0×10^{-4} and 4.0×10^{-4} M, 4.0×10^{-4} and 6.0×10^{-4} M, and 2.0×10^{-4} and 8.0×10^{-4} M, respectively; Figure S11: Extracted ion chromatogram and mass chromatograph of Northern Isatis Root (Heilongjiang); Figure S12: Extracted ion chromatogram and mass chromatograph of Southern Isatis Root (Sichuan); Figure S13. HPLC Chromatograms of Crude Extracts from Northern (Heilongjiang) and Southern (Sichuan) Isatidis Root; Figure S14. Loading plots of principal components from LDA analysis of Isatis Root samples. (a,b) Loading plots for northern Isatis Root samples. (c,d) Loading plots for southern Isatis Root samples. (e,f) Loading plots for Isatis Root samples with different geographical origins. Table S1: Regions and assignments of characteristic bands of flavones [1–3]; Table S2: Regions and assignments of characteristic bands of isoflavones [4,5]; Table S3. Regions and assignments of characteristic bands of flavanones [6,7]; Table S4. Regions and assignments of characteristic bands of flavonols [8,9]; Table S5. Regions and assignments of characteristic bands of flavanols [10,11]; Table S6. Regions and assignments of characteristic bands of chalcones [12,13]. References [40–48] are cited in supplementary materials.

Author Contributions: H.W.: Conceptualization, formal analysis, investigation, methodology, writing—original draft. S.L.: Data curation, software. Y.S.: Formal analysis, software. Y.G.: Methodology, software. J.L.: Visualization, methodology. L.S.: Writing—reviewing & editing, supervision, project administration. Y.X.: Writing—reviewing and editing, validation. W.J.: Supervision, validation, conceptualization, formal analysis, writing—review & editing. All authors have read and agreed to the published version of the manuscript.

Funding: This work was supported by the National Natural Science Foundation (22273050, 22073014, and 32261133623) of P. R. China. The authors also acknowledge the support from the Fundamental Research Funds for the Central Universities (2572023CT12), Natural Science Foundation of Heilongjiang Province (LH2024B005), and the Modern Agriculture Grant of Key Research and Development Program of Jiangsu Province (BE2023310).

Institutional Review Board Statement: Not applicable.

Informed Consent Statement: Not applicable.

Data Availability Statement: The data presented in this study are available in the article and Supplementary Materials.

Conflicts of Interest: The authors declare no conflict of interest.

Use of AI and AI-Assisted Technologies: No AI tools were utilized for this paper.

References

1. Chen, J.R.T.; Tan, E.X.; Tang, J.X.; Leong, S.X.; Hue, S.K.X.; Pun, C.S.; Phang, I.Y.; Ling, X.Y. Machine Learning-Based SERS Chemical Space for Two-Way Prediction of Structures and Spectra of Untrained Molecules. *J. Am. Chem. Soc.* **2025**, *147*, 6654–6664.
2. Luo, S.H.; Xu, J.; Wang, W.L.; Xiong, C.R.; Wang, L.P.; Tian, Z.Q.; Liu, G.K. SSNet: A Spectral Unmixing Framework for Enhancing the Qualitative Sensitivity of SERS to Trace Targets in Complex Mixtures. *J. Am. Chem. Soc.* **2025**, *147*, 43964–43972.
3. Son, W.K.; Choi, Y.S.; Han, Y.W.; Shin, D.W.; Min, K.Y.H.; Shin, J.; Lee, M.J.; Son, H.; Jeong, D.H.; Kwak, S.Y. *In vivo* surface-enhanced Raman scattering nanosensor for the real-time monitoring of multiple stress signalling molecules in plants. *Nat. Nanotechnol.* **2023**, *18*, 205–216.
4. Di, H.; Lei, Z.; Li, J.; Li, X. A Highly Sensitive Silver Nanostars/Silver Nanoisland Films Hybrid SERS Platform Assisted by a Convolutional Neural Network for Accurate Pesticide Detection. *J. Agric. Food Chem.* **2026**, *74*, 8707–8719.
5. Xu, Y.M.; Ge, X.Y.; Lv, Y.K.; Yang, Z.E.; Li, F.G.; Yang, Z.R. Engineering plant hosts for high-efficiency accumulation of flavonoids: Advances, challenges and perspectives. *Biotechnol. Adv.* **2025**, *84*, 108692.
6. Parmenter, B.H.; Thompson, A.S.; Bondonno, N.P.; Jennings, A.; Murray, K.; Perez-Cornago, A.; Hodgson, J.M.; Tresserra-Rimbau, A.; Kühn, T.; Cassidy, A. High diversity of dietary flavonoid intake is associated with a lower risk of all-cause mortality and major chronic diseases. *Nat. Food* **2025**, *6*, 668–680.
7. Shen, N.; Wang, T.F.; Gan, Q.; Liu, S.; Wang, L.; Jin, B. Plant flavonoids: Classification, distribution, biosynthesis, and antioxidant activity. *Food Chem.* **2022**, *383*, 132531.
8. Ji, W.; Li, L.F.; Song, W.; Wang, X.N.; Zhao, B.; Ozaki, Y. Enhanced Raman Scattering by ZnO Superstructures: Synergistic Effect of Charge Transfer and Mie Resonances. *Angew. Chem. Int. Ed.* **2019**, *58*, 14452–14456.
9. Li, J.F.; Xie, Q.H.; Li, J.B.; Sun, L.; Xie, Y.F.; Ozaki, Y.; Ji, W. Macroscale TiO_2 Microspherical Arrays with Multiple Synergistic Effect for Highly Sensitive Surface-Enhanced Raman Scattering. *Adv. Funct. Mater.* **2024**, *34*, 2400523.
10. Jin, Y.; Hu, Z.Y.; Xu, H.W.; Cheng, J.; Yu, Z.L.; Yao, W.R.; Zhao, T.C.; Ji, W.; Ozaki, Y.; Xie, Y.F. Bioinspired Turing-Nanoarchitected Needle for Solid Matrices Analysis: A Universal Platform Enabling Dual-Scale SERS Enhancement. *Adv. Mater.* **2025**, *37*, 2506426.
11. Xu, C.; Li, J.B.; Liu, J.; Ma, Y.X.; Wang, X.S.; Xie, Y.F.; Chen, C.X.; Ji, W. Rapid construction of interfacial plasmonic nanoarray for SERS sensing of flavonoids. *Biosens. Bioelectron.* **2025**, *271*, 117044.
12. Chen, J.J.; Li, M.Y.; Wang, X.M.; Liu, H.Y.; Jiang, W.J.; Zhao, B.; Song, W. Putting Charge Transfer Degree as a Bridge Connecting Surface-Enhanced Raman Spectroscopy and Photocatalysis. *Angew. Chem. Int. Ed.* **2025**, *64*, e202424986.
13. Guo, Y.G.; Zhang, M.Q.; Wang, X.L.; Yang, H.Y.; Zhang, D.; Zhang, M.Y.; Wang, X.H.; Ferrari, J.L.; Yang, K.K.; Nie, G.M.; et al. The role of QDs@MOFs composites in overcoming QDs' limitations for biomedicine. *Coord. Chem. Rev.* **2026,** *549*, 217235.
14. Kokulnathan, T.; Kumar, K.M.A.; Wang, T.-J.; Joseph Anthuvan, A.; Chang, C.-L. Unlocking the potential of bismuth oxybromide microflowers supported silver nanosphere as a SERS platform for detection of nitrofurantoin. *Appl. Surf. Sci.* **2025**, *686*, 162145.
15. Jinachandran, A.; Kokulnathan, T.; Wang, T.-J.; Panneerselvam, R. Highly SERS active microcomposite of silver nanoparticles-decorated nickel oxide microflowers on flexible substrates for detection of 4-nitrophenol on fish surfaces. *J. Alloys Compd.* **2025**, *1034*, 181358.
16. Jinachandran, A.; Kokulnathan, T.; Manivannan, S.; Wang, T.-J.; Abburi, J.; Shaik, S.; Panneerselvam, R. Development of Wearable MXene/Ag Nanopopcorn-Decorated Finger Caps for Rapid On-Site SERS Detection of Fipronil in Food and

Water Samples. *ACS Appl. Nano Mater.* **2026**, *9*, 4773–4783.
17. Vijayaragaventhiran, K.; Kumar, K.M.A.; Wang, T.-J.; Kokulnathan, T.; Chen, Y.-T.; Chang, S.-M. Bioinspired SERS microcomposite of cobalt oxide semiconductor microurchins photodecorated with silver nanoparticles for highly sensitive detection of 4-nitrophenol and tartrazine. *Sens. Actuators A Phys.* **2026**, *405*, 117769.
18. Ning, L.C.; Li, J.B.; Xie, Q.H.; Hu, J.N.; Liu, J.; Xu, C.; Peng, J.S.; Chen, C.X.; Ji, W. Plasmonic Coacervate as a Droplet-Based SERS Platform for Rapid Enrichment and Microanalysis of Hydrophobic Payloads. *Anal. Chem.* **2024**, *96*, 18772–18780.
19. Yang, Y.; Li, Y.F.; Xie, Q.H.; Jiang, B.; Li, J.B.; Xie, Y.F.; Ji, W. Evaluating the Kinetics and Molecular Mechanism for Biomimetic Metabolic Activation of PAHs by Surface-Enhanced Raman Scattering Spectroscopy. *Anal. Chem.* **2024**, *96*, 10365–10372.
20. Liu, J.Q.; Liu, Z.C.; Wang, W.K.; Tian, Y. Real-time Tracking and Sensing of Cu^{+} and Cu^{2+} with a Single SERS Probe in the Live Brain: Toward Understanding Why Copper Ions Were Increased upon Ischemia. *Angew. Chem. Int. Ed.* **2021**, *60*, 21351–21359.
21. Leong, S.X.; Kao, Y.C.; Han, X.M.; Poh, Z.W.; Chen, J.R.T.; Tan, E.X.; Leong, Y.X.; Lee, Y.H.; Teo, W.X.; Yip, G.W.; et al. Achieving Molecular Recognition of Structural Analogues in Surface-Enhanced Raman Spectroscopy: Inducing Charge and Geometry Complementarity to Mimic Molecular Docking. *Angew. Chem. Int. Ed.* **2023**, *62*, e202309610.
22. Zhao, J.J.; Sun, L.; Dong, Y.M.; Chang, Y.X.; Wang, H.S.; Liu, Z.H.; Li, J.B.; Xie, Y.F.; Ji, W. Semiconductor Superstructures with Multiple Synergistic Resonances for SERS Exploring Multiplex Noncovalent Interactions. *Nano Lett.* **2025**, *25*, 6645–6653.
23. Ji, W.; Li, L.F.; Guan, J.; Mu, M.; Song, W.; Sun, L.; Zhao, B.; Ozaki, Y. Hollow Multi-Shelled V_2O_5 Microstructures Integrating Multiple Synergistic Resonances for Enhanced Semiconductor SERS. *Adv. Opt. Mater.* **2021**, *9*, 2101866.
24. Guo, Y.G.; Xue, Y.; Shen, B.Q.; Dong, Y.X.; Zhang, H.; Yuan, J.W.; Liu, Z.J.; Li, L.H.; Ren, K.W. Modulating Electron Transfer between Pt and MOF Support through Pd Doping Promotes Nanozyme Catalytic Efficiency. *ACS Appl. Mater. Interfaces* **2024**, *16*, 27511–27522.
25. Storr, T.; Merkel, M.; Song-Zhao, G.X.; Scott, L.E.; Green, D.E.; Bowen, M.L.; Thompson, K.H.; Patrick, B.O.; Schugar, H.J.; Orvig, C. Synthesis, Characterization, and Metal Coordinating Ability of Multifunctional Carbohydrate-Containing Compounds for Alzheimer's Therapy. *J. Am. Chem. Soc.* **2007**, *129*, 7453–7463.
26. Li, Y.; Yu, Q.-X.; Yau, L.-F.; Huang, G.-K.; Lu, J.-G.; Liu, X.-X.; Jiang, Z.-H.; Wang, J.-R. Discrimination of Baphicacanthis Cusiae Rhizoma et radix and its adulterant species and establishment of an assay method for quality control. *Chin. Med.* **2023**, *18*, 65.
27. Chen, Q.; Lan, H.Y.; Peng, W.; Rahman, K.; Liu, Q.C.; Luan, X.; Zhang, H. Isatis indigotica: A review of phytochemistry, pharmacological activities and clinical applications. *J. Pharm. Pharmacol.* **2021**, *73*, 1137–1150.
28. Hsieh, Y.C.; Wu, M.S.; Lee, H.C.; Hsieh, C.Y.; Huang, S.S.; Tsai, C.F.; Lin, Y.T.; Lin, M.C.; Tseng, S.H.; Wang, D.Y. Development of the species-specific multiplex PCR and DNA sequencing methods for rapid authentication of Isatidis Folium and its adulterants. *J. Food Drug Anal.* **2021**, *29*, 303–310.
29. Hanuza, J.; Godlewska, P.; Kucharska, E.; Ptak, M.; Kopacz, M.; Mączka, M.; Hermanowicz, K.; Macalik, L. Molecular structure and vibrational spectra of quercetin and quercetin-5′-sulfonic acid. *Vib. Spectrosc.* **2017**, *88*, 94–105.
30. Paczkowska, M.; Lewandowska, K.; Bednarski, W.; Mizera, M.; Podborska, A.; Krause, A.; Cielecka-Piontek, J. Application of spectroscopic methods for identification (FT-IR, Raman spectroscopy) and determination (UV, EPR) of quercetin-3-O-rutinoside. Experimental and DFT based approach. *Spectrochim. Acta Part A Mol. Biomol. Spectrosc.* **2015**, *140*, 132–139.
31. Corredor, C.; Teslova, T.; Cañamares, M.V.; Chen, Z.G.; Zhang, J.; Lombardi, J.R.; Leona, M. Raman and surface-enhanced Raman spectra of chrysin, apigenin and luteolin. *Vib. Spectrosc.* **2009**, *49*, 190–195.
32. Krysa, M.; Szymanska-Chargot, M.; Zdunek, A. FT-IR and FT-Raman fingerprints of flavonoids—A review. *Food Chem.* **2022**, *393*, 133430.
33. Peng, Y.Y.; Li, L.; Yang, Y.H.; Zhang, D.J.; Bao, D.Y.; Li, X.J.; Hu, X.J.; Zeng, Q.; Li, X.; Zhang, Z.; et al. Raman Spectra-based Structural Classification Analysis of Flavones, Flavonols, and Isoflavones Using Machine Learning. *Curr. Anal. Chem.* **2025**, *21*, 1252–1260.
34. Govindammal, M.; Prasath, M.; Kamaraj, S.; Sathya, B. *In vivo*, molecular docking, spectroscopy studies of (S)-2,3-Dihydro-5,7-dihydroxy-2(3-hydroxy-4-methoxyphenyl)-4H-1-benzopyran-4-one: A potential uptake PI3/AKT inhibitor. *Biocatal. Agric. Biotechnol.* **2019**, *18*, 101086.
35. Unsalan, O.; Erdogdu, Y.; Gulluoglu, M.T. FT-Raman and FT-IR spectral and quantum chemical studies on some flavonoid derivatives: Baicalein and Naringenin. *J. Raman Spectrosc.* **2009**, *40*, 562–570.
36. Chen, J.; Zhu, Z.P.; Gao, T.H.; Chen, Y.; Yang, Q.S.; Fu, C.M.; Zhu, Y.N.; Wang, F.; Liao, W. Isatidis Radix and Isatidis Folium: A systematic review on ethnopharmacology, phytochemistry and pharmacology. *J. Ethnopharmacol.* **2022**, *283*, 114648.
37. Xu, P.; Marsafari, M.; Zha, J.; Koffas, M. Microbial Coculture for Flavonoid Synthesis. *Trends Biotechnol.* **2020**, *38*,

686–688.

38. Jiao, J.; Gai, Q.Y.; Yao, L.P.; Niu, L.L.; Zang, Y.P.; Fu, Y.J. Ultraviolet radiation for flavonoid augmentation in Isatis tinctoria L. hairy root cultures mediated by oxidative stress and biosynthetic gene expression. *Ind. Crops Prod.* **2018**, *118*, 347–354.
39. Yu, H.; Li, T.N.; Ran, Q.; Huang, Q.W.; Wang, J. Strobilanthes cusia (Nees) Kuntze, a multifunctional traditional Chinese medicinal plant, and its herbal medicines: A comprehensive review. *J. Ethnopharmacol.* **2021**, *265*, 113325.
40. Abbas, M.; Saeed, F.; Anjum, F.M.; Afzaal, M.; Tufail, T.; Bashir, M.S.; Ishtiaq, A.; Hussain, S.; Suleria, H.A.R. Natural polyphenols: An overview. *Int. J. Food Prop.* **2017**, *20*, 1689–1699.
41. Baranovic, G.; Segota, S. Infrared spectroscopy of flavones and flavonols. Reexamination of the hydroxyl and carbonyl vibrations in relation to the interactions of flavonoids with membrane lipids. *Spectrochim. Acta Part A Mol. Biomol. Spectrosc.* **2018**, *192*, 473–486.
42. Teslova, T.; Corredor, C.; Livingstone, R.; Spataru, T.; Birke, R.L.; Lombardi, J.R.; Cañamares, M.V.; Leona, M. Raman and surface-enhanced Raman spectra of flavone and several hydroxy derivatives. *J. Raman Spectrosc.* **2007**, *38*, 802–818.
43. Sekine, R.; Vongsvivut, J.; Robertson, E.G.; Spiccia, L.; McNaughton, D. Analysis of 5-Hydroxyisoflavones by Surface-Enhanced Raman Spectroscopy: Genistein and Methoxy Derivatives. *J. Phys. Chem. B* **2011**, *115*, 13943–13954.
44. Machado, N.F.L.; de Carvalho, L.B.; Otero, J.C.; Marques, M.P.M. A conformational study of hydroxylated isoflavones by vibrational spectroscopy coupled with DFT calculations. *Vib. Spectrosc.* **2013**, *68*, 257–265.
45. Xia, J.; Wang, D.; Liang, P.; Zhang, D.; Du, X.Q.; Ni, D.J.; Yu, Z. Vibrational (FT-IR, Raman) analysis of tea catechins based on both theoretical calculations and experiments. *Biophys. Chem.* **2020**, *256*, 106282.
46. Pompeu, D.R.; Larondelle, Y.; Rogez, H.; Abbas, O.; Pierna, J.A.F.; Baeten, V. Characterization and discrimination of phenolic compounds using Fourier transform Raman spectroscopy and chemometric tools. *Biotechnol. Agron. Soc. Environ.* **2018**, *22*, 13–28.
47. Lima, I.K.C.; de Sousa, F.D.; Bento, A.J.D.; Cruz, B.G.; da Silva, P.T.; Bandeira, P.N.; dos Santos, H.S.; Saraiva, G.D.; Barreto, A.C.H.; Freire, P.D.C.; et al. Structural and spectroscopic investigation of the chalcones (*E*)-1-(4-aminophenyl)-3-(4′-ethoxyphenyl)-prop-2-en-1-one and (*E*)-1-(aminophenyl)-3-(4′-methoxyphenyl)-prop-2-en-1-one. *Vib. Spectrosc.* **2020**, *110*, 103118.
48. Santiago, R.N.S.; Freire, P.T.C.; Teixeira, A.M.R.; Bandeira, P.N.; Santos, H.S.; Lemos, T.L.G.; Ferraz, C.A.N. FT-Raman and FT-IR spectra and DFT calculations of chalcone (2E)-1-(4-aminophenyl)-3-phenyl-prop-2-en-1-one. *Vib. Spectrosc.* **2018**, *97*, 1–7.

Materials and Interfaces

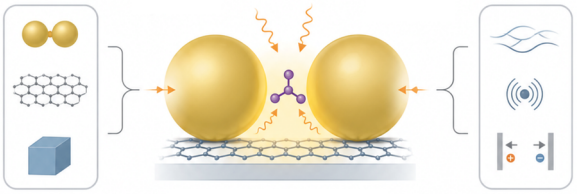
Review

Hybrid SERS Platforms for Enhanced Biochemical Sensing

Jiazheng Bao [1], Bin Lian [1], Hyungmok Joh [1,2], Alan Xiaolong Wang [3,*], and Donglei Emma Fan [1,2,4,5,*]

[1] Materials Science and Engineering Program, Texas Materials Institute, The University of Texas at Austin, Austin, TX 78712, USA
[2] Materials Nova Limited Liability Company, Austin, TX 78759, USA
[3] Department of Electrical and Computer Engineering, Baylor University, Waco, TX 76798, USA
[4] Department of Mechanical Engineering, The University of Texas at Austin, Austin, TX 78712, USA
[5] Chandra Family Department of Electrical and Computer Engineering, The University of Texas at Austin, Austin, TX 78712, USA
* Correspondence: alan_wang@baylor.edu (A.X.W.); dfan@austin.utexas.edu (D.E.F.)

Received: 10 April 2026; Revised: 6 July 2026; Accepted: 30 July 2026; Published: 27 August 2026



Abstract: Surface-enhanced Raman scattering (SERS) is a powerful analytical technique for label-free, ultrasensitive biochemical detection, offering broad potential for biomedical, environmental monitoring, and defense applications. However, conventional noble-metal SERS substrates remain limited by chemical instability, insufficient enhancement reproducibility, and slow analyte detection in dilute aqueous solutions. Recently, hybrid SERS platforms that integrate plasmonic nanostructures with functional material systems—such as semiconductors, two-dimensional materials, photonic crystals, and active robotic modules—have emerged as promising strategies to overcome these limitations. In this review, we examine recent advances in hybrid SERS platforms from the perspective of material systems. Their working principles can be broadly categorized into two types: functional materials that regulate interfacial electromagnetic and chemical enhancement, and robotized systems that promote targeted analyte access or active enrichment at sensing hotspots. By linking material properties, working mechanisms, and sensing performance, this review provides a materials-based perspective to guide the rational design of high-performance, application-oriented SERS platforms.

Keywords: surface-enhanced Raman scattering; hybrid nanomaterials; charge transfer; photonic crystals; nanomotors; analyte enrichment

1. Introduction

Surface-enhanced Raman scattering (SERS) amplifies weak Raman fingerprints of molecules near nanostructured plasmonic surfaces [1–5]. In conventional SERS substrates, noble metals such as Au, Ag, and Cu dominate because their localized surface plasmon resonances in the visible and near-infrared regions produce intense near-field enhancement with relatively low optical losses [5–7]. This plasmonic amplification has enabled chemical, environmental, and catalytic analysis [8–15], biological and biomedical sensing [2,16–25], and emerging active or multifunctional SERS formats [26–30].

Despite their great potential, conventional noble-metal SERS substrates face several persistent limitations for practical applications [31]. Hotspot heterogeneity complicates quantitative comparison and substrate-to-substrate reproducibility. These challenges are further compounded by the limited stability of many noble-metal nanostructures, which can undergo oxidation, contamination, or nonspecific fouling in complex media [31–38]. In addition, the enhancement mechanism of metallic SERS substrates relies primarily on localized surface plasmon resonance, which is governed by the optoelectronic properties, geometry, and dimensions of the metal nanostructures [16,39]. This reliance on plasmonic enhancement alone motivates the exploration of complementary material strategies to further improve sensing performance. To address these practical sensing

Copyright: © 2026 by the authors. This is an open access article under the terms and conditions of the Creative Commons Attribution (CC BY) license (https://creativecommons.org/licenses/by/4.0/).
Publisher's Note: Scilight stays neutral with regard to jurisdictional claims in published maps and institutional affiliations.

challenges, recent literature has reported various strategies aimed at significantly improving the signal-to-noise ratio and overall reliability of SERS measurements through optical interface engineering, background noise modulation, and advanced hybrid plasmonic coupling [40–42]. Beyond sensitivity and stability, passive noble-metal nanostructures also suffer from low detection throughput in dilute aqueous samples, where analyte capture is often limited by slow diffusion to nanoscale hotspots [43].

Hybrid SERS platforms are SERS-active architectures that integrate plasmonic nanostructures with functional materials or active components that can modify the local optical field, interfacial electronic structure, analyte adsorption, or molecular transport. Material hybridization can address several limitations of conventional SERS: semiconductors and two-dimensional materials introduce tunable charge transfer (CT) channels, photonic crystals redistribute optical fields and local concentration, and active or robotic components enable targeted analyte detection or their enrichment at nanoscale hotspots. Therefore, hybrid SERS platforms can not only introduce new routes for signal amplification but also actively control analyte transport kinetics for improved throughput.

Although prior reviews have examined various aspects of SERS and its applications [18,33–36,44–51], this review provides a distinct view of SERS progress through the lens of mechanistically driven hybrid material platforms. The working mechanisms of these platforms are broadly categorized into two types: functional materials that regulate interfacial electromagnetic and chemical enhancement, and robotized systems that promote targeted analyte detection or active enrichment at sensing hotspots. Figure 1 summarizes the different hybrid platforms reported in the literature. Semiconductor-, two-dimensional-material-, and photonic-crystal-based hybrids fall into the first category. These interface-regulated platforms enhance SERS performance by tuning charge transfer, electromagnetic–chemical mechanism coupling, and optical-field localization. In contrast, micro/nanomotor and magnetic hybrid systems are discussed as robotic platforms that directly target analytes or accelerate their enrichment at sensing hotspots. Finally, because both interface-regulated enhancement and active enrichment can generate localized signal variations, this review briefly discusses how digital counting and data-driven spectral analysis may improve quantitative SERS measurements.

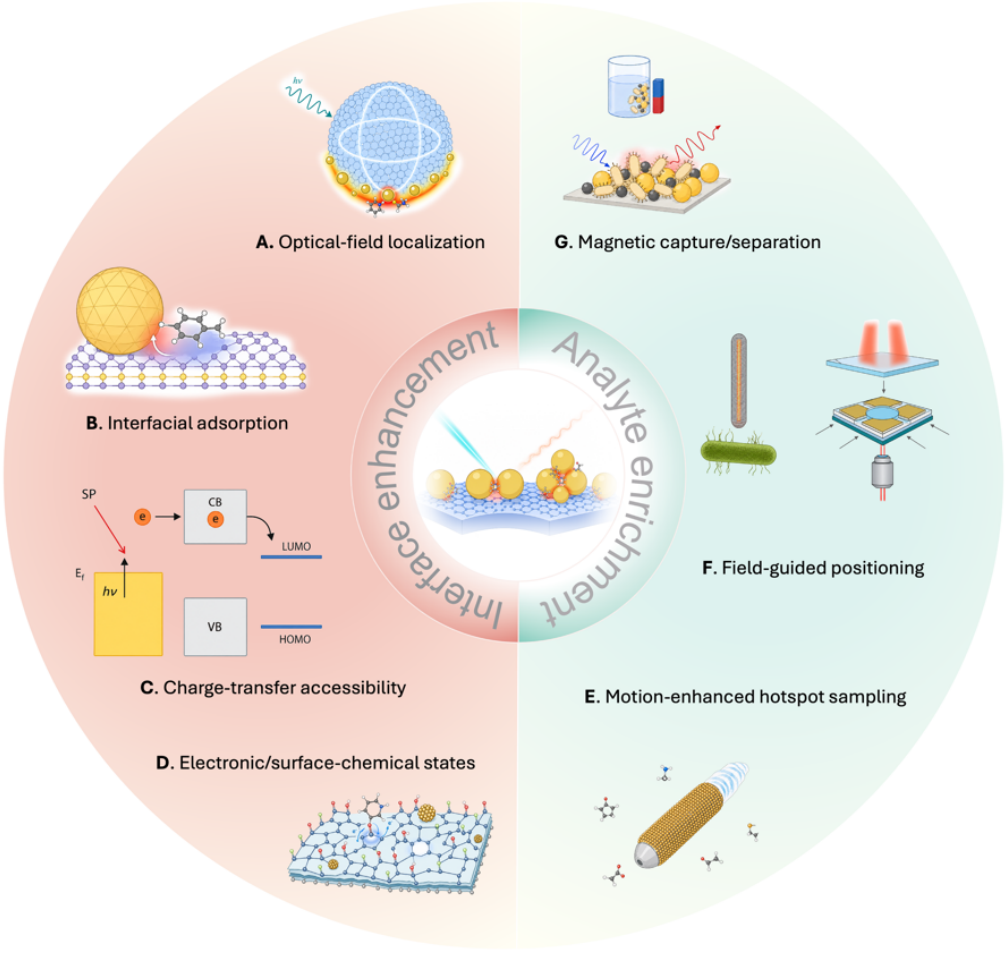


Figure 1. Mechanistic framework for hybrid SERS platforms. Hybrid SERS architectures improve sensing by regulating the SERS interface or by improving analyte access to SERS-active regions. (**A**) Optical-field localization, as in Mie-resonant ZnO superstructures [52], photonic-crystal-assisted plasmonic substrates [53,54],

and bio-photonic-crystal platforms [55,56]. (**B**) Interfacial adsorption and orientation, referring to analyte localization, binding geometry, and molecule–hotspot contact without necessarily requiring charge transfer; examples include graphene-spaced plasmonic junctions [11], RGO/Au breath-analyzer substrates [57], and carbonyl-functionalized organic-SERS interfaces [58]. (**C**) Charge-transfer accessibility, referring to whether band alignment, defect states, excitation energy, or adsorption geometry enables a charge-transfer pathway; examples include TiO_2–Ag–MPY–FePc interfaces [59], oxygen-vacancy-mediated TiO_2/PIERS systems [60], Ag/Ag-doped TiO_2 hybrids [61], and PIHET/PICTT metal–semiconductor systems such as Au–ZnO and Au–CdSe [62,63]. (**D**) Electronic/surface-chemical states, including surface terminations, vacancies, phase structures, oxidation states, conductivity, and active sites; examples include TiVC MXene [64,65], Ti_2N MXene [66], phase-engineered TMDs [67], and gas- or UV-modulated RGO/Ag hybrids [68]. (**E**) Motion-enhanced hotspot sampling, as in magnetic nanorobot SERS probes [69,70], light-powered nanomotor sensors [71], magnetic-film-actuated diatom frustules [26], and electric-field-driven rotary SERS nanomotors [72]. (**F**) Field-guided mobile hotspot positioning, in which optical or electric fields position, orient, or assemble SERS-active components at defined locations to form controllable nanogaps or localized sensing interfaces; examples include optical-tweezer-controlled Ag nanoparticle-coated silica beads [73,74], and 3D electrokinetic tweezer manipulation of SERS-active nanowire probes [75]. (**G**) Magnetic capture and separation, in which magnetic–plasmonic probes or magnetic enrichment substrates capture, isolate, and concentrate target species from complex matrices before Raman readout; examples include magnetic mesoporous nanosponges for pollutant enrichment [76], antibody-functionalized Mag-SERS strips for respiratory virus detection [77], and magnetic nanochain microfluidic biochips for rapid bioseparation and SERS detection [20].

2. Interface-Regulated Enhancement at Hybrid Interfaces

The electromagnetic and chemical contributions to SERS have been extensively reviewed [31,34,78] and are therefore discussed only briefly here to provide the necessary background. Building on this established understanding, this review focuses on what hybrid architectures contribute beyond conventional plasmonic enhancement. The approaches include regulation of optical fields, interfacial electronic structure, charge-transfer accessibility, surface chemistry, and analyte enrichment near SERS-active interfaces [3,6,39,43,79–81]. This emphasis provides the basis for comparing semiconductor, 2D material, photonic-crystal, and active-enrichment platforms without reducing their performance to EF or LOD alone. Therefore, EF and LOD are reported together with mechanistic studies, such as wavelength-dependent measurements, optical-field simulations, band alignment, defect-state control, adsorption tuning, and charge-transfer signatures.

2.1. Electromagnetic Enhancement Mechanism

Electromagnetic enhancement refers to the optical-field localization and antenna-mediated amplification of both Raman excitation and emission [82]. In noble-metal SERS, this contribution is commonly associated with localized surface plasmon resonance (LSPR), nanoscale junctions, sharp features, and spectral overlap between the excitation/Raman wavelengths and the plasmonic response. In hybrid platforms, however, optical-field localization can also be shaped by Mie-like resonances in semiconductor structures, guided-mode or slow-light effects in photonic crystals, and plasmonic gap engineering across atomically thin spacers such as graphene. This broader interpretation of EM enhancement facilitates a systematic comparison of plasmonic, dielectric, and photonic contributions within hybrid material architectures.

2.2. Chemical Enhancement Mechanism

Chemical enhancement is used here to describe interfacial electronic effects that alter molecular polarizability, directly modulating Raman emission, particularly through adsorption-mediated coupling and ground-state or photoinduced charge transfer (CT) [83–85]. In hybrid systems, this interfacial contribution often becomes a primary design target. Semiconductors, transition metal dichalcogenides (TMDs), MXenes, graphene, and molecular semiconductors can tune the energetic and chemical conditions for charge transfer through band alignment, density of states, defect levels, surface terminations, Fermi-level positions, and adsorption geometries. Together, these features can help hybrid interfaces support more selective electronic coupling between the substrate and the analyte, extending beyond simple molecular adsorption alone.

Photoinduced charge transfer, in addition, is particularly important in hybrid SERS because it connects optical excitation with interfacial electronic coupling. In metal-semiconductor hybrids, for example, this coupling can occur through several related but distinct pathways [79,85,86]. Plasmon-induced hot-electron transfer (PIHET) describes the injection of plasmon-generated hot carriers from a metal into an adjacent semiconductor before carrier relaxation. Direct interfacial charge-transfer transition (DICTT) refers to direct optical excitation across the

metal-semiconductor interface, whereas plasmon-induced interfacial charge-transfer transition (PICTT) describes plasmon-assisted interfacial transitions in strongly coupled heterostructures. These detailed pathways provide useful mechanistic distinctions for discussing hybrid interfaces, especially when correlated to wavelength-dependent measurements, band alignment, defect-state analysis, charge-transfer signatures, adsorption controls, and electromagnetic simulations.

While the transfer of plasmon-generated hot carriers facilitates chemical enhancement in SERS, these energetic carriers concurrently drive unintended plasmon-mediated photochemical reactions at the molecular interface [87,88]. Such processes have been reported to convert the molecules of interest into different chemical species during continuous laser excitation [89]. In these circumstances, the acquired Raman spectra reflect the newly formed photochemical products rather than the original analytes. This structural transformation can compromise the noninvasive nature of Raman spectroscopy, thereby limiting its reliability as an accurate molecular fingerprinting tool for quantitative sensing. Addressing this critical limitation is essential for the design of practical SERS sensors [90–93]. Within hybrid SERS platforms, structural and electronic engineering may offer viable strategies to preserve molecular integrity. For instance, it has been reported that introducing an ultrathin, inert dielectric spacer between the plasmonic surface and the target analyte can effectively block direct interfacial hot-carrier injection while maintaining the long-range electromagnetic field enhancement [91–94]. Furthermore, engineering the interfacial band alignment in metal-semiconductor heterostructures is reported to regulate hot carrier relaxation pathways, which may reduce the probability of analyte degradation [31,34,35,78,95]. These material-driven strategies illustrate how hybrid architectures can be designed to balance signal enhancement with molecular stability.

2.3. Coupled Contributions and Design Boundaries

The experimentally observed total enhancement (M_{total}) has often been discussed using the approximate relation ($M_{\mathrm{total}} \approx M_{\mathrm{EM}} \times M_{\mathrm{CM}}$), where M_{EM} and M_{CM} denote the electromagnetic and chemical contributions, respectively; this relation is useful for conceptual comparison. In hybrid interfaces, however, optical-field localization and interfacial charge redistribution can mutually reinforce one another: local electromagnetic fields can increase the probability of charge-transfer transitions, while electronic redistribution can alter the dielectric environment experienced by the optical mode. The relative contribution of each process therefore depends on material architecture, excitation wavelength, interfacial electronic structure, and analyte adsorption geometry.

Analyte enrichment is another important factor influencing SERS sensing performance. Active motion, magnetic capture, optical trapping, field-guided assembly, and related enrichment strategies can increase molecular delivery to hotspots, improve encounter probability, and shorten detection time. These processes are essential for practical sensing performance in addition to interfacial enhancement. They are discussed separately.

Collectively, this review is framed into the following sections. Section 3 discusses semiconductor, two-dimensional-material, and photonic-crystal hybrids as platforms that regulate optical fields, interfacial electronic structure, or charge-transfer accessibility. Section 4 then considers active and field-guided architectures that improve molecular delivery, enrichment, separation, and hotspot encounter. Together, these two sections connect hybrid-material design with both intrinsic enhancement and practical sensing performance.

3. Hybrid SERS Platforms for Interface-Regulated Enhancement

Semiconductors, two-dimensional materials, and photonic crystals can modify SERS performance by tuning charge-transfer pathways, interfacial electronic structure, surface chemistry, and optical-field localization [34,58,96]. These effects do not replace electromagnetic enhancement from plasmonic nanostructures, but reshape how electromagnetic and chemical contributions are coupled at hybrid interfaces. The various platforms provide a useful basis for understanding how material composition, band structure, surface states, and photonic architecture influence SERS sensitivity, reproducibility, and selectivity.

The section is organized according to the main interfacial role enabled by each material class. Semiconductor hybrids are discussed first because they provide clear examples of band alignment, defect-state regulation, and plasmon-mediated charge-transfer processes, including PIHET and PICTT. Two-dimensional-material hybrids are then considered as atomically thin interfaces in which phase structure, conductivity, surface terminations, and spacer effects regulate adsorption, charge transfer, and plasmonic coupling. Finally, photonic-crystal hybrids are discussed as architectures that redistribute optical fields through guided-mode, slow-light, or Mie-like effects. Table 1 summarizes representative platforms, enhancement factors, detection limits, and operating features, while the discussion focuses on the mechanistic role played by each hybrid component in the SERS measurement.

Table 1. Comparative summary of interface-regulated hybrid SERS architectures.

System	Material	Hotspot	λ_{ex} (nm)	Probe Analyte	LOD	EF	Dominant Mechanism	Note	Ref.
Au triangular nanoarrays/n-layer graphene/Au NPs	Graphene-noble metal hybrid	Sandwich w/subnm hotspots gated by graphene spacer	532 nm (Renishaw inVia, 100×, 0.5 mW, 10 s)	Hg^{2+} (TAMRA-DNA probe)	LOD 8.3×10^{-9} M	NR	EM (LSPR) + CM	Indirect detection via DNA probe; EF method NR	[11]
Ti_2N MXene	MXene (pristine)	2D paper-based substrate	532 nm (50× objective, NA = 0.55, 0.54 mW, 10 spectra × 5 s)	R6G (for the 10^{12} EF measurement)	NR	$\approx 10^{12}$	CM (ground-state CT)		[66]
1T′-WTe_2 atomic layers	TMD (plasmon-free)	Monolayer/few-layer atomically thin	532 nm (~1 μm spot, 1 mW, 40 s)	R6G	LOD 40 fM	1.8×10^9	CM (CT, high DOS at EF)	Plasmon-free baseline	[97]
4H-Au@1T′-WS_2 core-shell nanowires	TMD-noble metal hybrid	4H-Au NW core (~few-nm) + ~0.6 nm 1T′-WS_2 monolayer shell	532 nm (R6G, 100× objective, NA = 0.85, 0.1 mW, 40 s); 633 nm (SARS-CoV-2 spike, 1 mW, 10 s)	R6G; SARS-CoV-2 spike protein	LOD 1×10^{-18} M (attomolar)	NR	EM (4H-Au LSPR) + CM (1T′-WS_2 semi-metallic CT)	LOD reported for R6G dye and SARS-CoV-2 spike-protein	[98]
TiVC bimetallic solid-solution MXene	MXene (bimetallic)	2D MXene flakes	532 nm primary (100× objective, NA = 0.90, 0.2 mW, 20 spectra × 10 s); 785 nm tested	R6G (main); CV, MG, MB	fM detection	3.27×10^{12}	CM (PICT)		[64]
C_8-BTBT, D(C_7CO)-BTBT organic semiconductor films	Organic semiconductor	3D porous architecture (carbonyl-functionalized)	785 nm (Jasco NRS-4500, 20×, 30 mW, 10 s)	Methylene blue (selective)	NR	CT efficiency via anti-Stokes/Stokes ratio (D(C_7CO)-BTBT >> C_8-BTBT)	CM (analyte-specific resonance: HOMO/LUMO match only for MB)	Demonstrates molecular selectivity	[58]

Table 1. *Cont.*

System	Material	Hotspot	λ_{ex} (nm)	Probe Analyte	LOD	EF	Dominant Mechanism	Note	Ref.
$CoFe_2O_4$/Ag hybrid nanotubes	Magnetic spinel oxide/metal hybrid	Electrospun magnetic nanotubes decorated with Ag NPs	532 nm (Renishaw-1000)	PATP (sensitivity to 10^{-9} M); MB (catalytic monitoring)	PATP LOD = 10^{-9} M	≈10^9 (vs. 10^6 for Pd nanosphere, 10^8 for nanoporous Ag)	EM + CT ($CoFe_2O_4$ → Ag)	Dual SERS + catalytic platform	[15]
TiO_2-Ag-MPY-FePc	Semiconductor-metal hybrid	TiO_2 NPs with Ag and molecular MPY-FePc bridge	633 nm primary (also 473, 514, 785 nm)	MPY (Raman reporter); FePc (CT-active layer)	NR	NR	EM (Ag SPR) + CM (interfacial CT, direction-controlled)		[59]
$(Ag)_x(ZnS)_y$ co-sputtered films	Semiconductor-metal hybrid	Co-sputtered Ag-ZnS thin films	633 nm primary	4-MBA	NR	uses Lombardi b_2/a_1 ratio (I_{1012}/I_{1586}) vs. carrier density	EM (Ag LSPR) + CM (CT, carrier-density modulated; CTR + Herzberg-Teller)	Used to probe carrier-density/EF correlation, no absolute EF	[99]
Ag/Ag-doped TiO_2 hybrid	Semiconductor-metal hybrid (Ag-doped)	Molecule-linked Ag NPs on Ag-doped TiO_2	785 nm NIR (40 mW, 2 s)	4-MBA	NR	1.68×10^6	EM (Ag LSPR) + CM (TiO_2 → molecule CT, oxygen-vacancy-mediated)	Irreversibly accumulated SERS—EF measured under prolonged NIR Raman excitation	[61]
TiO_2 + plasmonic NPs (PIERS)	Semiconductor-metal hybrid (PIERS)	Pre-irradiated TiO_2 supporting plasmonic NPs	633 nm Raman; UVC pre-irradiation (Figure 2D)	Explosives (e.g., dinitrotoluene), pollutants, biomolecules	R6G LOD 10^{-7} M; DNT LOD 10^{-9} M; glucose 10^{-9} M; PETN/RDX 10^{-5} M; saturated TNT vapor calc 3.1×10^{-8} M	≈10× SERS → PIERS enhancement (1 order of magnitude); some bands up to 20×	Photo-induced enhancement (PIERS); UVC-generated O-vacancies → CT	EF decays over 30–60 min; regenerable by UVC	[60]

Table 1. *Cont.*

System	Material	Hotspot	λ_{ex} (nm)	Probe Analyte	LOD	EF	Dominant Mechanism	Note	Ref.
Cu_2O nanoarrays	Semiconductor (PIHET-driven)	Periodic Cu_2O nanoarrays	633 nm primary (also 532 nm)	PTCDA (primary); BCP, 4-MBA; SARS-CoV-2 RNA application	SARS-CoV-2 RNA LOD = 60 copies/mL in <5 min	3.19×10^{10}	PIHET: Cu_2O LSPR + LICT + hot-electron transfer	EF method NR	[100]
Amorphous MoO_3 (a-MoO_3) monolayers	Semiconductor (amorphous oxide)	Amorphous oxide monolayers	633 nm main; 514 nm tested	MO (primary); R6G, MB, o-AAT (target carcinogen)	MO LOD 10^{-8} M; o-AAT LOD 10^{-9} M	2.5×10^6	EM-PIHET synergistic mechanism; amorphous defect DOS	Amorphous structure → defect-rich states	[101]
Au-ZnO heterogeneous nanorods	Semiconductor-metal hybrid	Au-tipped ZnO nanorods	532 nm primary (Au plasmon match); 633, 785 nm tested	Dopamine	NR	$>1.2 \times 10^4$ (DA at 10^{-5} M)	PHET (Au → ZnO)	Recyclable via visible-light cleaning; quantitative EF NR	[62]
Cu-doped SnO_2-NiO p-n heterojunction	Semiconductor heterojunction	p-n hetero NPs	785 nm primary (5 mW, 0.5 s, 50×); 532, 633 nm tested	CuPc (reporter); pyrene, 2-naphthalenethiol, EBZA (VOC targets)	CuPc 10^{-9} M; PYR ≈ 7.6 ppb; 2-NT ≈ 5.3 ppb; EBZA ≈ 4.1 ppb	1.46×10^{10} (CuPc on SnO_2-NiOx/Cu)	CM (~92%, p-n junction CT resonance) + EM (~8%, NIR LSPR)	Bandgap & p-n alignment driven; absolute EF NR	[102]
ZnO submicron-sized spheres (superstructure)	Semiconductor (Mie-resonant)	Submicron spherical superstructures	532 nm (synergy demo); 633, 785 nm tested	4-MPy (non-resonant probe)	NR	$\approx 10^5$ (Mie + CT synergy at 532 nm; estimated as $EF_{total} \approx EF_{Mie} \times EF_{CT} \approx 10^2 \times 10^3 \approx 10^5$)	Mie resonance + ground-state CT (GSCT); synergistic	Mie size-dependent	[52]
DFP-4T organic semiconductor films	Organic semiconductor	π-conjugated DFP-4T thin films	785 nm (20× obj, 3 μm spot, 150 mW, 30 s)	MB (non-resonant at 785 nm by design)	LOD 10^{-9} M	2.7×10^5	Resonance CT (organic semi → analyte)	Metal-free organic semiconductor	[103]

Table 1. *Cont.*

System	Material	Hotspot	λ_{ex} (nm)	Probe Analyte	LOD	EF	Dominant Mechanism	Note	Ref.
DFH-4T films (alone) and DFH-4T + Au coating	Organic semiconductor/organic-metal hybrid	Nanostructured DFH-4T; Au-coated for high EF	785 nm (20× obj, 3 μm spot, 150 mW, 30 s)	MB (main); R6G	$<10^{-21}$ mol (sub-zeptomole, Au-coated)	3.4×10^3 (alone); $\approx 10^{10}$ (Au-coated)	CT + EM (with Au)	7-orders increase with Au coating	[104]
1T′@2H $Mo_{1-x}Re_xS_2$ lateral heterostructures	TMD alloy	Lateral 2H–1T′ phase heterostructure (CVD)	532 nm (Bruker Senterra II, 2.5 mW, 15 s)	R6G (main); RhB, CV, MB	10^{-15} M for R6G	2.0×10^{11} (alloy substrate)	CT (1T′ phase → high DOS at E_F)	Phase-tunable composition control	[67]
1T′-ReS_2 nanosheets	TMD (distorted 1T′ phase)	Mono- and few-layer ReS_2 nanosheets	532 nm primary (R6G/RhB/CV); 633 nm (MB)	CuPc (~1 nm thermal deposition); R6G, RhB, CV, MB (solution adsorption)	R6G & MB LOD ≈ 10^{-9} M; RhB & CV ≈ 10^{-8} M (on monolayer ReS_2)	REF ≈ 2.94 (CuPc 1539 cm^{-1} on monolayer ReS_2 vs. SiO_2/Si)	PICT (layer-dependent; monolayer optimal)	Layer-dependent SERS	[105]
MXene/graphene oxide/Au nanoclusters fiber	MXene + GO + plasmonic	Flexible plasmonic fiber	532 nm (WiTec Alpha300R, 50× L, 0.1 mW, 5 s)	R6G (main); TNT, Tetryl (via L-cysteine)	R6G LOD 1×10^{-11} M; TNT 0.1 μM	2.01×10^9 (R6G)	EM (Au LSPR) + CM (PICT via MXene $Ti_3C_2T_x$); synergistic	75% Raman intensity retained after 90 d	[106]
TiVC MXene flexible membrane (alkaline-treated)	MXene (active-site-maximized)	Flexible wearable membrane	Not stated (handheld Raman)	R6G (and physiological biomarkers)	LOD 1×10^{-15} M	8.08×10^{10}	EM (Au LSPR) + CM (CT via TiVC DOS at Fermi)	Wearable form factor	[65]
$Ti_3C_2T_x$ MXene + Au NP dimers	MXene-noble metal aptasensor	MXene loaded with Au NP dimer (aptamer-functionalized)	785 nm (Horiba LabRAM HR; 100 mW, 10× obj, 20 s × 2 accumulations)	AFB1 via BPE Raman reporter (1,2-bis(4-pyridyl)ethylene at AuNP dimer hotspot)	LOD 0.6 pg/mL	NR	EM (Au dimer hotspot) + biorecognition (aptamer)	Bioaffinity-mediated	[107]

Table 1. *Cont.*

System	Material	Hotspot	λ_{ex} (nm)	Probe Analyte	LOD	EF	Dominant Mechanism	Note	Ref.
Self-assembled MXene-Au nanocomposites	MXene-noble metal	Au NPs on MXene flakes	633 nm (4-MBA, adenine); 785 nm (bacteria); HORIBA LabRAM HR Evolution, 100×, 10 s	4-MBA, adenine, *E. coli*, B. subtilis	4-MBA & adenine ≈ 10^{-9} M; *E. coli* LOD 10^6 CFU/mL; B. subtilis LOD 3 × 10^5 CFU/mL	NR	EM + CM; photothermal	Multifunctional (sense + ≈100% germicidal in min); SERS EF/LOD not reported	[108]
Plasmonic MXene hydrogel microrobot	MXene hydrogel + plasmonic	Hydrogel-based microrobot	NR	R6G, MB (cationic); AR, AB (anionic)	R6G LOD 3.76 aM; MB 1.98 fM; AR 16.33 fM; AB 381.07 pM	5.5 × 10^6 (AEF, R6G)	EM (AuAgAu SPR) + MXene-driven analyte enrichment	Dual sense + remediation; EF NR	[109]
Graphene-Ag hybrids (theory + experiment)	Graphene-noble metal hybrid	Ag NPs (3–25 nm) on graphene layers	514.5 nm (Ar^+-ion laser, LabRam Jobin-Yvon T64000; 5 mW, ~2 μm spot, 20 s)	graphene's own G-band (no external probe molecule)	NR	≈10× over pristine graphene (relative)	EM + CT (Ag → graphene)	Ag-size-dependent; relative metric	[110]
rGO–PS@Ag substrate (UV-modulated)	Graphene-noble metal photoactive	RGO + Ag clusters; UV-modulated Fermi level under O_2/Ar atmosphere	532 nm Raman (7.8 W/cm^2, 2 s) + 365 nm UV modulation (135 mW/cm^2 optimal)	R6G primary; CV, 4-MBA, 4-NTP; methyl-parathion (MP) pesticide on fruit peels	MP LOD 1.54 × 10^{-6} → 8.31 × 10^{-7} mg/mL (with UV)	1.77 × 10^6 → 6.75 × 10^6 in O_2 under UV (~4× modulation); 4.07 × 10^6 in CO_2; 1.7× in N_2	Tunable Fermi level via UV-driven O_2 adsorption/desorption on RGO	Photo-actively modulated	[68]
RGO-coated Au film + Au NPs	Graphene-noble metal hybrid	RGO/Au sandwich (no organic stabilizer on AuNPs)	785 nm (~2 mW; 0.1 s mapping/1 s spectra)	R6G + naphthalene (calibration); 14 VOC biomarkers (clinical breath analysis)	NR	6.34 × 10^8 (R6G); 1.02 × 10^6 (naphthalene)	EM + selective π–π adsorption on RGO	Diagnostic application (gastric cancer); EF/LOD NR	[57]

Table 1. *Cont.*

System	Material	Hotspot	λ_{ex} (nm)	Probe Analyte	LOD	EF	Dominant Mechanism	Note	Ref.
Au NPs/graphene heterojunction	Graphene-noble metal hybrid	Au NPs on graphene	532 nm (Horiba HR800, 10 mW, 50× obj, 1 μm spot)	Hg^{2+}	Hg^{2+} LOD 0.1 nM (20 ppt); 0.1–6000 nM dynamic range	40× signal vs. blank substrate (before annealing)	EM + CT		[111]
Inkjet-printed diatom biosilica droplets + Ag NPs (Marangoni)	PC-plasmonic (bio-derived, evaporation-driven)	Diatomaceous biosilica with plasmonic NPs in evaporating droplet	532 nm (Horiba LabRam HR800; 100× obj; 1.5 μm spot; spectra range 800–1800 cm^{-1})	R6G (model dye, single-molecule regime via accumulation); TNT (label-free real target)	TNT 4.5×10^{-17} g (label-free); R6G ≈ 0.1 nM (single-molecule regime); 100 pL droplets, ~17× higher concentration on diatom vs. glass	10^6–10^7 optofluidic-SERS sensitivity improvement vs. conventional pipette SERS	PC field localization + Marangoni convective enrichment + LSPR		[112]
Diatom biosilica + self-assembled Ag NPs	PC-plasmonic (bio-derived)	Natural diatom frustule with Ag NPs	NR	NR (mapping demonstration)	NR	NR (intensity mapped on/off frustule)	PC slow-light/guided-mode resonance + LSPR	Demonstrates PC contribution by spatial SERS mapping; no absolute EF	[56]
PC-enhanced plasmonic mesocapsules + Ag NPs	PC-plasmonic (bio + meso)	Submicron porous mesocapsules with Ag NPs in microfluidic channel	532 nm (Horiba LabRam; 10× obj; 2.0 mW; 10 s integration)	R6G (model); benzene & chlorobenzene (real-water target)	R6G LOD ~10^{-13} M (single-molecule, in microfluidic channel); benzene/chlorobenzene 1×10^{-9} M in tap water	100× over ordinary Ag NPs (relative)	EM (Ag) + PC field localization + microfluidic mixing	Approaches single-molecule optofluidic-SERS; relative metric only	[113]
Diatom biosilica + Ag NPs + anti-mouse IgG	PC-plasmonic immunoassay	Sandwiched immunoassay on functionalized diatom PC	NR	Mouse IgG (with Raman reporter)	LOD 10 pg/mL	NR	EM + biorecognition + PC enhancement	Bioaffinity-mediated; immunoassay LOD	[114]

Table 1. *Cont.*

System	Material	Hotspot	λ_{ex} (nm)	Probe Analyte	LOD	EF	Dominant Mechanism	Note	Ref.
Diatomaceous earth fluidic-channel TLC-SERS	PC-plasmonic TLC-SERS	TLC stationary phase patterned with fluidic channels (lateral-diffusion suppressed)	785 nm (BWS465-785S BW&TEK portable, 30 mW, 5 s × 3 averaged)	Histamine in tuna (artificial-spiked + real spoiled samples; 0–48 h spoilage)	10 ppm artificial-spiked; quantified via PCA-SVR ML (FDA limit 50 ppm; EU 100 ppm)	NR	PC enhancement of plasmonic NPs + chromatographic preconcentration	TLC-SERS application	[115]
Microfluidic diatomite analytical device	PC-plasmonic TLC-SERS (microfluidic)	Diatomaceous earth in patterned microfluidic channels (suppresses lateral diffusion)	785 nm (Horiba LabRam HR800, 50× Olympus, 2 µm spot, 200 µm pinhole)	Pyrene + 4-MBA (model mixture); cocaine in human plasma	Pyrene LOD 1 ppb on µDADs (vs. 2 ppm normal TLC, ~1000× improvement); cocaine 10 ppb in plasma	NR	PC field enhancement + microfluidic preconcentration		[116]

Abbreviations & notes: EF—enhancement factor. **AEF/SSEF/SMEF**—analytical EF/SERS substrate EF/single-molecule EF (Le Ru & Etchegoin convention). "NR" indicates not reported. **CM/EM**—chemical/electromagnetic mechanism. **CT**—charge transfer. **PICT**—photo-induced charge transfer. **PIHET**—plasmon-induced hot electron transfer. **PICTT**—plasmon-induced interfacial charge-transfer transition. **PIERS**—photo-induced enhanced Raman spectroscopy. **LSPR**—localized surface plasmon resonance. **DOS**—density of states; "DOS at EF" = density of states at the Fermi level. **Resonant probe**—analyte with electronic absorption near the laser excitation wavelength (e.g., R6G, crystal violet, rhodamine B, methylene blue at 532 nm). **LOD**—limit of detection. **Relative EF**—value reported as a ratio against an internal reference (e.g., "100× over plain Ag NPs"). **NR**—not reported.

3.1. Semiconductor Hybrids for Charge-Transfer and Optical-Field Regulation

Semiconductor-mediated hybrid SERS platforms are not governed by a single enhancement mechanism; rather, they provide a versatile hybrid platform in which plasmonic field amplification can be coupled with tunable semiconductor electronic states. Semiconductors possess band gaps between those of conductors and insulators and offer adjustable electrical conductivity, Fermi-level position, intermediate electronic states, band-gap engineering, and high chemical stability [34,78,95]. At the same time, their lower free-carrier density relative to noble metals generally restricts visible-range localized surface plasmon resonance (LSPR), so standalone semiconductor-based SERS typically exhibits more modest enhancement, often on the order of $\approx 10^3$. The central value of semiconductor-mediated hybrid architectures therefore lies not simply in increasing the enhancement factor (EF), but in making several enhancement pathways experimentally tunable, including interfacial charge-transfer (CT) direction, carrier-density regulation, defect-assisted photoinduced charge transfer (PICT), plasmon-mediated hot-electron transfer, Mie-assisted field localization, and analyte-selective resonance CT.

One important route begins with interfacial CT and band-structure engineering. In these systems, the semiconductor component does not merely serve as a passive support for plasmonic nanoparticles, but actively modulates the direction, probability, or energetic feasibility of interfacial charge transfer. In a TiO_2-Ag-MPY-FePc system (Figure 2A), TiO_2 nanoparticles were shown to alter the direction and pathway of interfacial CT, contributing to CT-enhanced SERS and illustrating the usefulness of SERS for probing interfacial CT processes relevant to photovoltaic systems [59]. A related example is the $(Ag)_x(ZnS)_y$ system, where controlled ZnS doping was used to regulate carrier density [99]. The observed linear correlation between the SERS intensity ratio of non-totally symmetric to totally symmetric vibrational modes and carrier density indicates that carrier-density modulation can influence the CT contribution to SERS enhancement. Heterojunction engineering further extends this principle by introducing built-in electric fields and band alignment as additional handles for charge separation and resonant CT. For example, Cu-doped SnO_2–NiO p–n heterostructures have been used to illustrate how heterojunction design and band alignment can facilitate CT-related Raman enhancement [102]. These examples are mechanistically useful because they attempt to control interfacial electronic structure, rather than only reporting overall EF improvement.

Building on baseline CT control, defect and vacancy engineering provides a second route to semiconductor-mediated enhancement by introducing intermediate electronic states that improve energetic matching between the substrate and adsorbed molecules. Improving the efficiency of PICT generally requires favorable alignment between molecular orbitals, semiconductor band states, and the excitation photon energy [117,118]. Ag/Ag-doped TiO_2 hybrid systems, for instance, show an irreversible and accumulated SERS behavior under near-infrared (NIR) light irradiation, with the enhancement attributed to synergistic TiO_2-to-molecule CT and electromagnetic (EM) amplification from Ag nanoparticles (Figure 2B) [61]. Similarly, PIERS-type systems based on pre-irradiated TiO_2 demonstrate that photo-generated oxygen vacancies can transiently enhance Raman signals at plasmonic nanoparticle sites (Figure 2D) [60]. More broadly, oxygen incorporation or extraction, ultrathin defective nanosheets, and other defect-state engineering strategies can tune band-edge density of states (DOS), carrier density, and bandgap structure, thereby facilitating PICT [96,117,119–121]. These observations support a defect-assisted PICT interpretation, although strict separation from adsorption changes, conductivity variation, local-field redistribution, and stability effects remain challenging. Therefore, defect-mediated enhancement is most convincing when performance data are paired with controls that distinguish electronic-state modulation from other defect-induced changes in surface chemistry and morphology.

Beyond defect mediation, plasmon-mediated charge-transfer mechanisms, particularly plasmon-induced hot-electron transfer (PIHET) and plasmon-induced interfacial charge-transfer transition (PICTT), provide a more direct link between noble-metal plasmon decay and semiconductor electronic states. In PIHET, hot electrons generated by non-radiative plasmon decay in the metal component are injected into the coupled semiconductor before relaxation losses dominate [100,101,122]. Nanoarrays of Cu_2O and amorphous MoO_3 (a-MoO_3) monolayers, for instance, reported EFs of 3.19×10^{10} and 2.5×10^6, respectively; the enhancement was attributed in the original studies mainly to PIHET-related processes [100,101]. Au-ZnO heterogeneous nanorods provide another representative metal-semiconductor system, in which plasmon-generated hot electrons in Au are transferred into ZnO; the same architecture also shows reproducibility after visible-light-assisted cleaning, suggesting potential for recyclable SERS platforms [62]. In contrast, PICTT represents a more direct interfacial excitation pathway, in which plasmon decay promotes electron transfer from the metal into the semiconductor conduction band without relying solely on thermalized hot-carrier injection [63,123]. The Au–CdSe nanorods system is often used as a conceptual model for this distinction, because CdSe, with its narrow bandgap and Au-CdSe Schottky barrier, can facilitate electron-hole separation. However, direct assignment of PIHET or PICTT in

SERS systems generally requires careful control of excitation wavelength, band alignment, Schottky barrier energetics, hot-carrier dynamics, and competing EM contributions. The principal PIHET, PICTT, and DICTT pathways and their associated contact architectures are summarized in Table 2.

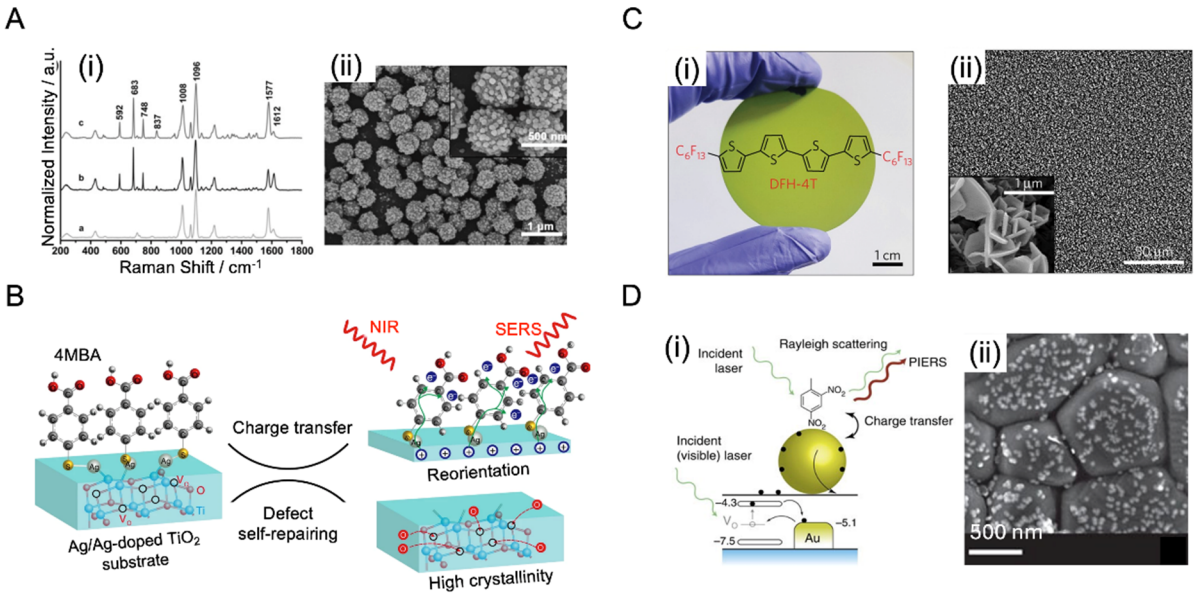


Figure 2. Semiconductor-Metal Hybrid SERS Substrates: Enhancement Mechanisms and Charge Transfer Dynamics. (**A**) Normalized SERS spectra of (**i**) Ag-MPY, Ag-MPY-FePc, and TiO_2-Ag-MPY-FePc systems in ethanol under 633 nm excitation. All spectra were normalized to the peak at 1008 cm^{-1}. (**ii**) SEM image of the TiO_2-Ag complex. Adapted with permission from Ref. [59]. Copyright 2019 Wiley-VCH Verlag GmbH & Co. KGaA. (**B**) NIR light-induced irreversible and accumulated SERS response of the 4MBA/Ag/Ag-doped TiO_2 hybrid system. The enhancement is attributed to a combination of synergistic effects, including NIR-induced thermal effects that increase crystallinity and modify polarizability, NIR-assisted charge transfer (CT) between the substrate and 4MBA via oxygen vacancies (V_O), and electrostatic attraction-driven molecular reorientation of 4MBA. Adapted from Ref. [61] under the terms of the Creative Commons Attribution 4.0 License; (**C**) (**i**) Optical image of a vapor-deposited DFH-4T film (5 cm diameter) with the chemical structure shown in the inset. (**ii**) Top-view SEM images of nanostructured DFH-4T films. Adapted with permission from Ref. [104]. Copyright 2017 Springer Nature. (**D**) Schematic of photo-induced enhanced Raman spectroscopy (PIERS). (**i**) Ultraviolet C light (UVC) pre-irradiation generates oxygen vacancies (V_O) in TiO_2 below the conduction band. Subsequent deposition of the analyte (e.g., dinitrotoluene) followed by 633 nm laser excitation promotes charge transfer from TiO_2 to the metal nanoparticles; the resulting increase in nanoparticle charge leads to PIERS enhancement. Furthermore, upon air exposure, oxygen fills the vacancies, reducing electron excitation and gradually diminishing the PIERS effect over 30 to 60 min, though the substrate can be subsequently regenerated by UVC exposure. (**ii**) SEM image of PIERS-active nanostructures. Adapted from Ref. [60] under the terms of the Creative Commons Attribution 4.0 License; changes were made.

Table 2. Representative Charge-Transfer Pathways in Molecule-Coupled Metal–Semiconductor Heterostructures.

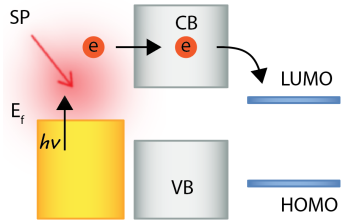
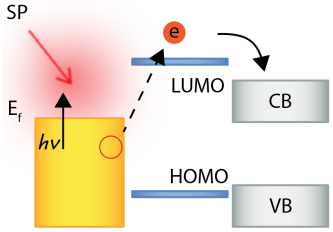
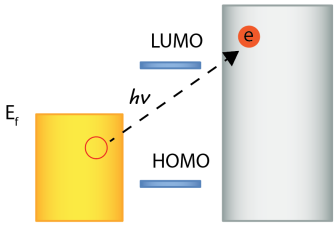
CT Pathway	Schematic Diagram	Mechanistic Description	Contact Architecture
Plasmon-Induced Hot-Electron Transfer (PIHET)		Plasmon decay generates hot electrons in metal, which are transferred to semiconductor and then to molecule	Single and Multiple contact modes

Table 2. *Cont.*

CT Pathway	Schematic Diagram	Mechanistic Description	Contact Architecture
Plasmon-Induced Interfacial Charge Transfer Transition (PICTT)		Direct excitation of electrons from metal to molecule to semiconductor via plasmon decay	Sandwich contact mode
Direct Interfacial Charge Transfer Transition (DICTT)		Direct CT from metal to semiconductor mediated by a molecule, independent of plasmon effects	Sandwich contact mode

The schematic diagrams are adapted from Ref. [34] with permission from The Royal Society of Chemistry.

In parallel with electronic-state manipulation, semiconductor superstructures can also enhance SERS through optical-field localization. Besides LSPR, Mie scattering resonances in semiconductor structures, such as submicrometer-sized ZnO spheres, can generate strong local electromagnetic fields and thereby increase the probability of exciting charge-transfer states when spatial and energetic overlap is satisfied [52]. In this case, Mie resonance should be interpreted as an optical antenna effect rather than a direct CT mechanism: it enhances the local field and photon-matter coupling conditions, whereas CT and PICT modify molecular polarizability through electronic coupling. Mathematically, Mie scattering can be described by the scattering cross-section:

$$C_{\mathrm{sca}} = \frac{2\pi}{k^2}\sum_{n=1}^{\infty}(2n+1)(|a_n|^2 + |b_n|^2) \quad (1)$$

Here, $k = 2\pi n_m/\lambda_0$ is the wavenumber in the surrounding medium, where n_m is the medium refractive index and λ_0 is the free-space wavelength; n is the multipole order, and a_n and b_n are the dimensionless electric and magnetic multipole scattering coefficients. Accordingly, C_{sca} has dimensions of area. Although the exact analytical framework is derived for highly symmetric geometries, Mie-like resonances can also arise in non-spherical semiconductor morphologies and are commonly evaluated using numerical methods such as discrete dipole approximation (DDA) or finite-difference time-domain (FDTD) simulations. In the context of hybrid SERS, this expression is most useful not as a direct quantitative predictor of EF, but as a conceptual boundary: Mie resonance describes optical field localization, whereas CT and PICT describe electronic coupling that modifies molecular polarizability. Distinguishing these contributions is important when interpreting semiconductor superstructures whose enhanced Raman response may arise from both optical antenna effects and interfacial charge transfer.

Organic semiconductors extend semiconductor-mediated SERS beyond inorganic heterostructures by demonstrating that charge-transfer enhancement can also be designed around molecular selectivity. Their advantages include structural versatility, solution-processable or vapor-deposited film fabrication, and tunable optoelectronic properties. For example, DFP-4T films with a fully π-conjugated structure exhibit an EF of 2.7×10^5 and a detection limit of 10^{-9} M, attributed to resonance CT between the organic semiconductor and the probe molecule, enabled by tuned molecular orbitals, electronic structure, and solid-state packing [103]. Nanostructured DFH-4T films similarly exhibit SERS activity even without a plasmonic layer, with an EF up to 3.4×10^3; after Au coating, the EF can increase to approximately 10^{10}, enabling sub-zeptomole-level detection (Figure 2C) [104]. More importantly, C_8-BTBT and D(C_7CO)-BTBT films demonstrate molecule-specific Raman enhancement only for methylene blue, the analyte with the lowest LUMO, suggesting an energy-feasible resonant transition from the organic semiconductor to the analyte frontier π orbitals [58]. These systems indicate that semiconductor-mediated SERS should not be evaluated solely by maximum EF, since orbital-level matching among the semiconductor, analyte, and excitation energy can introduce molecular selectivity into the enhancement pathway.

Overall, semiconductor-mediated hybrid SERS platforms should be evaluated by which enhancement pathway they render experimentally tunable, not only by their EF and limit of detection (LOD). These pathways include interfacial CT direction, carrier density, p-n band alignment, defect-assisted PICT, plasmon-mediated hot-electron transfer, Mie-assisted field localization, and analyte-selective resonance CT. EF and LOD remain key

performance metrics, but they do not by themselves identify the dominant enhancement pathway. Future studies would benefit from pairing performance evaluation with wavelength-dependent measurements, band-structure characterization, defect-state control, adsorption controls, and electromagnetic simulations, so that EM amplification, ground-state CT, PIHET/PICTT, Mie resonance, molecular adsorption, and analyte enrichment can be more clearly distinguished. Within the framework of this review, the systems discussed in this subsection correspond primarily to the synergistically coupled EM-CM, PIHET/PICTT-mediated, Mie-assisted, and analyte-selective CT entries summarized in Table 1.

3.2. Two-Dimensional Material Hybrids for Interface-Controlled Charge Transfer

Two-dimensional (2D) materials provide atomically thin platforms with rich physical and chemical properties for light–matter interactions, charge transfer, and molecular adsorption [124]. They are discussed here not as a simple list of SERS substrates, but as interfacial design platforms that control different variables in hybrid SERS enhancement. TMDs primarily tune phase-dependent density of states (DOS), band alignment, and layer-dependent charge-transfer (CT) efficiency; MXenes combine conductive carbide/nitride frameworks with termination-mediated adsorption and plasmonic assembly; and graphene regulates metal-molecule spacing, passivation, fluorescence quenching, adsorption, and externally induced CT modulation [125–129]. Table 1 provides coverage of representative 2D-material hybrid systems and analytical metrics, whereas the discussion below focuses on mechanistic design rules instead of ranking platforms by reported enhancement factor (EF) or limit of detection (LOD). The mechanism discussions are therefore based on the reported combination of energy-level alignment, phase/DOS analysis, wavelength dependence, molecular selectivity, CT or XPS evidence, electromagnetic/photonic simulations, and control experiments, rather than EF magnitude alone.

3.2.1. Phase and Layer Coupling in TMD Hybrid Interfaces

Two-dimensional TMDs have the general formula MX_2, where M is a transition metal and X is a chalcogen. Their layer-dependent band gaps, tunable light absorption, and multiple crystalline phases, including 2H, 1T, and 1T′, make them useful platforms for CT-mediated SERS [130,131]. In pristine semiconducting TMDs, the finite band gap and limited electronic coupling between substrate states and molecular frontier orbitals restrict the chemical mechanism (CM), even though the atomically flat surface can provide high spatial uniformity. Phase engineering therefore provides the first mechanistic handle: distorted 1T′ or quasi-metallic phases increase the DOS near the Fermi level, lower the energetic barrier for interfacial CT, and strengthen interfacial dipole formation. Lateral 1T′@2H $Mo_{1-x}Re_xS_2$ is best viewed as a phase-engineered model substrate, in which rhenium (Re) incorporation controls the coexistence of semiconducting and quasi-metallic domains and thereby tunes CT-active DOS and adsorption sites within a continuous 2D lattice [29,67,132–136].

Layer number provides a second, material-dependent control variable. The comparison between $PtSe_2$ and ReS_2 indicates that layer-dependent SERS is not governed by thickness alone, but by whether interlayer coupling is strong enough to alter band alignment and charge distribution [137]. This distinction is important because weakly coupled layers may add surface area without substantially changing the CT pathway, whereas strong interlayer interactions can make stacking an electronic-structure tuning parameter. Distorted 1T′-ReS_2 nanosheets further support a photo-induced charge-transfer (PICT) contribution rather than energy transfer, with monolayer structures showing the strongest response [97]. Plasmon-free 1T′-WTe_2 and $MoTe_2$ atomic layers extend this point by showing that high-DOS telluride surfaces can support strong CT-driven SERS without noble-metal hotspots when analyte energy levels and substrate states are favorably matched [105,137].

Once a CT-active TMD interface is established, optical structures can amplify it through different routes. In 4H-Au@1T′-WS_2 nanowires, the 4H-Au core provides plasmonic field enhancement, while the ultrathin semi-metallic 1T′-WS_2 shell supplies an electronically active interface for CM/CT contribution; this coupled EM-CM architecture underlies the attomolar SERS detection reported for R6G and SARS-CoV-2 spike proteins (Figure 3B) [98]. In contrast, DBR-integrated 1T′-WTe_2 amplifies a plasmon-free CT platform through photonic field localization rather than through a noble-metal plasmonic junction [97]. These examples show why TMD hybrid SERS should be read through a sequence of linked variables: phase determines whether CT is electronically accessible, layer coupling determines whether it is tunable, and plasmonic or photonic architectures determine how effectively the CT-active interface is optically amplified.

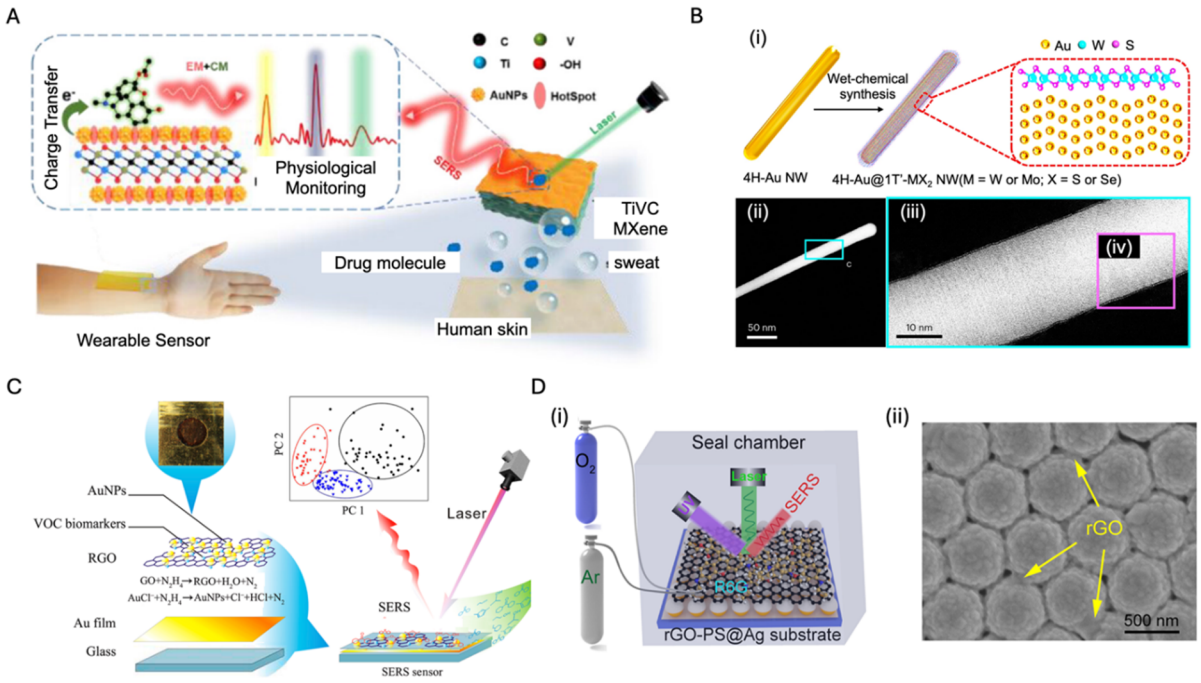


Figure 3. 2D Material–Hybrid Architectures for Advanced SERS Sensing. (**A**) Schematic illustration of a TiVC–OH–Au-based wearable SERS sensor for detecting drug molecules, such as nicotine, methotrexate, nikethamide and 6-acetylmorphine, from human sweat. Adapted with permission from Ref. [65]. Copyright 2024 American Chemical Society. (**B**) Synthesis and structural characterization of 4H-Au@1T′-WS_2 nanowires. (**i**) Schematic of the quasi-epitaxial growth of four types of 1T′-phase transition metal dichalcogenide (TMD) monolayers (WS_2, WSe_2, MoS_2, and $MoSe_2$) on 4H-phase gold nanowires (4H-Au NWs), forming 4H-Au@1T′-TMD core–shell nanowires. (**ii**) STEM image of a representative 4H-Au@1T′-WS_2 NW. (**iii**) HAADF-STEM image of the region marked in light blue in (**ii**). (**iv**) Corresponding FFT pattern obtained from the pink region in (**iii**). Adapted with permission from Ref. [98]. Copyright 2024 Springer Nature. (**C**) Schematic illustration of a SERS sensor integrated into a breath analysis platform, showing the overall sensing scheme. Adapted with permission from Ref. [57]. Copyright 2016 American Chemical Society. (**D**) Modulation of SERS signals in an O_2 atmosphere. (**i**) Schematic of in situ, real-time Raman measurements from a rGO–PS@Ag substrate under UV irradiation in O_2 (or Ar) atmosphere. The UV light is aligned with the Raman laser. (**ii**) SEM image of the rGO–PS@Ag substrate. Adapted with permission from Ref. [68]. Copyright 2022 American Chemical Society.

3.2.2. Surface Termination and Plasmonic Coupling in MXene Hybrid Interfaces

While TMDs primarily rely on phase and layer engineering to activate their semiconducting interfaces, MXenes introduce an alternative enhancement paradigm driven by their intrinsic metallic nature and rich surface chemistry. MXenes are transition-metal carbides and/or nitrides with the general formula $M_{n+1}X_nT_x$, derived from MAX phases by selective removal of the A element [66,138]. Their SERS behavior is distinguished from TMDs and graphene by the coexistence of metallic conductivity, high DOS, hydrophilicity, and chemically diverse surface terminations such as –O, –OH, and –F. These terminations are not merely structural labels: they determine adsorption geometry, localized dipole interactions, hydrophilicity, and the density of electronically active sites available for CT. Pristine or lightly modified MXenes therefore operate mainly through CM/CT pathways, while their limited intrinsic electromagnetic hotspots motivate integration with noble metals for coupled EM-CM enhancement [29,64,125,139].

Among intrinsic MXene examples, TiVC solid-solution MXene is a representative example because its high reported EF is linked to a bimetallic, high-DOS surface and a PICT-involved CM pathway [64]. Ti_2N paper substrates similarly show that conductive MXene surfaces can generate strong Raman enhancement without conventional noble-metal hotspots. Cross-study mechanistic comparisons require caution because EF definitions, resonant probe molecules, excitation wavelengths, adsorption protocols, and substrate uniformity vary substantially across reports [66]. The more defensible design rule is that MXene composition and surface chemistry should be selected to maximize electronically active adsorption sites and CT coupling for the target analyte [66]. Post-treatment can further turn this electronic potential into a more accessible sensing interface. For example,

alkaline-treated TiVC membranes increase the density of active sites and translate MXene-mediated CT into a flexible sensing format for molecular-level monitoring (Figure 3A) [65].

Noble-metal integration moves MXenes from predominantly CT-mediated substrates toward coupled EM-CM platforms. In MXene/graphene oxide/Au nanocluster fibers, Au nanoclusters provide plasmonic hotspots, while the MXene component contributes conductivity, CT participation, and mechanical flexibility; the reported retention of Raman intensity after long-term storage further highlights the translational value of stabilizing the MXene interface [106]. $Ti_3C_2T_x$/Au nanoparticle dimer aptasensors illustrate a complementary design: the MXene sheet acts as a conductive and functional scaffold that brings plasmonic nanogaps and biorecognition elements into the same interfacial region for target-selective detection [107]. Other MXene-Au nanocomposites and plasmonic MXene hydrogels add antibacterial, photothermal, pollutant-enrichment, or remediation functions. Yu et al. synthesized MXene-Au nanocomposites capable of both rapid bacterial detection and efficient photothermal sterilization, achieving nearly 100% germicidal rates within minutes [108]. For environmental remediation and sensing, Yang et al. introduced plasmonic MXene hydrogels that not only achieve over 90% dye removal but also identify organic dyes at femtomolar-to-attomolar concentrations [109]. These deployment advantages should be distinguished from the primary enhancement pathway, which arises from the coupling of MXene-mediated adsorption/CT with plasmonic field localization.

3.2.3. Spacer Control and Charge Modulation in Graphene Hybrid Interfaces

Moving beyond the highly active charge-transfer interfaces provided by TMDs and MXenes, graphene highlights the critical role of structural and environmental regulation in hybrid systems. Graphene, a two-dimensional atomically thin crystal composed of densely packed sp^2-hybridized carbon atoms in a honeycomb lattice, has attracted significant attention owing to its exceptional electrical, optical, mechanical, and thermal properties [140]. Graphene-based hybrids should be interpreted with a different emphasis. Pristine graphene can support molecule-graphene CT, while its visible-frequency plasmonic response and intrinsic Raman enhancement are weak relative to noble-metal substrates [110,140–142]. Its main contribution in hybrid SERS is therefore interfacial regulation. Graphene suppresses fluorescence, dissipates heat from plasmonic hotspots, protects analytes from photodamage, and provides π–π adsorption sites for aromatic molecules. These functions improve spectral cleanliness, reproducibility, and analyte localization, even when graphene is not the dominant source of Raman enhancement [68,124,143–147].

A clearly studied graphene-regulated architecture is the metal/graphene/metal junction. In Au triangular nanoarray/n-layer graphene/Au nanoparticle sandwich substrates, graphene acts as an atomically thin spacer that creates dense sub-nanometer plasmonic gaps while limiting uncontrolled metal-molecule contact; this enables sensitive and uniform Hg^{2+} detection through a TAMRA-tagged DNA probe [11]. This case is best described as EM-dominated hotspot engineering enabled by graphene-controlled spacing and passivation. Related Ag nanoparticle/graphene hybrids show that particle size and Ag-to-graphene CT can modulate the response, supporting a role for graphene-mediated interface control rather than a standalone high-EF graphene mechanism [110,111].

Graphene can also become an actively tunable CT medium when its Fermi level or surface electronic state is externally modulated. UV- and gas-atmosphere-controlled RGO/Ag hybrids demonstrate this behavior: exposure to O_2, CO_2, N_2, or air under illumination changes the graphene-derived electronic environment and modulates CT at the plasmonic interface (Figure 3D) [68]. In real-sample sensing, RGO/Au breath-analyzer substrates highlight a more practical graphene function, namely selective adsorption and enrichment of volatile biomarkers at a plasmonic interface (Figure 3C) [57]. Together, these examples show that graphene hybrid SERS is strongest as a platform for controlling junction spacing, passivation, adsorption, and CT modulation, rather than as a direct analogue of high-DOS TMD or MXene substrates.

Taken together, 2D-material-supported hybrids are most useful when compared by the interfacial variable they control. TMDs emphasize phase- and layer-engineered CT, MXenes combine conductive and termination-rich surfaces with plasmonic assembly, and graphene regulates metal-molecule spacing, passivation, adsorption, and external CT modulation. This distinction allows Table 1 to serve for a mechanism-indexed comparison of representative architectures, with EF and LOD retained as context-dependent performance indicators rather than universal ranking metrics.

3.3. Photonic-Crystal Hybrid Interfaces for Field Localization and Analyte Enrichment

Photonic crystals (PCs) are a class of materials that provide novel capabilities in manipulating the flow of photons [148,149]. These materials consist of nanoscale periodic arrays of materials with different refractive indices, creating “photonic band gaps” in which photons cannot propagate through the material. PCs can be fabricated by

high-precision microfabrication, which offers substantial design control at higher cost. Naturally occurring structures offer low-cost alternatives but less design control. For the latter, materials such as diatoms [150] and opals [151] are two representative examples that display vivid colors due to their porous, periodic silica nanostructures.

Integrating PCs with traditional plasmonic nanostructures can create a new class of hybrid SERS substrates with multiple functionalities. Since PCs can intensify optical fields by slow-light effects [152] and guided-mode resonances (GMRs) [153,154], they can be used to further amplify metallic-nanoparticle plasmonic resonances, creating high-intensity hotspots for optimized SERS sensing [53,54]. Alongside simulation results showing meaningful SERS improvement for both individual plasmonic NPs [55] and a collection of randomly distributed NPs [112], the enhancement has also been experimentally verified by mapping SERS signals around a diatom frustule (Figure 4a) [56].

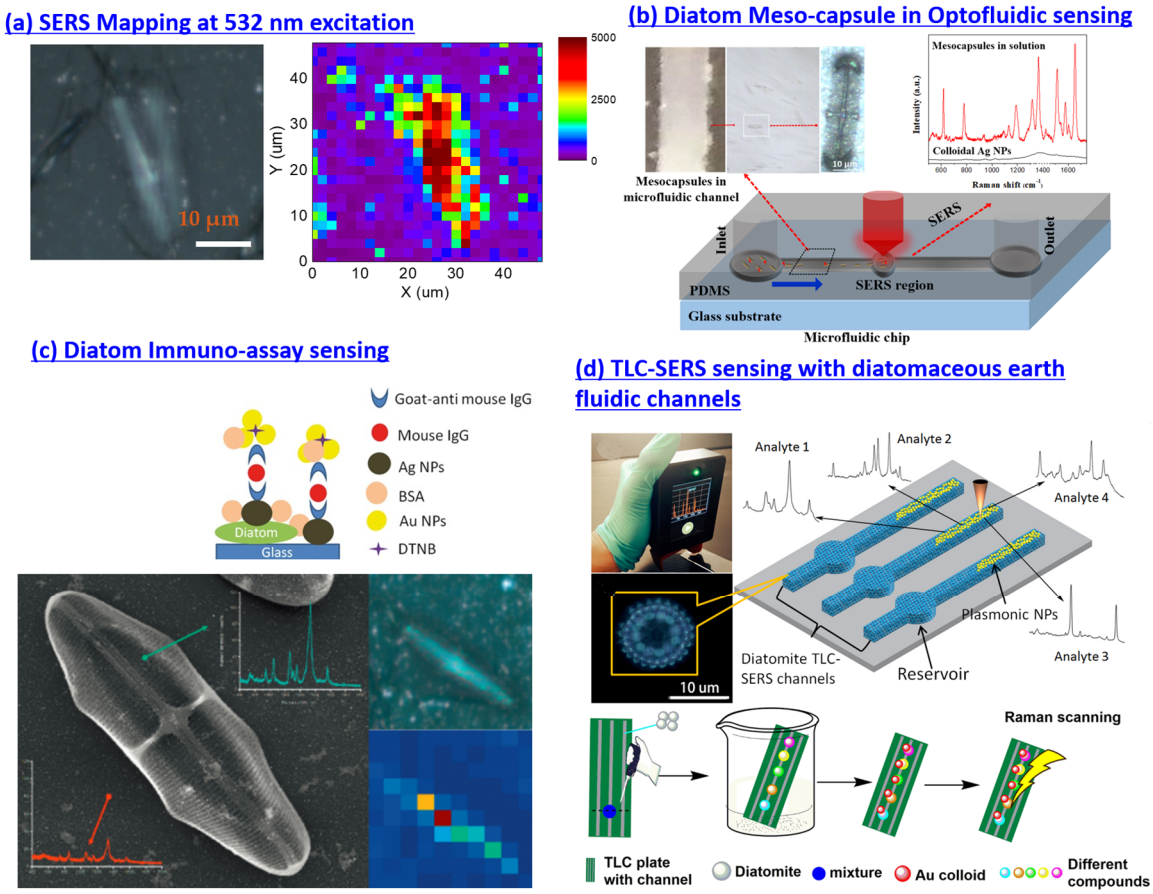


Figure 4. Diverse SERS sensing applications enabled by diatom photonic crystals. (**a**) Comparison of the optical image of a diatom frustule and its SERS mapping data (Reproduced with permission from Ref. [56]. Copyright 2014 IEEE.); (**b**) Schematic of diatom meso-capsule for optofluidic sensing with accelerated mass transport (Reproduced with permission from Ref. [113]. Copyright 2019 Wiley-VCH Verlag GmbH & Co. KGaA.); (**c**) Illustration of diatom SERS immunoassay and experimental results showing the enhanced sensitivity to detect mouse IgG (Adapted with permission from Ref. [114]. Copyright 2014 Wiley-VCH Verlag GmbH & Co. KGaA.); (**d**) Schematic of TLC-SERS sensing using diatomaceous earth fluidic channels (Adapted with permission from Ref. [116]. Copyright 2017 Elsevier B.V.).

Further improvements in SERS performance can be achieved by combining additional strategies such as (1) accelerating mass-transport to deliver trace analytes to the sensor surface in optofluidic sensing [112,155,156], or (2) subsequent functionalization of the PCs [157]. For the former, methods such as utilizing evaporation-based thermal Marangoni effects have shown that the resulting convection flow can combat the diffusive force, leading to label-free sensing of 4.5×10^{-17} g trinitrotoluene (TNT) at the diatom surface [112]. In another example, microfluidic channel-enabled mixing of PC-enhanced plasmonic meso-capsules and analytes, in conjunction with porous submicrometer mesocapsules decorated with Ag NPs, leads to an approximately 100-fold higher signal and a >1000-fold lower LOD, compared with ordinary Ag NPs (Figure 4b) [113]. For the latter, antibody functionalization of PCs has been explored for enhancing biosensing sensitivity and selectivity. One example

showcases a sandwiched SERS-active immunoassay substrate, functionalizing diatom PCs with anti-mouse IgG, showing the detection limit of mouse IgG down to 10 pg/mL (Figure 4c) [114]. Similar SERS immunoassays have also been applied to detect interleukins in blood plasma [158] and circulating cancer-specific protein biomarkers in serum [159].

PCs can also be used as the stationary phase of thin-layer chromatography (TLC). Compared with traditional analytical chemistry methods such as high-performance liquid chromatography (HPLC) and gas chromatography (GC), TLC is a rapid, cost-effective technique for separating and identifying mixed compounds [160]. The combination of TLC with SERS, or simply abbreviated as TLC-SERS, creates a lab-on-a-chip sensing platform that can simultaneously perform chemical separation and spectral sensing [161,162]. However, the biggest problem is that the TLC stationary phase is usually not a good SERS substrate, and the sensitivity of TLC-SERS is not sufficient for trace-level chemical sensing. Diatomaceous earth consisting of fossilized remains of ancient diatoms in geological deposits stands out as the TLC-SERS substrate because: (1) the porous hydrophilic feature makes it an excellent stationary phase for TLC separation, and (2) the photonic-crystal effect effectively enhances the plasmonic nanoparticles for SERS sensing. Diatomaceous TLC-SERS has been successfully applied to various real-world sensing applications, including identifying Sudan I in cooking oil [163], detecting histamine in seafood [115], and label-free sensing of phenethylamine and miR21cDNA in human plasma [164]. One noticeable improvement to TLC-SERS sensing is replacing traditional thin-layer plate with patterned fluidic channels formed by diatomaceous earth as shown in Figure 4d, which can prevent lateral diffusion of analytes as they move along the stationary phase [115,116]. As a result, the analyte concentration at the detecting spot is significantly improved, resulting in unprecedented sensitivity down to the parts-per-billion (ppb) level.

In summary, integrating PCs with SERS substrates can greatly improve SERS performance by utilizing their unique properties such as GMRs. Within the established mechanistic framework, bio-photonic-crystal–plasmonic platforms operate primarily in the electromagnetic (EM)-dominated regime, further augmented by photonic field localization. Notably, several of the systems surveyed in this subsection additionally result in localized mass-transport effects—such as Marangoni convection in evaporating diatomite droplets and chromatographic flow in TLC-SERS configurations. By dynamically concentrating analytes at the sensing interface, these transport phenomena effectively bridge passive architectures in Table 1 with the active platforms to be introduced in the following section and Table 3. Such mechanistically diverse PC-SERS platforms based on biological materials offer a framework for transitioning laboratory sensing into reliable, real-world biochemical applications.

Table 3. Comparative summary of active-enrichment and field-guided mobile SERS platforms.

System	Actuation Mode	Mechanism	Active Component	Target Analyte	LOD	Detection Time	Note	Operating Environment	Ref.
Ni/Au-decorated carbon helical nanorobots	Magnetic	Magnetic-field-driven helical propulsion	Carbon nanocoil with Ni/Au coating; helix length 8.6 ± 0.8 μm	Intracellular HeLa cytoplasm + nucleus (endogenous biomolecule fingerprints)	Subcellular fingerprints; LOD not reported	Real-time SERS at fixed cell location after entry	Magnetic corkscrew, 6.7 μm/s avg; B = 5 mT, f = 6–8 Hz; mechanical penetration of cell membrane + nuclear envelope	HeLa cells (intracellular); also DI water, FBS, PEG, intestinal fluid	[69]
MAuNS—Fe_3O_4 core + gold nanostar (AuNS) shell	Magnetic + Catalytic + Photothermal	Magnetic steering + glucose-oxidase-like nanozyme + photothermal	Core-island MAuNS = Fe_3O_4 core + Au-nanostar (AuNS) islands	CV + 4-MBA monolayer (model); intracellular HeLa contents	NR	Not stated; SERS integration 10 s	Glucose-fueled enhanced diffusion	Aqueous (glucose); intracellular HeLa	[165]
Ag-NP-coated diatom frustule + Ni magnetic film	Magnetic	Magnetic-field-driven rotational actuation (asymmetric Ni patch)	Bio-derived diatom photonic crystal frustule with self-assembled Ag NPs and asymmetric Ni magnetic coating	Salmon sperm DNA (large biomolecule, 724 & 1319 cm^{-1} peaks)	≈80 nM at S/N = 5; range 80 nM–4 μM	Characteristic capture time, τ_{cap}, scaled with rotation rate as $\tau_{cap} \propto \omega^{-0.41}$ over the reported operating range: ≈30 min at 1200 rpm vs. 2 h passive (≥4× capture-rate speedup); ~3× detection-speed improvement at 80 nM at 630 rpm	Magnetic rotation up to 1200 rpm; 532 nm Raman, 500 μW, 25 μm spot	Aqueous solution	[26]

Table 3. *Cont.*

System	Actuation Mode	Mechanism	Active Component	Target Analyte	LOD	Detection Time	Note	Operating Environment	Ref.
Magnetic nanochain integrated microfluidic biochip	Magnetic	Magnetic mixing + bioseparation in microfluidic channel	Magnetic nanochains in microfluidic biochip	Cancer biomarkers (PSA, AFP, CEA—clinical serum, n = 20); bacteria (*E. coli* O157:H7, S. aureus); SERS reporters MATT/DCTP/DFTP/TFTP	LOD ≈ 10 pg/mL (proteins); 4/10/5 ng/mL (PSA/AFP/CEA); bacteria 10^0–10^4 CFU/μL range; EF > 10^5	≈8 min from 1 μL body fluid	Magnetic nanochains as nanoscale stir bars; 4 orthogonal electromagnetic coils; 100× enrichment via volume difference (mixing vs. detection chamber); λ_{ex} 633 + 785 nm, 2–5 μm spot	Body fluid (1 μL)/clinical microfluidic chip	[20]
Photocatalytic matchstick-like nanomotor (Ag-NW/silica core-shell + AgCl tail)	Optical (photocatalytic)	Light-induced self-diffusiophoresis (phototaxis)	Silver nanowire/silica core-shell with AgCl photocatalytic tail	Crystal violet (CV, 10^{-4} M); MCF-7 breast cancer cells	10^{-4} M CV demonstrated; no LOD reported	≈10 s of focused UV irradiation to form aggregates	Light-powered self-diffusiophoresis (AgNW@SiO_2/AgCl matchlike, ~15 μm long); positive phototaxis aggregation; SHIERS via 5–10 nm SiO_2 shell	Aqueous (water); fixed MCF-7 cells (cellular)	[71]
Optoelectric Si-nanorod/Ag-NP Raman nanosensor	Electric + optical	Light-gated optoelectric enrichment at the laser spot	Si nanorod array with root electrodes and dense Ag NPs	Adenine; vertebrate DNA	0.6 fM adenine	≈15 min to reach ≈150-fold enhancement at −0.8 V	LOD improved by five orders of magnitude at −0.8 V	Aqueous electrochemical cell	[166]
Magnetic micromotors with spiky gold nanoshells	Magnetic	Magnetic-field-driven micromotor propulsion	Spiky Au nanoshell on magnetic core → high-curvature plasmonic hotspots	4-ATP (calibration reporter); thiram (target); *E. coli*, S. aureus (label-free)	Thiram LOD 10^{-8} M (Ag@Au); 4-ATP linear 10^{-11}–10^{-8} M	Bacterial capture from bulk: hours to overnight	3D rotating B-field ($B_{xy} = B_z = 4.5$ mT; $\omega_M = 40\pi$ rad s^{-1}); on hydrogel 2–3× faster than glass; closed-loop trajectory; λ_{ex} 785 nm, 0.438 mW, 10 s	DI water, lake water, salty culture medium; blood plasma	[70]

Table 3. *Cont.*

System	Actuation Mode	Mechanism	Active Component	Target Analyte	LOD	Detection Time	Note	Operating Environment	Ref.
Optical-tweezers-controlled hotspot—Ag-NP-coated silica beads	Optical (trapping)	Optical trapping → controllable plasmonic junction	Two AgNP-coated silica beads optically focused into a tunable plasmonic gap	Native protein structures—hemoglobin, lysozyme, BSA	100 nM hemoglobin; 1 μM lysozyme/BSA; 1 μM α-synuclein; 10^{-9} M and 10^{-11} M RhB	1 s acquisition; flow-through microfluidic continuous detection	Dual-trap optical tweezers; sub-nm interbead distance control (10–900 nm gap); 1.26 μm AgNP-coated silica beads; λ_{ex} 532 nm Raman + 1064 nm trap	Aqueous; native-conformation conditions (no surface tethering)	[73]
Optical plasmonic tweezer + microfluidic flow chamber	Optical (trapping) + microfluidic	Optical plasmonic tweezing in flow	Plasmonic tweezer-trapped hotspot in microfluidic channel	Amylin (hIAPP)—pH-dependent species; transient amyloid intermediates	500 nM NBA proof-of-concept; 10^{-7} M MB/10^{-8} M NBA (BiASERS); 10 μM hIAPP at pH 5.5 & 7.4; 50 μM Tyr	Continuous on/off switching in seconds; 24 h pH-incubation studies	Optical plasmonic trap of single AgNP into bead-dimer junction (~20 nm gap via oligonucleotide tether); λ_{ex} = 532 nm, P = 2.7 mW (Raman); λ_{trap} = 1064 nm, P_{trap} = 8.0 mW (trapping)	Aqueous; pH-controlled; microfluidic	[74]
3D electrokinetic tweezers—anisotropic nanowire bioprobe	Electric	Composite electrokinetic effects (electrophoresis, dielectrophoresis, electrorotation, electroalignment)	Anisotropic nanowire bioprobe in AC/DC electric field	General-purpose nanowire bioprobing platform	NR	NR	20 nm 2D position precision; 0.5° angular precision; rotation up to 18,000 rpm; 90 nm position accuracy at 2.7 μm/s; PI feedback anti-Brownian; 4 in-plane + 2 out-of-plane electrodes; λ_{ex} 532 nm Raman, 360 μW after 20× obj	Aqueous solution (low ionic strength implied)	[75]
Plasmonically active Au–Ni–Au rotary nanomotor	Electric (rotary)	Electric-field-driven rotation; rotation speed modulates molecular release	Au–Ni–Au three-layer nanowire core/silica shell/dense Ag-NP outer layer	Nile Blue and R6G (single and multiplex release)	NR	Quasi-real-time Raman monitoring (0.5 spectrum s^{-1}); release tracked for up to 30 min	Release rate increases with rotation speed through convection-induced diffusion-layer thinning	DI water; electrically actuated microelectrode platform	[27]

Table 3. *Cont.*

System	Actuation Mode	Mechanism	Active Component	Target Analyte	LOD	Detection Time	Note	Operating Environment	Ref.
Porous superstructural Au-nanorod/Ag-NP Raman nanosensor	Electric (transport/rotation and release control)	Electric-field-guided manipulation and AC-field-tuned molecular release	Au nanorod (~5 μm × 280 nm) with ~850 nm porous silica superstructure and dense Ag NPs in concentric nanocavities	R6G; BPE; Nile Blue; adenine	R6G LOD 10^{-15} M (1 fM); BPE 10^{-13} M	Quasi-real-time Raman monitoring	Dual-function ultrasensitive detection and tunable release; λex = 532 nm	Aqueous suspension under external electric fields	[167]
Ring-like Fe_3O_4/Au nanozyme	Magnetic + Catalytic	Magnetic separation + peroxidase-like catalysis	Reusable ring-like Fe_3O_4/Au nanozyme	TMB (probe via peroxidase oxidation); GSH and cholesterol (target biomolecules)	GSH LOD 0.10 μM (linear 1–150 μM); cholesterol LOD 0.08 μM (linear 1–100 μM); UV-vis comparison LODs 0.88/0.48 μM	30 min incubation at 37 °C for catalysis; 11 min reaction equilibrium for R-Fe_3O_4/Au	Superparamagnetic ring-Fe_3O_4 (160/60/50 nm OD/ID/thickness); magnetic recovery, 5 reuse cycles; λ_{ex} 785 nm portable Raman	Human serum (clinical, Xuzhou First People's Hospital); HAc-NaAc buffer pH 4.0	[168]
Fe_3O_4@TiO_2 exosome accumulation + target-triggered SERS	Magnetic	Magnetic-induced exosome accumulation	Fe_3O_4@TiO_2 core-shell + target-triggered Raman reporter	Exosomal microRNA (in situ)	0.21 fM exosomal miRNA-10b LOD; linear 0.33 fM–1.65 pM; tested 10^7–5×10^{10} exosomes/mL; 4 μL serum	3–4 h SERS-tag/exosome incubation + 10 min Fe_3O_4@TiO_2 magnetic capture (no ultracentrifuge, no lysis, no PCR amplification)	Fe_3O_4@TiO_2 (~200 nm) magnetic exosome capture via TiO_2-phosphate affinity (96.5% in 10 min); LNA-Au@DTNB hotspot trigger inside intact exosome; λ_{ex} 785 nm, 10 mW, 50× objective, NA = 0.75, 1 s	Serum from PDAC patients (n = 15) and healthy controls (n = 15); clinical liquid-biopsy	[169]

Table 3. *Cont.*

System	Actuation Mode	Mechanism	Active Component	Target Analyte	LOD	Detection Time	Note	Operating Environment	Ref.
Magnetic-induced mixing SERS—ternary specific antigens	Magnetic	Magnetic-induced mixing during SERS readout	Magnetic SERS substrate with ternary antigen-recognition labels	Liver cancer—simultaneous detection of three specific antigens	AFP 0.15 pg/mL; CEA 20 pg/mL; FER 4 pg/mL (LOD); ranges 0.5–500/50–2000/10–200 pg/mL	≈1 h immunoreaction at 37 °C × 2 (sandwich); plus magnetic separation	Carboxyl-coated Dynabeads MyOne (1.05 µm) for magnetic 3D packing/aggregation under external magnet; alkyne/nitrile reporters in biosilent 2105/2159/2227 cm^{-1} window; λ_{ex} 632.8 nm, 40× obj, 10 s	2% human serum; 39 clinical samples; 86.7% liver-cancer diagnostic accuracy	[170]
Label-free magnetic SERS for exosomes	Magnetic	Integrated magnetic separation + label-free SERS	Magnetic SERS platform with integrated separation chamber	Exosomes (label-free)	NR	5 h Fe_3O_4/Au internalization + 1 min magnetic separation	Magnetic separation in 1 min (external magnet); superparamagnetic Fe_3O_4 (~12 nm core) + Au shell (~20 nm); aggregation in exosome enhances SERS; FDTD validates hotspots	Cell culture supernatant (MCF-7, MDA-MB-231, MCF-10A, HepG2, Hep1-6, L02); mouse serum (healthy vs. tumor-bearing); PCA → 100% sens/spec	[171]
CRISPR-Cas-mediated SERS assay	Biomolecular (CRISPR) + plasmonic	dCas9/gRNA sequence-specific binding to target genomic DNA, followed by MB intercalation and magnetic enrichment; no trans-cleavage or target amplification	Au MNP–dCas9/gRNA probes with MB as an intercalating Raman reporter	Species-specific virulence-gene targets: spa (S. aureus), pgi (A. baumannii), and uge (K. pneumoniae)	14.1 fM (*S. aureus*); 9.7 fM (*A. baumannii*); 8.1 fM (*K. pneumoniae*)—without amplification	≈60.5 min for the listed assay steps (50 min target-binding incubation + 10 min MB intercalation + 30 s magnetic concentration), excluding washing and SERS readout; ≥6 h for PCR.	Au MNPs (Fe_3O_4 ~110 nm core + SiO_2 ~95 nm shell + Au; total ~390 nm); superparamagnetic (M_s = 58.7 emu g^{-1} (= 58.7 A m^2 kg^{-1})); λ_{ex} 632.8 nm He-Ne, 50× obj, ~2.5 µm spot	Mouse blood and tissue homogenates (in vivo–derived); 3D nanopillar swab samples (skin/tail/foot/glove)	[172]

Table 3. *Cont.*

System	Actuation Mode	Mechanism	Active Component	Target Analyte	LOD	Detection Time	Note	Operating Environment	Ref.
Magnetic mesoporous nanosponge (β-cyclodextrin polymer + magnetic NPs)	Magnetic	Magnetic-induced bulk enrichment + chromatographic-like adsorption	Mesoporous β-CD polymer nanosponge with embedded magnetic NPs	Organic micropollutants	Lowers LOD by 2–3 orders vs. static SERS	≈90% removal in <1 min	≈1000× concentration factor	Aqueous (environmental water)	[76]
Polydopamine-enabled plasmonic nanogapped nanoparticles	plasmonic	Polydopamine-mediated tailored nanogap engineering	Plasmonic nanogap NPs with polydopamine spacer	RhB and 4-NTP Raman reporters; *E. coli* O157:H7 (food-borne pathogen); also MOF and AuNR cores	Linear 10–10^8 CFU/mL; sensitivity ~10^2 CFU/mL	10 min magnetic separation	Magnetic separation enrichment via Fe_3O_4 core; polydopamine-templated 2 nm nanogap; λ_{ex} 633 nm (RhB) + 785 nm (pathogen)	Aqueous (general)	[173]
Fe_3O_4@Ag magnetic SERS nanotag + lateral-flow strip	Magnetic + immunoaffinity	Magnetic enrichment + dual-Raman-label sandwich on LFA strip	Fe_3O_4@Ag NPs functionalized with dual Raman dyes + virus-specific capture antibodies	Influenza A H1N1 + human adenovirus (HAdV)—simultaneous	H1N1: 50 pfu/mL; HAdV: 10 pfu/mL	≈20 min total assay (incubation + lateral flow); λ_{ex} 785 nm Renishaw inVia, 3 mW, 5 s, 50 μm spot, 20× obj	≈2000× sensitivity improvement vs. traditional colloidal-Au LFAs	Real biological samples (human throat/nasopharyngeal swabs); no pretreatment	[77]

Abbreviations & notes: LOD—limit of detection. **Relative metric**—performance reported as a fold-improvement against an internal reference (e.g., "2000× over colloidal-Au LFAs"). **LFA**—lateral flow assay. **MAuNS**—magnetic gold-nanostar nanozyme. **β-CD**—β-cyclodextrin (used as polymer host in mesoporous nanosponge). **CRISPR**—Clustered Regularly Interspaced Short Palindromic Repeats (here: dCas9/gRNA target recognition coupled with MB-based SERS reporting and magnetic enrichment). **hIAPP**—human islet amyloid polypeptide (amylin); single-molecule pH-dependent species used to probe amyloid intermediates. **NR**—not reported.

4. Hybrid SERS Platforms for Active Molecular Enrichment

Ultrasensitive SERS sensors that rely solely on passive molecular diffusion face an intrinsic barrier: the ultrahigh sensitivity enabled by nanoscale hotspots for detecting ultra-low-concentration analytes inevitably results in slow detection kinetics. Conventional nanosensors can require hours to detect analytes in the 1 pM–1 fM range [166]. Such prolonged detection times increase susceptibility to noise and compromise sensing fidelity.

To address this limitation, active and responsive SERS platforms improve analyte enrichment in three recurring ways. First, motion-enhanced platforms use mobile SERS-active probes or hotspots to increase molecular capture speed by a sensor's surface, reducing diffusion-limited detection times. Second, field-guided platforms use optical or electric fields to position plasmonic components, assemble hotspots, or bring analytes into defined sensing regions. Third, capture- and separation-assisted magnetic platforms isolate and concentrate targets from complex matrices before Raman readout. Across these cases, the inherited SERS enhancement pathway is coupled to an analyte-enrichment strategy. The examples listed in Table 3 therefore emphasize detection time, operating environment, and enrichment or actuation mode rather than EF alone.

4.1. Motion-Enhanced Hybrid SERS Platforms

This subsection focuses on hybrid SERS systems in which SERS-active probes or hotspots are actively transported, rotated, or propelled through the sample. Their main contribution is to accelerate molecular capture by a sensor's surface, while preserving the EM, CM, or coupled EM-CM enhancement mechanisms enabled by the sensing material.

Micro/nanomotors are miniaturized machines capable of dynamic responses such as transport, rotation, and swarming under chemical, magnetic, optical, or electric stimuli [36,174]. When integrated with SERS-active plasmonic structures, these platforms create "motile hotspots" that actively sample analyte-rich regions or enhance analyte–substrate interaction in solution. This strategy directly addresses a major limitation of static SERS sensors: at ultralow analyte concentrations, passive diffusion alone can make molecular capture at nanoscale hotspots slow and inefficient [26,27,175,176]. However, translating this "motile hotspot" concept from idealized, low-viscosity laboratory solutions to complex biological fluids presents significant challenges. Viscous biological media inherently limit propulsion efficiency due to the dominant viscous drag forces operating at low Reynolds numbers. Concurrently, the abundance of biomacromolecules in these environments leads to nonspecific surface adsorption that can physically block SERS-active nanogaps, impede targeted molecular enrichment, and generate severe background spectral interference. The propulsion mechanisms, summarized in Table 4, have been detailed in several review articles [175,177,178].

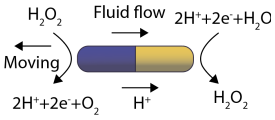
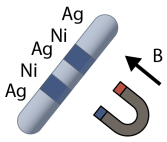
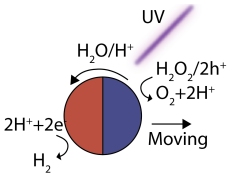
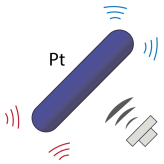
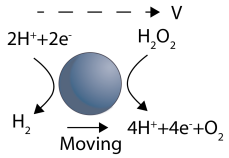
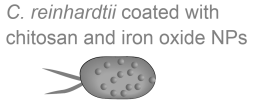
Magnetic Nanomotor Sensors: Magnetic-field-driven nanorobots represent a particularly attractive class of active SERS platforms due to their precise spatiotemporal control, fuel-free actuation, high reconfigurability, and generally benign operation in biological environments. Compared with chemically powered systems, magnetic actuation avoids the introduction of reactive fuels and offers superior controllability, which is advantageous for in vivo or intracellular applications. For instance, Ni/Au-decorated carbon helical nanorobots have demonstrated the capability to mechanically penetrate single-cell membranes and nuclear envelopes, enabling intracellular SERS interrogation of both cytoplasmic and nuclear compartments [69]. While such demonstrations highlight the potential for precise cancer theranostics with minimal cytotoxicity, challenges remain in achieving in vivo precision control and long-term stability.

Magnetic microrobots have also been explored for selective bacterial detection, including discrimination between *E. coli* and *S. aureus*, through active approach, contact formation, and localized SERS acquisition. Detection limits down to 10 nM for thiram have been reported, with operational stability maintained over weeks [70].

More recently, nanozymatic magnetic nanomotors (MAuNS), integrating a magnetic Fe_3O_4 core with gold nanostars, have combined magnetic propulsion with plasmonic and catalytic functionalities [165]. The Fe_3O_4 core enables remote magnetic steering, whereas the AuNS provide both strong SERS activity and glucose oxidase–like catalytic behavior, enhancing mass transport and cellular uptake for improved photothermal therapy. In addition, multimodal imaging, via magnetic resonance imaging of Fe_3O_4 and photoacoustic imaging of AuNS, facilitates real-time tracking. Despite these advances, integrating propulsion, hotspot uniformity, and quantitative SERS readout into a single robust platform remains an ongoing challenge.

Another notable strategy involves the active actuation of magnetic-film-coated bioparticles to accelerate biomolecule enrichment and detection [26]. In this study, Ag-nanoparticle-coated diatom frustules were asymmetrically functionalized with a magnetic Ni film, enabling rotational actuation under an external magnetic field while providing abundant plasmonic hotspots for SERS detection.

Table 4. Propulsion mechanisms of typical nanomotors.

Driven Type	Schematic	Components	Propulsion Mechanism	Advantage
Chemical		– Catalytic materials: Pt, Au, Ni, MnO_2 – Asymmetric structures: Janus microspheres, bimetallic nanowires	– Self-electrophoresis – Bubble recoil – Self-diffusiophoresis	– High-speed movement – Performance in high-ionic-strength media depends strongly on the propulsion mechanism and surface chemistry – Requires specific fuels
Magnetic Field		– Ferromagnetic materials: Fe, Ni – Ferrimagnetic material: γ-Fe_2O_3 – Helical or flexible structures	– Magnetic field gradients – Rotating magnetic fields induce helical motion – Oscillating magnetic fields drive flexible chains	– Fuel-free operation with remote controllability – Suitable for complex environments – Adjustable helix pitch for optimized propulsion efficiency
Light-Driven		– Photocatalysts: TiO_2, ZnO, Fe_2O_3, Au – Semiconductor materials	– Photochemical reactions – Photothermal interactions – Generation of electron-hole pairs leading to diffusiophoresis or bubble propulsion – Thermophoresis driven by local thermal gradients	– High temporal and spatial resolution control – Enables smart behaviors such as phototaxis and swarming – Can operate without externally added fuel in suitable photochemical systems – Precise trajectory control via light parameters
Ultrasound		– Asymmetric metallic nanowires – Bimetallic rods: Au or Pt with Rh, Ru, Pd, Ag)	– Acoustic radiation pressure generates net propulsion force – Structural density and shape influence propulsion	– High biocompatibility – Suitable for biomedical applications – Optimization of propulsion efficiency through acoustic field parameters
Electric Field		– Electrochemically active conductive micro-/nanoparticles – Asymmetric catalytic or bipolar-electrode interfaces	– Applied voltage drives electrochemical redox reactions – Ionic gradients and/or gas evolution generate self-electrophoretic or bubble-recoil propulsion	– Remote electrical control with adjustable propulsion speed – Performance depends on electrolyte composition and interfacial reactions – Requires suitable electrolytes and applied electric fields
Biohybrid		– Natural biological robots: sperm, bacteria, algae – Synthetic microstructures: microtubes	– Flagellar motion of biological robots combined with synthetic structures – Cell-driven self-powered propulsion	– Long-lasting and rapid movement – Enhanced biocompatibility – Supports chemotactic behavior and autofluorescence

In both cases, detection kinetics were rationally enhanced through active motion—specifically, increased rotational or translational speeds—which increased analyte flux toward the sensing surface. Numerical simulations and theoretical analyses revealed that such active propulsion effectively reduces the effective diffusion-boundary-layer thickness, thereby accelerating molecular flux to the sensor interface. As a result, detection speed is substantially improved while preserving high sensitivity [26].

Light-Powered Nanomotor Sensors: Light represents another widely adopted energy source for remotely actuating nanomotors, offering high spatial and temporal precision without direct physical contact [179]. Photocatalytically powered, matchstick-like nanomotors, which are composed of a silver nanowire/silica core–shell structure with a silver chloride tail, have been propelled via light-induced self-diffusiophoresis [71]. Their phototactic motion enhances local analyte concentration and signal intensity for biochemical sensing. Such systems have demonstrated light-controlled SERS detection of crystal violet as well as MCF-7 breast cancer cells, highlighting their potential for smart, on-demand sensing at the micro- and nanoscale. Nevertheless, challenges related to propulsion efficiency in complex media and long-term photostability remain to be addressed. In addition, optical scattering and inherent light absorption characteristics of complex biological tissues can significantly attenuate the penetration depth and intensity of driving optical fields, making in vivo applications challenging. Photocatalytic surfaces can be passivated by biological fluids, which directly suppresses light-induced diffusiophoresis, making it difficult to maintain sufficient propulsive force.

Electric Nanomotor Sensors: Electric fields are highly versatile for precise manipulation of various nanostructures, including metals, semiconductors, insulators, and their hybrids. Strategically applied electric fields can realize multimodal manipulation, including translocation, alignment, and rotation. The rich working mechanisms, depending on AC frequency, include electrophoresis, dielectrophoresis, electroosmosis, electrorotation, and electroalignment [75]. In motion-enhanced SERS, these mechanisms are most relevant when they translate, rotate, or reorient SERS-active probes to improve molecular transport and diffusion near plasmonic sensing interfaces. Kim et al. reported the rotary NEMS architecture and its operation at more than 18,000 rpm for 15 h [72]. In a related SERS-functionalized implementation, Ag-coated rotors were used to monitor rotation-dependent molecular release by Raman spectroscopy [27].

Taken together, motion-enhanced hybrid SERS platforms improve sensing primarily by increasing the mass transport of analyte molecules to (or away from) a sensor. Their value is therefore best assessed not only by EF or LOD, but also by detection time, dynamics, operational efficiency and durability in complex media, hotspot stability, and compatibility with quantitative readout.

4.2. Field-Guided Hotspot Positioning and Assembly

Field-guided platforms differ from motion-enhanced nanomotors because the external field is used primarily to position SERS-active components, assemble plasmonic junctions, or bring analytes into defined sensing regions, rather than to propel probes continuously through the sample. This strategy is particularly useful when SERS performance depends on forming reproducible nanogaps, interrogating a specific molecular interface, or maintaining spatial control over transient analyte–hotspot interactions.

Optical tweezers provide a representative field-guided strategy because highly focused laser beams can mechanically manipulate plasmonic components at defined locations [180]. When combined with plasmonic materials, such as Ag-nanoparticle-distributed silica beads, optical trapping enables the dynamic formation and control of plasmonic hotspots. By optically focusing and precisely positioning two AgNP-coated silica beads, a controllable plasmonic junction with single-molecule sensitivity has been achieved [73]. This dynamic detection configuration allows interrogation of protein structures, including hemoglobin, lysozyme, and bovine serum albumin, without perturbing their native conformations.

Furthermore, integration with microfluidic flow chambers enables real-time detection of globular proteins and facilitates studies of pH-dependent structural evolution of amylin (hIAPP), successfully capturing low-concentration, transient intermediates relevant to amyloid formation [74]. The capacity for continuous measurement at well-defined spatial locations makes optical tweezer-assisted SERS a powerful platform for probing molecular dynamics in complex biological environments.

Electric-field-guided manipulation provides another approach to hotspot positioning and probe orientation. Depending on AC frequency and field geometry, electrokinetic forces can translate, rotate, align, or orient anisotropic nanostructures in solution. Li et al. developed a versatile 3D electrokinetic tweezers technique that enables simultaneous 2D positional and 3D orientational control of anisotropic nanoparticles, with precision of 20 nm in position and 0.5° in angle (Figure 5B) [75]. Such control is valuable for SERS because the signal often depends strongly on probe orientation, molecule–surface contact geometry, and the precise placement of

plasmonic nanostructures near target interfaces. By growing dense Ag nanoparticles on the surface of Au nanowires, the electrically driven SERS-active motors enable probing of cellular surfaces at the subcellular level and direct detection of metabolite release [75]. When integrated into a magnetically anchored rotary micromotor, controlled probe rotation enhanced molecular release from the sensing surface while enabling simultaneous SERS monitoring [27]. Importantly, this strategy can be generalized to various electronic materials, whose electrical conductivity can be tuned by light or other stimuli, opening new opportunities for adaptive SERS sensing [181–183]. Meanwhile, extending electric-field-guided SERS manipulation to complex biological media will require careful control of ionic strength, medium composition, and electrode configuration.

Taken together, field-guided SERS platforms improve analytical performance by controlling where and when hotspots are positioned for deterministic sensing or targeted detection. The techniques are mostly suitable for on-chip *in vitro* applications.

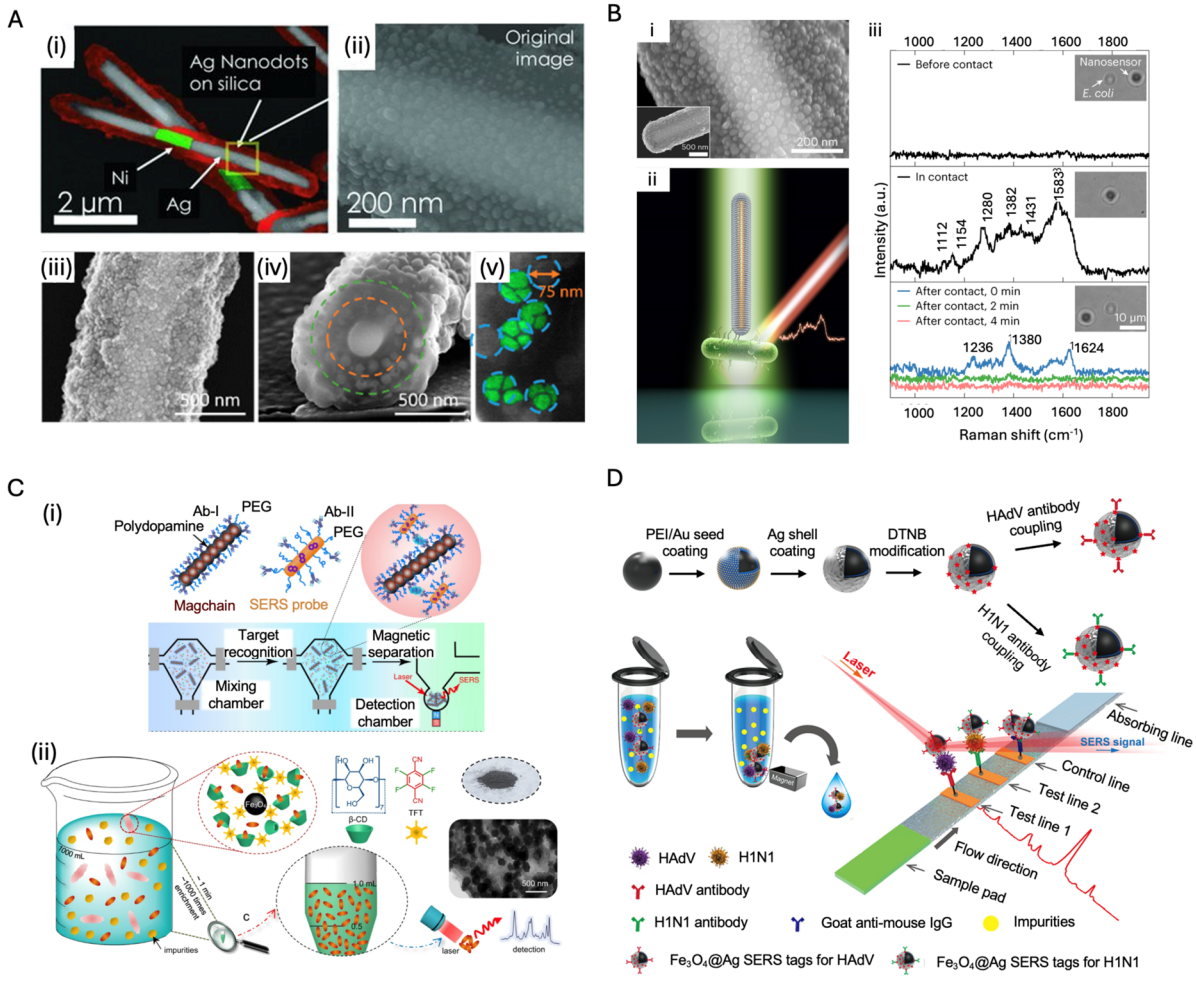


Figure 5. Stimuli-Responsive Nanostructures for SERS Bioanalysis and Molecular Sensing. (**A**) (**i-ii**) Low- and high-magnification SEM images of Ag/Ni/Ag-core, silica-shell nanocapsules decorated with Ag nanoparticles. Adapted with permission from Ref. [184]. Copyright 2012 Wiley-VCH Verlag GmbH & Co. KGaA. (**iii-v**) Surface, cross-sectional, and close-up SEM images of Ag nanoparticles and nanocavities in an Au-core nanoporous Raman nanosensor. Adapted with permission from Ref. [167]. Copyright 2018 American Chemical Society. (**B**) Localized detection of metabolites from a single *E. coli* cell using SERS-active nanocapsule sensors. (**i**) SEM image and (**ii**) schematic of a vertically aligned, silica-encapsulated nanowire coated with high-density Ag nanoparticles, enabling direct contact SERS measurement from a bacterial cell. (**iii**) Raman spectra collected at three positions (20 μm away, in contact, and 15 μm away after contact), with insets showing the corresponding optical images. Adapted with permission from Ref. [75]. Copyright 2023 Springer Nature. (**C**) (**i**) Schematic of the MiChip assay for biomarker detection. A sample is mixed with antibody-conjugated magnetic nanochains (Magchains) and SERS-encoded probes to form sandwich immunocomplexes, which are magnetically isolated and detected via Raman spectroscopy. Adapted from Ref. [20] under the terms of the Creative Commons Attribution 4.0 License; changes were made. (**ii**) Schematic of analyte enrichment and detection using magnetic nanoparticle-immobilized porous β-cyclodextrin polymer (MN-PCDP): (a) adsorption of organic pollutants from aqueous solution followed by

magnetic separation of MN-PCDP; (b) optical photograph and TEM image of MN-PCDP; and (c) desorption of the captured pollutants into ethanol for subsequent spectroscopic detection. The adsorption–desorption process enables up to approximately 1000-fold enrichment. Adapted from Ref. [76] under the terms of the Creative Commons Attribution 4.0 License; changes were made. (**D**) Synthetic route for antibody-modified Fe_3O_4@Ag magnetic tags and schematic of a magnetic SERS strip for the simultaneous detection of two respiratory viruses. Adapted with permission from Ref. [77]. Copyright 2019 American Chemical Society.

4.3. Magnetic Capture and Separation for Enrichment-Assisted SERS

In contrast to motion-enhanced nanomotor platforms and field-guided hotspot positioning, magnetic enrichment-assisted SERS platforms mainly use magnetic components to capture, isolate, and concentrate target species from complex samples before Raman readout. Magnetic hybrid nanomaterials, often referred to as magnetic–plasmonic (MP) nanocomposites, represent a versatile class of substrates for SERS, particularly in bioanalysis [37,185]. These composites integrate the unique magnetic properties of materials such as iron oxides (Fe_3O_4 or Fe_2O_3) with the strong plasmonic capabilities of noble metals within a single particle system. In these systems, the magnetic component does not necessarily provide the primary electromagnetic or chemical Raman enhancement. Instead, it improves the probability that low-abundance analytes, target-bound probes, or pathogen-containing complexes are collected at SERS-active regions while reducing interference from the surrounding matrix [186].

First, the magnetic component enables efficient and rapid separation of target analytes from complex biological or environmental matrices, greatly simplifying sample pretreatment and improving analytical precision by reducing matrix interference [168]. This function is particularly important for detecting low-concentration biomarkers, pathogens, or contaminants that coexist with abundant interfering species.

Second, Mag-SERS platforms integrate enrichment functions, enabling ultrasensitive detection, even at the single-molecule level [169–172,187]. For example, Zhang et al. reported an enrichment-assisted sensing strategy based on a magnetic mesoporous nanosponge [76]. The nanosponges are made of porous β-cyclodextrin polymers combined with magnetic nanoparticles. When dispersed in solution, the nanosponges enabled rapid and efficient removal of organic micropollutants, achieving approximately 90% removal within 1 min and concentrating pollutants by up to ~1000-fold. This enrichment approach greatly enhances detection sensitivity for common organic pollutants, lowering detection limits by two to three orders of magnitude (Figure 5C(ii)). Here, the central contribution of the magnetic component is the physical concentration of target molecules before spectral acquisition.

The magnetic properties also allow for controllable aggregation and manipulation of these SERS substrates, which can dynamically create “hotspots” (regions of highly concentrated electromagnetic fields) at interparticle junctions, further boosting signal intensity and reproducibility [186]. However, in enrichment-assisted magnetic SERS, such hotspot formation should be interpreted together with target concentration and probe collection rather than treated as the sole origin of improved performance. When functionalized with biorecognition molecules such as antibodies or aptamers, magnetic–plasmonic probes can combine target isolation, enrichment, and SERS detection within the same assay format [173]. Additionally, the reusability of these magnetic substrates may further improve their cost-effectiveness and environmental friendliness [37].

Finally**,** the modular design and tunable surface chemistry of Mag-SERS platforms allow integration into diagnostic formats such as clinical assays and automated detection systems. For example, combining SERS-active particles with lateral flow assays (LFAs) or microfluidic systems can yield rapid, sensitive, and user-friendly diagnostic solutions [77,188]. In one study, a Mag-SERS-based LFA strip employing Fe_3O_4@Ag nanoparticles was developed for simultaneous detection of influenza A H1N1 virus and human adenovirus (HAdV) (Figure 5D) [77]. The magnetic nanotags, functionalized with dual Raman dyes and virus-specific capture antibodies, enabled both magnetic enrichment and specific viral recognition. The detection limits for H1N1 and HAdV were 50 PFU mL^{-1} and 10 PFU mL^{-1}, respectively, representing a 2000-fold sensitivity improvement over traditional colloidal gold-based LFAs. Microfluidic integration further enhances the potential of Mag-SERS platforms for clinical diagnostics. As shown in Figure 5C(i), Xiong et al. reported a microfluidic biochip featuring magnetic nanochains that enable rapid mixing, bioseparation, and detection [20]. This system eliminates the need for external mixers or sensors and achieves highly sensitive detection of cancer biomarkers and bacterial species from just 1 μL of body fluid within 8 min. These integrated formats are useful when the analytical challenge involves not only Raman signal generation, but also sample preparation, target recovery, and reproducible probe placement in complex matrices.

Overall, active-enrichment hybrid SERS platforms improve sensing performance by addressing different stages of the detection process. Motion-enhanced platforms increase convective mass transport and analyte flux to (or away) from a sensing surface through probe propulsion or rotation. Field-guided platforms enable active

hotspot positioning and local interrogation. Magnetic capture-assisted systems improve target isolation, enrichment, and matrix removal. These strategies do not replace electromagnetic or chemical enhancement, but address a different aspect of nanosensing by improving analyte transport and capture, as well as targeted detection.

5. Summary and Perspective

First observed in 1974, SERS has transitioned from a fundamental spectroscopic phenomenon into a highly versatile analytical tool with single-molecule sensitivity over the last 50 years. As discussed throughout this review, hybrid SERS platforms can alleviate persistent limitations of conventional noble-metal substrates. By strategically integrating plasmonic nanostructures with semiconductors, two-dimensional materials, photonic crystals, and responsive nanomotor systems, these architectures combine localized electromagnetic field amplification and charge-transfer processes with dynamic hotspot manipulation and localized analyte enrichment for active sensing in complex biological media.

Despite the remarkable advancements, the translation of SERS into a practical quantitative tool for ultralow concentration analytes remains a major obstacle. Even in a simple dilute molecular solution, different molecular orientations and uneven electromagnetic field distributions within nanostructured hotspots frequently lead to notable single-molecule intensity fluctuations (SIFs) [189,190]. Standard quantification methods, which rely on the integrated intensity of all single-molecule signals, often struggle to maintain reproducibility and accuracy under these highly fluctuating conditions. To overcome this bottleneck, recent developments in digital (nano)colloid-enhanced Raman spectroscopy (d(n)CERS) present a promising solution [191,192]. By dispersing metallic colloidal nanoparticles in aqueous solutions to ensure uniform colloid-molecule interaction, this approach converts variable analog signals into discrete single-molecule counting events. Fundamentally, let $\lambda = N_{events}/N_{voxels}$ denote the mean number of analyte–hotspot events per voxel. Under a Poisson occupancy model, the ratio of positive voxels (RPV) is $RPV = 1 - e^{-\lambda}$, equivalently $\lambda = -\ln(1 - RPV)$. Consequently, the detection probability is directly dictated by the number and density of available hotspots. While an increase in hotspot density enhances molecular occupancy probability, excessive colloidal concentrations may increase background scattering and reduce the number of effective hotspots. Furthermore, the accuracy of digital counting relies heavily on establishing a rigorous signal threshold to define an "on" event. A higher threshold can reduce false-positive detections, but it inevitably increases the false negative rate by filtering out authentic weak signals arising from hotspot heterogeneity. To mitigate these statistical fluctuations, practical substrate design must prioritize the spatial and temporal uniformity of the hotspots. Governed by Poisson statistics, this digitization effectively circumvents the limitations imposed by SIFs, facilitating reproducible quantification that is ultimately limited by the intrinsic Poisson noise of the measurement process.

Beyond solution-based colloidal dispersions, the spatial discretization of targets across solid-state arrays offers a complementary strategy for digital SERS by structurally enforcing the Poisson sampling requirements. For instance, the physical compartmentalization of molecular targets within uniform, plasmonically active microchamber arrays can facilitate the sensitive, molecular-selective, and multiplexed monitoring of single-enzyme reactions [193]. Similarly, digital nanopillar platforms leverage spatially isolated nanostructures to anchor and detect individual analytes at discrete plasmonic hotspots. Such architectures have demonstrated the capacity for attomolar-level quantification of cytokine biomarkers, enabling the longitudinal tracking of immune toxicities in cancer patients [194]. However, the translation of these digital SERS platforms into field-deployable sensors introduces a critical trade-off between the acquisition time needed for statistical confidence and the practical demand for rapid detection. Under ideal Poisson counting, the relative standard deviation of the accumulated "on" event count scales as $RSD \approx 1/\sqrt{N_{on}}$, where N_{on} denotes the accumulated number of "on" event. Achieving a statistically significant count at ultralow concentrations thus requires collecting a large number of discrete sampling events, which prolongs the data acquisition process and challenges the feasibility of rapid diagnostics. It has been reported that integrating wide-field illumination with wavelength-tunable narrow bandpass filters may offer a potential strategy to accelerate large-area imaging without compromising the extensive statistical sampling size [193]. Together, these array-based digitalization strategies illustrate the significant translational potential of converting highly variable spectroscopic phenomena into robust counting metrics for precision clinical diagnostics and dynamic disease monitoring [195,196].

However, as these solid-state digital platforms scale to accommodate multiplexed analysis across thousands of discrete spatial entities, they inherently generate massive, high-dimensional spectral datasets. The sheer volume and intricate complexity of these data—encompassing subtle spectral variations and spatially resolved molecular fingerprints—frequently surpass the processing efficiency and interpretive capacity of conventional analytical methods. Consequently, the successful translation and broad implementation of these high-throughput digital and

hybrid SERS methodologies will increasingly depend on the integration of artificial intelligence (AI) and machine learning (ML). Rather than operating as isolated analytical add-ons, AI frameworks can be intrinsically woven into both the design and data-processing phases of SERS development [197–199].

In the foundational design phase, deep learning algorithms, such as generative adversarial networks (GANs) and variational autoencoders (VAEs), may help map relationships among molecular structures, substrate properties, and topologies [200]. Such models could support data-driven optimization of hybrid substrates, although direct experimental validation of inverse-designed SERS substrates remains limited.

During data processing, AI-assisted methods can improve spectral quality, feature extraction, and interpretation [201,202]. The cited tools serve distinct purposes: RADAR removes spectral artifacts [203], SSNet performs spectral unmixing [204], PyFasma and RamanSPy provide preprocessing and multivariate-analysis pipelines [205,206], and peak-sensitive logistic regression (PSE-LR) supports spectral classification and interpretation [207]. SRS-Net, by contrast, is a physics-informed framework for modeling stimulated Raman scattering rather than a general SERS preprocessing tool [208]. Deep-learning classification has also been demonstrated for Raman-based liver-cancer diagnosis [209]. Recent studies have applied deep learning to distinct SERS tasks, including colloidal digital SERS analysis, therapeutic-drug monitoring on plasmonic metasurfaces, and leukemia classification [210–212]. More broadly, AI-assisted SERS workflows can support spectral classification and quality control across diverse sensing platforms [213–215]; these studies do not by themselves establish direct integration with digital single-molecule counting.

Looking ahead, a particularly promising direction is the development of broadly trained large Raman models built from expansive, multi-center spectral databases. However, the practical realization of these foundational models relies on overcoming significant data standardization challenges. SERS datasets frequently exhibit high variability across different instruments, substrate architectures, and analytical conditions. A major underlying issue, as previously noted, is the inherent non-reproducibility of SERS hotspots, which produces inconsistent absolute signal intensities and spectral profiles. To ensure that training datasets are sufficiently standardized and generalizable, researchers can adopt rigorous data curation protocols, including comprehensive metadata reporting and the utilization of universal calibration reference materials across different laboratories. Moreover, the integration of digital SERS methodologies can structurally mitigate this challenge; by converting highly variable analog signals into threshold-based binary molecular counts, the dependence of the final dataset on spatial heterogeneity among individual hotspots is partially reduced, thereby providing more reproducible inputs for model training. Although this field is still emerging, such models could provide a unifying foundation for the SERS workflow. When strengthened by transfer learning, these models could be efficiently adapted to new analytical tasks without requiring large task-specific datasets. At the same time, explainable AI could reveal which spectral features drive each prediction, improving transparency, scientific insight, and user confidence. Collectively, these advances could link rational nanomaterial design with automated, reliable practical diagnostics. More broadly, hybrid and digital SERS platforms with integrated AI could offer a potential route toward converting sensitive SERS analysis into standardized, rapid platforms for real-world applications.

Author Contributions: J.B. led the efforts, including literature search, analysis, and writing with important contributions from B.L., H.J. and A.X.W.; A.X.W. and D.E.F. initiated the scope and framework of this review; J.B. and D.E.F. substantially revised the manuscript to its final form; D.E.F. supervised the project. All authors have read and agreed to the published version of the manuscript.

Funding: This research was funded by the National Institutes of Health (grant number 1R43ES037145-01 and 1R41ES038039-01), National Science Foundation (grant number: 2506603, 2219221), National Science Foundation under Grant No.2610250 and Baylor University Mearse Chair Endowment fund in Biological and Biomedical Engineering.

Data Availability Statement: Not applicable.

Acknowledgments: We are thankful for the reviewers' helpful comments.

Conflicts of Interest: The authors declare no conflict of interest.

Use of AI and AI-Assisted Technologies: During the preparation of this work, the authors used AI-assisted tools for language refinement and the visual enhancement of selected figures. The authors reviewed the final content and took full responsibility for the published article.

References

1. Daniel, M.C.; Astruc, D. Gold nanoparticles: Assembly, supramolecular chemistry, quantum-size-related properties, and applications toward biology, catalysis, and nanotechnology. *Chem. Rev.* **2004**, *104*, 293–346. https://doi.org/10.1021/cr030698.
2. Cialla-May, D.; Zheng, X.S.; Weber, K.; Popp, J. Recent progress in surface-enhanced Raman spectroscopy for biological and biomedical applications: From cells to clinics. *Chem. Soc. Rev.* **2017**, *46*, 3945–3961. https://doi.org/10.1039/c7cs00172j.

3. Nam, J.M.; Oh, J.W.; Lee, H.; Suh, Y.D. Plasmonic Nanogap-Enhanced Raman Scattering with Nanoparticles. *Acc. Chem. Res.* **2016**, *49*, 2746–2755. https://doi.org/10.1021/acs.accounts.6b00409.
4. Kim, G.H.; Son, J.; Nam, J.M. Advances, Challenges, and Opportunities in Plasmonic Nanogap-Enhanced Raman Scattering with Nanoparticles. *ACS Nano* **2025**, *19*, 2992–3007. https://doi.org/10.1021/acsnano.4c14557.
5. Cardinal, M.F.; van der Ende, E.V.; Hackler, R.A.; McAnally, M.O.; Stair, P.C.; Schatz, G.C.; Van Duyne, R.P. Expanding applications of SERS through versatile nanomaterials engineering. *Chem. Soc. Rev.* **2017**, *46*, 3886–3903. https://doi.org/10.1039/c7cs00207f.
6. Pérez-Jiménez, A.I.; Lyu, D.; Lu, Z.; Liu, G.; Ren, B. Surface-enhanced Raman spectroscopy: Benefits, trade-offs and future developments. *Chem. Sci.* **2020**, *11*, 4563–4577. https://doi.org/10.1039/d0sc00809e.
7. Wang, X.; Huang, S.-C.; Hu, S.; Yan, S.; Ren, B. Fundamental understanding and applications of plasmon-enhanced Raman spectroscopy. *Nat. Rev. Phys.* **2020**, *2*, 253–271. https://doi.org/10.1038/s42254-020-0171-y.
8. Guerrini, L.; Rodriguez-Loureiro, I.; Correa-Duarte, M.A.; Lee, Y.H.; Ling, X.Y.; García de Abajo, F.J.; Alvarez-Puebla, R.A. Chemical speciation of heavy metals by surface-enhanced Raman scattering spectroscopy: Identification and quantification of inorganic- and methyl-mercury in water. *Nanoscale* **2014**, *6*, 8368–8375. https://doi.org/10.1039/c4nr01464b.
9. Wang, B.; Lv, X.; Feng, D.; Xie, L.; Zhang, J.; Li, M.; Xie, Y.; Li, J.; Zhou, H. Highly Stable Zr(IV)-Based Metal-Organic Frameworks for the Detection and Removal of Antibiotics and Organic Explosives in Water. *J. Am. Chem. Soc.* **2016**, *138*, 6204–6216. https://doi.org/10.1021/jacs.6b01663.
10. Hu, Y.; Liao, J.; Wang, D.; Li, G. Fabrication of Gold Nanoparticle-Embedded Metal-Organic Framework for Highly Sensitive Surface-Enhanced Raman Scattering Detection. *Anal. Chem.* **2014**, *86*, 3955–3963. https://doi.org/10.1021/ac5002355.
11. Zhang, X.; Dai, Z.; Si, S.; Zhang, X.; Wu, W.; Deng, H.; Wang, F.; Xiao, X.; Jiang, C. Ultrasensitive SERS Substrate Integrated with Uniform Subnanometer Scale "Hot Spots" Created by a Graphene Spacer for the Detection of Mercury Ions. *Small* **2017**, *13*, 1603347. https://doi.org/10.1002/smll.201603347.
12. Hu, R.; Tang, R.; Xu, J.; Lu, F. Chemical nanosensors based on molecularly-imprinted polymers doped with silver nanoparticles for the rapid detection of caffeine in wastewater. *Anal. Chim. Acta* **2018**, *1034*, 176–183. https://doi.org/10.1016/j.aca.2018.06.012.
13. Castro-Grijalba, A.; Montes-García, V.; Cordero-Ferradás, M.; Coronado, E.; Pérez-Juste, J.; Pastoriza-Santos, I. SERS-Based Molecularly Imprinted Plasmonic Sensor for Highly Sensitive PAH Detection. *ACS Sens.* **2020**, *5*, 693–702. https://doi.org/10.1021/acssensors.9b01882.
14. Li, S.; Shi, B.; He, D.; Zhou, H.; Gao, Z. DNA origami-mediated plasmonic dimer nanoantenna-based SERS biosensor for ultrasensitive determination of trace diethylstilbestrol. *J. Hazard. Mater.* **2023**, *458*, 131874. https://doi.org/10.1016/j.jhazmat.2023.131874.
15. Song, W.; Yang, Z.; Ma, F.; Chi, M.; Zhao, B.; Lu, X. Electrospun magnetic $CoFe_2O_4$/Ag hybrid nanotubes for sensitive SERS detection and monitoring of the catalytic degradation of organic pollutants. *RSC Adv.* **2017**, *7*, 40334–40341. https://doi.org/10.1039/c7ra07786f.
16. Plou, J.; Valera, P.S.; García, I.; de Albuquerque, C.D.L.; Carracedo, A.; Liz-Marzán, L.M. Prospects of Surface-Enhanced Raman Spectroscopy for Biomarker Monitoring toward Precision Medicine. *ACS Photonics* **2022**, *9*, 333–350. https://doi.org/10.1021/acsphotonics.1c01934.
17. Zhang, K.; Wang, Y.; Wu, M.; Liu, Y.; Shi, D.; Liu, B. On-demand quantitative SERS bioassays facilitated by surface-tethered ratiometric probes. *Chem. Sci.* **2018**, *9*, 8089–8093. https://doi.org/10.1039/c8sc03263g.
18. Arabi, M.; Ostovan, A.; Zhang, Z.; Wang, Y.; Mei, R.; Fu, L.; Wang, X.; Ma, J.; Chen, L. Label-free SERS detection of Raman-Inactive protein biomarkers by Raman reporter indicator: Toward ultrasensitivity and universality. *Biosens. Bioelectron.* **2021**, *174*, 112825. https://doi.org/10.1016/j.bios.2020.112825.
19. Song, L.; Chen, J.; Xu, B.; Huang, Y. Flexible Plasmonic Biosensors for Healthcare Monitoring: Progress and Prospects. *ACS Nano* **2021**, *15*, 18822–18847. https://doi.org/10.1021/acsnano.1c07176.
20. Xiong, Q.; Lim, C.; Ren, J.; Zhou, J.; Pu, K.; Chan-Park, M.; Mao, H.; Lam, Y.; Duan, H. Magnetic nanochain integrated microfluidic biochips. *Nat. Commun.* **2018**, *9*, 1743. https://doi.org/10.1038/s41467-018-04172-1.
21. Zhang, D.; Huang, L.; Liu, B.; Ni, H.; Sun, L.; Su, E.; Chen, H.; Gu, Z.; Zhao, X. Quantitative and ultrasensitive detection of multiplex cardiac biomarkers in lateral flow assay with core-shell SERS nanotags. *Biosens. Bioelectron.* **2018**, *106*, 204–211. https://doi.org/10.1016/j.bios.2018.01.062.
22. Fu, X.; Cheng, Z.; Yu, J.; Choo, P.; Chen, L.; Choo, J. A SERS-based lateral flow assay biosensor for highly sensitive detection of HIV-1 DNA. *Biosens. Bioelectron.* **2016**, *78*, 530–537. https://doi.org/10.1016/j.bios.2015.11.099.
23. Tian, S.; Li, H.; Li, Z.; Tang, H.; Yin, M.; Chen, Y.; Wang, S.; Gao, Y.; Yang, X.; Meng, F.; et al. Polydiacetylene-based ultrastrong bioorthogonal Raman probes for targeted live-cell Raman imaging. *Nat. Commun.* **2020**, *11*, 81. https://doi.org/10.1038/s41467-019-13784-0.

24. Su, X.; Liu, X.; Xie, Y.; Chen, M.; Zheng, C.; Zhong, H.; Li, M. Integrated SERS-Vertical Flow Biosensor Enabling Multiplexed Quantitative Profiling of Serological Exosomal Proteins in Patients for Accurate Breast Cancer Subtyping. *ACS Nano* **2023**, *17*, 4077–4088. https://doi.org/10.1021/acsnano.3c00449.
25. Lin, X.; Wang, Y.; Wang, L.; Lu, Y.; Li, J.; Lu, D.; Zhou, T.; Huang, Z.; Huang, J.; Huang, H.; et al. Interference-free and high precision biosensor based on surface enhanced Raman spectroscopy integrated with surface molecularly imprinted polymer technology for tumor biomarker detection in human blood. *Biosens. Bioelectron.* **2019**, *143*, 111599. https://doi.org/10.1016/j.bios.2019.111599.
26. Guo, J.; Liang, Z.; Huang, Y.; Kim, K.; Vandeventer, P.; Fan, D. Acceleration of Biomolecule Enrichment and Detection with Rotationally Motorized Opto-Plasmonic Microsensors and the Working Mechanism. *ACS Nano* **2020**, *14*, 15204–15215. https://doi.org/10.1021/acsnano.0c05429.
27. Xu, X.; Kim, K.; Fan, D. Tunable Release of Multiplex Biochemicals by Plasmonically Active Rotary Nanomotors. *Angew. Chem. Int. Ed.* **2015**, *54*, 2525–2529. https://doi.org/10.1002/anie.201410754.
28. Zhang, C.; Huang, L.; Pu, H.; Sun, D. Magnetic surface-enhanced Raman scattering (MagSERS) biosensors for microbial food safety: Fundamentals and applications. *Trends Food Sci. Technol.* **2021**, *113*, 366–381. https://doi.org/10.1016/j.tifs.2021.05.007.
29. Zhu, X.; Zhang, Y.; Liu, M.; Liu, Y. 2D titanium carbide MXenes as emerging optical biosensing platforms. *Biosens. Bioelectron.* **2021**, *171*, 112730. https://doi.org/10.1016/j.bios.2020.112730.
30. Liang, X.; Li, N.; Zhang, R.; Yin, P.; Zhang, C.; Yang, N.; Liang, K.; Kong, B. Carbon-based SERS biosensor: From substrate design to sensing and bioapplication. *NPG Asia Mater.* **2021**, *13*, 8. https://doi.org/10.1038/s41427-020-00278-5.
31. Alessandri, I.; Lombardi, J. Enhanced Raman Scattering with Dielectrics. *Chem. Rev.* **2016**, *116*, 14921–14981. https://doi.org/10.1021/acs.chemrev.6b00365.
32. Li, J.; Zhang, Y.; Ding, S.; Panneerselvam, R.; Tian, Z. Core-Shell Nanoparticle-Enhanced Raman Spectroscopy. *Chem. Rev.* **2017**, *117*, 5002–5069. https://doi.org/10.1021/acs.chemrev.6b00596.
33. Li, J.; Anema, J.; Wandlowski, T.; Tian, Z. Dielectric shell isolated and graphene shell isolated nanoparticle enhanced Raman spectroscopies and their applications. *Chem. Soc. Rev.* **2015**, *44*, 8399–8409. https://doi.org/10.1039/c5cs00501a.
34. Liu, Y.; Ma, H.; Han, X.; Zhao, B. Metal-semiconductor heterostructures for surface-enhanced Raman scattering: Synergistic contribution of plasmons and charge transfer. *Mater. Horizons* **2021**, *8*, 370–382. https://doi.org/10.1039/d0mh01356k.
35. Han, X.; Ji, W.; Zhao, B.; Ozaki, Y. Semiconductor-enhanced Raman scattering: Active nanomaterials and applications. *Nanoscale* **2017**, *9*, 4847–4861. https://doi.org/10.1039/c6nr08693d.
36. Becerril-Castro, I.; Salgueiriño, V.; Correa-Duarte, M.; Alvarez-Puebla, R. Nano/Micromotor-Driven SERS for Highly Sensitive and Spatially Controlled Sensing. *Adv. Funct. Mater.* **2024**, *34*, 2314084. https://doi.org/10.1002/adfm.202314084.
37. Song, D.; Yang, R.; Long, F.; Zhu, A. Applications of magnetic nanoparticles in surface-enhanced Raman scattering (SERS) detection of environmental pollutants. *J. Environ. Sci.* **2019**, *80*, 14–34. https://doi.org/10.1016/j.jes.2018.07.004.
38. Xu, K.; Zhou, R.; Takei, K.; Hong, M. Toward Flexible Surface-Enhanced Raman Scattering (SERS) Sensors for Point-of-Care Diagnostics. *Adv. Sci.* **2019**, *6*, 1900925. https://doi.org/10.1002/advs.201900925.
39. Laing, S.; Jamieson, L.E.; Faulds, K.; Graham, D. Surface-enhanced Raman spectroscopy for in vivo biosensing. *Nat. Rev. Chem.* **2017**, *1*, 0060. https://doi.org/10.1038/s41570-017-0060.
40. Shin, M.; Kim, K.; Jeong, D.H. Enhancement of the signal-to-noise ratio in fiber-optics based SERS detection by rough-cutting the end surface. *Opt. Express* **2023**, *31*, 12645–12652. https://doi.org/10.1364/OE.485021.
41. Choi, M.; Kim, S.; Choi, S.H.; Park, H.-H.; Byun, K.M. Highly reliable SERS substrate based on plasmonic hybrid coupling between gold nanoislands and periodic nanopillar arrays. *Opt. Express* **2020**, *28*, 3598–3606. https://doi.org/10.1364/OE.386726.
42. Ranasinghe, J.C.; Sanders, S.K.; Wang, Z.; Mehrani, J.; Wu, W.; Dimitrov, E.; Wang, X.; Minns, A.M.; Rossi, R.M.; Lindner, S.E.; et al. Noise Management of Surface-Enhanced Raman Spectroscopy Using Two-Dimensional Materials. *ACS Sens.* **2026**, *11*, 1920–1932. https://doi.org/10.1021/acssensors.5c03074.
43. Zhou, L.; Huang, Q.; Xia, Y. Plasmon-Induced Hot Electrons in Nanostructured Materials: Generation, Collection, and Application to Photochemistry. *Chem. Rev.* **2024**, *124*, 8597–8619. https://doi.org/10.1021/acs.chemrev.4c00165.
44. Chang, K.; Zhao, Y.; Wang, M.; Xu, Z.; Zhu, L.; Xu, L.; Wang, Q. Advances in metal-organic framework-plasmonic metal composites based SERS platforms: Engineering strategies in chemical sensing, practical applications and future perspectives in food safety. *Chem. Eng. J.* **2023**, *459*, 141539. https://doi.org/10.1016/j.cej.2023.141539.
45. Ma, L.; Liu, M.; Zhou, X.; Li, C.; Wang, T. Metal-organic framework-based SERS sensing platforms for life and health detection. *Mater. Chem. Front.* **2023**, *7*, 4880–4899. https://doi.org/10.1039/d3qm00471f.
46. Allegretto, J.; Dostalek, J. Metal-Organic Frameworks in Surface Enhanced Raman Spectroscopy-Based Analysis of Volatile Organic Compounds. *Adv. Sci.* **2024**, *11*, 2401437. https://doi.org/10.1002/advs.202401437.
47. Zhang, Y.; Radjenovic, P.; Zhou, X.; Zhang, H.; Yao, J.; Li, J. Plasmonic Core-Shell Nanomaterials and their Applications in Spectroscopies. *Adv. Mater.* **2021**, *33*, 2005900. https://doi.org/10.1002/adma.202005900.

48. Ahmad, R.; Griffete, N.; Lamouri, A.; Felidj, N.; Chehimi, M.; Mangeney, C. Nanocomposites of Gold Nanoparticles@Molecularly Imprinted Polymers: Chemistry, Processing, and Applications in Sensors. *Chem. Mater.* **2015**, *27*, 5464–5478. https://doi.org/10.1021/acs.chemmater.5b00138.
49. Li, Y.; Yang, Y.; Han, S. Surface molecular imprinting technology integrated SERS sensing: Emerging trends and future perspectives toward on-site hazardous analysis. *TrAC Trends Anal. Chem.* **2024**, *179*, 117866. https://doi.org/10.1016/j.trac.2024.117866.
50. Guo, X.; Li, J.; Arabi, M.; Wang, X.; Wang, Y.; Chen, L. Molecular-Imprinting-Based Surface-Enhanced Raman Scattering Sensors. *ACS Sens.* **2020**, *5*, 601–619. https://doi.org/10.1021/acssensors.9b02039.
51. Bharati, M.; Soma, V. Flexible SERS substrates for hazardous materials detection: Recent advances. *Opto-Electron. Adv.* **2021**, *4*, 210048. https://doi.org/10.29026/oea.2021.210048.
52. Ji, W.; Li, L.; Song, W.; Wang, X.; Zhao, B.; Ozaki, Y. Enhanced Raman Scattering by ZnO Superstructures: Synergistic Effect of Charge Transfer and Mie Resonances. *Angew. Chem. Int. Ed.* **2019**, *58*, 14452–14456. https://doi.org/10.1002/anie.201907283.
53. Kim, S.M.; Zhang, W.; Cunningham, B.T. Coupling discrete metal nanoparticles to photonic crystal surface resonant modes and application to Raman spectroscopy. *Opt. Express* **2010**, *18*, 4300–4309. https://doi.org/10.1364/Oe.18.004300.
54. Xu, X.B.; Hasan, D.H.; Wang, L.; Chakravarty, S.; Chen, R.T.; Fan, D.L.; Wang, A.X. Guided-mode-resonance-coupled plasmonic-active SiO_2 nanotubes for surface enhanced Raman spectroscopy. *Appl. Phys. Lett.* **2012**, *100*, 191114. https://doi.org/10.1063/1.4714710.
55. Ren, F.H.; Campbell, J.; Wang, X.Y.; Rorrer, G.L.; Wang, A.X. Enhancing surface plasmon resonances of metallic nanoparticles by diatom biosilica. *Opt. Express* **2013**, *21*, 15308–15313. https://doi.org/10.1364/Oe.21.015308.
56. Ren, F.; Campbell, J.; Rorrer, G.L.; Wang, A.X. Surface-Enhanced Raman Spectroscopy Sensors From Nanobiosilica With Self-Assembled Plasmonic Nanoparticles. *IEEE J. Sel. Top. Quantum Electron.* **2014**, *20*, 127–132. https://doi.org/10.1109/JSTQE.2014.2301016.
57. Chen, Y.; Zhang, Y.; Pan, F.; Liu, J.; Wang, K.; Zhang, C.; Cheng, S.; Lu, L.; Zhang, W.; Zhang, Z.; et al. Breath Analysis Based on Surface-Enhanced Raman Scattering Sensors Distinguishes Early and Advanced Gastric Cancer Patients from Healthy Persons. *ACS Nano* **2016**, *10*, 8169–8179. https://doi.org/10.1021/acsnano.6b01441.
58. Deneme, I.; Liman, G.; Can, A.; Demirel, G.; Usta, H. Enabling three-dimensional porous architectures via carbonyl functionalization and molecular-specific organic-SERS platforms. *Nat. Commun.* **2021**, *12*, 6119. https://doi.org/10.1038/s41467-021-26385-7.
59. Wang, Y.; Liu, J.; Ozaki, Y.; Xu, Z.; Zhao, B. Effect of TiO_2 on Altering Direction of Interfacial Charge Transfer in a TiO2-Ag-MPY-FePc System by SERS. *Angew. Chem. Int. Ed.* **2019**, *58*, 8172–8176. https://doi.org/10.1002/anie.201900589.
60. Ben-Jaber, S.; Peveler, W.; Quesada-Cabrera, R.; Cortés, E.; Sotelo-Vazquez, C.; Abdul-Karim, N.; Maier, S.; Parkin, I. Photo-induced enhanced Raman spectroscopy for universal ultra-trace detection of explosives, pollutants and biomolecules. *Nat. Commun.* **2016**, *7*, 12189. https://doi.org/10.1038/ncomms12189.
61. Zhou, L.; Zhou, J.; Lai, W.; Yang, X.; Meng, J.; Su, L.; Gu, C.; Jiang, T.; Pun, E.; Shao, L.; et al. Irreversible accumulated SERS behavior of the molecule-linked silver and silver-doped titanium dioxide hybrid system. *Nat. Commun.* **2020**, *11*, 1785. https://doi.org/10.1038/s41467-020-15484-6.
62. Zhou, J.; Zhang, J.; Yang, H.; Wang, Z.; Shi, J.; Zhou, W.; Jiang, N.; Xian, G.; Qi, Q.; Weng, Y.; et al. Plasmon-induced hot electron transfer in Au-ZnO heterogeneous nanorods for enhanced SERS. *Nanoscale* **2019**, *11*, 11782–11788. https://doi.org/10.1039/c9nr02969a.
63. Wu, K.; Chen, J.; McBride, J.R.; Lian, T. Efficient hot-electron transfer by a plasmon-induced interfacial charge-transfer transition. *Science* **2015**, *349*, 632–635. https://doi.org/10.1126/science.aac5443.
64. He, Z.; Rong, T.; Li, Y.; Ma, J.; Li, Q.; Wu, F.; Wang, Y.; Wang, F. Two-Dimensional TiVC Solid-Solution MXene as Surface-Enhanced Raman Scattering Substrate. *ACS Nano* **2022**, *16*, 4072–4083. https://doi.org/10.1021/acsnano.1c09736.
65. Liu, X.; Li, T.; Lee, T.; Sun, Y.; Liu, Y.; Shang, L.; Han, Y.; Deng, W.; Yuan, Z.; Dang, A. Wearable Plasmonic Sensors Engineered via Active-Site Maximization of TiVC MXene for Universal Physiological Monitoring at the Molecular Level. *ACS Sens.* **2024**, *9*, 483–493. https://doi.org/10.1021/acssensors.3c02285.
66. Soundiraraju, B.; George, B. Two-Dimensional Titanium Nitride (Ti_2N) MXene: Synthesis, Characterization, and Potential Application as Surface-Enhanced Raman Scattering Substrate. *ACS Nano* **2017**, *11*, 8892–8900. https://doi.org/10.1021/acsnano.7b03129.
67. Liu, Z.; Yang, J.; Liu, T.; Guan, G.; Han, M. Homogeneous $Mo_{1-x}Re_xS_2$ monolayer and lateral 1T′@2H heterostructures for significantly enhanced and highly reproducible SERS responses and mechanistic insights. *Appl. Surf. Sci.* **2025**, *682*, 161661. https://doi.org/10.1016/j.apsusc.2024.161661.
68. Zhou, L.; Pusey-Nazzaro, L.; Ren, G.; Chen, L.; Liu, L.; Zhang, W.; Yang, L.; Zhou, J.; Han, J. Photoactive Control of Surface-Enhanced Raman Scattering with Reduced Graphene Oxide in Gas Atmosphere. *ACS Nano* **2022**, *16*, 577–587. https://doi.org/10.1021/acsnano.1c07695.

69. Chen, Y.; Pan, R.; Wang, Y.; Guo, P.; Liu, X.; Ji, F.; Hu, J.; Yan, X.; Wang, G.; Zhang, L.; et al. Carbon Helical Nanorobots Capable of Cell Membrane Penetration for Single Cell Targeted SERS Bio-Sensing and Photothermal Cancer Therapy. *Adv. Funct. Mater.* **2022**, *32*, 2200600. https://doi.org/10.1002/adfm.202200600.
70. Yang, T.; Zhou, J.; Wang, Y.; Fan, B.; Qiao, J.; Chen, L.; Wang, X.; Guo, L.; Yang, H.; Li, Q. Magnetic Micromotors with Spiky Gold Nanoshells as SERS Sensors for Thiram and Bacteria Detection. *Small* **2024**, *20*, 2405193. https://doi.org/10.1002/smll.202405193.
71. Wang, Y.; Zhou, C.; Wang, W.; Xu, D.; Zeng, F.; Zhan, C.; Gu, J.; Li, M.; Zhao, W.; Zhang, J.; et al. Photocatalytically Powered Matchlike Nanomotor for Light-Guided Active SERS Sensing. *Angew. Chem. Int. Ed.* **2018**, *57*, 13110–13113. https://doi.org/10.1002/anie.201807033.
72. Kim, K.; Xu, X.; Guo, J.; Fan, D.L. Ultrahigh-speed rotating nanoelectromechanical system devices assembled from nanoscale building blocks. *Nat. Commun.* **2014**, *5*, 3632. https://doi.org/10.1038/ncomms4632.
73. Dai, X.; Fu, W.; Chi, H.; Mesias, V.; Zhu, H.; Leung, C.; Liu, W.; Huang, J. Optical tweezers-controlled hotspot for sensitive and reproducible surface-enhanced Raman spectroscopy characterization of native protein structures. *Nat. Commun.* **2021**, *12*, 1292. https://doi.org/10.1038/s41467-021-21543-3.
74. Fu, W.; Chi, H.; Dai, X.; Zhu, H.; Mesias, V.; Liu, W.; Huang, J. Efficient optical plasmonic tweezer-controlled single-molecule SERS characterization of pH-dependent amylin species in aqueous milieus. *Nat. Commun.* **2023**, *14*, 6996. https://doi.org/10.1038/s41467-023-42812-3.
75. Li, H.; Teal, D.; Liang, Z.; Kwon, H.; Huo, D.; Jin, A.; Fischer, P.; Fan, D. Precise electrokinetic position and three-dimensional orientation control of a nanowire bioprobe in solution. *Nat. Nanotechnol.* **2023**, *18*, 1213–1221. https://doi.org/10.1038/s41565-023-01439-7.
76. Zhang, L.; Guo, Y.; Hao, R.; Shi, Y.; You, H.; Nan, H.; Dai, Y.; Liu, D.; Lei, D.; Fang, J. Ultra-rapid and highly efficient enrichment of organic pollutants via magnetic mesoporous nanosponge for ultrasensitive nanosensors. *Nat. Commun.* **2021**, *12*, 6849. https://doi.org/10.1038/s41467-021-27100-2.
77. Wang, C.; Wang, C.; Wang, X.; Wang, K.; Zhu, Y.; Rong, Z.; Wang, W.; Xiao, R.; Wang, S. Magnetic SERS Strip for Sensitive and Simultaneous Detection of Respiratory Viruses. *ACS Appl. Mater. Interfaces* **2019**, *11*, 19495–19505. https://doi.org/10.1021/acsami.9b03920.
78. Itoh, T.; Prochazka, M.; Dong, Z.; Ji, W.; Yamamoto, Y.; Zhang, Y.; Ozaki, Y. Toward a New Era of SERS and TERS at the Nanometer Scale: From Fundamentals to Innovative Applications. *Chem. Rev.* **2023**, *123*, 1552–1634. https://doi.org/10.1021/acs.chemrev.2c00316.
79. Le Ru, E.C.; Etchegoin, P.G. Preface. In *Principles of Surface-Enhanced Raman Spectroscopy and Related Plasmonic Effects*; Elsevier: Amsterdam, The Netherlands, 2009; pp. xvii–xix. https://doi.org/10.1016/B978-0-444-52779-0.00005-2.
80. Cirera, B.; Litman, Y.; Lin, C.F.; Akkoush, A.; Hammud, A.; Wolf, M.; Rossi, M.; Kumagai, T. Charge Transfer-Mediated Dramatic Enhancement of Raman Scattering upon Molecular Point Contact Formation. *Nano Lett.* **2022**, *22*, 2170–2176. https://doi.org/10.1021/acs.nanolett.1c02626.
81. Otto, A.; Bruckbauer, A.; Chen, Y.X. On the chloride activation in SERS and single molecule SERS. *J. Mol. Struct.* **2003**, *661–662*, 501–514. https://doi.org/10.1016/j.molstruc.2003.07.026.
82. Stewart, M.E.; Anderton, C.R.; Thompson, L.B.; Maria, J.; Gray, S.K.; Rogers, J.A.; Nuzzo, R.G. Nanostructured plasmonic sensors. *Chem. Rev.* **2008**, *108*, 494–521. https://doi.org/10.1021/cr068126n.
83. Han, X.X.; Rodriguez, R.S.; Haynes, C.L.; Ozaki, Y.; Zhao, B. Surface-enhanced Raman spectroscopy. *Nat. Rev. Methods Primers* **2021**, *1*, 87. https://doi.org/10.1038/s43586-021-00083-6.
84. Wang, X.T.; Shi, W.S.; She, G.W.; Mu, L.X. Using Si and Ge Nanostructures as Substrates for Surface-Enhanced Raman Scattering Based on Photoinduced Charge Transfer Mechanism. *J. Am. Chem. Soc.* **2011**, *133*, 16518–16523. https://doi.org/10.1021/ja2057874.
85. Lee, J.; Crampton, K.T.; Tallarida, N.; Apkarian, V.A. Visualizing vibrational normal modes of a single molecule with atomically confined light. *Nature* **2019**, *568*, 78–82. https://doi.org/10.1038/s41586-019-1059-9.
86. Ye, J.; Arul, R.; Nieuwoudt, M.K.; Dong, J.; Zhang, T.; Dai, L.; Greenham, N.C.; Rao, A.; Hoye, R.L.Z.; Gao, W.; et al. Understanding the Chemical Mechanism behind Photoinduced Enhanced Raman Spectroscopy. *J. Phys. Chem. Lett.* **2023**, *14*, 4607–4616. https://doi.org/10.1021/acs.jpclett.3c00478.
87. Zhan, C.; Chen, X.-J.; Huang, Y.-F.; Wu, D.-Y.; Tian, Z.-Q. Plasmon-Mediated Chemical Reactions on Nanostructures Unveiled by Surface-Enhanced Raman Spectroscopy. *Acc. Chem. Res.* **2019**, *52*, 2784–2792. https://doi.org/10.1021/acs.accounts.9b00280.
88. Zhan, C.; Moskovits, M.; Tian, Z.-Q. Recent Progress and Prospects in Plasmon-Mediated Chemical Reaction. *Matter* **2020**, *3*, 42–56. https://doi.org/10.1016/j.matt.2020.03.019.
89. Xie, W.; Schlücker, S. Hot electron-induced reduction of small molecules on photorecycling metal surfaces. *Nat. Commun.* **2015**, *6*, 7570. https://doi.org/10.1038/ncomms8570.

90. Anema, J.R.; Li, J.-F.; Yang, Z.-L.; Ren, B.; Tian, Z.-Q. Shell-Isolated Nanoparticle-Enhanced Raman Spectroscopy: Expanding the Versatility of Surface-Enhanced Raman Scattering. *Annu. Rev. Anal. Chem.* **2011**, *4*, 129–150. https://doi.org/10.1146/annurev.anchem.111808.073632.
91. Li, J.; Tian, X.; Li, S.; Anema, J.; Yang, Z.; Ding, Y.; Wu, Y.; Zeng, Y.; Chen, Q.; Ren, B.; et al. Surface analysis using shell-isolated nanoparticle-enhanced Raman spectroscopy. *Nat. Protoc.* **2013**, *8*, 52–65. https://doi.org/10.1038/nprot.2012.141.
92. Li, C.; Le, J.; Wang, Y.; Chen, S.; Yang, Z.; Li, J.; Cheng, J.; Tian, Z. *In situ* probing electrified interfacial water structures at atomically flat surfaces. *Nat. Mater.* **2019**, *18*, 697–701. https://doi.org/10.1038/s41563-019-0356-x.
93. Wang, Y.; Zheng, S.; Yang, W.; Zhou, R.; He, Q.; Radjenovic, P.; Dong, J.; Li, S.; Zheng, J.; Yang, Z.; et al. In situ Raman spectroscopy reveals the structure and dissociation of interfacial water. *Nature* **2021**, *600*, 81–85. https://doi.org/10.1038/s41586-021-04068-z.
94. Li, J.; Huang, Y.; Ding, Y.; Yang, Z.; Li, S.; Zhou, X.; Fan, F.; Zhang, W.; Zhou, Z.; Wu, D.; et al. Shell-isolated nanoparticle-enhanced Raman spectroscopy. *Nature* **2010**, *464*, 392–395. https://doi.org/10.1038/nature08907.
95. Wang, X.; Guo, L. SERS Activity of Semiconductors: Crystalline and Amorphous Nanomaterials. *Angew. Chem. Int. Ed.* **2020**, *59*, 4231–4239. https://doi.org/10.1002/anie.201913375.
96. Song, G.; Gong, W.; Cong, S.; Zhao, Z. Ultrathin Two-Dimensional Nanostructures: Surface Defects for Morphology-Driven Enhanced Semiconductor SERS. *Angew. Chem. Int. Ed.* **2021**, *60*, 5505–5511. https://doi.org/10.1002/anie.202015306.
97. Tao, L.; Chen, K.; Chen, Z.; Cong, C.; Qiu, C.; Chen, J.; Wang, X.; Chen, H.; Yu, T.; Xie, W.; et al. 1T′ Transition Metal Telluride Atomic Layers for Plasmon-Free SERS at Femtomolar Levels. *J. Am. Chem. Soc.* **2018**, *140*, 8696–8704. https://doi.org/10.1021/jacs.8b02972.
98. Li, Z.; Zhai, L.; Zhang, Q.; Zhai, W.; Li, P.; Chen, B.; Chen, C.; Yao, Y.; Ge, Y.; Yang, H.; et al. 1T′-transition metal dichalcogenide monolayers stabilized on 4H-Au nanowires for ultrasensitive SERS detection. *Nat. Mater.* **2024**, *23*, 1355–1362. https://doi.org/10.1038/s41563-024-01860-w.
99. Ma, N.; Chen, L.; Jing, T.; Zhang, X.; Han, B.; Xue, X.; Zhang, Y.; Zhao, B. New Insight into Charge-Transfer Enhancement for SERS in Cosputtering (Ag)x(ZnS)y System: The Carrier Density Effect. *J. Phys. Chem. C* **2019**, *123*, 28846–28851. https://doi.org/10.1021/acs.jpcc.9b09922.
100. Feng, E.; Zheng, T.; He, X.; Chen, J.; Gu, Q.; He, X.; Hu, F.; Li, J.; Tian, Y. Plasmon-Induced Charge Transfer-Enhanced Raman Scattering on a Semiconductor: Toward Amplification-Free Quantification of SARS-CoV-2. *Angew. Chem. Int. Ed.* **2023**, *62*, e202309249. https://doi.org/10.1002/anie.202309249.
101. Meng, X.; Yu, J.; Shi, W.; Qiu, L.; Qiu, K.; Li, A.; Liu, Z.; Wang, Y.; Wu, J.; Lin, J.; et al. SERS Detection of Trace Carcinogenic Aromatic Amines Based on Amorphous MoO3 Monolayers. *Angew. Chem. Int. Ed.* **2024**, *63*, e202407597. https://doi.org/10.1002/anie.202407597.
102. Zhou, Y.; Gu, Q.; Qiu, T.; He, X.; Chen, J.; Qi, R.; Huang, R.; Zheng, T.; Tian, Y. Ultrasensitive Sensing of Volatile Organic Compounds Using a Cu-Doped SnO_2-NiO p-n Heterostructure That Shows Significant Raman Enhancement. *Angew. Chem. Int. Ed.* **2021**, *60*, 26260–26267. https://doi.org/10.1002/anie.202112367.
103. Demirel, G.; Gieseking, R.; Ozdemir, R.; Kahmann, S.; Loi, M.; Schatz, G.; Facchetti, A.; Usta, H. Molecular engineering of organic semiconductors enables noble metal-comparable SERS enhancement and sensitivity. *Nat. Commun.* **2019**, *10*, 5502. https://doi.org/10.1038/s41467-019-13505-7.
104. Yilmaz, M.; Babur, E.; Ozdemir, M.; Gieseking, R.; Dede, Y.; Tamer, U.; Schatz, G.; Facchetti, A.; Usta, H.; Demirel, G. Nanostructured organic semiconductor films for molecular detection with surface-enhanced Raman spectroscopy. *Nat. Mater.* **2017**, *16*, 918–924. https://doi.org/10.1038/nmat4957.
105. Miao, P.; Qin, J.; Shen, Y.; Su, H.; Dai, J.; Song, B.; Du, Y.; Sun, M.; Zhang, W.; Wang, H.; et al. Unraveling the Raman Enhancement Mechanism on 1T′-Phase ReS_2 Nanosheets. *Small* **2018**, *14*, 1704079. https://doi.org/10.1002/smll.201704079.
106. Liu, X.; Dang, A.; Li, T.; Sun, Y.; Lee, T.C.; Deng, W.; Wu, S.; Zada, A.; Zhao, T.; Li, H. Plasmonic Coupling of Au Nanoclusters on a Flexible MXene/Graphene Oxide Fiber for Ultrasensitive SERS Sensing. *ACS Sens.* **2023**, *8*, 1287–1298. https://doi.org/10.1021/acssensors.2c02808.
107. Wu, Z.; Sun, D.; Pu, H.; Wei, Q.; Lin, X. $Ti_3C_2T_x$ MXenes loaded with Au nanoparticle dimers as a surface-enhanced Raman scattering aptasensor for AFB1 detection. *Food Chem.* **2022**, *372*, 131293. https://doi.org/10.1016/j.foodchem.2021.131293.
108. Yu, Z.; Jiang, L.; Liu, R.; Zhao, W.; Yang, Z.; Zhang, J.; Jin, S. Versatile self-assembled MXene-Au nanocomposites for SERS detection of bacteria, antibacterial and photothermal sterilization. *Chem. Eng. J.* **2021**, *426*, 131914. https://doi.org/10.1016/j.cej.2021.131914.
109. Yang, K.; Dong, Q.; Liu, H.; Wu, L.; Zong, S.; Wang, Z. A MXene Hydrogel-Based Versatile Microrobot for Controllable Water Pollution Management. *Adv. Sci.* **2024**, *11*, 2309257. https://doi.org/10.1002/advs.202309257.
110. Kaushik, V.; Kagdada, H.; Singh, D.; Pathak, S. Enhancement of SERS effect in Graphene-Silver hybrids. *Appl. Surf. Sci.* **2022**, *574*, 151724. https://doi.org/10.1016/j.apsusc.2021.151724.

111. Ding, X.; Kong, L.; Wang, J.; Fang, F.; Li, D.; Liu, J. Highly Sensitive SERS Detection of Hg^{2+} Ions in Aqueous Media Using Gold Nanoparticles/Graphene Heterojunctions. *ACS Appl. Mater. Interfaces* **2013**, *5*, 7072–7078. https://doi.org/10.1021/am401373e.
112. Kong, X.M.; Xi, Y.T.; LeDuff, P.; Li, E.W.; Liu, Y.; Cheng, L.J.; Rorrer, G.L.; Tan, H.; Wang, A.X. Optofluidic sensing from inkjet-printed droplets: The enormous enhancement by evaporation-induced spontaneous flow on photonic crystal biosilica. *Nanoscale* **2016**, *8*, 17285–17294. https://doi.org/10.1039/c6nr05809d.
113. Sivashanmugan, K.; Squire, K.; Kraai, J.A.; Tan, A.L.; Zhao, Y.; Rorrer, G.L.; Wang, A.X. Biological Photonic Crystal-Enhanced Plasmonic Mesocapsules: Approaching Single-Molecule Optofluidic-SERS Sensing. *Adv. Opt. Mater.* **2019**, *7*, 1900415. https://doi.org/10.1002/adom.201900415.
114. Yang, J.; Zhen, L.; Ren, F.; Campbell, J.; Rorrer, G.L.; Wang, A.X. Ultra-sensitive immunoassay biosensors using hybrid plasmonic-biosilica nanostructured materials. *J. Biophotonics* **2015**, *8*, 659–667. https://doi.org/10.1002/jbio.201400070.
115. Tan, A.L.; Zhao, Y.; Sivashanmugan, K.; Squire, K.; Wang, A.X. Quantitative TLC-SERS detection of histamine in seafood with support vector machine analysis. *Food Control* **2019**, *103*, 111–118. https://doi.org/10.1016/j.foodcont.2019.03.032.
116. Kong, X.M.; Chong, X.Y.; Squire, K.; Wang, A.X. Microfluidic diatomite analytical devices for illicit drug sensing with ppb-Level sensitivity. *Sens. Actuators B Chem.* **2018**, *259*, 587–595. https://doi.org/10.1016/j.snb.2017.12.038.
117. Wang, X.; Shi, W.; Wang, S.; Zhao, H.; Lin, J.; Yang, Z.; Chen, M.; Guo, L. Two-Dimensional Amorphous TiO_2 Nanosheets Enabling High-Efficiency Photoinduced Charge Transfer for Excellent SERS Activity. *J. Am. Chem. Soc.* **2019**, *141*, 5856–5862. https://doi.org/10.1021/jacs.9b00029.
118. Yang, L.; Peng, Y.; Yang, Y.; Liu, J.; Huang, H.; Yu, B.; Zhao, J.; Lu, Y.; Huang, Z.; Li, Z.; et al. A Novel Ultra-Sensitive Semiconductor SERS Substrate Boosted by the Coupled Resonance Effect. *Adv. Sci.* **2019**, *6*, 1900310. https://doi.org/10.1002/advs.201900310.
119. Cong, S.; Yuan, Y.; Chen, Z.; Hou, J.; Yang, M.; Su, Y.; Zhang, Y.; Li, L.; Li, Q.; Geng, F.; et al. Noble metal-comparable SERS enhancement from semiconducting metal oxides by making oxygen vacancies. *Nat. Commun.* **2015**, *6*, 7800. https://doi.org/10.1038/ncomms8800.
120. Zheng, Z.; Cong, S.; Gong, W.; Xuan, J.; Li, G.; Lu, W.; Geng, F.; Zhao, Z. Semiconductor SERS enhancement enabled by oxygen incorporation. *Nat. Commun.* **2017**, *8*, 1993. https://doi.org/10.1038/s41467-017-02166-z.
121. Wang, X.; Shi, W.; Jin, Z.; Huang, W.; Lin, J.; Ma, G.; Li, S.; Guo, L. Remarkable SERS Activity Observed from Amorphous ZnO Nanocages. *Angew. Chem. Int. Ed.* **2017**, *56*, 9851–9855. https://doi.org/10.1002/anie.201705187.
122. Boerigter, C.; Aslam, U.; Linic, S. Mechanism of Charge Transfer from Plasmonic Nanostructures to Chemically Attached Materials. *ACS Nano* **2016**, *10*, 6108–6115. https://doi.org/10.1021/acsnano.6b01846.
123. Rao, V.G.; Aslam, U.; Linic, S. Chemical Requirement for Extracting Energetic Charge Carriers from Plasmonic Metal Nanoparticles to Perform Electron-Transfer Reactions. *J. Am. Chem. Soc.* **2019**, *141*, 643–647. https://doi.org/10.1021/jacs.8b11949.
124. Zhang, L.; Yi, W.; Li, J.; Wei, G.; Xi, G.; Mao, L. Surfactant-free interfacial growth of graphdiyne hollow microspheres and the mechanistic origin of their SERS activity. *Nat. Commun.* **2023**, *14*, 6318. https://doi.org/10.1038/s41467-023-42038-3.
125. Huang, K.; Li, Z.; Lin, J.; Han, G.; Huang, P. Two-dimensional transition metal carbides and nitrides (MXenes) for biomedical applications. *Chem. Soc. Rev.* **2018**, *47*, 5109–5124. https://doi.org/10.1039/c7cs00838d.
126. Kannan, P.K.; Shankar, P.; Blackman, C.; Chung, C.-H. Recent Advances in 2D Inorganic Nanomaterials for SERS Sensing. *Adv. Mater.* **2019**, *31*, 1803432. https://doi.org/10.1002/adma.201803432.
127. Liu, Y.; Qin, Z.; Deng, J.; Zhou, J.; Jia, X.; Wang, G.; Luo, F. The Advanced Applications of 2D Materials in SERS. *Chemosensors* **2022**, *10*, 455. https://doi.org/10.3390/chemosensors10110455.
128. Luo, W.; Xiong, W.; Han, Y.; Yan, X.; Mai, L. Application of two-dimensional layered materials in surface-enhanced Raman spectroscopy (SERS). *Phys. Chem. Chem. Phys.* **2022**, *24*, 26398–26412. https://doi.org/10.1039/d2cp03650a.
129. Lin, J.; Liang, L.; Ling, X.; Zhang, S.; Mao, N.; Zhang, N.; Sumpter, B.; Meunier, V.; Tong, L.; Zhang, J. Enhanced Raman Scattering on In-Plane Anisotropic Layered Materials. *J. Am. Chem. Soc.* **2015**, *137*, 15511–15517. https://doi.org/10.1021/jacs.5b10144.
130. Huang, Y.; Yu, K.; Li, H.; Xu, K.; Liang, Z.; Walker, D.; Ferreira, P.; Fischer, P.; Fan, D. Scalable Fabrication of Molybdenum Disulfide Nanostructures and their Assembly. *Adv. Mater.* **2020**, *32*, 2003439. https://doi.org/10.1002/adma.202003439.
131. Huang, Y.; Guo, J.; Li, Y.; Li, H.; Fan, D.E. 2D-Material-Integrated Micromachines: Competing Propulsion Strategy and Enhanced Bacterial Disinfection. *Adv. Mater.* **2022**, *34*, 2203082. https://doi.org/10.1002/adma.202203082.
132. Dutta, R.; Bala, A.; Sen, A.; Spinazze, M.; Park, H.; Choi, W.; Yoon, Y.; Kim, S. Optical Enhancement of Indirect Bandgap 2D Transition Metal Dichalcogenides for Multi-Functional Optoelectronic Sensors. *Adv. Mater.* **2023**, *35*, 2303272. https://doi.org/10.1002/adma.202303272.

133. Guselnikova, O.; Lim, H.; Kim, H.; Kim, S.; Gorbunova, A.; Eguchi, M.; Postnikov, P.; Nakanishi, T.; Asahi, T.; Na, J.; et al. New Trends in Nanoarchitectured SERS Substrates: Nanospaces, 2D Materials, and Organic Heterostructures. *Small* **2022**, *18*, 2107182. https://doi.org/10.1002/smll.202107182.
134. Yin, X.; Tang, C.; Zheng, Y.; Gao, J.; Wu, J.; Zhang, H.; Chhowalla, M.; Chen, W.; Wee, A. Recent developments in 2D transition metal dichalcogenides: Phase transition and applications of the (quasi-)metallic phases. *Chem. Soc. Rev.* **2021**, *50*, 10087–10115. https://doi.org/10.1039/d1cs00236h.
135. Thakur, A.; Singh, R.; Yadav, V.; Siddhanta, S.; Jayaramulu, K. Advancing SERS Applications of 2D Materials through the Interplay of Rational Design and Structure-Property Relationships. *Small Methods* **2025**, *9*, 2402056. https://doi.org/10.1002/smtd.202402056.
136. Tang, X.; Hao, Q.; Hou, X.; Lan, L.; Li, M.; Yao, L.; Zhao, X.; Ni, Z.; Fan, X.; Qiu, T. Exploring and Engineering 2D Transition Metal Dichalcogenides toward Ultimate SERS Performance. *Adv. Mater.* **2024**, *36*, 2312348. https://doi.org/10.1002/adma.202312348.
137. Li, M.; Gao, Y.; Fan, X.; Wei, Y.; Hao, Q.; Qiu, T. Origin of layer-dependent SERS tunability in 2D transition metal dichalcogenides. *Nanoscale Horiz.* **2021**, *6*, 186–191. https://doi.org/10.1039/d0nh00625d.
138. Chen, J.; Huang, Y.; Kannan, P.; Zhang, L.; Lin, Z.; Zhang, J.; Chen, T.; Guo, L. Flexible and Adhesive Surface Enhance Raman Scattering Active Tape for Rapid Detection of Pesticide Residues in Fruits and Vegetables. *Anal. Chem.* **2016**, *88*, 2149–2155. https://doi.org/10.1021/acs.analchem.5b03735.
139. Anasori, B.; Lukatskaya, M.; Gogotsi, Y. 2D metal carbides and nitrides (MXenes) for energy storage. *Nat. Rev. Mater.* **2017**, *2*, 16098. https://doi.org/10.1038/natrevmats.2016.98.
140. Xu, W.; Xiao, J.; Chen, Y.; Chen, Y.; Ling, X.; Zhang, J. Graphene-Veiled Gold Substrate for Surface-Enhanced Raman Spectroscopy. *Adv. Mater.* **2013**, *25*, 928–933. https://doi.org/10.1002/adma.201204355.
141. Cao, Y.; Cheng, Y.; Sun, M. Graphene-based SERS for sensor and catalysis. *Appl. Spectrosc. Rev.* **2023**, *58*, 1–38. https://doi.org/10.1080/05704928.2021.1910286.
142. Wang, L.; Li, C.; Cao, C.; Lei, F.; Zhao, X.; Li, Z.; Zhang, C.; Jiao, Y.; Yu, J. Multifunctional Polymeric Nanoneedles with "Full-Spectrum Intrinsic Internal Standard" for Precise SERS Biosensing. *Adv. Funct. Mater.* **2025**, *35*, 2416789. https://doi.org/10.1002/adfm.202416789.
143. Wang, Z.; Ye, J.; Zhang, K.; Ding, L.; Granzier-Nakajima, T.; Ranasinghe, J.C.; Xue, Y.; Sharma, S.; Biase, I.; Terrones, M.; et al. Rapid Biomarker Screening of Alzheimer's Disease by Interpretable Machine Learning and Graphene-Assisted Raman Spectroscopy. *ACS Nano* **2022**, *16*, 6426–6436. https://doi.org/10.1021/acsnano.2c00538.
144. Chen, S.; Wu, Q.; Mishra, C.; Kang, J.; Zhang, H.; Cho, K.; Cai, W.; Balandin, A.A.; Ruoff, R.S. Thermal conductivity of isotopically modified graphene. *Nat. Mater.* **2012**, *11*, 203–207. https://doi.org/10.1038/nmat3207.
145. Balandin, A.A. Thermal properties of graphene and nanostructured carbon materials. *Nat. Mater.* **2011**, *10*, 569–581. https://doi.org/10.1038/nmat3064.
146. Qu, L.; Wang, N.; Xu, H.; Wang, W.; Liu, Y.; Kuo, L.; Yadav, T.; Wu, J.; Joyner, J.; Song, Y.; et al. Gold Nanoparticles and g-C3N4-Intercalated Graphene Oxide Membrane for Recyclable Surface Enhanced Raman Scattering. *Adv. Funct. Mater.* **2017**, *27*, 1701714. https://doi.org/10.1002/adfm.201701714.
147. Xu, W.; Mao, N.; Zhang, J. Graphene: A Platform for Surface-Enhanced Raman Spectroscopy. *Small* **2013**, *9*, 1206–1224. https://doi.org/10.1002/smll.201203097.
148. John, S. Strong Localization of Photons in Certain Disordered Dielectric Superlattices. *Phys. Rev. Lett.* **1987**, *58*, 2486–2489. https://doi.org/10.1103/PhysRevLett.58.2486.
149. Yablonovitch, E. Inhibited Spontaneous Emission in Solid-State Physics and Electronics. *Phys. Rev. Lett.* **1987**, *58*, 2059–2062. https://doi.org/10.1103/PhysRevLett.58.2059.
150. Fuhrmann, T.; Landwehr, S.; El Rharbi-Kucki, M.; Sumper, M. Diatoms as living photonic crystals. *Appl. Phys. B* **2004**, *78*, 257–260. https://doi.org/10.1007/s00340-004-1419-4.
151. Aguirre, C.I.; Reguera, E.; Stein, A. Tunable Colors in Opals and Inverse Opal Photonic Crystals. *Adv. Funct. Mater.* **2010**, *20*, 2565–2578. https://doi.org/10.1002/adfm.201000143.
152. Notomi, M.; Yamada, K.; Shinya, A.; Takahashi, J.; Takahashi, C.; Yokohama, I. Extremely large group-velocity dispersion of line-defect waveguides in photonic crystal slabs. *Phys. Rev. Lett.* **2001**, *87*, 253902. https://doi.org/10.1103/PhysRevLett.87.253902.
153. Lin, C.Y.; Wang, X.L.; Chakravarty, S.; Lee, B.S.; Lai, W.C.; Luo, J.D.; Jen, A.K.Y.; Chen, R.T. Electro-optic polymer infiltrated silicon photonic crystal slot waveguide modulator with 23 dB slow light enhancement. *Appl. Phys. Lett.* **2010**, *97*, 093304. https://doi.org/10.1063/1.3486225.
154. Wang, S.S.; Magnusson, R. Theory and Applications of Guided-Mode Resonance Filters. *Appl. Opt.* **1993**, *32*, 2606–2613. https://doi.org/10.1364/Ao.32.002606.
155. Huang, M.; Yanik, A.A.; Chang, T.Y.; Altug, H. Sub-wavelength nanofluidics in photonic crystal sensors. *Opt. Express* **2009**, *17*, 24224–24233. https://doi.org/10.1364/Oe.17.024224.

156. Eftekhari, F.; Escobedo, C.; Ferreira, J.; Duan, X.B.; Girotto, E.M.; Brolo, A.G.; Gordon, R.; Sinton, D. Nanoholes As Nanochannels: Flow-through Plasmonic Sensing. *Anal. Chem.* **2009**, *81*, 4308–4311. https://doi.org/10.1021/ac900221y.
157. Gale, D.K.; Gutu, T.; Jiao, J.; Chang, C.H.; Rorrer, G.L. Photoluminescence Detection of Biomolecules by Antibody-Functionalized Diatom Biosilica. *Adv. Funct. Mater.* **2009**, *19*, 926–933. https://doi.org/10.1002/adfm.200801137.
158. Kaminska, A.; Sprynskyy, M.; Winkler, K.; Szymborski, T. Ultrasensitive SERS immunoassay based on diatom biosilica for detection of interleukins in blood plasma. *Anal. Bioanal. Chem.* **2017**, *409*, 6337–6347. https://doi.org/10.1007/s00216-017-0566-5.
159. Saridag, A.M.; Karagoz, I.D.; Wachsmann-Hogiu, S.; Kahraman, M. Diatomite-Based, Flexible SERS Immunosensor Platform for Rapid, Specific, and Sensitive Detection of Circulating Cancer-Specific Protein Biomarkers in Serum Using Raman Probes. *ACS Appl. Bio Mater.* **2024**, *7*, 1878–1887. https://doi.org/10.1021/acsabm.3c01253.
160. Sherma, J.; Rabel, F. Review of thin layer chromatography in pesticide analysis: 2016–2018. *J. Liq. Chromatogr. Relat. Technol.* **2018**, *41*, 1052–1065. https://doi.org/10.1080/10826076.2018.1557055.
161. Pozzi, F.; Shibayama, N.; Leona, M.; Lombardi, J.R. TLC-SERS study of Syrian rue (Peganum harmala) and its main alkaloid constituents. *J. Raman Spectrosc.* **2013**, *44*, 102–107. https://doi.org/10.1002/jrs.4140.
162. Li, D.W.; Qu, L.L.; Zhai, W.L.; Xue, J.Q.; Fossey, J.S.; Long, Y.T. Facile On-Site Detection of Substituted Aromatic Pollutants in Water Using Thin Layer Chromatography Combined with Surface-Enhanced Raman Spectroscopy. *Environ. Sci. Technol.* **2011**, *45*, 4046–4052. https://doi.org/10.1021/es104155r.
163. Kong, X.M.; Squire, K.; Chong, X.Y.; Wang, A.X. Ultra-sensitive lab-on-a-chip detection of Sudan I in food using plasmonics-enhanced diatomaceous thin film. *Food Control* **2017**, *79*, 258–265. https://doi.org/10.1016/j.foodcont.2017.04.007.
164. Kong, X.M.; Li, E.W.; Squire, K.; Liu, Y.; Wu, B.; Cheng, L.J.; Wang, A.X. Plasmonic nanoparticles-decorated diatomite biosilica: Extending the horizon of on-chip chromatography and label-free biosensing. *J. Biophotonics* **2017**, *10*, 1473–1484. https://doi.org/10.1002/jbio.201700045.
165. Liu, S.; Xu, D.; Chen, J.; Peng, N.; Ma, T.; Liang, F. Nanozymatic magnetic nanomotors for enhancing photothermal therapy and targeting intracellular SERS sensing. *Nanoscale* **2023**, *15*, 12944–12953. https://doi.org/10.1039/d3nr02739b.
166. Lian, B.; Li, H.; Guo, J.; Fan, D.E. Optoelectric Raman Nanosensors: Overcoming Intrinsic Limit in Nano-biosensing. *Res. Sq.* **2024**. https://doi.org/10.21203/rs.3.rs-4732904/v1.
167. Liu, J.; Guo, J.; Meng, G.; Fan, D. Superstructural Raman Nanosensors with Integrated Dual Functions for Ultrasensitive Detection and Tunable Release of Molecules. *Chem. Mater.* **2018**, *30*, 5256–5263. https://doi.org/10.1021/acs.chemmater.8b01979.
168. Huang, Y.; Gu, Y.; Liu, X.; Deng, T.; Dai, S.; Qu, J.; Yang, G.; Qu, L. Reusable ring-like Fe_3O_4/Au nanozymes with enhanced peroxidase-like activities for colorimetric-SERS dual-mode sensing of biomolecules in human blood. *Biosens. Bioelectron.* **2022**, *209*, 114253. https://doi.org/10.1016/j.bios.2022.114253.
169. Jiang, S.; Li, Q.; Wang, C.; Pang, Y.; Sun, Z.; Xiao, R. *In Situ* Exosomal MicroRNA Determination by Target-Triggered SERS and Fe_3O_4@TiO_2-Based Exosome Accumulation. *ACS Sens.* **2021**, *6*, 852–862. https://doi.org/10.1021/acssensors.0c01900.
170. Bai, X.; Wang, L.; Ren, J.; Bai, X.; Zeng, L.; Shen, A.; Hu, J. Accurate Clinical Diagnosis of Liver Cancer Based on Simultaneous Detection of Ternary Specific Antigens by Magnetic Induced Mixing Surface-Enhanced Raman Scattering Emissions. *Anal. Chem.* **2019**, *91*, 2955–2963. https://doi.org/10.1021/acs.analchem.8b05153.
171. Han, L.; Zhu, C.; Tan, Z.; Wang, J.; Liao, X.; Xia, X.; Wang, C. Integrated separation and detection of exosomes via a label-free magnetic SERS platform. *Chem. Commun.* **2023**, *59*, 7967–7970. https://doi.org/10.1039/d3cc01530k.
172. Kim, H.; Lee, S.; Seo, H.; Kang, B.; Moon, J.; Lee, K.; Yong, D.; Kang, H.; Jung, J.; Lim, E.; et al. Clustered Regularly Interspaced Short Palindromic Repeats-Mediated Surface-Enhanced Raman Scattering Assay for Multidrug-Resistant Bacteria. *ACS Nano* **2020**, *14*, 17241–17253. https://doi.org/10.1021/acsnano.0c07264.
173. Zhou, J.; Xiong, Q.; Ma, J.; Ren, J.; Messersmith, P.; Chen, P.; Duan, H. Polydopamine-Enabled Approach toward Tailored Plasmonic Nanogapped Nanoparticles: From Nanogap Engineering to Multifunctionality. *ACS Nano* **2016**, *10*, 11066–11075. https://doi.org/10.1021/acsnano.6b05951.
174. Duan, W.; Liu, R.; Sen, A. Transition between Collective Behaviors of Micromotors in Response to Different Stimuli. *J. Am. Chem. Soc.* **2013**, *135*, 1280–1283. https://doi.org/10.1021/ja3120357.
175. Kim, K.; Guo, J.; Liang, Z.; Fan, D. Artificial Micro/Nanomachines for Bioapplications: Biochemical Delivery and Diagnostic Sensing. *Adv. Funct. Mater.* **2018**, *28*, 1705867. https://doi.org/10.1002/adfm.201705867.
176. Wu, J.; Balasubramanian, S.; Kagan, D.; Manesh, K.M.; Campuzano, S.; Wang, J. Motion-based DNA detection using catalytic nanomotors. *Nat. Commun.* **2010**, *1*, 36. https://doi.org/10.1038/ncomms1035.
177. Chen, C.; Ding, S.; Wang, J. Materials consideration for the design, fabrication and operation of microscale robots. *Nat. Rev. Mater.* **2024**, *9*, 159–172. https://doi.org/10.1038/s41578-023-00641-2.
178. Pacheco, M.; López, M.; Jurado-Sánchez, B.; Escarpa, A. Self-propelled micromachines for analytical sensing: A critical review. *Anal. Bioanal. Chem.* **2019**, *411*, 6561–6573. https://doi.org/10.1007/s00216-019-02070-z.

179. Akolpoglu, M.B.; Dogan, N.O.; Bozuyuk, U.; Ceylan, H.; Kizilel, S.; Sitti, M. High-Yield Production of Biohybrid Microalgae for On-Demand Cargo Delivery. *Adv. Sci.* **2020**, *7*, 2001256. https://doi.org/10.1002/advs.202001256.
180. Shih, K.; Zaidi, N.; Lee, S.H.; Li, H.; Fan, D.E. Nanotweezers for Manipulating Untethered Micro/Nanoscale Bio-Tools: Principles, Performance, and Highlighted Applications. *Adv. NanoBiomed Res.* **2025**, *5*, 2400130. https://doi.org/10.1002/anbr.202400130.
181. Liang, Z.; Teal, D.; Fan, D. Light programmable micro/nanomotors with optically tunable in-phase electric polarization. *Nat. Commun.* **2019**, *10*, 5275. https://doi.org/10.1038/s41467-019-13255-6.
182. Joh, H.; Fan, D.E. Materials and Schemes of Multimodal Reconfigurable Micro/Nanomachines and Robots: Review and Perspective. *Adv. Mater.* **2021**, *33*, 2101965. https://doi.org/10.1002/adma.202101965.
183. Liang, Z.X.; Fan, D.L. Visible light-gated reconfigurable rotary actuation of electric nanomotors. *Sci. Adv.* **2018**, *4*, eaau0981. https://doi.org/10.1126/sciadv.aau0981.
184. Xu, X.; Kim, K.; Li, H.; Fan, D.L. Ordered Arrays of Raman Nanosensors for Ultrasensitive and Location Predictable Biochemical Detection. *Adv. Mater.* **2012**, *24*, 5457–5463. https://doi.org/10.1002/adma.201201820.
185. Lai, H.; Xu, F.; Wang, L. A review of the preparation and application of magnetic nanoparticles for surface-enhanced Raman scattering. *J. Mater. Sci.* **2018**, *53*, 8677–8698. https://doi.org/10.1007/s10853-018-2095-9.
186. Wang, Z.; Zong, S.; Wang, Y.; Li, N.; Li, L.; Lu, J.; Wang, Z.; Chen, B.; Cui, Y. Screening and multiple detection of cancer exosomes using an SERS-based method. *Nanoscale* **2018**, *10*, 9053–9062. https://doi.org/10.1039/c7nr09162a.
187. Huang, X.; Wu, S.; Hu, H.; Sun, J. AuNanostar@4-MBA@Au Core-Shell Nanostructure Coupled with Exonuclease III-Assisted Cycling Amplification for Ultrasensitive SERS Detection of Ochratoxin A. *ACS Sens.* **2020**, *5*, 2636–2643. https://doi.org/10.1021/acssensors.0c01162.
188. Zhang, W.; Tang, S.; Jin, Y.; Yang, C.; He, L.; Wang, J.; Chen, Y. Multiplex SERS-based lateral flow immunosensor for the detection of major mycotoxins in maize utilizing dual Raman labels and triple test lines. *J. Hazard. Mater.* **2020**, *393*, 122348. https://doi.org/10.1016/j.jhazmat.2020.122348.
189. Bell, S.E.J.; Charron, G.; Cortés, E.; Kneipp, J.; de la Chapelle, M.L.; Langer, J.; Procházka, M.; Tran, V.; Schlücker, S. Towards Reliable and Quantitative Surface-Enhanced Raman Scattering (SERS): From Key Parameters to Good Analytical Practice. *Angew. Chem. Int. Ed.* **2020**, *59*, 5454–5462. https://doi.org/10.1002/anie.201908154.
190. Qian, X.M.; Nie, S.M. Single-molecule and single-nanoparticle SERS: From fundamental mechanisms to biomedical applications. *Chem. Soc. Rev.* **2008**, *37*, 912–920. https://doi.org/10.1039/B708839F.
191. Bi, X.; He, Z.; Luo, Z.; Huang, W.; Diao, X.; Ye, J. Digital colloid-enhanced Raman spectroscopy for the pharmacokinetic detection of bioorthogonal drugs. *Chem. Sci.* **2024**, *15*, 13998–14008. https://doi.org/10.1039/D4SC02553A.
192. Bi, X.; Czajkowsky, D.M.; Shao, Z.; Ye, J. Digital colloid-enhanced Raman spectroscopy by single-molecule counting. *Nature* **2024**, *628*, 771–775. https://doi.org/10.1038/s41586-024-07218-1.
193. Ando, J.; Murai, K.; Michiyuki, T.; Takahashi, I.; Iida, T.; Kogo, Y.; Toyoda, M.; Saito, Y.; Murayama, S.; Kurihara, M.; et al. Digital SERS bioanalysis of single-enzyme biomarkers. *Proc. Natl. Acad. Sci. USA* **2025**, *122*, e2510559122. https://doi.org/10.1073/pnas.2510559122.
194. Li, J.; Wuethrich, A.; Sina, A.A.I.; Cheng, H.-H.; Wang, Y.; Behren, A.; Mainwaring, P.N.; Trau, M. A digital single-molecule nanopillar SERS platform for predicting and monitoring immune toxicities in immunotherapy. *Nat. Commun.* **2021**, *12*, 1087. https://doi.org/10.1038/s41467-021-21431-w.
195. Wen, P.; Yang, F.; Zhao, H.; Li, S.; Xu, Y.; Chen, L. Microcavity Array-Based Digital SERS Chip for Rapid and Accurate Label-free Quantitative Detection of Live Bacteria. *ACS Sens.* **2024**, *9*, 6167–6173. https://doi.org/10.1021/acssensors.4c02007.
196. Liu, W.; Wang, Z.; Liu, Z.; Chen, J.; Shi, L.; Huang, L.; Liu, Y.; Cui, S.; He, X. Utilizing an Automated SERS-Digital Microfluidic System for High-Throughput Detection of Explosives. *ACS Sens.* **2023**, *8*, 1733–1741. https://doi.org/10.1021/acssensors.3c00012.
197. Kim, W.; Han, J.; Kim, Y.J.; Lee, H.; Kim, T.G.; Shin, J.-H.; Kim, D.-H.; Jung, H.S.; Moon, S.W.; Choi, S. Molybdenum Disulfide-Assisted Spontaneous Formation of Multistacked Gold Nanoparticles for Deep Learning-Integrated Surface-Enhanced Raman Scattering. *ACS Nano* **2024**, *18*, 17557–17569. https://doi.org/10.1021/acsnano.4c00978.
198. Kim, M.G.; Jue, M.; Lee, K.H.; Lee, E.Y.; Roh, Y.; Lee, M.; Lee, H.J.; Lee, S.; Liu, H.; Koo, B.; et al. Deep Learning Assisted Surface-Enhanced Raman Spectroscopy (SERS) for Rapid and Direct Nucleic Acid Amplification and Detection: Toward Enhanced Molecular Diagnostics. *ACS Nano* **2023**, *17*, 18332–18345. https://doi.org/10.1021/acsnano.3c05633.
199. Zhao, Y.; Zhan, K.; Xin, P.-L.; Chen, Z.; Li, S.; De Angelis, F.; Huang, J.-A. Single-Molecule SERS Discrimination of Proline from Hydroxyproline Assisted by a Deep Learning Model. *Nano Lett.* **2025**, *25*, 7499–7506. https://doi.org/10.1021/acs.nanolett.5c01177.
200. Bi, X.; Lin, L.; Chen, Z.; Ye, J. Artificial Intelligence for Surface-Enhanced Raman Spectroscopy. *Small Methods* **2024**, *8*, 2301243. https://doi.org/10.1002/smtd.202301243.

201. Xue, B.; Bi, X.; Dong, Z.; Xu, Y.; Liang, M.; Fang, X.; Yuan, Y.; Wang, R.; Liu, S.; Jiao, R.; et al. Deep spectral component filtering as a foundation model for spectral analysis demonstrated in metabolic profiling. *Nat. Mach. Intell.* **2025**, *7*, 743–757. https://doi.org/10.1038/s42256-025-01027-5.
202. Xie, Y.; Su, X.; Wen, Y.; Zheng, C.; Li, M. Artificial Intelligent Label-Free SERS Profiling of Serum Exosomes for Breast Cancer Diagnosis and Postoperative Assessment. *Nano Lett.* **2022**, *22*, 7910–7918. https://doi.org/10.1021/acs.nanolett.2c02928.
203. Sjöberg, J.; Siminea, N.; Păun, A.; Lita, A.; Larion, M.; Petre, I. RADAR: Raman Spectral Analysis Using Deep Learning for Artifact Removal. *Adv. Opt. Mater.* **2025**, *13*, 2500736. https://doi.org/10.1002/adom.202500736.
204. Luo, S.-H.; Xu, J.; Wang, W.-L.; Xiong, C.-R.; Wang, L.-P.; Tian, Z.-Q.; Liu, G.-K. SSNet: A Spectral Unmixing Framework for Enhancing the Qualitative Sensitivity of SERS to Trace Targets in Complex Mixtures. *J. Am. Chem. Soc.* **2025**, *147*, 43964–43972. https://doi.org/10.1021/jacs.5c16529.
205. Pavlou, E.; Kourkoumelis, N. PyFasma: An open-source, modular Python package for preprocessing and multivariate analysis of Raman spectroscopy data. *Analyst* **2025**, *150*, 3112–3122. https://doi.org/10.1039/D5AN00452G.
206. Georgiev, D.; Pedersen, S.V.; Xie, R.; Fernández-Galiana, Á.; Stevens, M.M.; Barahona, M. RamanSPy: An Open-Source Python Package for Integrative Raman Spectroscopy Data Analysis. *Anal. Chem.* **2024**, *96*, 8492–8500. https://doi.org/10.1021/acs.analchem.4c00383.
207. Wang, Z.; Ranasinghe, J.C.; Wu, W.; Chan, D.C.Y.; Gomm, A.; Tanzi, R.E.; Zhang, C.; Zhang, N.; Allen, G.I.; Huang, S. Machine Learning Interpretation of Optical Spectroscopy Using Peak-Sensitive Logistic Regression. *ACS Nano* **2025**, *19*, 15457–15473. https://doi.org/10.1021/acsnano.4c16037.
208. Song, Y.; Zhang, M.; Jiang, X.; Zhang, F.; Ju, C.; Huang, S.; Lau, A.P.T.; Wang, D. SRS-Net: A universal framework for solving stimulated Raman scattering in nonlinear fiber-optic systems by physics-informed deep learning. *Commun. Eng.* **2024**, *3*, 109. https://doi.org/10.1038/s44172-024-00253-w.
209. Huang, L.; Sun, H.; Sun, L.; Shi, K.; Chen, Y.; Ren, X.; Ge, Y.; Jiang, D.; Liu, X.; Knoll, W.; et al. Rapid, label-free histopathological diagnosis of liver cancer based on Raman spectroscopy and deep learning. *Nat. Commun.* **2023**, *14*, 48. https://doi.org/10.1038/s41467-022-35696-2.
210. Zheng, P.; Wu, L.; Lee, M.K.H.; Nelson, A.; Betenbaugh, M.; Barman, I. Deep Learning-Powered Colloidal Digital SERS for Precise Monitoring of Cell Culture Media. *Nano Lett.* **2025**, *25*, 6284–6291. https://doi.org/10.1021/acs.nanolett.5c01071.
211. Zheng, P.; Semancik, S.; Barman, I. Deep Learning-Assisted SERS for Therapeutic Drug Monitoring of Clozapine in Serum on Plasmonic Metasurfaces. *Nano Lett.* **2025**, *25*, 5342–5349. https://doi.org/10.1021/acs.nanolett.5c00391.
212. Zhang, D.; Cheng, Z.; Song, Y.; Li, H.; Shi, L.; Wang, N.; Peng, Y.; Chen, R.; Sun, N.; Han, M.; et al. Rapid and sensitive acute leukemia classification and diagnosis platform using deep learning-assisted SERS detection. *Cell Rep. Med.* **2025**, *6*, 102320. https://doi.org/10.1016/j.xcrm.2025.102320.
213. Zaki, J.K.; Tomasik, J.; McCune, J.A.; Bahn, S.; Lió, P.; Scherman, O.A. Explainable Deep Learning Framework for SERS Bioquantification. *ACS Sens.* **2025**, *10*, 6597–6606. https://doi.org/10.1021/acssensors.5c01058.
214. Li, M.; He, X.; Wu, C.; Wang, L.; Zhang, X.; Gong, X.; Zeng, X.; Huang, Y. Deep Learning Enabled SERS Identification of Gaseous Molecules on Flexible Plasmonic MOF Nanowire Films. *ACS Sens.* **2024**, *9*, 979–987. https://doi.org/10.1021/acssensors.3c02519.
215. Lin, X.; Lin, D.; Chen, Y.; Lin, J.; Weng, S.; Song, J.; Feng, S. High Throughput Blood Analysis Based on Deep Learning Algorithm and Self-Positioning Super-Hydrophobic SERS Platform for Non-Invasive Multi-Disease Screening. *Adv. Funct. Mater.* **2021**, *31*, 2103382. https://doi.org/10.1002/adfm.202103382.

Materials and Interfaces

Scilight

Communication

Check for updates

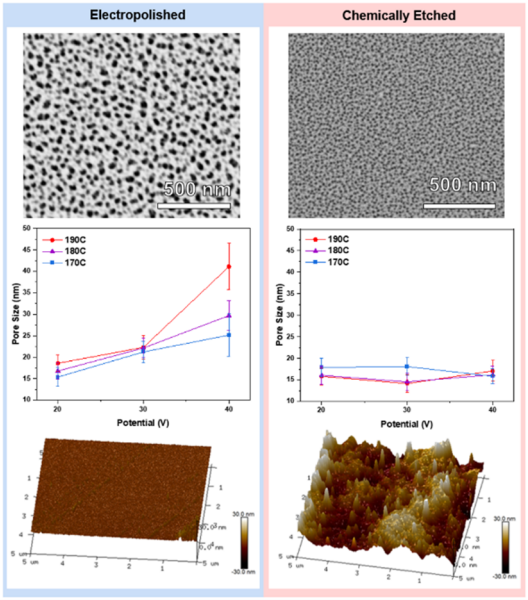
Effect of Electropolishing on Morphology and Adhesion of Nanostructured Anodic Tantalum Oxide Thin Films

Sarah E. Pooley [1], Cyrus Koroni [1], Shinthia Binte Eskender [1], Jacob Olson [1], Joshua A. Russell [1], Max Bork [1], Timothy Merrell [1], Gage Cook [1], Scarlet Fields [1], Kaden Kunz [1], Kiev Dixon [1], Pete Barnes [2], Brian Jaques [1], and Hui Xiong [1,*]

[1] Micron School of Materials Science and Engineering, Boise State University, Boise, ID 83720, USA
[2] Idaho National Laboratory, Idaho Falls, ID 83415, USA
* Correspondence: clairexiong@boisestate.edu

Received: 17 July 2026; Revised: 13 August 2026; Accepted: 24 August 2026; Published: 3 September 2026

Abstract: Anodic tantalum oxide films have attracted significant interest due to their highly favorable properties, such as corrosion resistance and biocompatibility, as well as the cost-effective and scalable nature of anodization as a fabrication method. However, the need for morphological control as well as strong adhesion of the resulting films to the substrate pose barriers to their application. In this work, the morphology and adhesion of anodic tantalum oxide films grown on electropolished, chemically etched, and pristine tantalum metal substrates in a fluoride-free electrolyte containing potassium phosphate and glycerol under varying voltage and temperature conditions were systematically investigated. Electropolishing significantly reduced substrate surface roughness and promoted the growth of native suboxide species. Current density-time characteristics during anodization suggest noticeable kinetic effects related to substrate pre-preparation, which were corroborated by significantly increased pore size in oxide films grown on electropolished substrates. Systematic variation in voltage and temperature provided evidence of improved control over size and morphology of the nanoporous anodized oxide films via anodization parameters in electropolished samples. In addition, pull tests demonstrated increased film-substrate adhesion in anodized oxide films on both chemically etched and electropolished substrates. These findings demonstrate that electropolishing is an effective strategy for improving the controllability of nanostructure morphology, film uniformity, and adhesion of anodic tantalum oxide coatings.



Keywords: electropolishing; anodization; morphology; adhesion; tantalum oxide

1. Introduction

Tantalum oxide has attracted considerable interest for use in a variety of technologically significant applications, including catalysts [1], information storage devices [2–5], and protective coatings for biomedical applications [6]. Across these diverse fields, nanostructure plays a key role by affecting material properties such as photocatalytic activity [1], hydrophilicity [7], and memristive behavior [8]. In particular, nanoporous and nanotubular oxide films have been demonstrated to improve lithium ion diffusion kinetics for energy storage applications [9], as well as increase photocatalytic efficiency of water splitting for hydrogen generation [10]. For biomedical and photoelectrochemical applications, film structure and adhesion are especially critical, as they directly affect implant biocompatibility [6] and catalyst performance [11,12]. Consequently, strategies that enable precise control over oxide nanostructure and adhesion are of significant interest.

Copyright: © 2026 by the authors. This is an open access article under the terms and conditions of the Creative Commons Attribution (CC BY) license (https://creativecommons.org/licenses/by/4.0/).
Publisher's Note: Scilight stays neutral with regard to jurisdictional claims in published maps and institutional affiliations.

Electrochemical anodization utilizes competing field-assisted oxide formation and dissolution reactions during electrochemical oxidation of a valve metal substrate to grow nanostructured anodic oxide layers of controlled thickness and porosity [13,14]. It is notably cost-effective and scalable among the synthesis methods used for forming oxide coatings, particularly for Ta_2O_5. In order to facilitate the formation of highly ordered and well-adhered nanostructures, electropolishing is a popular substrate preparation technique prior to anodic oxide growth, as it enables efficient polishing to nanoscale smoothness [15,16]. The two techniques have previously been used in tandem to improve uniformity of oxide films grown via anodization such as Al_2O_3 [17,18], TiO_2 [19], and Nb_2O_5 [16]. However, limited work has been done in understanding the effect of electropolishing on the anodization of tantalum [6,20–22].

The wide variety of electrolyte systems and conditions which have been investigated for tantalum anodization have been comprehensively summarized in recent review articles [23,24]. Fluoride-containing solutions predominate in prior work concerning nanostructured films [23], and the effect of fluoride concentration on oxide growth rate [25] and porosity [26] has been investigated in detail. However, several studies have indicated that the incorporation of fluoride ions into the anodic tantalum oxide films is a major factor responsible for film detachment and poor substrate adhesion [23,27–29], as a result of the enhanced inward mobility of fluoride ions compared to oxygen [30] and the subsequent build up of fluoride containing species between the oxide layer and the substrate [28]. Consequently, the use of non-fluoride-containing electrolyte solutions serves as an alternative to improve film adhesion, which is critical for a wide range of applications [23] including photoelectrochemical [11] and biomedical [6] purposes. Melody et al. first reported the anodization of tantalum foil using 10% dibasic potassium phosphate in glycerol at elevated temperatures (90–190 °C) and anodizing potential of 20 V [13]. Later, Lee and Schmuki investigated the effect of temperature and time on pore ordering and film thickness in the same electrolyte system, identifying a 1-h anodization procedure at 20 V and 180 °C as the conditions for optimal pore ordering. The formation of a 25 nm barrier layer at the anodic oxide-substrate interface was identified, but its effect on film adhesion was not studied [31]. By improving overall homogeneity of the substrate via electropolishing as well as removing the highly soluble fluoride-based barrier layer, strong attachment of the anodic oxide to the substrate may be facilitated.

Here, we report a systematic study on the effect of electropolishing of Ta substrates on the morphology and adhesion of anodic Ta_2O_5 films grown in 10% potassium phosphate in glycerol electrolyte. The influence of anodization potential, electrolyte temperature, and the presence of the native suboxide species on the substrate were investigated. Atomic force microscopy (AFM) and x-ray photoelectron spectroscopy (XPS) were utilized to examine the roughness and surface chemistry of electropolished, chemically etched, and pristine tantalum foils. Current density transients during anodization were obtained to investigate the effect of native suboxide species on the anodization process. The morphology and thickness of the resulting anodic oxide films was examined using scanning electron microscopy (SEM). In addition, pull tests were used to investigate film adhesion. We demonstrate that while both chemical etching and electropolishing improve film-substrate adhesion compared to pristine samples, electropolishing offers more control over pore size and morphology of the resulting anodic oxide films, by facilitating the continuous competition between oxide growth & dissolution fundamental to nanostructure formation.

2. Materials and Methods

2.1. Substrate Preparation

Pieces of tantalum foil (33 × 40 × 0.127 mm, 99.95% purity, Thermo Fisher Scientific, Waltham, MA, USA) were cleaned by sonication in acetone, isopropanol, and deionized water, for five minutes each, and dried prior to substrate preparation. The back of each piece was masked using packing tape, with the top edge of the foil left exposed to ensure good electrical contact in the case of electropolishing. Chemically etched samples were allowed to soak in a solution of 10% sulfuric acid in methanol for at least one hour before being rinsed in deionized water and dried immediately prior to anodization. Electropolishing was performed in a two-electrode cell with Ta foil as both the working and counter electrode using a solution of 10% sulfuric acid in methanol (Thermo Fisher Scientific, Waltham, MA, USA), prepared as previously described by Barnes et al. [16]. During electropolishing, the solution was kept below −10 °C in a bath of dry ice and acetone and continuously stirred. Samples were electropolished at a constant current of 0.1 A for 2 h using a BK 9206 power supply (B&K Precision Corporation, Yorba Linda, CA, USA). Following polishing, the foils were removed from solution, rinsed in deionized water, dried, and immediately placed under vacuum and transferred into an inert atmosphere glovebox (Ar, O_2 <0.5 ppm).

2.2. Anodization

Total air exposure for both chemically etched and electropolished substrates prior to anodization was kept to less than 10 min. Kapton tape was used to mask the back of all samples prior to anodization. Exposed working electrode area was 33 × 40 mm. Anodization was performed in a two-electrode cell using 10% dibasic potassium phosphate (98% pure, Thermo Fisher Scientific, Waltham, MA, USA) in glycerol (Thermo Fisher Scientific, Waltham, MA, USA) with Pt mesh as the counter electrode. Anodization was carried out under constant voltage with a current limit of 2 A. Anodization time was fixed at 5 min, while solution temperature (170–190 °C) and applied potential (20–40 V) conditions were systematically varied. Following anodization, samples were rinsed in deionized water and ethanol before being allowed to dry.

2.3. Characterization

The surface roughness of pristine, chemically etched, and electropolished samples was characterized using a Bruker Dimension Icon atomic force microscope (AFM) with a Nanoscope V controller operated in PeakForce Tapping Mode by Nanoscope 9.4 software using a ScanAsyst Air probe (2 nm nominal tip radius). 5 × 5 μm images were taken with a scan rate of 0.5 Hz, 256 samples per line, and Peak Force setpoint of 2 nN. AFM images were processed using Nano Scope Analysis (Bruker Nano, Santa Barbara, CA, USA). Scanning electron microscopy (SEM) images were recorded using an FEI Teneo FESEM (Field Electron and Ion Company, Hillsboro, OR, USA) at 3–5 kV. X-ray photoelectron spectroscopy (XPS) was performed using a Physical Electronics (PHI) 5600 ESCA system (Physical Electronics, Chanhassen, MN, USA) with a monochromated Al K-alpha source and 3 × 10 mm analysis area. Survey scans were performed using 187.85 eV pass energy and 0.8 eV step size; high resolution scans were performed using 23.50 eV pass energy and 0.05 eV step size. XPS data was analyzed using MultiPak 9.6 (Physical Electronics, Chanhassen, MN, USA) and CasaXPS (Casa Software Ltd., casaxps.com; accessed 26 August 2026). All spectra were referenced to the 1s peak (284.8 eV) of adventitious carbon. Spectra were background subtracted and subsequently deconvoluted using the standard FWHM positions for each of the known valence states. Fit constraints included constant binding energy separation and area ratios of 1.91 eV and 4:3 respectively. Adhesion tests were performed in accordance with ASTM standard D4541-22 using a DeFelsko AT-A20 A-B adhesion tester (DeFelsko, Ogdensburg, NY, USA). ResinLab EP11HT 2-Part Epoxy (ResinLab, Germantown, WI, USA) was used to adhere 10 mm Al dollies to the anodic oxide coating prior to pull tests, where the coating was exposed to 7550 N of pressure for 129.1 s at a rate of 60 N/s with 5 s hold. Measurements were duplicated for each sample grown on pristine, chemically etched, and electropolished substrates.

3. Results and Discussion

3.1. Effect of Substrate Preparation on Oxide Morphology

Ta foil substrates were prepared under three conditions prior to anodization: (1) pristine foil, which was degreased via sonication in acetone, isopropyl alcohol, and deionized water for 5 min each prior to use; (2) chemically etched foil, which was degreased and then soaked in a solution of 10% sulfuric acid (H_2SO_4) in methanol for at least 60 min prior to use; and (3) electropolished foils, which were prepared based upon a method adapted from Barnes et al. [16] and Piotrowski et al. [15]. The effects of pretreatment on substrate morphology were characterized using AFM and are shown in Figure 1a–c. Surface roughness increased following chemical etching (R_q = 10.6 nm) compared to the pristine sample (R_q = 8.54 nm). For the electropolished sample, roughness decreased by approximately 3.81 nm (R_q = 4.73 nm) and surface homogeneity significantly improved. AFM measurements were conducted on duplicates for the electropolished condition, with <0.36 nm standard deviation in R_q.

Tantalum metal is known to have native oxide and suboxide species present on the surface, which have been theorized to be responsible for its notable corrosion resistance and biocompatibility [32]. Consequently, one of the reasons for the use of hydrofluoric acid (HF) in the majority of anodization solutions used in the literature is the need for chemicals capable of etching through the native passivation layer. In order to investigate the effect of surface preparation on the native suboxide, samples were prepared and immediately transferred to an Ar-atmosphere glovebox, where an air-free vessel was used to enable chemical characterization with XPS (Figure 1d–f); for the electropolished condition, measurements on duplicates were performed in order to check for differential charging and verify reproducibility. All XPS spectra were calibrated to the position of the 1s peak of adventitious carbon (284.8 eV) prior to deconvolution and fitting. For the electropolished sample, the Ta^{5+} 4f peak doublet appears at 26.74 eV ($4f_{7/2}$) and 28.64 eV ($4f_{5/2}$). These values are very close to those previously reported in the literature (26.8 ± 0.2 and 28.6 ± 0.2) [33,34]. Interestingly, the 4f peak doublet is shifted in both the pristine and chemically etched foils, located at 25.79 eV & 27.74 eV and 25.99 eV & 27.89 eV, respectively. Previous work

by Chakraborti et al. ascribes the peak shift towards lower binding energies as indicative of the presence of non-stoichiometric oxides of tantalum [35], an observation which has been further corroborated by other researchers [36,37]. This implies that electropolishing may facilitate the formation of more stoichiometric native oxides, a phenomenon which may be related to the improvement in surface homogeneity. Analysis of the oxygen spectra for the same set of samples (Figure S1, Supplementary Information**)** revealed that the O1s peak for both the chemically etched and electropolished samples appears at 531.9 eV and 532.2 eV respectively, which is consistent with pentavalent tantalum oxide [35]. For the pristine sample, two distinct peaks can be observed, located at 530.1 eV and 532.0 eV. One possible explanation for this phenomenon may be the presence of lower oxidation states of tantalum within the native oxide present on the surface [35].

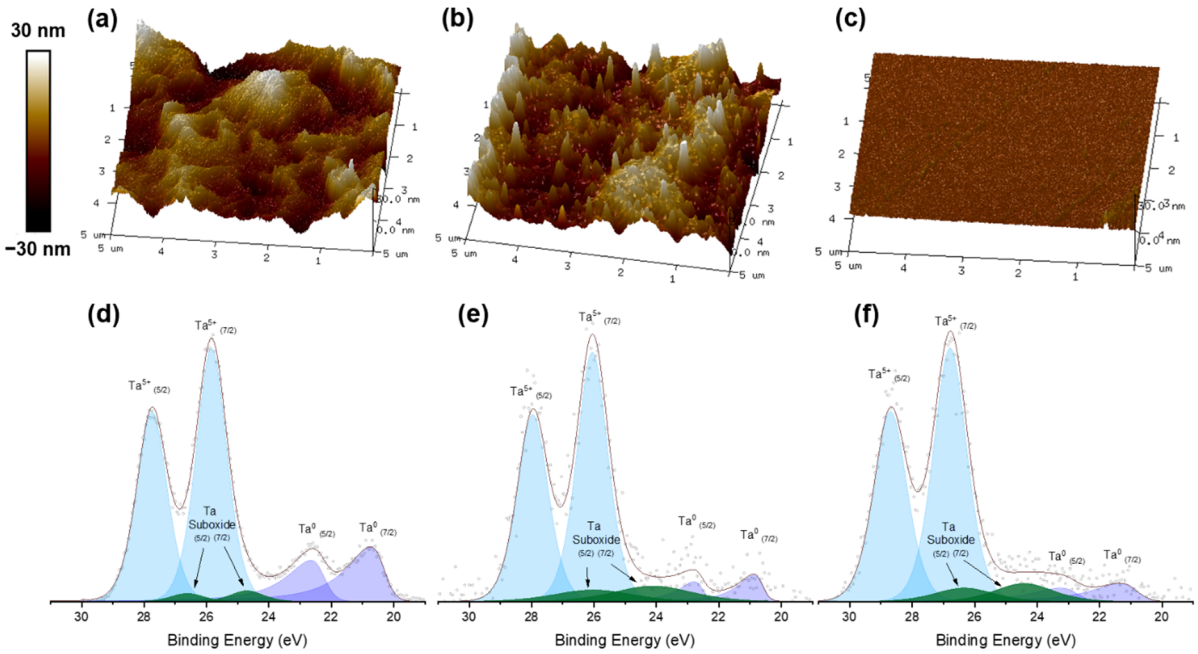


Figure 1. Topographic AFM images of (**a**) pristine, (**b**) chemically etched, and (**c**) electropolished Ta foil; Ta 4f XPS spectra of (**d**) pristine, (**e**) chemically etched, and (**f**) electropolished samples. Solid lines represent fitted curves and open dots are the experimental data.

With regard to the signal from the metal substrate, the Ta^0 peak doublet is most prominent in the spectra for the pristine sample before becoming substantially decreased following both chemical etching and electropolishing. The intensity of the suboxide peaks (24.66 eV & 26.59 eV) follows an inverse trend, increasing significantly following both substrate preparation techniques and nearly surpassing the signal from the metal substrate in the electropolished sample spectra. Quantitative oxidation-state fractions for tantalum oxide, metal, and suboxide are reported in Table S1 (Supplementary Information). These results indicate that the surface treatment of tantalum foil by chemical etching or electropolishing, even in cases involving very limited exposure to air following treatment, facilitates the growth of native suboxides.

In order to study the practical effects of surface roughness and native suboxide prevalence, anodization studies were performed for 5 min at 20 V 180 °C and a fixed current of 2 A, to allow for direct comparison of the effects of chemical and electrochemical treatment compared to the pristine foil. The current density-time ($j - t$) curves recorded during anodization are shown in Figure 2. The initial current density is between 0.111 and 0.099 A/cm^2 for all three samples, with the pristine and chemically etched samples having the highest and lowest values, respectively. Variations in duration of the current density decay reflect similar trends: for the pristine sample, its current density shows the most precipitous drop within the first minute before levelling out to a plateau until the end of the anodization period. The chemically etched sample exhibits the greatest level of decay, dropping below 0.001 A/cm^2 at just over three minutes. The electropolished sample retains higher overall current density compared to the chemically etched sample, but the curve decays continuously throughout the entire five minute period, as opposed to levelling out into the plateau characteristic of the continuous-growth behavior described by Melody et al. [13] and observed for the pristine foil within this study. One explanation for this behavior may be the increase in native suboxide prevalence following substrate preparation, which would consequently increase overall resistance at the interface and slow the electrochemical anodization process.

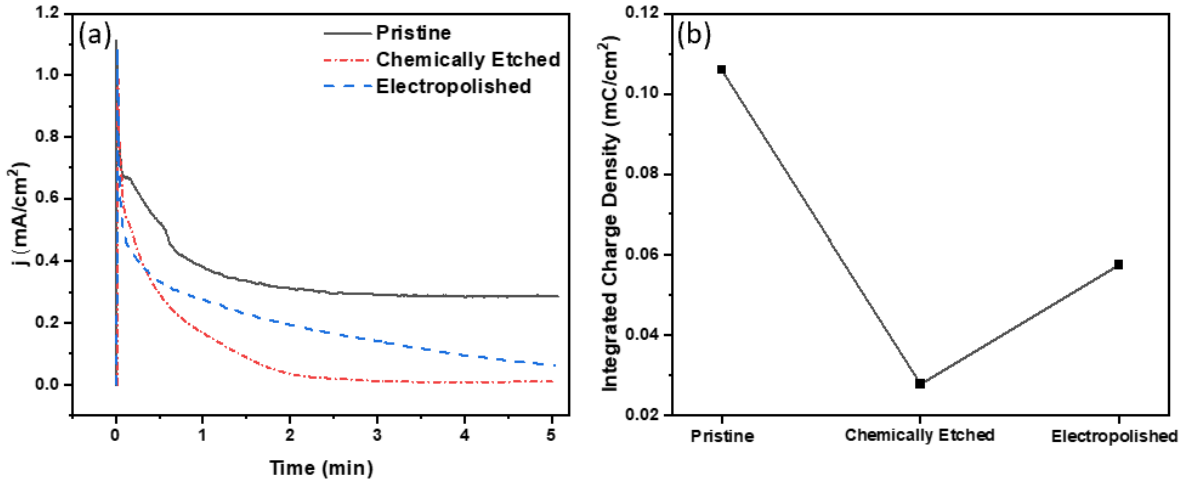


Figure 2. (**a**) Current density-time curves and (**b**) integrated charge density for anodization of pristine, chemically etched, and electropolished substrates at 20 V 180 °C.

With regard to the difference between the chemically etched and electropolished samples, namely the improved current density following electropolishing despite the increase in suboxide as indicated by XPS—the competing dissolution-growth reactions characteristic of anodization may shed some light on this phenomenon.

Nanostructuring during anodization depends upon the balance between field-assisted oxide dissolution vs. growth [14,38]. Upon formation of an initial oxide layer, field-aided ion transport of O^{2-} and Ta^{5+} ions controls further growth [38]. By continued exposure of the growing oxide to an electric field, the Ta-O bond is weakened by polarization, resulting in field-assisted metal cation dissolution, in addition to chemical dissolution by the electrolyte [39]. As a result of the interaction between these processes, suppression of oxide growth is one approach for promoting a relative increase in oxide dissolution. The shallower decay curve exhibited by the electropolished sample is consistent with continuous competition between oxide growth and dissolution, as opposed to the distinct stages seen in the pristine and chemically etched samples for continuous oxide growth. Consequently, the continuous dissolution of the oxide during relatively slow oxide growth may manifest increased current density at the electropolished surface by decreasing oxide thickness and subsequent resistance, compared to the increased resistance produced by faster oxide growth on the chemically etched surface. In order to further elucidate the effect of electropolishing and chemical etching on the balance between oxide growth and dissolution, the morphology of the anodized oxide layers, as well as their thickness and porosity, were characterized using SEM (Figure 3a–c). All three samples exhibited nanoporous morphologies with pore diameters ranging from 10 to 17 nm and an average pore size of 14.35 nm ± 0.366 nm. Interestingly, cross-sectional SEM of a total of six samples revealed substantial differences in oxide film thickness as a function of surface preparation (Figure 3d–f), providing further evidence that substrate pretreatment significantly influences anodization kinetics. The oxide film grown on the pristine substrate reached a thickness of approximately 1.43 μm, whereas the chemically etched and electropolished substrates produced progressively thinner films of approximately 0.928 μm and 0.405 μm, respectively. In addition to the reduction in thickness, the chemically etched and electropolished samples exhibited more uniform oxide layers throughout the film cross section. Several possible explanations for this phenomenon exist, such as changes in surface composition as a consequence of pre-preparation, and changes in local electric fields and surface wettability with surface roughness. Furthermore, native oxide thickness may also play a role by influencing reaction rate, as well as resistance at the electrode-electrolyte interface. With regard to the experimental results of this work, the thicker oxide formed on the pristine substrate is consistent with the XPS results, which showed a lower abundance of native suboxide species prior to anodization. A thinner native suboxide barrier facilitates ionic transport during the early stages of anodization, leading to more rapid field-assisted oxide growth and ultimately a thicker anodic film. In contrast, the higher abundance of native suboxide species on the chemically etched and electropolished substrates may increase the initial resistance to ion transport, slowing anodic oxide growth and resulting in thinner films. Notably, the electropolished substrate produced the thinnest anodic oxide layer despite exhibiting enhanced pore uniformity and nanostructural control. Combined with the current density transients, this observation suggests that electropolishing shifts the anodization mechanism toward a dynamic balance between field-assisted anodic oxide growth and oxide dissolution. In comparison, anodization of the chemically etched substrate appears to remain predominantly growth-controlled during the plateau region, resulting in greater film thickness. These findings indicate that electropolishing may modify the substrate surface

properties in a manner that promotes a more balanced anodization process, leading to improved control over anodic oxide morphology while limiting overall film growth.

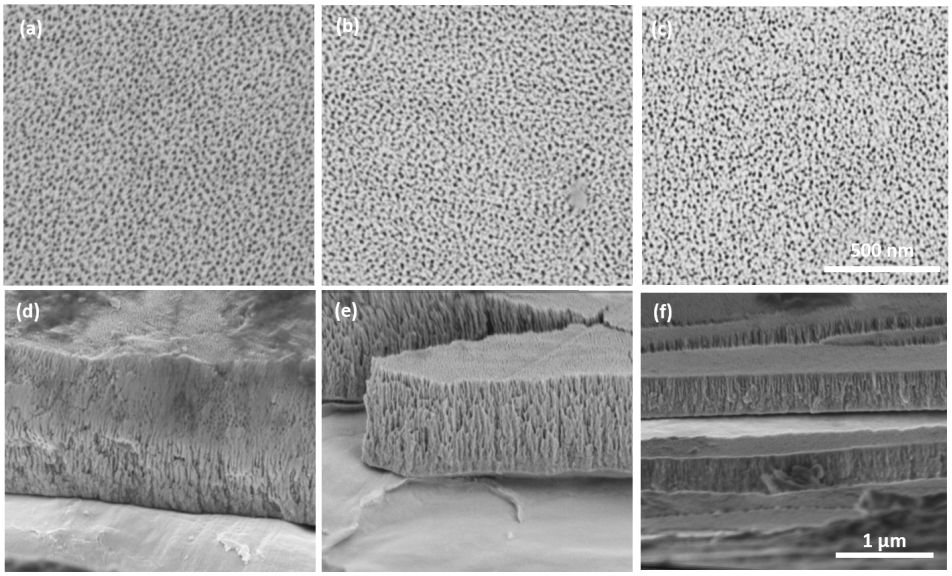


Figure 3. SEM of the top-view surface and cross-section of anodic tantalum oxide films grown at 20 V 180 °C on (**a**,**d**) pristine, (**b**,**e**) chemically etched, and (**c**,**f**) electropolished Ta foil.

3.2. Effect of Anodization Voltage and Temperature

The nanostructure of anodized films plays a key role in coating properties such as hydrophilicity [40] and diffusion kinetics [41]. During anodization, the relative rate of oxide growth versus dissolution is key to control over the size and morphology of produced nanostructures. The most typical method of increasing the rate of dissolution is via the use of stronger chemical etchants like HF, or higher applied potentials which facilitate field-assisted dissolution in addition to chemical etching. An alternative strategy is to suppress the oxide growth rate while maintaining a relatively constant dissolution rate. In the previous section, we demonstrate that substrate surface preparation modifies the abundance of native suboxide species, as well as influences anodic oxide growth kinetics without directly altering the electrolyte chemistry or anodization conditions. Next, we will investigate how anodization conditions influence the morphology of the anodized films.

To investigate how substrate pretreatment influences the morphology of the anodic oxide films in relation to anodization conditions, tantalum substrates with pristine, chemically etched, and electropolished surfaces were anodized over a range of applied voltages (20–40 V) and electrolyte temperatures (170–190 °C). Overall, electropolished substrates produced significantly larger nanopores (15–41 nm) compared to chemically etched (14–18 nm) substrates (Figure 4; Table S2, Supplementary Information). Only minor differences were observed between anodic oxide samples grown on chemically etched versus pristine substrates (Figure 3a–f). For each condition, 2–3 samples were synthesized for analysis. Pore morphology and uniformity remained relatively consistent across all conditions and substrates, with some merging of pores present in samples with increased pore sizes. More importantly, electropolished substrates exhibited a clear relationship between pore size and anodization conditions. Specifically, pore diameter exhibited a distinct increase with applied voltage (Figure 5a and Table S2), indicating that electropolishing enhances the responsiveness of pore formation to the role of the applied voltage in facilitating oxide dissolution. These observations are consistent with previous studies of tantalum anodization in fluoride-containing electrolytes. Almeida Alvez et al. [30] reported a strong linear relationship between pore size and applied voltage (20–50 V) for anodization in H_2SO_4 with HF electrolytes at room temperature, in agreement with earlier work by El-Sayed et al. [42] and more recent reviews by Mohapatra and Sulka [23]. In contrast, chemically etched samples showed no discernible correlation between pore size and anodization voltage over the same range (Figure 5b and Table S2).

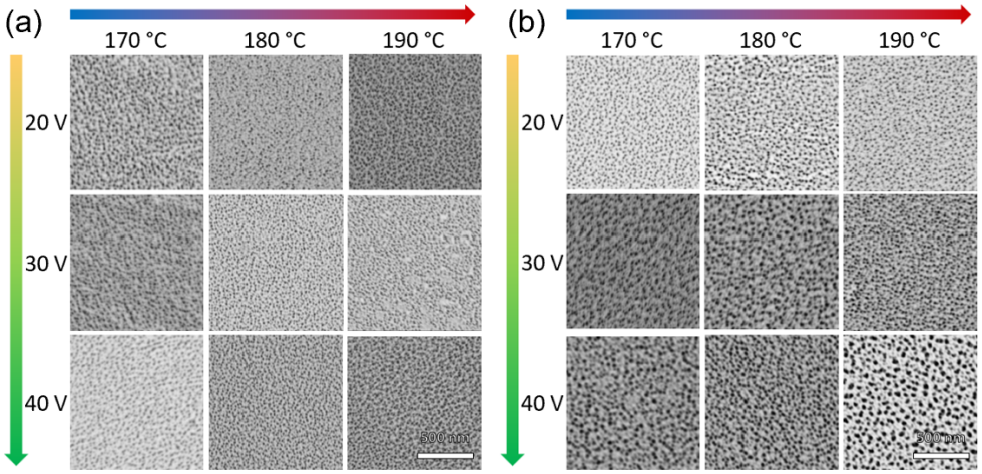


Figure 4. Top view SEM images of anodic oxide films grown at a range of voltage (20–40 V) and temperature (170–190°) conditions on (**a**) chemically etched and (**b**) electropolished substrates.

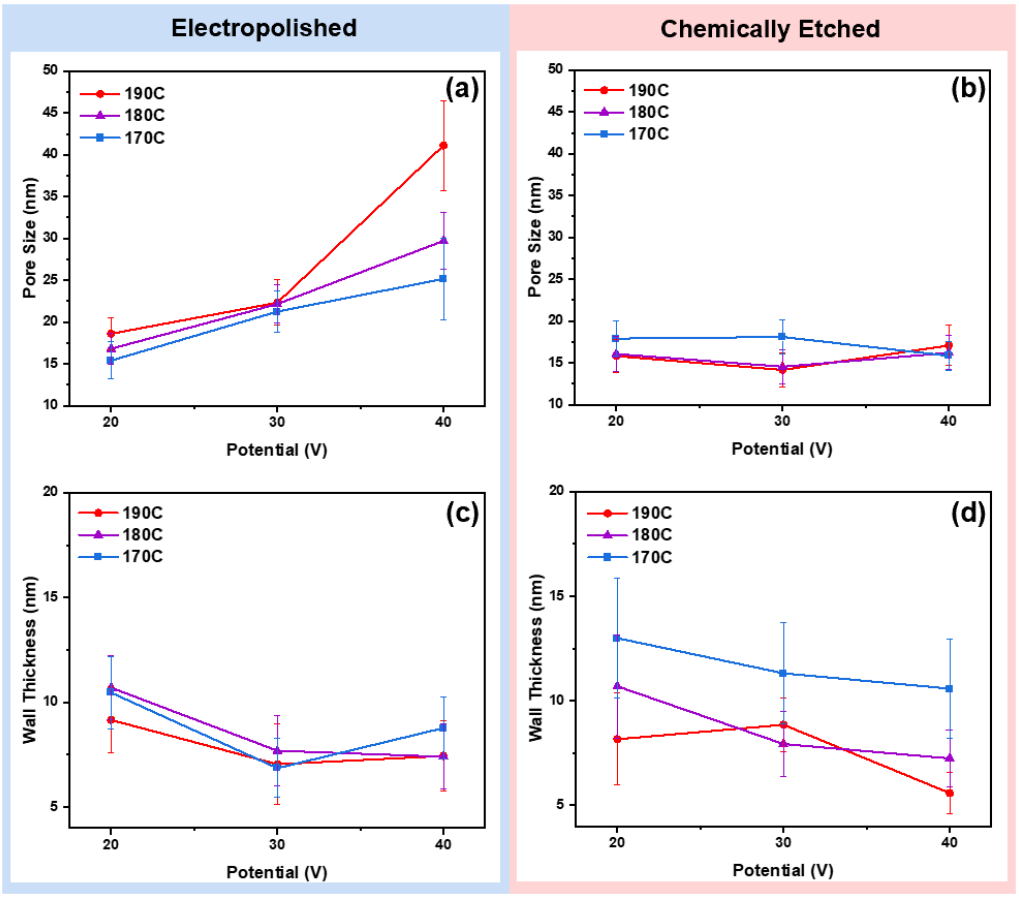


Figure 5. Trends in pore size (**a**,**b**) and wall thickness (**c**,**d**) as a function of anodization parameters for anodic tantalum oxide films grown on electropolished vs. chemically etched substrates. Error bars represent standard deviation in pore size measurements.

A similar trend was observed with electrolyte solution temperature. Increasing the solution temperature led to an average 7.53 nm increase in pore size with each 10 °C interval for electropolished substrates (Figure 5a), while the chemically etched samples remained largely insensitive to temperature. Wall thickness exhibited similar behavior between the two surface preparations (Figure 5c,d). Electropolished samples showed smaller distribution of wall thicknesses across all conditions (6.9–10.5 nm) as well as decreased standard deviation in wall thickness measurements (Table S2, Supplementary Information), while chemically etched samples displayed substantially greater variability (5.6–13.0 nm) as well as higher standard deviation (Figure 5d; Table S2, Supplementary

Information). For both substrate types, a weak dependence of wall thickness on temperature was observed, consistent with enhanced ionic diffusion and accelerated oxide dissolution at elevated temperatures.

Overall, the anodic oxide films grown on chemically etched substrates exhibited limited sensitivity to changes in anodization voltage and temperature, whereas electropolished substrates showed systematic and predictable variations in pore morphology. We hypothesize that this enhanced sensitivity results from the suppression of oxide growth kinetics by the electropolished surface, which shifts anodization toward a regime in which pore morphology is governed more strongly by the competing effects of field-assisted oxide growth and dissolution. As a result, changes in anodization voltage and electrolyte temperature have a more pronounced influence on the resulting nanostructure.

3.3. Effect of Substrate Preparation on Film Adhesion

One of the practical properties of anodized Tantalum critical to the performance of protective and biocompatible coatings is anodic oxide film adhesion to the substrate. One of the previously identified limitations of current anodization methods for tantalum is the need for coatings capable of withstanding the minimum 30 N adhesion requirement for abrasion resistant applications [43,44]. Towards this goal, the presence of a fluoride or oxyfluoride rich barrier layer between the anodic oxide and the substrate is one of the drawbacks of fluorinated electrolytes due to the increased likelihood of film delamination [10,27–29]. A previous study of films grown in potassium phosphate-glycerol electrolyte reported the formation of a dense barrier layer over the course of 1-h anodization [31], and we observed formation of a similar layer in this study (Figure S1, Supplementary Information). Despite the presence of this barrier layer, films grown in potassium phosphate-glycerol electrolytes have previously been reported to display exceptional adhesion properties across multiple anodic metal oxides [45]. One possible mechanism for the improved adhesion of such films may be differences in the rate determining step for formation of the barrier layer between fluoride-containing and phosphate/glycerol electrolytes. Tsuji et al. investigated the relationship between barrier layer thickness and formation potential during formation of anodic TiO_2 in hot phosphate/glycerol electrolyte via cyclic voltammetry [46]. In fluoride-containing electrolyte, the electric field strength at the barrier layer was reported to decrease during the negative potential sweep, indicating a continuous increase in barrier layer thickness. In contrast, current density did not decrease even during the negative sweep in the hot phosphate/glycerol electrolyte, suggesting that diffusion of the oxygen sources in the electrolyte, rather than ion migration, may act as the rate determining step in barrier layer formation [46]. In the case of both their work on TiO_2 and our investigation of Ta_2O_5, the decrease in build up of foreign species at the interface may correspondingly promote direct contact between the anodic oxide and the metal substrate, improving oxide-substrate adhesion [28,47].

In order to investigate the influence of substrate pre-preparation and this type of barrier layer on the adhesion properties of the anodic oxide film, pull tests were performed in accordance with ASTM standard D4541-22 [48] on films grown at 20 V 180 °C on pristine, chemically etched, and electropolished substrates. The adhesion of anodic oxide layers grown on both chemically etched and electropolished samples showed significant improvement compared to oxide grown on the pristine substrate, resisting 96 MPa at a pull rate of 60 N/s even through repeated tests. Oxide removal was only achieved for the pristine sample following a 5 s hold under the same conditions, resulting in delamination of the oxide coating. No delamination or film rupture were observed for coatings grown on chemically etched and electropolished substrates, indicating a pull-off adhesion strength > 96 MPa. An inverse correlation was observed between the adhesion strength of the films and the oxide thickness measured by SEM (Figure 3). These results are in agreement with the higher strain resistance of thinner films previously reported by Choo and Devereux for films grown on chemically polished substrates, which was attributed to the ability of thin films to accommodate certain degrees of substrate slip not permitted in thicker films [49]. Further study would be necessary to determine the precise adhesion strength of the oxide films as well as deconvolute the effects of substrate roughness versus oxide thickness on film adhesion; however, the resistance of films grown on pre-prepared substrates to delamination under the tested conditions provides encouraging data with regard to the lower bounds of adhesion for coatings synthesized by this method. These results demonstrate the highly promising mechanical characteristics of films grown in potassium phosphate-based electrolyte as well as the potential benefits of substrate pre-preparation for such applications.

4. Conclusions

An effective strategy for improving the morphology and adhesion of anodic tantalum oxide films has been developed via electropolishing Ta foil substrates prior to anodization. Electropolishing reduced the substrate surface roughness below 6 nm while increasing the abundance of native suboxide species at the metal surface.

These surface modifications are hypothesized to alter the anodization kinetics by suppressing field-assisted oxide growth, thereby shifting the balance between anodic oxide growth and dissolution. As a result, films grown on electropolished substrates exhibited enhanced control over nanopore size and morphology as a function of anodization voltage, together with improved coating uniformity and stronger film–substrate adhesion. These results indicate that engineering the initial surface condition through electropolishing provides an effective route for tailoring anodic oxide growth. This approach offers a promising strategy for improving the fabrication of tantalum oxide coatings and may be extended to other anodic tantalum nanostructures, including highly ordered nanotubular architectures.

Supplementary Materials: The following supporting information can be downloaded at: https://media.sciltp.com/articles/others/2609031334329283/MI-26070174-SI.pdf. Figure S1: XPS O1s spectra for (a) pristine, (b) chemically etched, and (c) electropolished Ta foil.; Figure S2: Cross-sectional SEM of anodic tantalum oxide films grown at 20V180°C on (a) electropolished, (b) chemically etched, and (c) pristine substrates. Table S1: Quantitative oxidation-state fractions for XPS of pristine, chemically-etched, and electropolished samples.; Table S2: Pore sizes and wall thicknesses for films grown on chemically etched and electropolished substrates.

Author Contributions: H.X., S.E.P., C.K. and P.B. conceived and designed all experiments. S.E.P., C.K., M.B., T.M., G.C., S.F., K.K. and K.D. performed electropolishing and anodization. S.E.P. collected and analyzed SEM images. S.B.E. and J.A.R. performed AFM characterization. S.E.P. and S.B.E. performed XPS characterization, and S.E.P. and J.A.R. analyzed the data. J.O. performed adhesion testing utilizing equipment supplied by B.J. S.E.P. and H.X. drafted and revised the manuscript. All authors discussed the experimental results and coedited the manuscript.

Funding: This research was supported by the Department of Energy Office of Science, Basic Energy Sciences via award number DE-SC002648. S.P. acknowledges the support of the National Science Foundation (NSF) Graduate Research Fellowship Program (GRFP) (Grant No. 1946726) and the NSF Louis Stokes Alliance for Minority Participation (LSAMP) program, and gratefully acknowledges Dr. Elton Graugnard for use of the XPS in the Atomic Films Laboratory at Boise State University. T.M. and G.C. acknowledge support from ACS Project SEED. K.K. acknowledges support from NSF Award No. 1950305 (Boise State University, Materials for Society REU). This research utilized the AFM, XRD, and SEM instruments in the Boise State University FaCT Core Facility, RRID: SCR_024733, which receives support from the National Institutes of Health (NIH) under the Institutional Development Awards [IDeA] Program of the National Institute of General Medical Sciences (NIGMS) via Grants P20GM148321 and P20GM103408.

Institutional Review Board Statement: Not applicable.

Informed Consent Statement: Not applicable.

Data Availability Statement: The data that support the findings of this study are available from the corresponding authors on reasonable request.

Conflicts of Interest: The authors declare no conflict of interest.

Use of AI and AI-Assisted Technologies: No AI tools were utilized for this paper.

References

1. Momeni, M.M.; Mirhosseini, M.; Chavoshi, M.; Hakimizade, A. The Effect of Anodizing Voltage on Morphology and Photocatalytic Activity of Tantalum Oxide Nanostructure. *J. Mater. Sci. Mater. Electron.* **2016**, *27*, 3941–3947. https://doi.org/10.1007/s10854-015-4246-y.
2. Wang, W.; Yin, F.; Niu, H.; Li, Y.; Kim, E.S.; Kim, N.Y. Tantalum Pentoxide (Ta_2O_5 and Ta_2O_5-x)-Based Memristor for Photonic in-Memory Computing Application. *Nano Energy* **2023**, *106*, 108072. https://doi.org/10.1016/j.nanoen.2022.108072.
3. Li, J.; Jalbert, A.J.; Lee, S.; Simakas, L.S.; Geisler, N.J.; Watkins, V.J.; Cline, L.A.; Fuller, E.J.; Talin, A.A.; Li, Y. Nonvolatile Electrochemical Memory at 600 °C Enabled by Composition Phase Separation. *Device* **2025**, *3*, 100623. https://doi.org/10.1016/j.device.2024.100623.
4. Panda, D.; Hui, Y.-F.; Tseng, T.-Y. Diffusion Limiting Layer Induced Tantalum Oxide Based Memristor as Nociceptor. *Mater. Today Electron.* **2023**, *3*, 100031. https://doi.org/10.1016/j.mtelec.2023.100031.
5. Talin, A.A.; Li, Y.; Robinson, D.A.; Fuller, E.J.; Kumar, S. ECRAM Materials, Devices, Circuits and Architectures: A Perspective. *Adv. Mater.* **2023**, *35*, 2204771. https://doi.org/10.1002/adma.202204771.
6. Fialho, L.; Carvalho, S. Surface Engineering of Nanostructured Ta Surface with Incorporation of Osteoconductive Elements by Anodization. *Appl. Surf. Sci.* **2019**, *495*, 143573. https://doi.org/10.1016/j.apsusc.2019.143573.
7. Fialho, L.; Grenho, L.; Fernandes, M.H.; Carvalho, S. Porous Tantalum Oxide with Osteoconductive Elements and Antibacterial Core-Shell Nanoparticles: A New Generation of Materials for Dental Implants. *Mater. Sci. Eng. C* **2021**, *120*, 111761. https://doi.org/10.1016/j.msec.2020.111761.
8. Diamanti, M.V.; Pisoni, R.; Cologni, A.; Brenna, A.; Corinto, F.; Pedeferri, M. Anodic Oxidation as a Means to Produce Memristive Films. *J. Appl. Biomater. Funct. Mater.* **2016**, *14*, e290–e295. https://doi.org/10.5301/jabfm.5000290.

9. Dang, H.X.; Lin, Y.-M.; Klavetter, K.C.; Cell, T.H.; Heller, A.; Mullins, C.B. Lithium Insertion/Deinsertion Characteristics of Nanostructured Amorphous Tantalum Oxide Thin Films. *ChemElectroChem* **2014**, *1*, 158–164. https://doi.org/10.1002/celc.201300139.
10. Gonçalves, R.V.; Migowski, P.; Wender, H.; Eberhardt, D.; Weibel, D.E.; Sonaglio, F.C.; Zapata, M.J.M.; Dupont, J.; Feil, A.F.; Teixeira, S.R. Ta_2O_5 Nanotubes Obtained by Anodization: Effect of Thermal Treatment on the Photocatalytic Activity for Hydrogen Production. *J. Phys. Chem. C* **2012**, *116*, 14022–14030. https://doi.org/10.1021/jp303273q.
11. Su, Z.; Grigorescu, S.; Wang, L.; Lee, K.; Schmuki, P. Fast Fabrication of Ta_2O_5 Nanotube Arrays and Their Conversion to Ta3N5 for Efficient Solar Driven Water Splitting. *Electrochem. Commun.* **2015**, *50*, 15–19. https://doi.org/10.1016/j.elecom.2014.10.017.
12. Han, C.; Wang, T. Tantalum Pentoxide: From Crystal Structures to Applications in Water Splitting. *Energy Fuels* **2023**, *37*, 13624–13644. https://doi.org/10.1021/acs.energyfuels.3c02295.
13. Melody, B. The Non-Thickness-Limited Growth of Anodic Oxide Films on Valve Metals. *Electrochem. Solid-State Lett.* **1999**, *1*, 126. https://doi.org/10.1149/1.1390659.
14. Zhou, X.; Nguyen, N.T.; Özkan, S.; Schmuki, P. Anodic TiO_2 Nanotube Layers: Why Does Self-Organized Growth Occur—A Mini Review. *Electrochem. Commun.* **2014**, *46*, 157–162. https://doi.org/10.1016/j.elecom.2014.06.021.
15. Piotrowski, O.; Madore, C.; Landolt, D. Electropolishing of Tantalum in Sulfuric Acid–Methanol Electrolytes. *Electrochimica Acta* **1999**, *44*, 3389–3399. https://doi.org/10.1016/S0013-4686(99)00056-0.
16. Barnes, P.; Savva, A.; Dixon, K.; Bull, H.; Rill, L.; Karsann, D.; Croft, S.; Schimpf, J.; Xiong, H. Electropolishing Valve Metals with a Sulfuric Acid-Methanol Electrolyte at Low Temperature. *Surf. Coat. Technol.* **2018**, *347*, 150–156. https://doi.org/10.1016/j.surfcoat.2018.04.082.
17. Wu, M.T.; Leu, I.C.; Hon, M.H. Effect of Polishing Pretreatment on the Fabrication of Ordered Nanopore Arrays on Aluminum Foils by Anodization. *J. Vac. Sci. Technol. B Microelectron. Nanometer Struct. Process. Meas. Phenom.* **2002**, *20*, 776–782. https://doi.org/10.1116/1.1467657.
18. Rauf, A.; Mehmood, M.; Asim Rasheed, M.; Aslam, M. The Effects of Electropolishing on the Nanochannel Ordering of the Porous Anodic Alumina Prepared in Oxalic Acid. *J. Solid State Electrochem.* **2009**, *13*, 321–332. https://doi.org/10.1007/s10008-008-0550-2.
19. Lee, B.G.; Hong, S.-Y.; Yoo, J.E.; Choi, J. Electropolishing for the Formation of Anodic Nanotubular TiO2 with Uniform Length and Density. *Appl. Surf. Sci.* **2011**, *257*, 7190–7194. https://doi.org/10.1016/j.apsusc.2011.03.089.
20. Fialho, L.; Almeida Alves, C.F.; Marques, L.S.; Carvalho, S. Development of Stacked Porous Tantalum Oxide Layers by Anodization. *Appl. Surf. Sci.* **2020**, *511*, 145542. https://doi.org/10.1016/j.apsusc.2020.145542.
21. Singh, S.; Barden, W.R.T.; Kruse, P. Nanopatterning of Transition Metal Surfaces via Electrochemical Dimple Array Formation. *ACS Nano* **2008**, *2*, 2453–2464. https://doi.org/10.1021/nn8003789.
22. Shimizu, K.; Kobayashi, K.; Thompson, G.E.; Skeldon, P.; Wood, G.C. Anodic Oxide Films on Tantalum: Incorporation and Mobilities of Electrolyte-Derived Species. *Philos. Mag. B* **1996**, *73*, 461–485. https://doi.org/10.1080/13642819608239129.
23. Mohapatra, B.D.; Sulka, G.D. Review of Anodic Tantalum Oxide Nanostructures: From Morphological Design to Emerging Applications. *ACS Appl. Nano Mater.* **2024**, *7*, 13865–13892. https://doi.org/10.1021/acsanm.4c02000.
24. Ngadiman, N.L.S.; Abdul Rani, R.; Makhsin, S.R.; Ayub, M.A.; Aryani, D.; Zoolfakar, A.S. Properties and Application of Electrochemically Anodized Ta_2O_5 Nanostructures: A Review. *J. Mech. Eng.* **2022**, *11*, 1–48. https://doi.org/10.24191/jmeche.v11i1.23580.
25. Horwood, C.A.; El-Sayed, H.A.; Birss, V.I. Precise Electrochemical Prediction of Short Tantalum Oxide Nanotube Length. *Electrochimica Acta* **2014**, *132*, 91–97. https://doi.org/10.1016/j.electacta.2014.03.128.
26. Barton, J.E.; Stender, C.L.; Li, P.; Odom, T.W. Structural Control of Anodized Tantalum Oxide Nanotubes. *J. Mater. Chem.* **2009**, *19*, 4896–4898. https://doi.org/10.1039/B904964A.
27. El-Sayed, H.A.; Birss, V.I. Controlled Interconversion of Nanoarray of Ta Dimples and High Aspect Ratio Ta Oxide Nanotubes. *Nano Lett.* **2009**, *9*, 1350–1355. https://doi.org/10.1021/nl803010v.
28. Singh, S.; Festin, M.; Barden, W.R.T.; Xi, L.; Francis, J.T.; Kruse, P. Universal Method for the Fabrication of Detachable Ultrathin Films of Several Transition Metal Oxides. *ACS Nano* **2008**, *2*, 2363–2373
29. Gonçalves, R.V.; Wojcieszak, R.; Uberman, P.M.; Teixeira, S.R.; Rossi, L.M. Insights into the Active Surface Species Formed on Ta_2O_5 Nanotubes in the Catalytic Oxidation of CO. *Phys. Chem. Chem. Phys.* **2014**, *16*, 5755. https://doi.org/10.1039/c3cp54887b.
30. Almeida Alves, C.F.; Calderon, V.S.; Ferreira, P.J.; Marques, L.; Carvalho, S. Passivation and Dissolution Mechanisms in Ordered Anodic Tantalum Oxide Nanostructures. *Appl. Surf. Sci.* **2020**, *513*, 145575. https://doi.org/10.1016/j.apsusc.2020.145575.
31. Lee, K.; Schmuki, P. Highly Ordered Nanoporous Ta_2O_5 Formed by Anodization of Ta at High Temperatures in a Glycerol/Phosphate Electrolyte. *Electrochem. Commun.* **2011**, *13*, 542–545. https://doi.org/10.1016/j.elecom.2011.03.005.

32. Uslu, E.; Mimiroglu, D.; Ercan, B. Nanofeature Size and Morphology of Tantalum Oxide Surfaces Control Osteoblast Functions. *ACS Appl. Bio Mater.* **2021**, *4*, 780–794. https://doi.org/10.1021/acsabm.0c01354.
33. Sanz, J.M.; Hofmann, S. Auger Electron Spectroscopy and X-Ray Photoelectron Spectroscopy Studies of the Oxidation of Polycrystalline Tantalum and Niobium at Room Temperature and Low Oxygen Pressures. *J. Common Met.* **1983**, *92*, 317–327. https://doi.org/10.1016/0022-5088(83)90498-8.
34. *NIST X-ray Photoelectron Spectroscopy Database*, Version 5.0; NIST X-ray Photoelectron Spectroscopy Database (SRD 20); NIST: Washington, DC, USA, 2023. https://doi.org/10.18434/T4T88K.
35. Chakraborti, P.; Sharma, H.; Pulugurtha, M.R.; Gandhi, S.; Tummala, R.R. Oxide Composition Studies of Electrochemically Grown Tantalum Oxide on Sintered Tantalum Using XPS Depth-Profiling and Co-Relation with Leakage Properties. *J. Mater. Sci. Mater. Electron.* **2017**, *28*, 18773–18780. https://doi.org/10.1007/s10854-017-7826-1.
36. Khanuja, M.; Sharma, H.; Mehta, B.R.; Shivaprasad, S.M. XPS Depth-Profile of the Suboxide Distribution at the Native Oxide/Ta Interface. *J. Electron Spectrosc. Relat. Phenom.* **2009**, *169*, 41–45. https://doi.org/10.1016/j.elspec.2008.10.004.
37. Díaz, B.; Światowska, J.; Maurice, V.; Seyeux, A.; Härkönen, E.; Ritala, M.; Tervakangas, S.; Kolehmainen, J.; Marcus, P. Tantalum Oxide Nanocoatings Prepared by Atomic Layer and Filtered Cathodic Arc Deposition for Corrosion Protection of Steel: Comparative Surface and Electrochemical Analysis. *Electrochimica Acta* **2013**, *90*, 232–245. https://doi.org/10.1016/j.electacta.2012.12.007.
38. Macak, J.M.; Tsuchiya, H.; Ghicov, A.; Yasuda, K.; Hahn, R.; Bauer, S.; Schmuki, P. TiO_2 Nanotubes: Self-Organized Electrochemical Formation, Properties and Applications. *Curr. Opin. Solid State Mater. Sci.* **2007**, *11*, 3–18. https://doi.org/10.1016/j.cossms.2007.08.004.
39. Mor, G.K.; Varghese, O.K.; Paulose, M.; Shankar, K.; Grimes, C.A. A Review on Highly Ordered, Vertically Oriented TiO_2 Nanotube Arrays: Fabrication, Material Properties, and Solar Energy Applications. *Sol. Energy Mater. Sol. Cells* **2006**, *90*, 2011–2075. https://doi.org/10.1016/j.solmat.2006.04.007.
40. Ma, J.-W.; Zan, R.; Chen, W.-Z.; Ni, J.-H.; Zhang, X.-N. Cell Behaviors on Surface of Pure Tantalum with Nano-Dimpled Structure. *Rare Met.* **2019**, *38*, 543–551. https://doi.org/10.1007/s12598-019-01226-1.
41. Schmuki, P. Self-Organized Oxide Nanotube Layers on Titanium and Other Transition Metals. In *Electrochemistry at the Nanoscale*; Schmuki, P., Virtanen, S., Eds.; Springer: New York, NY, 2009; pp 435–466. https://doi.org/10.1007/978-0-387-73582-5_12.
42. El-Sayed, H.A.; Molero, H.M.; Birss, V.I. The Impact of Fabrication Conditions on the Quality of Au Nanoparticle Arrays on Dimpled Ta Templates. *Nanotechnology* **2012**, *23*, 435602. https://doi.org/10.1088/0957-4484/23/43/435602.
43. Ding, Z.; Tang, Y.; Liu, L.; Ding, Z.; Tan, Y.; He, Q. Improving the Adhesive, Mechanical, Tribological Properties and Corrosion Resistance of Reactive Sputtered Tantalum Oxide Coating on Ti6Al4V Alloy via Introducing Multiple Interlayers. *Ceram. Int.* **2022**, *48*, 5983–5994. https://doi.org/10.1016/j.ceramint.2021.11.134.
44. Hogmark, S.; Jacobson, S.; Larsson, M. Design and Evaluation of Tribological Coatings. *Wear* **2000**, *246*, 20–33. https://doi.org/10.1016/S0043-1648(00)00505-6.
45. Li, P.; Li, C.; Zhang, Z.; Zhu, X.; Song, Y. Anodic Oxide Films Grown in Dehydrated Phosphate/Glycerol Electrolytes at High Temperatures. *Langmuir* **2024**, *40*, 25758–25771. https://doi.org/10.1021/acs.langmuir.4c03777.
46. Tsuji, E.; Matsuura, S.; Aoki, Y.; Habazaki, H. Diffusion-Controlled Growth of TiO_2 Mesoporous Anodic Films in Hot Phosphate/Glycerol Electrolytes. *Electrochemistry* **2018**, *86*, 184–189. https://doi.org/10.5796/electrochemistry.18-00005.
47. Singh, S.; Greiner, M.T.; Kruse, P. Robust Inorganic Membranes from Detachable Ultrathin Tantalum Oxide Films. *Nano Lett.* **2007**, *7*, 2676–2683. https://doi.org/10.1021/nl071061z.
48. *ASTM D4541-22*; Standard Test Method for Pull-Off Strength of Coatings Using Portable Adhesion Testers. ASTM: West Conshohocken, PA, USA, 2026.
49. Choo, Y.H.; Devereux, O.F. Mechanical Failure of Anodic Films on Aluminum and Tantalum. *J. Electrochem. Soc.* **1976**, *123*, 1868. https://doi.org/10.1149/1.2132714.

Materials and Interfaces

Scilight

Article

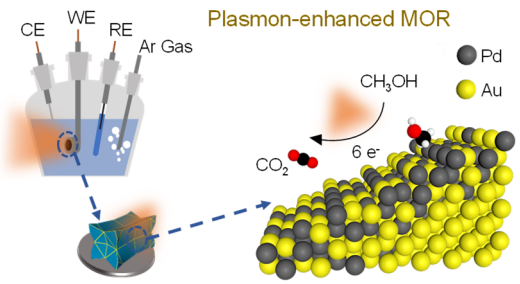
Check for updates

Structurally Modulated AuPd Alloy Nanorods for Plasmon-Promoted Methanol Electrooxidation

Zixu Wang [1,†], Guoxin Cao [1,†], Guizeng Yang [1], Lichao Sun [1,2,3,*], Vladimir Bochenkov [4,*], and Qingfeng Zhang [1,*]

[1] Hubei Key Laboratory of Electrochemical Power Sources, College of Chemistry and Molecular Sciences, Wuhan University, Wuhan 430072, China
[2] National Key Laboratory of New Textile Materials and Advanced Processing Technologies, School of Biomedical Engineering and Health, Wuhan Textile University, Wuhan 430200, China
[3] Suzhou Institute of Wuhan University, Suzhou 215123, China
[4] Department of Chemistry, Lomonosov Moscow State University, 119234 Moscow, Russia
* Correspondence: lichaosun@whu.edu.cn (L.S.); boch@kinet.chem.msu.ru (V.B.); zhangqf@whu.edu.cn (Q.Z.)
† These authors contributed equally to this work.
Received: 14 July 2026; Revised: 17 August 2026; Accepted: 3 September 2026; Published: 10 September 2026

Abstract: The spatial arrangement of plasmonic metals relative to catalytically active components directly governs the coupling efficiency between hot carriers and the local electromagnetic field at the catalytic interface, thereby profoundly affecting the activity and selectivity of plasmon-enhanced electrocatalytic reactions. However, relying solely on a catalytic metal as the dominant surface species often results in significant plasmon damping. At the same time, synergistically optimizing plasmonic enhancement and intrinsic catalytic activity through precise control of the composition, facets, and thickness of bimetallic alloys remains a major challenge in synthesis and structural design. In this study, Au@Au_xPd_y alloy core-shell nanorods with tunable shell composition and thickness were constructed, achieving a balance between plasmonic enhancement and intrinsic catalytic activity toward the methanol oxidation reaction (MOR). Through a combination of experimental observations, single-particle dark-field scattering spectroscopy, and numerical simulations, the alloy-shell-dependent extinction characteristics and their correlation with the plasmonic enhancement effect were elucidated. Under light irradiation, the optimal Au@Au_5Pd_5 nanorods show a 1.88-fold enhancement in current density for MOR. The as-designed bimetallic nanocatalysts can also be used as active substrates for *in situ* Raman spectroscopic studies of MOR. This work provides important insights for designing bimetallic nanostructures that integrate efficient plasmonic enhancement with high catalytic activity for plasmon-promoted catalysis.



Keywords: plasmonics; bimetallic nanoparticles; Au-Pd alloy; plasmon-enhanced electrocatalysis; methanol oxidation reaction

1. Introduction

Facing the dual pressures of global energy scarcity and environmental degradation, the development of efficient and stable catalytic systems for clean energy conversion has become a critical direction in scientific research [1–3]. Metal-based nanomaterials, owing to their unique physicochemical properties, exhibit broad application prospects in numerous catalytic reactions [4–10]. Through precise regulation of the morphology, facets, and composition of metal nanomaterials, researchers have significantly enhanced their catalytic performance [11–14]. Among these strategies, alloying two or more different metals can effectively integrate the advantages of each component, yielding catalytic behavior superior to that of single metals [15–18]. However, relying solely on compositional and structural optimization still struggles to overcome the intrinsic activity limits of catalysts, prompting researchers to explore strategies that introduce external energy, such as light, to further promote catalytic reactions.

Copyright: © 2026 by the authors. This is an open access article under the terms and conditions of the Creative Commons Attribution (CC BY) license (https://creativecommons.org/licenses/by/4.0/).
Publisher's Note: Scilight stays neutral with regard to jurisdictional claims in published maps and institutional affiliations.

Among various external energy sources, solar energy is highly attractive due to its renewability and abundance [19–22]. Plasmonic metal nanoparticles (NPs), leveraging their localized surface plasmon resonance (LSPR) characteristics, can interact strongly with visible light, thereby converting light energy into chemical energy efficiently [23–29]. Studies have shown that incorporating plasmonic metals into conventional catalytic systems significantly enhances the catalytic efficiency of various reactions, including hydrogen evolution, oxygen evolution, methanol oxidation, and oxygen reduction, under light irradiation [30–34]. The enhancement is primarily attributed to the hot carriers generated upon LSPR excitation, and these high-energy electrons or holes can effectively lower reaction barriers and accelerate reaction kinetics [35–40]. Nevertheless, despite substantial progress in plasmon-assisted catalysis, the full integration of plasmonic functionality and electrocatalytic functionality at the nanoscale design remains a challenge.

To integrate plasmonic and catalytic functions, bimetallic nanostructures represent an important design strategy [11,41]. Forming an alloy between a plasmonic metal like Au and a catalytic metal like Pd offers the prospect of simultaneously introducing light absorption capability and catalytically active sites within a single nanoparticle [42–45]. However, conventional alloy structures face a significant dilemma. If the proportion of the plasmonic metal is too low, the LSPR effect is weak, and light utilization becomes insufficient. Conversely, if the catalytic metal content is too low, the intrinsic catalytic activity fails to meet the requirements [46–49]. Moreover, the atomic arrangement, facet structure, and particle size and thickness of the different metals in the alloy all exert complex influences on both plasmonic properties and catalytic performance [50–52]. Indeed, systematically tuning the composition, facets, and thickness of bimetallic nanostructures, and thereby optimizing the alloy composition and morphology design, holds promise for greatly improving light utilization efficiency and generating a significant synergistic effect between plasmonic and electrocatalytic functions [53]. However, complex heterogeneous alloy structures are not only difficult to synthesize but also challenging to model clearly for studying their plasmonic properties, which poses numerous obstacles to the implementation of the above regulation strategies.

In this work, we demonstrate a synthetic strategy that incorporates plasmonic components into the catalytic shell, substantially alleviating the LSPR damping induced by Pd and overcoming the limitations of existing plasmonic alloy catalysts. Specifically, we synthesized a series of Au@Au_xPd_y alloy core-shell bimetallic nanorods (NRs). By precisely controlling the synthetic parameters, we were able to continuously and controllably tune the AuPd alloy shell from high-index to low-index facets, thus achieving an optimal balance between catalytic performance and plasmonic enhancement. Using the methanol oxidation reaction (MOR) as a model electrochemical reaction, the Au@Au_5Pd_5 NRs exhibited a 1.88-fold increase in peak current under light irradiation. With the appropriate addition of Ag, the plasmon-promoted catalytic performance could be further enhanced. Through combined single-particle spectroscopy, numerical simulations, and *in situ* surface-enhanced Raman spectroscopy (SERS), we show the advantages of the alloy shell in tuning plasmonic characteristics as well as spectroscopically monitoring intermediate species during the MOR. This work creates a framework for designing bimetallic nanostructures that integrate efficient plasmonic enhancement with high MOR catalytic activity.

2. Material and Methods

2.1. Chemicals and Materials

Gold (III) chloride trihydrate ($HAuCl_4 \cdot 3H_2O$, 99%), sodium borohydride ($NaBH_4$, 99%), and L-ascorbic acid (AA, 99.9%) were obtained from Sigma-Aldrich (St. Louis, MO, USA). Palladium (II) chloride ($PdCl_2$, 99%), methanol (CH_3OH, 99.9%), and anhydrous potassium hydroxide (KOH, granular) were purchased from Sinopharm Chemical Reagent Co., Ltd. (Shanghai, China). Silver nitrate ($AgNO_3$, 99.9995% metals basis) was obtained from Alfa Aesar (Tewksbury, MA, USA). Cetyltrimethylammonium bromide (CTAB, >98%) and sodium oleate (NaOL, >97%) were purchased from Tokyo Chemical Industry Co., Ltd. (Tokyo, Japan). HCl (37 wt% in water, 12.1 M) was purchased from Fisher Scientific (Pittsburgh, PA, USA). All reagents were used as received without further purification. Millipore ultrapure water (18.2 MΩ resistivity) was used for all experiments.

2.2. Synthesis of Au NRs

Au NRs were synthesized using a previously published seed-mediated growth protocol with minor modifications (see more details in Supporting Information) [11]. The Au seeds were prepared by reducing $HAuCl_4$ with $NaBH_4$ in the presence of CTAB. The seed solution was stirred for 2 min and then left undisturbed for 30 min before use. The growth solution was prepared by reducing $HAuCl_4$ with AA in the presence of CTAB, NaOL, and $AgNO_3$, followed by the addition of Au seeds to grow Au NRs. The resulting particles were collected by centrifugation, followed by removal of the supernatant, and finally redispersed in 30 mL of 100 mM CTAB.

2.3. Synthesis of Au@Au$_x$Pd$_y$ and Au@Au$_x$Pd$_y$Ag$_n$ Core-Shell NRs

Au@Au$_x$Pd$_y$ core-shell NRs with different structures were prepared through overgrowth of the Au NRs in the presence of $HAuCl_4$, $PdCl_2$, CTAB, and AA, following previously published work with some modifications (see more details in Supporting Information) [11].The synthesis method for adding Ag to the shell is generally the same, except that the corresponding proportion of $AgNO_3$ is added to the growth solution. The resulting core-shell NRs were washed twice with water through centrifugation/redispersion cycles and finally redispersed in 200 μL of 20 mM CTAB.

2.4. Characterizations

The optical extinction spectra of the nanoparticles were measured on aqueous colloidal suspensions at room temperature using a Shimadzu UV-2600i spectrophotometer. The morphologies and structures of the nanoparticles were characterized by scanning electron microscopy (SEM) using a Zeiss Merlin Compact and a Zeiss GeminiSEM 500 field emission scanning electron microscope (Carl Zeiss AG, Oberkochen, Germany). The samples for SEM were dispersed in water and drop-dried on silicon wafers. Transmission electron microscopy (TEM) images and EDS elemental maps were obtained using a JEOL JEM-2100 Plus transmission electron microscope (JEOL Ltd., Tokyo, Japan) operated at an accelerating voltage of 200 kV. All samples for TEM measurements were dispersed in water and drop-dried on 300 mesh Formvar/carbon-coated Cu grids.

2.5. Plasmon-Enhanced MOR Measurements

MOR tests were performed in a highly transparent quartz electrolytic cell with a CHI-760e electrochemical analyzer (Austin, TX, USA) using a three-electrode cell system. The three-electrode cell consisted of a glassy carbon electrode (GCE, 3 mm diameter) with a catalyst, a graphite rod, and a Hg/HgO electrode (in 1 M KOH), which served as the working, counter, and reference electrodes, respectively. The MOR test was carried out in 1 M KOH + 0.5 M methanol solution by applying 0 V to 1.2 V vs. RHE at a scan rate of 50 mV s^{-1}. Plasmon-enhanced tests were performed by illuminating the center of the GCE with an Xe lamp (350 W) from the side of the cell and then starting the CV test. The incident light power density was measured to be 127.39 mW/cm^2 using a power meter. Thus, the incident photon-to-current conversion efficiency (*IPCE*) was calculated based on the following equation [54]:

$$IPCE = 1239.8 \times \frac{J_p}{\lambda \cdot P_L} \quad (1)$$

where J_p is the photocurrent density (mA/cm^2), λ is the incident light wavelength (nm), and P_L is the light power density at the corresponding wavelength (mW/cm^2).

2.6. Single-Particle Dark-field Scattering (DFS) Measurements

Single-particle DFS measurements were conducted on a home-built dark-field microscope based on an inverted microscope body (Zeiss AxioObserver ml, Carl Zeiss AG, Oberkochen, Germany) with a hyperspectral detection system [55]. Light generated from a tungsten-halogen lamp and filtered through a visible band-pass filter (500–800 nm, LBTEK, MEFH10-800SP) was circularly polarized and directed through an oil-immersion dark-field condenser (Carl Zeiss AG, Oberkochen, Germany, numerical aperture (NA) = 1.4) to create annular symmetric excitation with an incident angle of 69°, resulting in a total internal reflection (TIR) excitation condition for NPs deposited onto an indexed ITO glass substrate. The annular symmetric excitation geometry effectively eliminates the effects of extrinsic chirality. The scattered light was collected with a 50× air-spaced objective (Carl Zeiss AG, Oberkochen, Germany, NA = 0.8) and passed to a hyperspectral detection system consisting of an imaging spectrograph with a slit aperture (SpectraPro 2156, Teledyne Princeton Instruments, Acton, MA, USA) coupled to a thermoelectrically cooled back-illuminated CCD camera (Pixis 400BR, Teledyne Princeton Instruments, Acton, MA, USA) and mounted on a computer-controlled translation stage (LTA-HL, Newport Corporation, Irvine, CA, USA).

2.7. Numerical Simulations

Simulations of the far-field and near-field optical properties of Au NRs, Au@AuPd NR, and Au@Pd NRs were performed using the finite-difference time-domain (FDTD) method (Lumerical). The geometric models of Au NRs, Au@AuPd NR, and Au@Pd NRs were constructed based on orientation-dependent SEM and TEM images. The dielectric permittivity tabulated by Johnson and Christy was used for Au and Pd [56], and water was used as a background with a refractive index of 1.33. For the Au-Pd alloys, the composition-dependent dielectric

function reported by Stofela et al. was adopted [57]. The minimum mesh size was set to 1 nm to guarantee the convergence of the calculations.

2.8. In situ Surface-Enhanced Raman Scattering (SERS) Measurements

SERS was measured with an XploRA PLUS spectrometer (HORIBA, Ltd., Kyoto, Japan) with an excitation wavelength of 638 nm. The power of the excitation laser that focused on the samples was adjusted using a 1% neutral density filter. A 50× objective lens (N.A. = 0.5) and a holographic grating of 600 grooves/mm with a 5 s acquisition time were used for data collection unless mentioned otherwise. The Raman spectrometer was calibrated using a standard silicon wafer before measurements. For the *in-situ* electrochemical SERS measurements of MOR intermediates, a three-electrode cell system was also employed. The sample was drop-cast onto a custom-made platinum-carbon electrode surface as the work electrode. A platinum wire and a saturated calomel electrode (SCE) were employed as the counter electrode and reference electrode, respectively.

3. Results and Discussions

Au@Au_xPd_y NRs represent a class of bimetallic functional materials that integrate Au with strong LSPR and Pd with excellent electrocatalytic activity at the nanoscale, enabling efficient light harvesting across a broad visible-NIR spectral range while retaining the high intrinsic catalytic activity of Pd for catalytic reactions [58–60]. Since both the plasmonic effect and catalytic performance of the alloy are governed by its composition, we systematically varied the Au/Pd ratio in the shell over a wide range to balance plasmonic enhancement and catalytic activity. In this study, the Au@Au_xPd_y NRs (*x* and *y* are used to show the estimated ratio of Au/Pd in the alloy shell) were synthesized via overgrowth on the Au NRs (see Figure S1A in Supporting Information) reported previously [11], and under the same conditions, we also synthesized Pd nanosheets (Pd NSs) without adding Au NRs as a control (Figure S1B). As shown in Figure 1A, when only a small amount of Pd precursor ($[H_2PdCl_4]/[HAuCl_4]$ = 2:8) was added during the synthesis, elongated hexoctahedral (ETOH) NRs were formed. As the proportion of Pd precursor increased ($[H_2PdCl_4]/[HAuCl_4]$ = 5:5), truncated concave cuboidal (TCCB) NRs were formed. When the $[H_2PdCl_4]/[HAuCl_4]$ ratio was further increased (($[H_2PdCl_4]/[HAuCl_4]$ = 8:2), the high-index-faceted TCCB NRs gradually transformed into low-index-faceted quasi-cuboidal (QCB) NRs. The structural evolution of these morphologies has been reported in previous work [11], and the SEM images of Au NRs, Au@Au_8Pd_2 NRs, Au@Au_5Pd_5 NRs, and Au@Au_2Pd_8 NRs in Figure 1B confirm the structural features described above. The HAADF-STEM image in Figure 1C reveals the TCCB morphology of Au@Au_5Pd_5 NRs, and the EDS mappings clearly confirm their core-shell structure with an AuPd alloy shell.

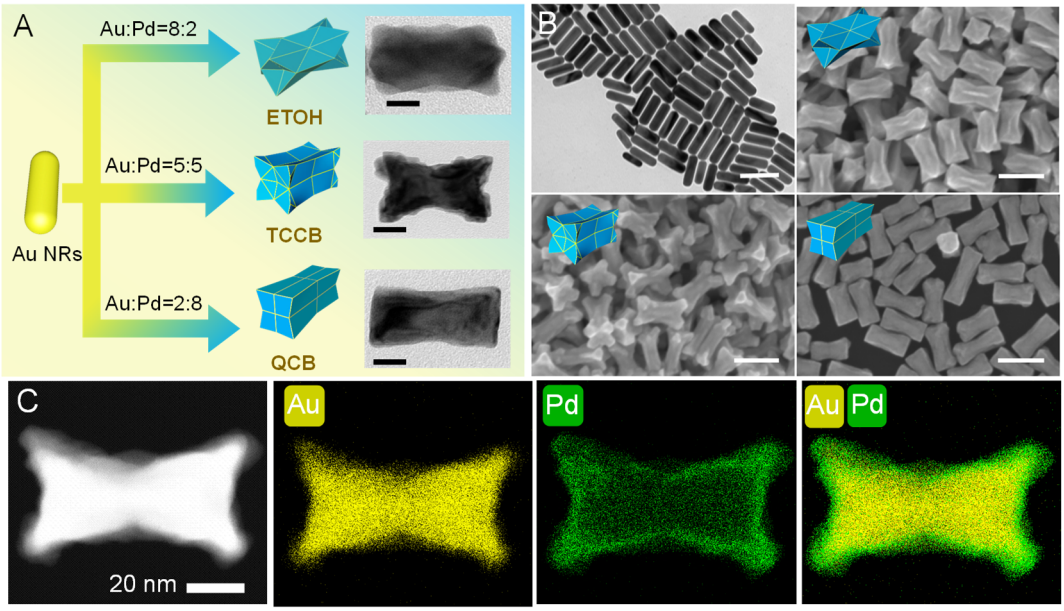


Figure 1. Structurally Modulated AuPd Alloy NRs. (**A**) Schematic illustration of the geometric and compositional control of AuPd alloy NRs by tuning the ratio between Au and Pd precursors. Insets: corresponding TEM images. Scale bars: 20 nm. (**B**) SEM images of Au NRs, ETOH NRs, TCCB NRs, and QCB NRs. Scale bars: 100 nm. (**C**) HAADF-STEM image and EDS elemental mapping of individual Au@Au_5Pd_5 TCCB NRs.

Photoelectrocatalytic measurements were conducted using a typical three-electrode system in a highly transparent quartz electrolytic cell, as shown in Figure 2A. In this system, a power-adjustable xenon lamp illuminated the L-shaped glassy carbon electrode from the side to achieve plasmonic enhancement of methanol electrooxidation. Numerous studies have demonstrated that Au exhibits LSPR under light illumination, generating hot carriers, whereas Pd does not [32]. To verify the plasmonic enhancement effect on MOR, electrochemical tests were performed on Au@Au_5Pd_5 NRs, Pd NSs, and Au NRs before and after light exposure, respectively. As shown in Figure 2B, the oxidation current of Au@Au_5Pd_5 NRs was significantly enhanced after illumination (from 1.71 mA/cm^2 to 3.23 mA/cm^2 at 0.79 V vs. RHE). In contrast, the MOR current of Pd NSs was hardly enhanced, and the enhancement of Au NRs was minimal. This can be explained by the fact that Pd exhibits weak LSPR and therefore cannot effectively promote MOR. For Au, the reaction current indicates that it is not an ideal MOR catalyst (only 0.059 mA/cm^2 at 0.79 V vs. RHE), and thus its contribution to the MOR current is negligible, even though it can generate hot carriers under illumination. The above results demonstrate that combining a plasmonic metal with a catalytically active metal enables effective utilization of LSPR to enhance electrocatalytic performance.

The MOR activities of the three representative nanostructures were evaluated both in darkness and under light illumination (Figure 2C). For Au@Au_8Pd_2 NRs and Au@Au_5Pd_5 NRs, the MOR peak currents (1.64 mA/cm^2 at 0.81 V vs. RHE and 1.71 mA/cm^2 at 0.79 V vs. RHE, respectively) are higher than that of Au@Au_2Pd_8 NRs (1.18 mA/cm^2 at 0.78 V vs. RHE), which can be attributed to the high-index facets of the ETOH and TCCB structures that are believed to provide highly active catalytic sites [11]. Under light illumination, the MOR current of Au@Au_5Pd_5 NRs increased significantly to 3.23 mA/cm^2, which is higher than that of Au@Au_8Pd_2 NRs (2.55 mA/cm^2). For Au@Au_2Pd_8 NRs, the MOR current increased from 1.18 to 1.88 mA/cm^2. Notably, Au@Au_5Pd_5 NRs exhibit the best enhancement effect for MOR. We also performed MOR enhancement tests on various other catalysts with different AuPd shell compositions (Figure S2). To compare catalytic performance more accurately, we normalized the currents by the real electrochemical surface areas (A_{real}), as the compositions differ. The A_{real} values were calculated from cyclic voltammetry (CV) curves measured in 1 M KOH aqueous solution saturated with Ar (see Figure S3 for details). The PdO reduction peaks for all samples exhibit complete and well-shaped profiles, with stable peak positions and no significant peak distortion or severe deterioration of the signal-to-noise ratio as the Pd content decreases. The normalized currents of each catalyst were summarized in Figure 2D. Overall, the catalytic activities of these catalysts in darkness can be roughly divided into three groups according to their geometric structures, which are related to their compositions. Au@Au_6Pd_4, Au@Au_5Pd_5, and Au@Au_4Pd_6 NRs share a similar TCCB structure and exhibit the best intrinsic MOR activity owing to their high-index facets and appropriate AuPd ratios [11]. By contrast, Au@Au_9Pd_1, Au@Au_8Pd_2, and Au@Au_7Pd_3 NRs, the three catalysts with an ETOH structure, possess even more abundant high-index facets. However, due to their low Pd content, there are insufficient reaction sites, resulting in slightly lower activity. As for the other catalysts with a high Pd content, their MOR performance is the poorest, which may be attributed to their low-index facet structure and the weak electron modulation effect arising from the small amount of Au. Nevertheless, their MOR performance changed markedly after light irradiation.

To directly evaluate the plasmonic enhancement effect of different structures on MOR, we defined the ratio of the peak current after illumination to that before illumination as the enhancement factor (EF). As shown in Figure 2E, the EF values of different catalysts exhibit a volcano-shaped relationship. The closer the Au/Pd ratio, the better the plasmonic enhancement effect on MOR. We attribute this phenomenon to the matching between the hot carrier donor and acceptor. Specifically, when Au is the majority component in the alloy shell, the LSPR is very strong, and abundant hot holes are generated upon illumination. However, owing to the lack of Pd catalytic sites, these hot holes cannot be effectively utilized. Conversely, an excessively high Pd content weakens the LSPR and fails to generate sufficient hot holes to promote the MOR, which is in line with recent observations [52]. A schematic illustration of the methanol oxidation process driven by hot carriers generated via the plasmonic effect is shown in Figure S4. Additionally, in the alkaline MOR system, photogenerated hot electrons are mainly dissipated via external circuit extraction, recombination with hot holes, and the hydrogen evolution reaction (HER). While we proposed that the hot holes were mainly used for the oxidation of methanol, while the hot electrons could be transferred to reduce H_2O to form H_2, the underlying mechanisms could be much more complicated and require further scrutiny. We also quantitatively evaluated the incident photon-to-current conversion efficiency (IPCE) of materials. The calculation was performed on the Au@Au_5Pd_5 sample under 750 nm monochromatic light excitation. The photocurrent density, taken as the difference between the light and dark CV curves at the oxidation peak potential, was ~1.71 mA/cm^2, and the incident light power density was measured to be 127.39 mW/cm^2. The IPCE value was determined to be approximately 2.21%. This value falls within a reasonable range for complex multi-electron reaction systems in photoelectrocatalysis, confirming that plasmon-generated hot carriers indeed participate effectively in the MOR.

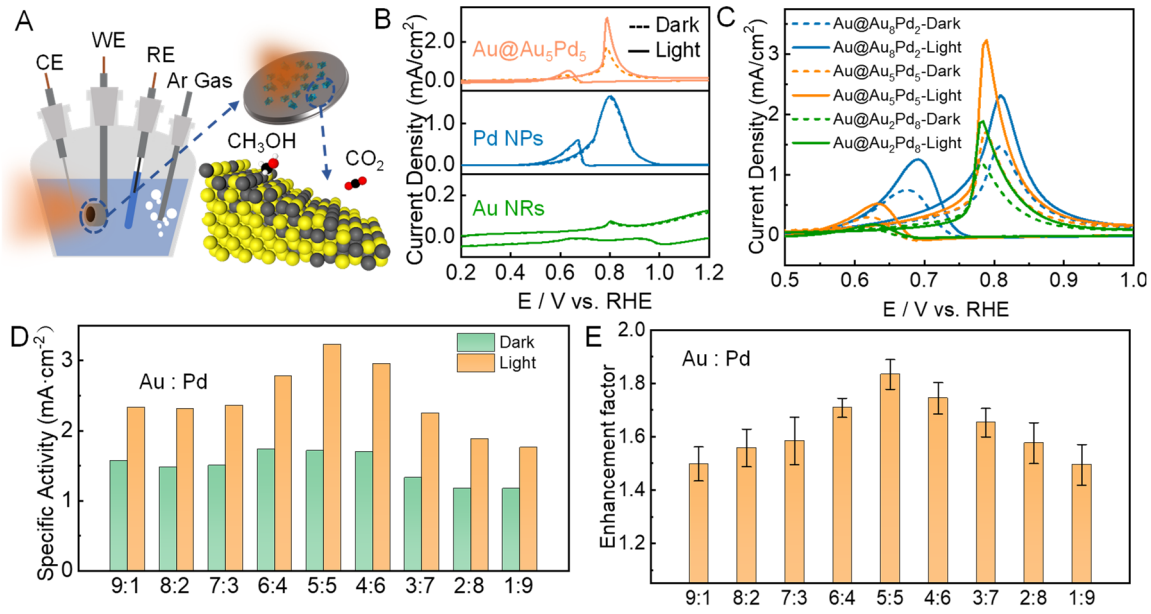


Figure 2. Plasmon-promoted MOR on Au@Au$_x$Pd$_y$ alloy NRs. (**A**) Schematic of the electrochemical reaction cell, atomic model of the catalyst, and MOR reaction diagram. (**B**) MOR curves of Au@Au$_5$Pd$_5$ NRs, Pd NSs, and Au NRs obtained in 1 M KOH + 0.5 M methanol at a scan rate of 50 mV s^{-1} under darkness (dashed lines) and light illumination (solid lines). (**C**) MOR curves of Au@Au$_8$Pd$_2$, Au@Au$_5$Pd$_5$, and Au@Au$_2$Pd$_8$ NRs representing ETOH, TCCB, and QCB structures, respectively. The test was performed in 1 M KOH + 0.5 M methanol at a scan rate of 50 mV s^{-1} under darkness (dashed lines) and light illumination (solid lines). (**D**) Comparison of the specific activities of catalysts with different Au/Pd ratios before and after illumination. The specific activity was calculated by normalizing the current by the area of each catalyst. (**E**) The plasmonic enhancement factor (EF) of each catalyst as a function of different Au/Pd ratios. The EF was calculated as the ratio of the MOR peak current after light illumination to that before light illumination.

From the above studies, we have identified the optimal conditions for synthesizing Au@Au$_x$Pd$_y$ core-shell NRs with the best plasmonic enhancement effect. However, one issue still exists: variations in the Au/Pd ratio occurred simultaneously with facet transformation, and we have previously discussed how facet evolution affects MOR performance. In addition, it is difficult to evaluate whether different facet structures affect the plasmonic enhancement of electrocatalysis. To investigate this issue, we synthesized a series of Au@Au$_x$Pd$_y$ NRs with the same Au/Pd ratio but different geometric structures by controlling the reaction conditions (Figure 3). As shown in Figure 3A, when the Au/Pd ratio was fixed at 1:1, the catalyst gradually evolves from TCB NRs to quasi-cuboidal (QCB) NRs, and eventually to TCCB NRs (denoted as Au$_5$Pd$_5$-1, Au$_5$Pd$_5$-2, and Au$_5$Pd$_5$-3, respectively) with increasing AA concentration. The extinction spectra of these catalysts are changed, indicating the geometry-dependent LSPR (Figure S5). As shown in Figure 3B, their MOR performance in darkness differs, and this trend is maintained after light illumination. However, the MOR test results in Figure 3C indicate that their EFs are very similar. Although slight differences exist, they are negligible compared to the significant changes observed in Figure 2E. This indicates that different facet structures have little influence on the EF. Meanwhile, the intrinsic activity of the catalyst could be regulated by designing the geometric structure. We further performed controlled experiments with the Au/Pd ratio fixed at 8:2 and 2:8, and similar results were obtained (Figure S6). In addition, by appropriately adjusting the AA and CTAB concentrations, TCB NRs with different Au/Pd ratios can also be obtained (Figure 3D). In this way, we can focus solely on the effect of the Au/Pd alloy composition on plasmonic enhancement. The extinction spectra confirm the continuous and controllable structural evolution of the synthesized TCB shell. In addition, SEM characterization reveals that the as-prepared nanoparticles exhibit uniform morphology and good reproducibility (Figure S5). Figure 3E shows the MOR enhancement ratios of this series of catalysts, and the results still exhibit a volcano-shaped relationship, similar to the trend observed in Figure 2E. Based on the above results, we can draw two conclusions. First, the intrinsic activity of the alloy can be effectively improved by tuning the facets, whereas the effect on plasmonic enhancement is negligible. Second, the proportion of the plasmonic metal in the alloy is the main factor determining the enhancement effect of MOR.

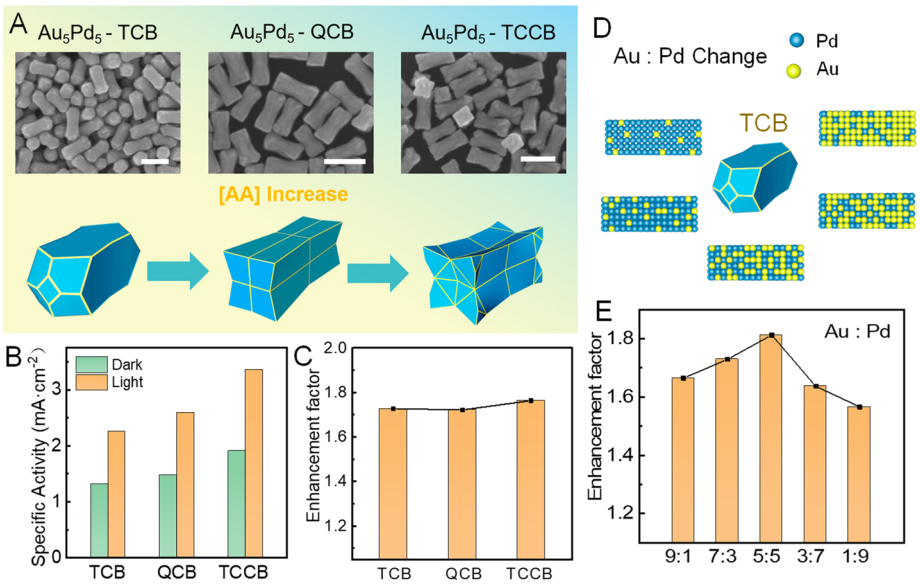


Figure 3. Impact of surface structure and alloy composition of Au@Au$_x$Pd$_y$ NRs on plasmon-promoted MOR. (**A**) Schematic illustration of the facet transformation and corresponding SEM images of Au@Au$_5$Pd$_5$ NRs into TCB, QCB, and TCCB structures with the same Au/Pd compositional ratios. The reactions were carried out in the presence of 40 mM CTAB and increasing concentrations of AA at a [H_2PdCl_4]/[$HAuCl_4$] molar ratio of 1:1. Scale bar: 100 nm. (**B**,**C**) Comparison of the (**B**) specific activity and (**C**) EFs of Au@Au$_5$Pd$_5$ NRs with TCB, QCB, and TCCB structures before and after light illumination. (**D**) Schematic illustration of the adjustment of the Au/Pd alloy ratio with a fixed TCB structure. The reactions were carried out in the presence of 20 mM CTAB, 10 mM AA, and various [H_2PdCl_4]/[$HAuCl_4$] molar ratios with the total concentration of H_2PdCl_4 + $HAuCl_4$ fixed at 0.4 mM. (**E**) EFs of TCB NRs with different [H_2PdCl_4]/[$HAuCl_4$] molar ratios.

Although similar core-shell nanostructures have been reported for plasmonic-enhanced electrocatalysis, their synthesis often requires careful control of the shell thickness, because an increase in shell thickness causes exponential attenuation of the properties of the plasmonic properties of the core metal. Interestingly, when plasmonic metals were incorporated into the shell, the catalysts overcame this limitation to some extent. We speculate that with Au incorporated into the shell, the plasmonic metal in the shell can co-generate LSPR with the internal Au NRs as an integrated whole under illumination. This greatly alleviates the LSPR damping induced by Pd. Meanwhile, alloying Au with Pd induces hybridization of the Au d-band, which activates interband transitions in the near-IR region and thereby generates additional high-energy hot holes. Also, the interplay between interband and intraband excitations can be manipulated by varying the alloy compositions, which could also contribute to the effect of plasmon-enhanced MOR [57,61]. In addition, the Au atoms in the shell are randomly dispersed around the Pd atoms, which can be regarded as forming hot carrier transfer channels. In this way, the hot carriers can efficiently participate in the catalytic reaction. Therefore, plasmon-enhanced MOR, in this case, can be attributed to the balance between plasmonic hot carrier generation and interband/intraband transition contributions. To confirm this hypothesis, we synthesized Au@Au$_5$Pd$_5$ NRs with different shell thicknesses by controlling the concentration of the metal precursors. The TEM images in Figure S7A clearly show the variation in shell thickness. In addition, we synthesized Au@Pd NRs with only Pd in the shell as a control. With increasing Pd precursor concentration, Pd grows into a cuboidal shape along the Au NRs (Figure S7C). From the EDS mapping images in Figure S8, the Au NR core can be clearly distinguished from the Pd shell, which is markedly different from the alloyed Au@Au$_5$Pd$_5$ NRs (Figure 1C). When tested under the same conditions, the EF values for MOR before and after light illumination were obtained (Figure S7B). It can be seen that the MOR enhancement effect decreases with increasing shell thickness, but the attenuation trend is very gradual. In contrast, the EF of the pure Pd-coated catalyst decreases rapidly with increasing shell thickness (Figure S7D). The shell thickening may alter particle dimensions and LSPR properties, but the aspect-ratio change is modest, and the EF was measured under broadband Xe lamp illumination, where minor LSPR shifts remain within the effective spectral coverage. Therefore, the size effect contributes minimally to EF variation. Furthermore, we fixed the Au/Pd ratio in the shell at 8:2 and 2:8, and investigated the influence of shell thickness on LSPR for these compositions. As expected, the higher the proportion of Au in the shell, the smaller the effect of thickness variation on the MOR enhancement (Figure S9). The above experimental results provide strong evidence for our initial hypothesis that incorporating plasmonic

metals into the shell can help preserve the LSPR effect of the inner Au core. This greatly simplifies the design of core-shell catalysts with LSPR properties.

We further introduced a second plasmonic metal (Ag) into the alloy to improve the plasmonic enhancement of MOR (Figure 4). Again, we continued to use the seed-mediated method, but added $AgNO_3$ in an appropriate proportion to the synthesis of $Au@Au_5Pd_5$ NRs. From the SEM image in Figure 4A,B, the $Au@Au_5Pd_5Ag_1$ structure is close to that of TCB with a highly rough surface. This change is also reflected in their extinction spectra (Figure S10), where three peaks are observed for $Au@Au_5Pd_5Ag_{0.5}$, located around 780, 540, and 400 nm, respectively. When the Ag content increased, the peak at 780 nm blue-shifted to 730 nm, while the other two peaks showed no significant change. As the Ag content continued to increase, the peaks around 540 and 730 nm disappeared and were replaced by a new peak around 560 nm. This phenomenon is accompanied by the precipitation of small Ag NPs on the catalyst surface, giving rise to complex spectral coupling behavior. When the catalyst composition reached $Au@Au_5Pd_5Ag_3$, the peak near 400 nm also became weaker, and eventually the coupled peak red-shifted to around 590 nm. The addition of Ag brings substantial changes to the optical properties of the entire system, which inspires us to further investigate their performance in plasmon-promoted MOR. In Figure 4D, we compared the MOR curves of $Au@Au_5Pd_5$ and $Au@Au_5Pd_5Ag_1$ in darkness and under light illumination. It was found that the addition of a small amount of Ag slightly affected the intrinsic performance of the catalyst, and the peak current measured in darkness decreased. However, under light illumination, the current of $Au@Au_5Pd_5Ag_1$ exceeded that of $Au@Au_5Pd_5$, indicating a stronger plasmonic enhancement effect. By comparing catalysts with different Ag contents, we observed an interesting phenomenon. The enhancement effect improved with the addition of a small amount of Ag, but when the Ag content increased beyond a certain level (beyond 10%), the EF began to decline, showing a volcano curve (Figure 4E). The maximum EF was found to be ~2.02 for $Au@Au_5Pd_5Ag_1$. [d2.1]We attribute this to the precipitation of excess Ag NPs on the surface, which occupy the catalytic sites. Meanwhile, the excess Ag NPs themselves may undergo oxidation under these conditions, further consuming the photogenerated holes and resulting in a decreased EF. Furthermore, we synthesized $Au@Au_8Pd_2Ag_n$ and $Au@Au_2Pd_8Ag_n$ NRs for comparison and obtained similar results (Figure S11).

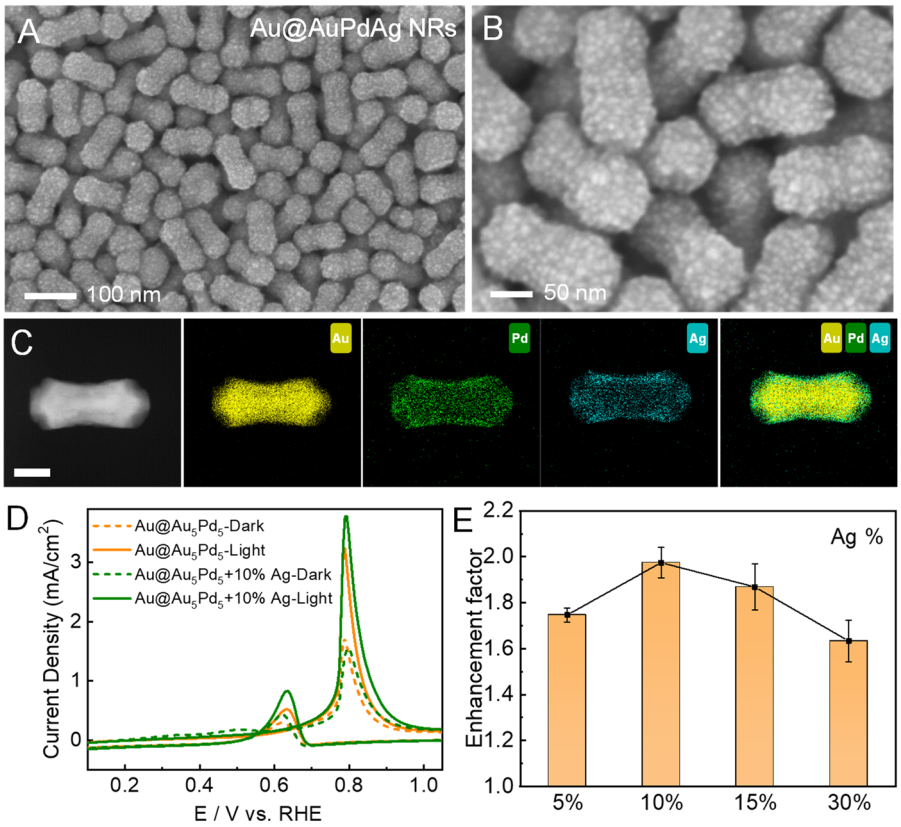


Figure 4. Integration of Ag with $Au@Au_5Pd_5$ NRs for plasmon-promoted MOR. (**A**,**B**) SEM images of Au@AuPdAg alloy NRs. (**C**) HAADF image and EDS mapping of $Au@Au_5Pd_5Ag_1$ NRs. Scale bar: 20 nm. (**D**) MOR curves of $Au@Au_5Pd_5$ NRs and $Au@Au_5Pd_5Ag_1$ NRs, obtained in 1 M KOH + 0.5 M methanol at a scan rate of 50 mV s^{-1} under darkness (dashed lines) and light illumination (solid lines). (**E**) EFs of $Au@Au_5Pd_5Ag_n$ NRs obtained with different amounts of Ag.

The underlying mechanism for plasmonic-enhanced electrocatalysis is complex, including several different contributions that intertwine with each other, such as hot carrier injection, electromagnetic field enhancement, and local lattice heating. These phenomena are accompanied by plasmon damping, and this process is completed within 5–20 fs. It is difficult to measure it directly in time-resolved experiments with such fast relaxation. Since the linewidth Γ of the LSPR is proportional to its decay rate, the relaxation process can be indirectly inferred by measuring the linewidth. For the homogeneous linewidth of an LSPR, there are four main damping pathways [48,62],

$$\Gamma = \Gamma_b + \Gamma_{rad} + \Gamma_{surf} + \Gamma_{HCT} \quad (2)$$

Here, Γ_b and Γ_{surf} denote bulk damping and electron-surface scattering, respectively. Γ_{rad} denotes radiative damping, while Γ_{HCT} represents plasmon damping, arising from charge transfer at the heterogeneous interface. This refers to the energy attenuation caused by the inability of hot electrons and hot holes to recombine after separation under plasmon excitation. The attenuation mechanisms mentioned above are related to the shape, size, material, and dielectric constant of the nanoparticles. For any synthesis method, it is difficult to obtain perfectly uniform particles. Consequently, the measured ensemble spectra are typically inhomogeneous (Figure 5A). Thus, single-particle scattering measurements are promising to provide optical properties of individual particles that are free from the averaging effect.

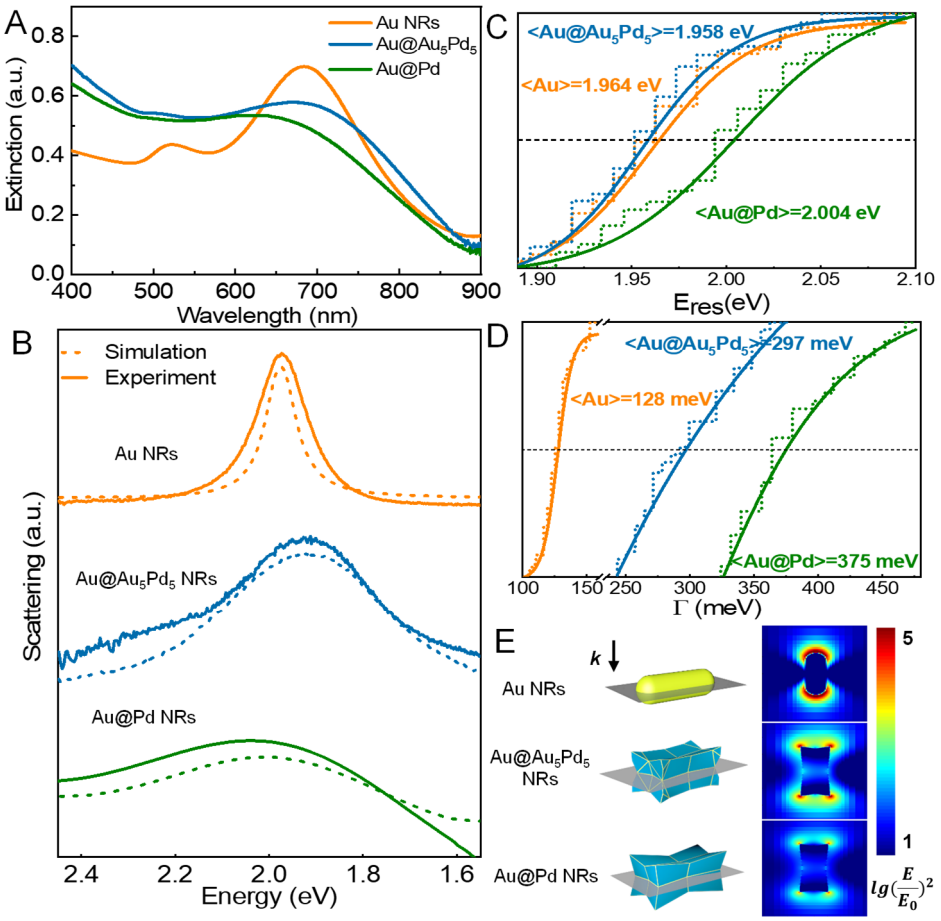


Figure 5. Experimental and simulated optical properties of Au@AuPd alloy NRs. (**A**) Optical extinction spectra of Au, Au@Au5Pd5, and Au@Pd NRs. (**B**) Single-particle scattering spectra of Au, Au@Au5Pd5, and Au@Pd NRs, together with their corresponding simulated scattering spectra. (**C**,**D**) Fitted cumulative distribution functions (CDFs) of the resonance energy E_{res} and linewidth Γ extracted from single-particle scattering spectra of Au NRs (orange lines), Au@Au5Pd5 NRs (blue lines), and Au@Pd NRs (green lines). Dotted lines represent the experimental CDF values, and solid lines are the fitted CDFs. (**E**) Simulated electromagnetic field intensity distribution profiles of Au, Au@Au5Pd5, and Au@Pd NRs upon the excitation of 680 nm light.

Under dark-field microscopy, the samples were imaged under white-light illumination, allowing true-color images of the particles on the glass substrate to be recorded (Figure S12). We measured three samples, namely Au NRs, Au@Au5Pd5 NRs, and Au@Pd NRs, and obtained their representative single-particle scattering spectra (Figures 5B and S12). These spectra conform to a Lorentzian distribution and are in good agreement with the

spectra obtained by FDTD simulation. From the single-particle scattering spectra in Figure 5B, it can be seen that after the AuPd shell grows on the Au NRs, the spectral peak is clearly red-shifted and broadened, indicating that the presence of Pd induces plasmon damping of the Au core. For Au@Pd NRs, the peak position is blue-shifted with more severe peak broadening, and the peak shape no longer conforms to a Lorentzian distribution. This indicates that the Pd shell severely hinders the LSPR of Au, and the spectrum of these particles is closer to that of Pd black. Each uniform bright spot in the dark-field image represents a single particle. With software assistance, the scattering spectrum of each bright spot can be scanned and recorded, allowing statistical data to be collected (Figure S12). All spectral data were compiled as cumulative distribution functions (CDFs) in Figure 5C,D, where Figure 5C shows the resonance energy (Eres) and Figure 5D shows the linewidth Γ. As shown in Figure 5C, compared with Au NRs, the AuPd alloy shell induces a relatively small shift in Eres, indicating that Au@Au_5Pd_5 NRs largely retain the plasmon resonance of Au NRs. In contrast, the Eres of Au@Pd NRs shifted significantly. As mentioned above, the behavior observed here is closer to that of pure Pd. The plasmonic behavior can be more clearly understood from the change in Γ shown in Figure 5D. The Γ of Au@Au_5Pd_5 NRs increases by 297 meV compared with that of Au NRs. Since Au@Au_5Pd_5 NRs still retain the plasmonic characteristics of Au NRs, this portion of the damping can be attributed to the energy loss from hot carrier transfer at the Au-Pd interface, namely, Γ_{HCT}. In contrast, Au@Pd NRs exhibit an obvious increase in Γ, indicating that their hot carrier utilization efficiency is much lower than that of Au@Au_5Pd_5 NRs. The simulated electromagnetic field enhancement profiles of the three particles in Figure 5E further demonstrate their differences in LSPR at 680 nm light excitation. The hot spots of both Au@Au_5Pd_5 NRs and Au@Pd NRs are concentrated at the four corners, but the former are clearly stronger than the latter.

The as-prepared core-shell NPs are also an excellent substrate for surface-enhanced Raman scattering (SERS) measurement, which allows *in situ* SERS characterization of MOR (Figure 6) [63]. Under the plasmonic enhancement effect of the Au core, weak Raman scattering signals can be amplified by a factor of more than 10^6. Importantly, Raman spectroscopy is highly capable of identifying signals at low wavenumbers (<800 cm^{-1}), which contain information on various oxidizing species, hydroxides, and metal-oxygen bonds [64–69]. This capability is essential for understanding the processes and mechanisms of complex electrocatalytic reactions such as MOR [70], oxygen reduction reaction (ORR) [71–74], and CO_2 reduction reaction (CO_2RR) [75–78]. To compare the enhancement effects of different Au/Pd ratios on SERS signals, we first performed Raman spectroscopy measurements on a series of Au@Au_xPd_y using thiophenol (TP) as the probe molecule (Figure 6A). Owing to the presence of a benzene ring in the TP molecule and the strong binding affinity between sulfur and noble metals, the Raman signal of TP is readily identifiable and can be used to evaluate the SERS effect of the substrate. In Figure 6B, a series of SERS peaks belonging to TP can be observed at approximately 944, 1004, 1025, and 1578 cm^{-1} (Table S1) [35]. The peak at 520 cm^{-1} corresponds to the silicon substrate, and this peak was used to normalize all Raman signals. It can be seen that as the proportion of Au in the shell decreased, the intensity of the TP Raman signal in the SERS spectra also decreased. When the Au/Pd ratio in the shell was reduced to 2:8, the TP signal could hardly be detected, indicating that the plasmonic enhancement effect had been significantly weakened. This demonstrates that the Au in the shell indeed plays a role in extending the plasmonic effect of the core.

Since Au@Au_5Pd_5 NRs exhibited a pronounced SERS enhancement effect and excellent MOR catalytic performance, we further conducted *in situ* SERS tests of MOR using the *in situ* electrochemical cell (Figure 6C). The SERS spectra were recorded from negative to positive potentials to avoid irreversible signal interference caused by oxidation of the catalyst surface and CO poisoning. As shown in Figure 6D, a consistently sharp peak at 1022 cm^{-1} can be attributed to the C-O stretching mode of methanol. At low potentials (below 0.5 V vs. RHE), a SERS band near 471 cm^{-1} can be observed (Table S2) [79]. As the potential was shifted from 0.5 to 0.9 V, this band became less distinct. Upon further increasing the potential, the SERS band near 471 cm^{-1} disappeared and was replaced by a band near 527 cm^{-1}. These two SERS bands correspond to Pd-C stretching of adsorbed CO and Pd-O stretching, respectively [80]. Regarding the possible contribution of Au-CO species, the adsorption of CO on Au is considerably weaker than on Pd, and therefore the Au-CO Raman signal can be reasonably neglected. The disappearance of the Pd-C band and the appearance of the Pd-O band represent a classical CO oxidation process, indicating that CO adsorbed on the Pd surface is oxidized as the potential increases. Correspondingly, a SERS band above 2000 cm^{-1} was observed, and its intensity increased with increasing potential before abruptly disappearing beyond 1.2 V. This SERS band is also attributed to the C-O stretching of adsorbed CO. The increase in its intensity indicates that the MOR process involves the accumulation of CO intermediates. The abrupt disappearance of this signal beyond 1.2 V coincides with the appearance of the Pd-O band, suggesting that the Pd surface becomes largely covered by oxygen species at this stage. This prevents further CO adsorption and its subsequent conversion to CO_2, signaling the termination of methanol oxidation. This also explains the decrease in MOR current at high potentials observed in the CV curves (Figure 2B,C). Admittedly, the potentials obtained from

the *in-situ* SERS measurements do not perfectly match those in the CV curves. This discrepancy may arise from the lag caused by the limited capacity and insufficient diffusion within the *in situ* electrolytic cell. The bands located near 1500 cm^{-1} are more complex. The band observed at 1490 cm^{-1} can be attributed to the stretching vibrations of COO^- and CO_3^{2-}. In the potential range of 0.6 to 1.0 V, the band that appears at 1581 cm^{-1} may belong to the intermediates of surface-adsorbed CO_2, as its appearance and disappearance are slightly delayed relative to CO adsorption. Although the peak positions differ somewhat from those reported in the literature (Table S2) [79], we assign this band based on the relative positions of the two sets of peaks, and we attribute the observed shift to the presence of Au in the catalyst shell. With the aid of *in situ* SERS spectroscopy, the reaction mechanism of MOR can be elucidated through analysis of the intermediate species.

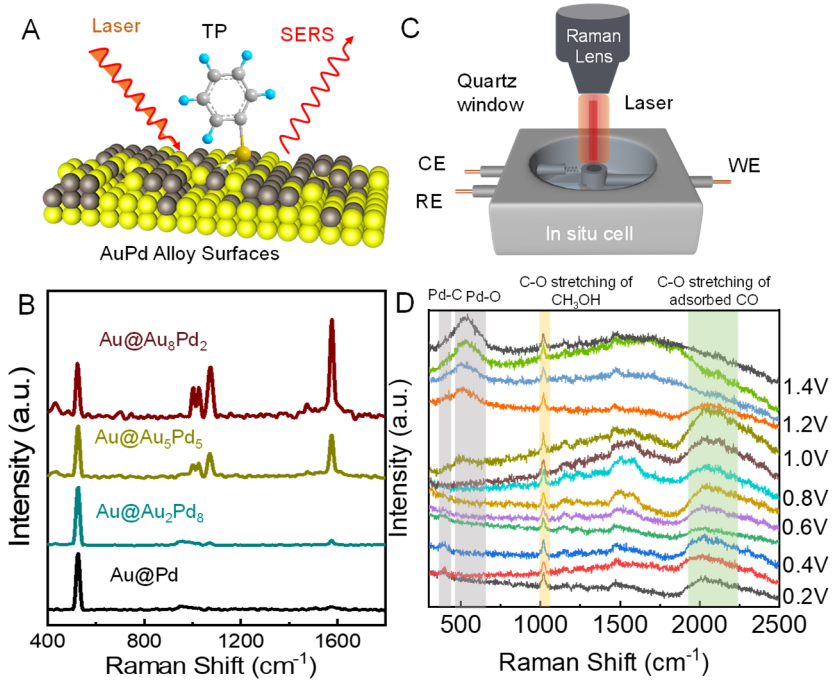


Figure 6. Applications of $Au@Au_xPd_y$ NRs in SERS measurements of MOR. (**A**) Schematic diagram of the collection of SERS signals of TP that is adsorbed on the surface of AuPd alloy. TP: thiolphenol. (**B**) SERS spectra obtained by adsorption of TP molecules on $Au@Au_xPd_y$ NRs of different compositions, as marked in the panel. (**C**) Diagram of the *in situ* electrochemical cell integrated with SERS measurements. (**D**) *In situ* SERS spectra of $Au@Au_5Pd_5$ NRs obtained by varying the potential under MOR test conditions. The potential was varied from 0.2 to 1.4 V vs. RHE in steps of 0.1 V. The highlighted bars in different colors correspond to the Raman vibration modes as marked on the top of each bar.

4. Conclusions

In summary, we report a strategy for promoting plasmon-enhanced MOR through rational regulation of the structure and composition of the AuPd alloy shell. By balancing the active sites and plasmonic enhancement effects, the as-synthesized $Au@Au_5Pd_5$ NRs achieved a 1.88-fold enhancement in MOR current under light irradiation. With the addition of an appropriate amount of Ag, this enhancement was further increased to 2.02-fold. Most importantly, this structure, which integrates both plasmonic and catalytic functionalities, is highly suitable for *in situ* electrochemical SERS studies. The proposed synthesis strategy can also be extended to other multimetallic catalytic systems. It holds great potential for applications in plasmon-enhanced electrocatalysis and in mechanistic studies of electrocatalytic reactions.

Supplementary Materials: The following supporting information can be downloaded at: https://media.sciltp.com/articles/others/2609081417086798/MI-26070137-SI.pdf, with additional experimental details on sample preparation, together with figures and tables including SEM/TEM images, optical extinction spectra, dark-field images, single-particle scattering spectra, EDX mapping, and MOR results, as noted in the text.

Author Contributions: Z.W. and G.C. contributed equally to this work. Q.Z., L.S., Z.W. and G.C. conceived and designed the experiments. Z.W., G.C. and G.Y. performed the synthesis, analysis, simulations, and measurements. Z.W., G.C., L.S., V.B. and Q.Z. co-wrote the paper. Q.Z. and L.S. supervised the entire study. All the authors contributed to the final version of the manuscript. All authors have read and agreed to the published version of the manuscript.

Funding: This work was supported by the National Natural Science Foundation of China (Grant Nos. 22472119, 22174104, 22405195). This work was also supported by the Fundamental Research Funds for the Central Universities (Grant No. 2042026kf0048). This work was also funded by the Basic Research Program of Jiangsu (Grant No. BK20240448 to L.S.). L.S. acknowledges the support of Hubei Provincial Natural Science Foundation of China (Grant No. 2025AFB642).

Acknowledgement: The authors acknowledge the support of the Large-scale Instrument and Equipment Sharing Foundation of Wuhan University and the Core Facility of Wuhan University. The authors also thank the Core Research Facility of the CCMS at Wuhan University for SEM and TEM characterizations.

Institutional Review Board Statement: Not applicable.

Informed Consent Statement: Not applicable.

Data Availability Statement: The data that support the findings of this study are available from the corresponding authors on reasonable request.

Conflicts of Interest: The authors declare no conflict of interest.

Use of AI and AI-Assisted Technologies: No AI tools were utilized for this paper.

References

1. Chen, Y.X.; Kanan, M.W. Thermal Ca^{2+}/Mg^{2+} exchange reactions to synthesize CO_2 removal materials. *Nature* **2025**, *638*, 972–979.
2. Zhou, L.A.; Martirez, J.M.P.; Finzel, J.; Zhang, C.; Swearer, D.F.; Tian, S.; Robatjazi, H.; Lou, M.H.; Dong, L.L.; Henderson, L.; et al. Light-driven methane dry reforming with single atomic site antenna-reactor plasmonic photocatalysts. *Nat. Energy* **2020**, *5*, 61–70.
3. Bhattacharjee, S.; Linley, S.; Reisner, E. Solar reforming as an emerging technology for circular chemical industries. *Nat. Rev. Chem.* **2024**, *8*, 87–105.
4. Xia, Y.N.; Xiong, Y.J.; Lim, B.; Skrabalak, S.E. Shape-Controlled Synthesis of Metal Nanocrystals: Simple Chemistry Meets Complex Physics? *Angew. Chem. Int. Ed.* **2009**, *48*, 60–103.
5. Li, W.; Elzatahry, A.; Aldhayan, D.; Zhao, D. Core–shell structured titanium dioxide nanomaterials for solar energy utilization. *Chem. Soc. Rev.* **2018**, *47*, 8203–8237.
6. Liu, J.X.; Ma, H.; Yuan, S.F.; Zhang, J.N.; Liang, J.G.; Zhou, R.; Li, D.S.; Chen, W.; Li, M.D.; Wu, T. Semiconductor clusters enable high-efficiency extraction of hot electrons from gold nanorods for photocatalytic organic conversions. *Sci. China Chem.* **2025**, *68*, 3574–3585.
7. Aslam, U.; Rao, V.G.; Chavez, S.; Linic, S. Catalytic conversion of solar to chemical energy on plasmonic metal nanostructures. *Nat. Catal.* **2018**, *1*, 656–665.
8. Gong, J.L.; Li, C.; Wasielewski, M.R. Advances in solar energy conversion. *Chem. Soc. Rev.* **2019**, *48*, 1862–1864.
9. Zou, L.; Sa, R.J.; Zhong, H.; Lv, H.W.; Wang, X.C.; Wang, R.H. Photoelectron Transfer Mediated by the Interfacial Electron Effects for Boosting Visible-Light-Driven CO_2 Reduction. *ACS Catal.* **2022**, *12*, 3550–3557.
10. Lan, Z.A.; Wu, M.; Fang, Z.P.; Zhang, Y.F.; Chen, X.; Zhang, G.G.; Wang, X.C. Ionothermal Synthesis of Covalent Triazine Frameworks in a NaCl-KCl-$ZnCl_2$ Eutectic Salt for the Hydrogen Evolution Reaction. *Angew. Chem. Int. Ed.* **2022**, *61*, e202201482.
11. Sun, L.C.; Zhang, Q.F.; Li, G.G.; Villarreal, E.; Fu, X.Q.; Wang, H. Multifaceted Gold–Palladium Bimetallic Nanorods and Their Geometric, Compositional, and Catalytic Tunabilities. *ACS Nano* **2017**, *11*, 3213–3228.
12. Xu, C.P.; Ravi Anusuyadevi, P.; Aymonier, C.; Luque, R.; Marre, S. Nanostructured materials for photocatalysis. *Chem. Soc. Rev.* **2019**, *48*, 3868–3902.
13. Lin, Y.H.; Deng, C.Y.; Wu, L.; Zhang, Y.C.; Chen, C.C.; Ma, W.H.; Zhao, J.C. Quantitative isotope measurements in heterogeneous photocatalysis and electrocatalysis. *Energy Environ. Sci.* **2020**, *13*, 2602–2617.
14. Li, A.; Zhu, W.J.; Li, C.C.; Wang, T.; Gong, J.L. Rational design of yolk–shell nanostructures for photocatalysis. *Chem. Soc. Rev.* **2019**, *48*, 1874–1907.
15. Rebello Sousa Dias, M.; Leite, M.S. Alloying: A Platform for Metallic Materials with On-Demand Optical Response. *Acc. Chem. Res.* **2019**, *52*, 2881–2891.
16. Zhao, Y.H.; Wu, F.X.; Wei, J.P.; Sun, H.D.; Yuan, Y.L.; Bao, H.B.; Li, F.H.; Zhang, Z.C.; Han, S.; Niu, W.X. Designer Gold-Framed Palladium Nanocubes for Plasmon-Enhanced Electrocatalytic Oxidation of Ethanol. *Chem.-Eur. J.* **2022**, *28*, e202200494.
17. Lee, S.; Lee, J.; Lee, S.; Haddadnezhad, M.; Oh, M.J.; Zhao, Q.; Yoo, S.; Liu, L.; Jung, I.; Park, S. Multi-Layered PtAu Nanoframes and Their Light-Enhanced Electrocatalytic Activity via Plasmonic Hot Spots. *Small* **2023**, *19*, 2206377.

18. Zhang, L.; Zhang, J.W.; Kuang, Q.; Xie, S.F.; Jiang, Z.Y.; Xie, Z.X.; Zheng, L.S. Cu^{2+}-Assisted Synthesis of Hexoctahedral Au-Pd Alloy Nanocrystals with High-Index Facets. *J. Am. Chem. Soc.* **2011**, *133*, 17114–17117.
19. Helveston, J.P.; He, G.; Davidson, M.R. Quantifying the cost savings of global solar photovoltaic supply chains. *Nature* **2022**, *612*, 83–87.
20. Dai, C.H.; Liu, B. Conjugated polymers for visible-light-driven photocatalysis. *Energy Environ. Sci.* **2020**, *13*, 24–52.
21. Ding, B.; Ding, Y.; Peng, J.; Romano-deGea, J.; Frederiksen, L.E.K.; Kanda, H.; Syzgantseva, O.A.; Syzgantseva, M.A.; Audinot, J.-N.; Bour, J.; et al. Dopant-additive synergism enhances perovskite solar modules. *Nature* **2024**, *628*, 299–305.
22. Liu, J.; He, Y.C.; Ding, L.; Zhang, H.; Li, Q.Y.; Jia, L.B.; Yu, J.; Lau, T.W.; Li, M.H.; Qin, Y.; et al. Perovskite/silicon tandem solar cells with bilayer interface passivation. *Nature* **2024**, *635*, 596–603.
23. Yang, Y.H.; Zhang, B.B.; Sun, X.H.; Tao, Y.L.; Yang, G.Z.; Liu, C.; Wang, Z.X.; Sun, L.C.; Zhang, Q.F. Tuning the modal coupling in three-dimensional Au@Cu_2O@Au core–shell–satellite nanostructures for enhanced plasmonic photocatalysis. *Chem. Sci.* **2025**, *16*, 8069–8081.
24. Yu, Z.J.; Wang, J.M.; Chen, Z.L.; Liu, S.Q.; Zhang, Y.C.; Zhao, J.C. Plasmon-assisted photothermal catalysis for efficient styrene epoxidation on Au/$NiCo_2O_4$ photoanodes. *Sci. China Chem.* **2026**, *69*, 961–969.
25. Zhang, Z.L.; Zhang, C.Y.; Zheng, H.R.; Xu, H.X. Plasmon-Driven Catalysis on Molecules and Nanomaterials. *Acc. Chem. Res.* **2019**, *52*, 2506–2515.
26. Gellé, A.; Jin, T.; de la Garza, L.; Price, G.D.; Besteiro, L.V.; Moores, A. Applications of Plasmon-Enhanced Nanocatalysis to Organic Transformations. *Chem. Rev.* **2020**, *120*, 986–1041.
27. Brongersma, M.L.; Halas, N.J.; Nordlander, P. Plasmon-induced hot carrier science and technology. *Nat. Nanotechnol.* **2015**, *10*, 25–34.
28. Clavero, C. Plasmon-induced hot-electron generation at nanoparticle/metal-oxide interfaces for photovoltaic and photocatalytic devices. *Nat. Photon.* **2014**, *8*, 95–103.
29. Zeng, Y.J.; Yang, G.Z.; Yang, Y.H.; Tao, Y.L.; Zhang, B.B.; Cheng, Q.Q.; Sun, X.H.; Wang, Z.X.; Sun, L.C.; Zhang, Q.F. Au@TiN hybrid nanostructures with geometric, compositional, and optical tunability. *Sci. China Mater.* **2026**, *69*, 2860–2870.
30. Hu, Q.; Li, P.P.; Li, M.Q.; Wu, J.C.; Ding, J.Y.; Fan, W.Y.; Hu, Q.Y.; Chen, Q.X.; Jiao, X.C. High-index faceted jagged PtPdTe nanotubes for methanol oxidation reaction. *Sci. China Chem.* **2025**, *68*, 4216–4223.
31. Cao, S.Y.; Li, M.F.; Guo, Z.H.; Gong, L.; Lu, Y.F.; Zhang, W.H.; Ni, Y.; Gao, L.; Ma, C.; Huang, H.W. Crystal-phase-controlled PtSn intermetallic nanowires for efficient methanol oxidation. *Sci. China Chem.* **2024**, *67*, 4142–4148.
32. Zhao, J.; Xue, S.; Ji, R.R.; Li, B.; Li, J.H. Localized surface plasmon resonance for enhanced electrocatalysis. *Chem. Soc. Rev.* **2021**, *50*, 12070–12097.
33. Li, S.W.; Miao, P.; Zhang, Y.Y.; Wu, J.; Zhang, B.; Du, Y.C.; Han, X.J.; Sun, J.M.; Xu, P. Recent Advances in Plasmonic Nanostructures for Enhanced Photocatalysis and Electrocatalysis. *Adv. Mater.* **2021**, *33*, 2000086.
34. Choi, C.H.; Chung, K.; Nguyen, T.T.H.; Kim, D.H. Plasmon-Mediated Electrocatalysis for Sustainable Energy: From Electrochemical Conversion of Different Feedstocks to Fuel Cell Reactions. *ACS Energy Lett.* **2018**, *3*, 1415–1433.
35. Zhang, Q.F.; Chen, K.X.; Wang, H. Hot-Hole-Induced Molecular Scissoring: A Case Study of Plasmon-Driven Decarboxylation of Aromatic Carboxylates. *J. Phys. Chem. C* **2021**, *125*, 20958–20971.
36. Besteiro, L.V.; Yu, P.; Wang, Z.M.; Holleitner, A.W.; Hartland, G.V.; Wiederrecht, G.P.; Govorov, A.O. The fast and the furious: Ultrafast hot electrons in plasmonic metastructures. Size and structure matter. *Nano Today* **2019**, *27*, 120–145.
37. Kale, M.J.; Avanesian, T.; Christopher, P. Direct Photocatalysis by Plasmonic Nanostructures. *ACS Catal.* **2014**, *4*, 116–128.
38. Bohren, C.F. How can a particle absorb more than the light incident on it? *Am. J. Phys.* **1983**, *51*, 323–327.
39. Dombi, P.; Hörl, A.; Rácz, P.; Márton, I.; Trügler, A.; Krenn, J.R.; Hohenester, U. Ultrafast Strong-Field Photoemission from Plasmonic Nanoparticles. *Nano Lett.* **2013**, *13*, 674–678.
40. Wang, T.; Wang, H.J.; Lin, J.S.; Yang, J.L.; Zhang, F.L.; Lin, X.M.; Zhang, Y.J.; Jin, S.Z.; Li, J.F. Plasmonic photocatalysis: Mechanism, applications and perspectives. *Chin. J. Struct. Chem.* **2023**, *42*, 100066.
41. Jung, H.; Kwon, Y.; Kim, Y.; Ahn, H.; Ahn, H.; Wy, Y.; Han, S.W. Directing Energy Flow in Core–Shell Nanostructures for Efficient Plasmon-Enhanced Electrocatalysis. *Nano Lett.* **2023**, *23*, 1774–1780.
42. Ding, J.W.; Wang, F.M.; Pan, F.; Yu, P.; Gao, N.; Goldsmith, R.H.; Cai, S.F.; Yang, R.; He, J. Two-Dimensional Palladium Nanosheet Intercalated with Gold Nanoparticles for Plasmon-Enhanced Electrocatalysis. *ACS Catal.* **2021**, *11*, 13721–13732.
43. Stete, F.; Kesarwani, S.; Ruhmlieb, C.; Askes, S.H.C.; Schulz, F.; Bargheer, M.; Lange, H. Inverted temperature gradients in gold–palladium antenna-reactor nanoparticles. *Nat. Commun.* **2025**, *16*, 8168.
44. da Silva, K.N.; Shetty, S.; Sullivan-Allsop, S.; Cai, R.S.; Wang, S.Q.; Quiroz, J.; Chundak, M.; dos Santos, H.L.S.; Abdelsalam, I.; Oropeza, F.E.; et al. Au@AuPd Core-Alloyed Shell Nanoparticles for Enhanced Electrocatalytic Activity and Selectivity under Visible Light Excitation. *ACS Nano* **2024**, *18*, 24391–24403.

45. Bezerra, L.S.; Brasseur, P.; Sullivan-Allsop, S.; Cai, R.S.; da Silva, K.N.; Wang, S.Q.; Singh, H.; Yadav, A.K.; Santos, H.L.S.; Chundak, M.; et al. Ultralow Catalytic Loading for Optimised Electrocatalytic Performance of AuPt Nanoparticles to Produce Hydrogen and Ammonia. *Angew. Chem. Int. Ed.* **2024**, *63*, e202405459.
46. Xie, X.M.; Feng, J.G.; Cui, X.J.; Liu, J.; Jiang, L.H.; Dong, L.F. Plasmon-Enhanced Photocatalysis Coupling Electrocatalysis Steering Methanol Oxidation toward a CO-Free Dominant Pathway. *ACS Catal.* **2021**, *11*, 13160–13168.
47. Zhang, H.W.; Itoi, T.; Konishi, T.; Izumi, Y. Dual Photocatalytic Roles of Light: Charge Separation at the Band Gap and Heat via Localized Surface Plasmon Resonance to Convert CO_2 into CO over Silver-Zirconium Oxide. *J. Am. Chem. Soc.* **2019**, *141*, 6292–6301.
48. Forcherio, G.T.; Ostovar, B.; Boltersdorf, J.; Cai, Y.Y.; Leff, A.C.; Grew, K.N.; Lundgren, C.A.; Link, S.; Baker, D.R. Single-Particle Insights into Plasmonic Hot Carrier Separation Augmenting Photoelectrochemical Ethanol Oxidation with Photocatalytically Synthesized Pd–Au Bimetallic Nanorods. *ACS Nano* **2022**, *16*, 12377–12389.
49. Sytwu, K.; Vadai, M.; Hayee, F.; Angell, D.K.; Dai, A.; Dixon, J.; Dionne, J.A. Driving energetically unfavorable dehydrogenation dynamics with plasmonics. *Science* **2021**, *371*, 280–283.
50. Mohan, P.; Takahashi, M.; Higashimine, K.; Mott, D.; Maenosono, S. AuFePt Ternary Homogeneous Alloy Nanoparticles with Magnetic and Plasmonic Properties. *Langmuir* **2017**, *33*, 1687–1694.
51. Luo, M.; Guo, S. Strain-controlled electrocatalysis on multimetallic nanomaterials. *Nat. Rev. Mater.* **2017**, *2*, 17059.
52. Liu, T.; Li, W.; Wang, D.Z.; Luo, T.; Fei, M.; Shin, D.; Waegele, M.M.; Wang, D. Low Catalyst Loading Enhances Charge Accumulation for Photoelectrochemical Water Splitting. *Angew. Chem. Int. Ed.* **2023**, *62*, e202307909.
53. Aguilar-Ferrer, D.; Vasileiadis, T.; Iatsunskyi, I.; Ziółek, M.; Żebrowska, K.; Ivashchenko, O.; Błaszkiewicz, P.; Grześkowiak, B.; Pazos, R.; Moya, S.; et al. Understanding the Photothermal and Photocatalytic Mechanism of Polydopamine Coated Gold Nanorods. *Adv. Funct. Mater.* **2023**, *33*, 2304208.
54. Patel, M.; Park, H.H.; Bhatnagar, P.; Kumar, N.; Lee, J.; Kim, J. Transparent integrated pyroelectric-photovoltaic structure for photo-thermo hybrid power generation. *Nat. Commun.* **2024**, *15*, 3466.
55. Zhang, Q.; Hernandez, T.; Smith, K.W.; Hosseini Jebeli, S.A.; Dai, A.X.; Warning, L.; Baiyasi, R.; McCarthy, L.A.; Guo, H.; Chen, D.-H.; et al. Unraveling the origin of chirality from plasmonic nanoparticle-protein complexes. *Science* **2019**, *365*, 1475–1478.
56. Johnson, P.B.; Christy, R.W. Optical constants of the noble metals. *Phys. Rev. B* **1972**, *6*, 4370–4379.
57. Stofela, S.K.F.; Kizilkaya, O.; Diroll, B.T.; Leite, T.R.; Taheri, M.M.; Willis, D.E.; Baxter, J.B.; Shelton, W.A.; Sprunger, P.T.; McPeak, K.M. A Noble-Transition Alloy Excels at Hot-Carrier Generation in the Near Infrared. *Adv. Mater.* **2020**, *32*, 1906478.
58. Wang, L.B.; Zhao, S.T.; Liu, C.X.; Li, C.; Li, X.; Li, H.L.; Wang, Y.C.; Ma, C.; Li, Z.Y.; Zeng, J. Aerobic Oxidation of Cyclohexane on Catalysts Based on Twinned and Single-Crystal AuPd Bimetallic Nanocrystals. *Nano Lett.* **2015**, *15*, 2875–2880.
59. Hong, J.W.; Kim, D.; Lee, Y.W.; Kim, M.; Kang, S.W.; Han, S.W. Atomic-Distribution-Dependent Electrocatalytic Activity of Au-Pd Bimetallic Nanocrystals. *Angew. Chem. Int. Ed.* **2011**, *50*, 8876–8880.
60. Lim, B.; Kobayashi, H.; Yu, T.; Wang, J.G.; Kim, M.J.; Li, Z.Y.; Rycenga, M.; Xia, Y.N. Synthesis of Pd-Au Bimetallic Nanocrystals via Controlled Overgrowth. *J. Am. Chem. Soc.* **2010**, *132*, 2506–2507.
61. Sun, M.Q.; Wang, A.K.; Zhang, M.; Zou, S.L.; Wang, H. Interband and Intraband Hot Carrier-Driven Photocatalysis on Plasmonic Bimetallic Nanoparticles: A Case Study of Au-Cu Alloy Nanoparticles. *ACS Nanosci. Au* **2024**, *4*, 360–373.
62. Foerster, B.; Joplin, A.; Kaefer, K.; Celiksoy, S.; Link, S.; Sönnichsen, C. Chemical Interface Damping Depends on Electrons Reaching the Surface. *ACS Nano* **2017**, *11*, 2886–2893.
63. Willets, K.A.; Van Duyne, R.P. Localized Surface Plasmon Resonance Spectroscopy and Sensing. *Annu. Rev. Phys. Chem.* **2007**, *58*, 267–297.
64. Ding, S.Y.; Yi, J.; Li, J.F.; Ren, B.; Wu, D.Y.; Panneerselvam, R.; Tian, Z.Q. Nanostructure-based plasmon-enhanced Raman spectroscopy for surface analysis of materials. *Nat. Rev. Mater.* **2016**, *1*, 16021.
65. Li, J.F.; Huang, Y.F.; Ding, Y.; Yang, Z.L.; Li, S.B.; Zhou, X.S.; Fan, F.R.; Zhang, W.; Zhou, Z.Y.; Wu, D.Y.; et al. Shell-isolated nanoparticle-enhanced Raman spectroscopy. *Nature* **2010**, *464*, 392–395.
66. Zhang, Q.F.; Wang, H. Mechanistic Insights on Plasmon-Driven Photocatalytic Oxidative Coupling of Thiophenol Derivatives: Evidence for Steady-State Photoactivated Oxygen. *J. Phys. Chem. C* **2018**, *122*, 5686–5697.
67. Zhang, Q.F.; Zhou, Y.D.; Fu, X.Q.; Villarreal, E.; Sun, L.C.; Zou, S.L.; Wang, H. Photothermal Effect, Local Field Dependence, and Charge Carrier Relaying Species in Plasmon-Driven Photocatalysis: A Case Study of Aerobic Nitrothiophenol Coupling Reaction. *J. Phys. Chem. C* **2019**, *123*, 26695–26704.
68. Cao, Y.T.; Li, Y.L.; Du, A.X.; Zhang, Y.Y.; Xie, W. Unlocking Plasmonic Hot Electron Utilization on Palladium Nanoparticles via Modulation of the Bimetallic Interface for Enhanced Photocatalysis. *J. Am. Chem. Soc.* **2026**, *148*, 893–901.

69. Wang, T.; Zhang, M.D.; Huang, Z.Z.; Yue, X.X.; Zhu, A.N.; Tong, L.B.; Du, X.M.; Xie, W. Unveiling Exciton-Molecular Crosstalk Mediating Photocatalysis on Perovskite Quantum Dots via In-Situ SERS. *J. Am. Chem. Soc.* **2026**, *148*, 1662–1671.
70. Li, D.Z.; Kuang, Y.B.; Wang, S.L.; Feng, L.G. Carbon-encapsulated RuO_2 clusters supported Pt nanoparticles for effective methanol electrooxidation. *Sci. China Chem.* **2025**, *68*, 6083–6091.
71. Dong, J.C.; Zhang, X.G.; Briega-Martos, V.; Jin, X.; Yang, J.; Chen, S.; Yang, Z.L.; Wu, D.Y.; Feliu, J.M.; Williams, C.T.; et al. *In Situ* Raman spectroscopic evidence for oxygen reduction reaction intermediates at platinum single-crystal surfaces. *Nat. Energy* **2019**, *4*, 60–67.
72. Ze, H.J.; Chen, X.; Wang, X.T.; Wang, Y.H.; Chen, Q.Q.; Lin, J.S.; Zhang, Y.J.; Zhang, X.G.; Tian, Z.Q.; Li, J.F. Molecular Insight of the Critical Role of Ni in Pt-Based Nanocatalysts for Improving the Oxygen Reduction Reaction Probed Using an *In Situ* SERS Borrowing Strategy. *J. Am. Chem. Soc.* **2021**, *143*, 1318–1322.
73. Jiao, W.L.; Chen, C.; You, W.B.; Zhao, X.R.; Zhang, J.; Feng, Y.Z.; Wang, P.; Che, R.C. Hollow Palladium-Gold Nanochains with Periodic Concave Structures as Superior ORR Electrocatalysts and Highly Efficient SERS Substrates. *Adv. Energy Mater.* **2020**, *10*, 1904072.
74. Cheng, Y.; Sun, H.R.; Shen, Y.; Zhan, C.H.; Huang, Z.L.; Huang, W.H.; Pao, C.W.; Su, D.; Liu, W.; Huang, X.Q.; et al. Molybdenum-Pocket Driven Low-Platinum Oxygen Reduction Catalysts for 100-Watt-Scale Fuel Cell Stacks. *Adv. Mater.* **2026**, *38*, e73444.
75. Shan, W.Y.; Liu, R.; Zhao, H.C.; He, Z.L.; Lai, Y.J.; Li, S.S.; He, G.Z.; Liu, J.F. *In Situ* Surface-Enhanced Raman Spectroscopic Evidence on the Origin of Selectivity in CO_2 Electrocatalytic Reduction. *ACS Nano* **2020**, *14*, 11363–11372.
76. Herzog, A.; Bergmann, A.; Jeon, H.S.; Timoshenko, J.; Kühl, S.; Rettenmaier, C.; Lopez Luna, M.; Haase, F.T.; Roldan Cuenya, B. Operando Investigation of Ag-Decorated Cu_2O Nanocube Catalysts with Enhanced CO_2 Electroreduction toward Liquid Products. *Angew. Chem. Int. Ed.* **2021**, *60*, 7426–7435.
77. Jiang, S.; Klingan, K.; Pasquini, C.; Dau, H. New aspects of operando Raman spectroscopy applied to electrochemical CO_2 reduction on Cu foams. *J. Chem. Phys.* **2019**, *150*, 041718.
78. Mao, T.J.; Lin, D.; Han, X.; Huang, J.L.; Chen, Y.R.; Wang, J.; Jin, H.L.; Wang, S.; Huang, X.Q. Fluorine–Mediated Interfacial Microenvironment for Boosting pH–Universal CO_2 Reduction. *Adv. Mater.* **2025**, *37*, 2509720.
79. Ding, Y.M.; Liu, Y.L.; Rao, G.S.; Wang, G.F.; Zhong, Q.L.; Ren, B.; Tian, Z.Q. Electrooxidation Mechanism of Methanol at Pt-Ru Catalyst Modified GC Electrode in Electrolytes with Different pH Using Electrochemical and SERS Techniques. *Chin. J. Chem.* **2007**, *25*, 1617–1621.
80. Chen, X.; Liang, M.M.; Xu, J.; Sun, H.L.; Wang, C.; Wei, J.; Zhang, H.; Yang, W.M.; Yang, Z.L.; Sun, J.J.; et al. Unveiling the size effect of Pt-on-Au nanostructures on CO and methanol electrooxidation by *in situ* electrochemical SERS. *Nanoscale* **2020**, *12*, 5341–5346.

Materials and Interfaces

Scilight

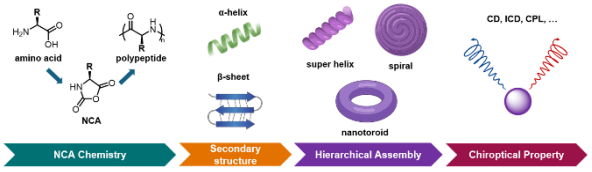
Review

N-Carboxyanhydride-Derived Polypeptides as Programmable Platforms for Hierarchical Chiral Assembly and Chiroptical Materials

Shuo Wang, Mingyue Zhang, Minju Kim, Wenxuan Wu and Zhiqun Lin *

Department of Chemical and Biomolecular Engineering, National University of Singapore, Singapore 117585, Singapore
* Correspondence: z.lin@nus.edu.sg
Received: 29 August 2026; Revised: 20 September 2026; Accepted: 22 September 2026; Published: 30 September 2026

Abstract: *N*-carboxyanhydride (NCA)-derived polypeptides are programmable platforms for hierarchical chiral assembly and chiroptical materials. Their controlled stereochemistry, chain length, architecture, and functionality regulate secondary structures such as α-helices and β-sheets, which further guide assembly into nanostructures, liquid-crystalline phases, and bulk ordered materials. This review summarizes how polymer structure and secondary conformation govern chiral assembly, chirality transfer, and chiroptical responses, including circular dichroism, induced circular dichroism, and circularly polarized luminescence. Recent examples of liquid-crystalline polypeptides, homopolypeptide nanotoroids, chromophore co-assemblies, and phosphorescent aggregates are discussed. Challenges and opportunities in structural diversity, performance, and block copolypeptide platforms are also highlighted.



Keywords: NCA polymerization; synthetic polypeptides; chiral assembly; chiroptical materials; chirality transfer; circularly polarized luminescence

1. Introduction

In recent years, chiroptical polymer materials have attracted increasing research interest as they organically integrate optical asymmetry with the processability, robustness, and structural hierarchy of macromolecules [1–4]. By interacting differently with left- and right-handed circularly polarized light, chiral materials can display circular dichroism, induced circular dichroism, circularly polarized luminescence, and other polarization-dependent responses. These properties are relevant to chiral sensing, optical encryption, bioimaging, photonic materials, and polarized optoelectronic devices [5]. Compared with small-molecule chiroptical systems, polymers help amplify molecular chirality into mesoscopic and macroscopic order through chain conformation, self-assembly, phase separation, and processing, opening opportunities to better chiroptical performance, flexibility, and scalability [3].

As structural analogues of natural proteins and peptides, synthetic polypeptides are uniquely suited for translating molecular chirality into hierarchical chiral structures and chiroptical responses. Composed of chiral amino acid residues linked by peptide bonds, polypeptides possess intrinsic stereochemical information and can adopt well-defined secondary structures, including α-helix, β-sheet, polyproline helix, and coil-like conformations [6–8]. These secondary structures serve as intermediate chiral motifs that bridge molecular stereochemistry and higher-order assembly. Depending on chain length, side-chain structure, monomer sequence, tacticity, and polymer topology, as well as solvent, temperature, and pH, polypeptides can further organize into micelles [9], vesicles [10], fibers [11,12], ribbons [13], toroids [14–20], liquid-crystalline phases [21–25], and thin films [26–29]. Such structural hierarchy provides a pathway for amplifying the molecular chirality of amino acid into material-level chiroptical responses.

Ring-opening polymerization (ROP) of amino acid *N*-carboxyanhydrides (NCAs) is one of the most efficient methods for preparing high-molecular-weight synthetic polypeptides with tunable molecular and architectural features [6,30]. Together with post-polymerization modification (PPM), NCA ROP enables access to homopolypeptides, statistical copolypeptides, block copolypeptides, hybrid block copolymers, and end- or side-chain-functionalized polypeptides [31]. Key parameters such as L/D configuration, degree of polymerization,

Copyright: © 2026 by the authors. This is an open access article under the terms and conditions of the Creative Commons Attribution (CC BY) license (https://creativecommons.org/licenses/by/4.0/).
Publisher's Note: Scilight stays neutral with regard to jurisdictional claims in published maps and institutional affiliations.

dispersity, block sequence, side-chain functionality, and terminal groups can be adjusted to regulate secondary structure and assembly. Thus, NCA-derived polypeptides represent programmable platforms for hierarchical chiral assembly [32].

This review focuses on NCA-derived polypeptides as synthetic platforms for hierarchical chiral assembly and chiroptical materials (Figure 1). Particular attention is given to the relationship between polymer architecture, secondary structure, hierarchical assembly, chirality transfer, and chiroptical properties. The discussion covers homopolypeptides, copolypeptides, block copolypeptides, and selected polypeptide-containing hybrids, while short peptides, proteins, and purely small-molecule systems are not the main focus. A wide range of intriguing chiroptical properties, including circular dichroism (CD), induced circular dichroism (ICD), and circularly polarized luminescence (CPL), and their relationship with the chiral structures will be examined.

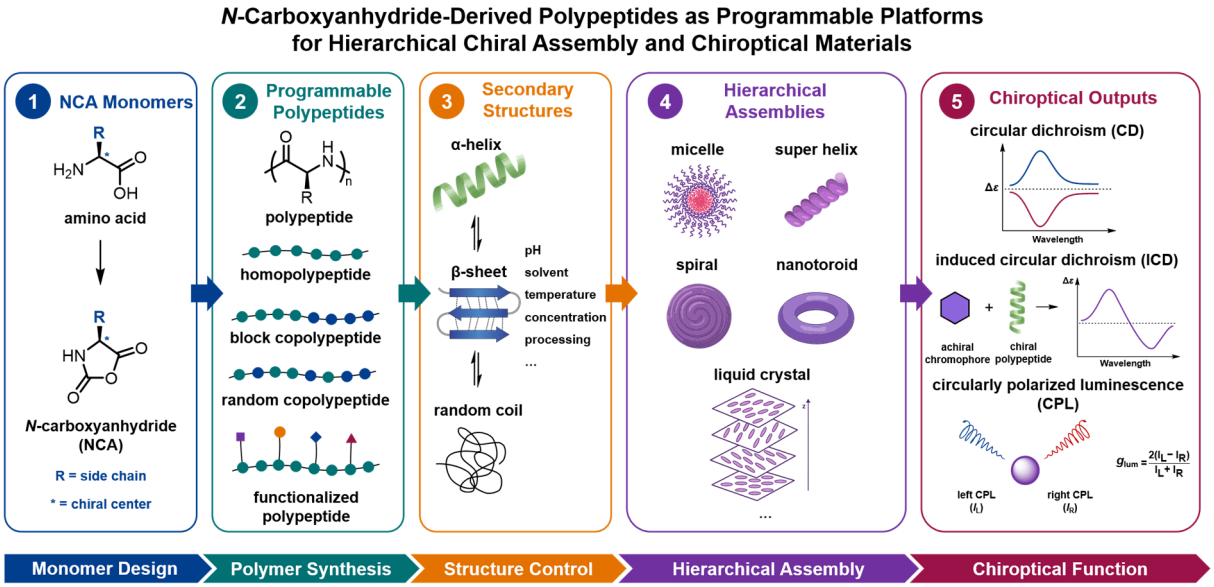


Figure 1. Schematic overview of NCA-derived polypeptides as programmable platforms for hierarchical chiral assembly and chiroptical materials.

2. NCA Polymerization and Secondary Structures of Polypeptides

The chemistry of NCA ROP has been comprehensively reviewed in several review and perspective articles (Figure 2) [6,30,33–36]. Typically, the five-member ring NCA monomers are first synthesized from the corresponding amino acid derivatives by a cyclization reaction (Figure 2a) [37], after which nucleophilic initiators such as amines are added to open the NCA ring and generate a growing polypeptide chain. The chain propagation is known to follow the normal amine mechanism with chain-end amines as the living species and give carbon dioxide as a byproduct (Figure 2b). Under optimized conditions, NCA ROP can proceed in a living/controlled manner, yielding polypeptides with predetermined degrees of polymerization defined by the monomer-to-initiator ratio, while retaining the stereochemical configuration of the amino acid precursor. Sequential monomer addition enables the synthesis of block copolypeptides, whereas copolymerization of monomer mixtures produces statistical or gradient copolypeptides depending on the monomer reactivity ratios (Figure 2c). Additionally, when multifunctional initiators are used, polymers with nonlinear topologies, such as star-like or bottlebrush-like, can also be prepared.

Beyond these primary structural parameters, one of the most distinctive features of NCA-derived polypeptides is their ability to adopt ordered secondary structures (Figure 3) [7,8,38]. Unlike many conventional synthetic polymers whose chain conformations are highly flexible and statistically disordered, polypeptides can form α-helices, β-sheets, polyproline-type I or II helices, and random-coil conformations depending on molecular design parameters and external conditions, including monomer structure, degree of polymerization, side-chain functionality, polymer topology, solvent environment, pH, and temperature. Among these secondary structures, the α-helix is particularly important for chiral assembly and chiroptical materials (Figure 3a). Typical examples include poly(γ-benzyl-$_L$-glutamate) (PBLG), poly(γ-benzyl-$_D$-glutamate) (PBDG), poly($_L$-lysine), and poly($_L$-glutamic acid) under appropriate conditions [39–42]. The α-helical conformation possesses a well-defined handedness and a macrodipole along the helical axis, which can influence interchain packing, liquid-crystalline ordering, and the spatial arrangement of attached or co-assembled chromophores [8,25].

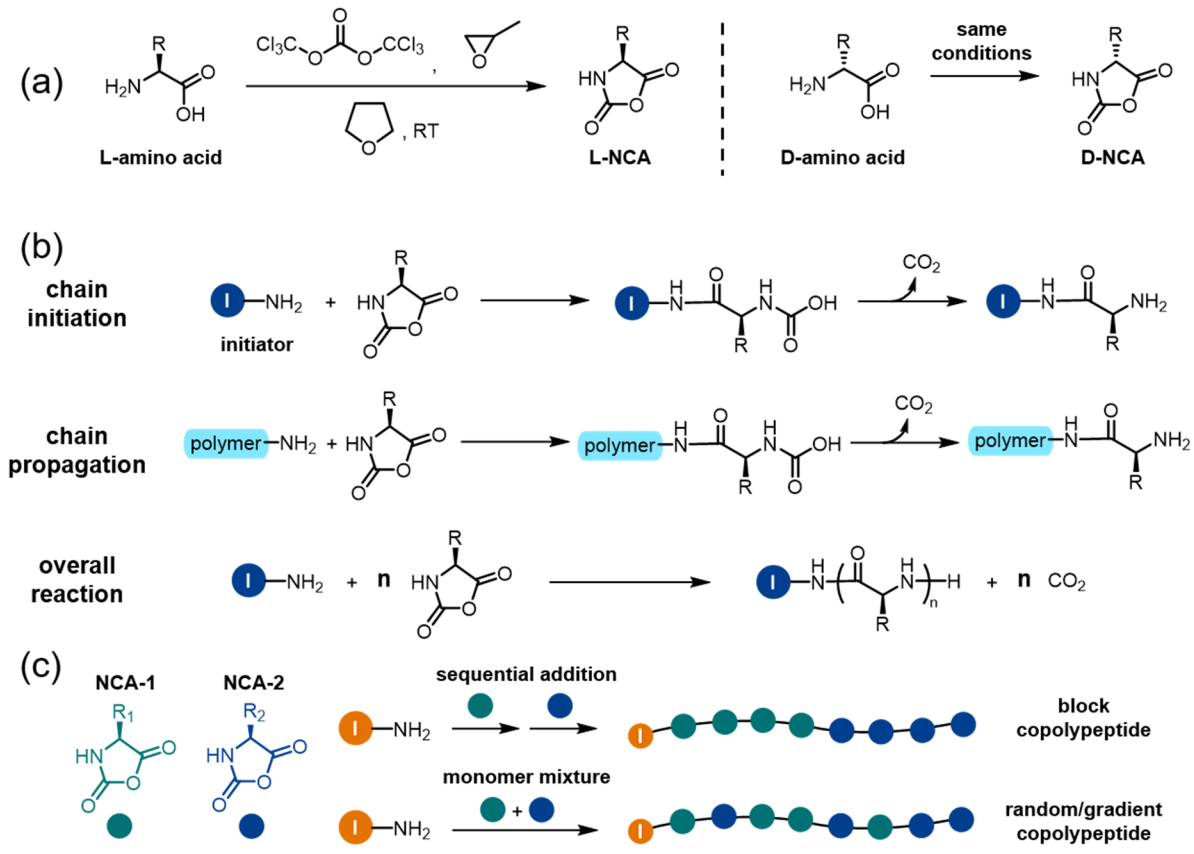


Figure 2. Chemistry of NCA ROP. (**a**) Representative method for preparation of NCA monomers. (**b**) Mechanism for primary amine-initiated ROP of NCAs. (**c**) The synthesis of block and random/gradient copolypeptides.

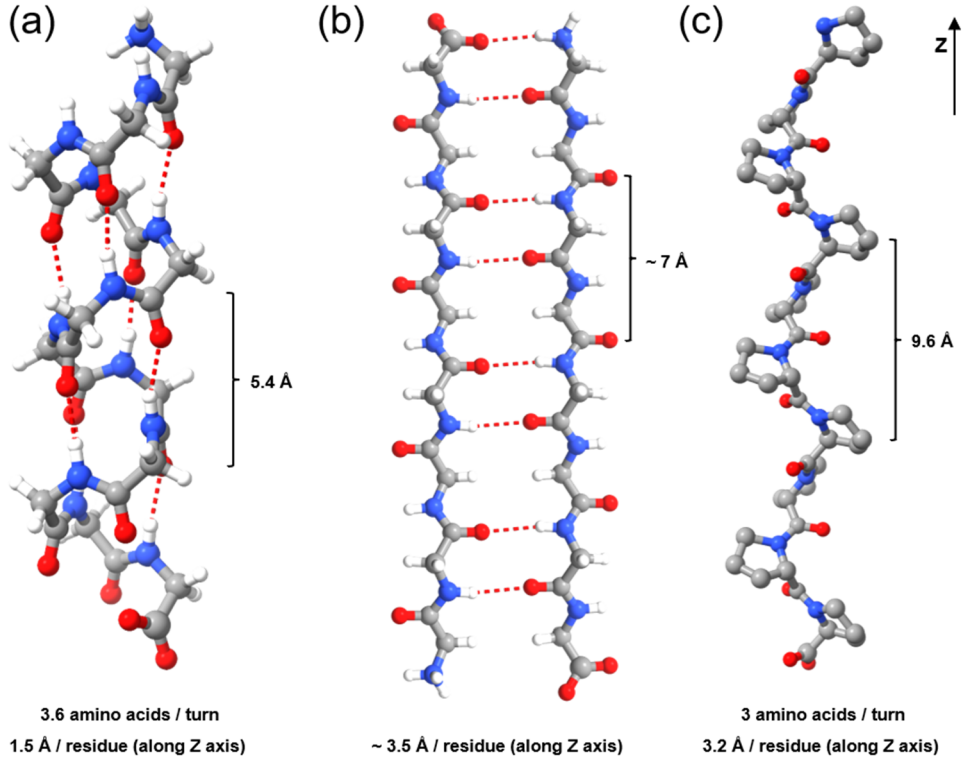


Figure 3. Representative secondary structures of polypeptides. (**a**) *α*-Helix. (**b**) *β*-Sheet. (**c**) Polyproline type-II helix. Carbon, hydrogen, oxygen, nitrogen atoms are in gray, white, red, and blue colors, respectively. For (**a**) and (**b**), oligomers of glycine are used for simplicity. Hydrogen bonds are represented by red dotted lines. For (**c**), hydrogen atoms are omitted for simplicity.

β-Sheet-forming polypeptides represent another important class of chiral structural motifs (Figure 3b). Unlike *α*-helices, which are mainly stabilized by intrachain hydrogen bonding, *β*-sheet structures are often stabilized by strong interchain hydrogen bonding and can promote the formation of fibrils, ribbons, lamellae, and other anisotropic assemblies [33,43,44]. In these systems, chirality is expressed not only through the configuration of individual amino acid residues but also through the twist, lateral packing, and long-range organization of *β*-sheet-rich domains [13].

Importantly, polypeptide secondary structures are not static after formation; they can undergo reversible and stimulus-responsive transitions governed by molecular design and external conditions. Depending on the processing method, the same polypeptide may form materials with different secondary structures, as conformational transitions can be kinetically hindered and metastable states may be preserved [40]. Charged polypeptides such as poly(L-lysine) and poly(L-glutamic acid) can undergo pH-dependent coil–helix transitions, while solvent polarity, ionic strength, temperature, and counterions further regulate hydrogen bonding, electrostatic interactions, and interchain association [39,42,45]. In block copolypeptides, secondary structures are coupled with amphiphilicity and phase separation; for example, a helix-forming block can act as a rigid rod, whereas a hydrophilic or coil-like block can form a flexible corona, enabling rod–coil self-assembly [46].

3. Hierarchical Chiral Assembly of Polypeptides

3.1. Solution Assemblies

Solution self-assembly of polypeptides and polypeptide-containing block copolymers often follows principles similar to conventional amphiphilic block copolymers. In selective solvents, the morphology is mainly governed by the balance between core-forming and corona-forming blocks, solvent quality, ionic strength, temperature, and the interfacial curvature of the aggregate [47]. Reviews on polypeptide-based block copolymer amphiphiles summarized that typical solution morphologies include spherical micelles, cylindrical micelles, and vesicles, with the curvature of the core–corona interface largely determined by block volume fractions and environmental conditions [46,48].

Representative experimental systems include polypeptide-based diblock copolymers that form well-defined micelles or vesicles after direct dissolution in water or organic solvents [49–52]. Notably, in these solution assemblies, the strong tendency of polypeptides to form secondary structures still shows significant effects on the final morphology, which distinguishes polypeptides from random coil polymers. In this regard, a landmark example was reported in 2004, which developed diblock copolypeptide vesicles through conformation-specific assembly (Figure 4a) [51]. The copolypeptides, named $K^{P}_{x}L_{y}$, contain a longer block of hydrophilic side chain-modified poly(L-lysine) and a shorter block of hydrophobic poly(L-leucine). As both blocks favor *α*-helical conformation, the copolypeptides prefer alignment of helical axes, giving well defined micrometer-scale vesicles with tunable sizes. In contrast, when racemic monomers were used to disrupt the ordered helical conformations, no vesicle was observed.

Recent polymerization-induced self-assembly (PISA) approaches further couple NCA chain growth with self-assembly. For example, the research groups of Du and Bonduelle/Lecommandoux independently reported the ring-opening polymerization-induced self-assembly of NCA monomers, often referred to as ROPISA or NCA-PISA, yielding biodegradable polypeptide vesicles or well-dispersed nanoparticles (Figure 4b,c) [53–56]. Poly(L-proline)-stabilized polypeptide nanostructures have also been prepared by consecutive NCA polymerization through a ROPISA process, producing rod-like, worm-like, or vesicular morphologies [57]. These examples establish solution self-assembly as a versatile route to polypeptide nanoobjects, although in many cases the observed micelles or vesicles mainly reflect amphiphilic packing rather than a direct morphological expression of chirality.

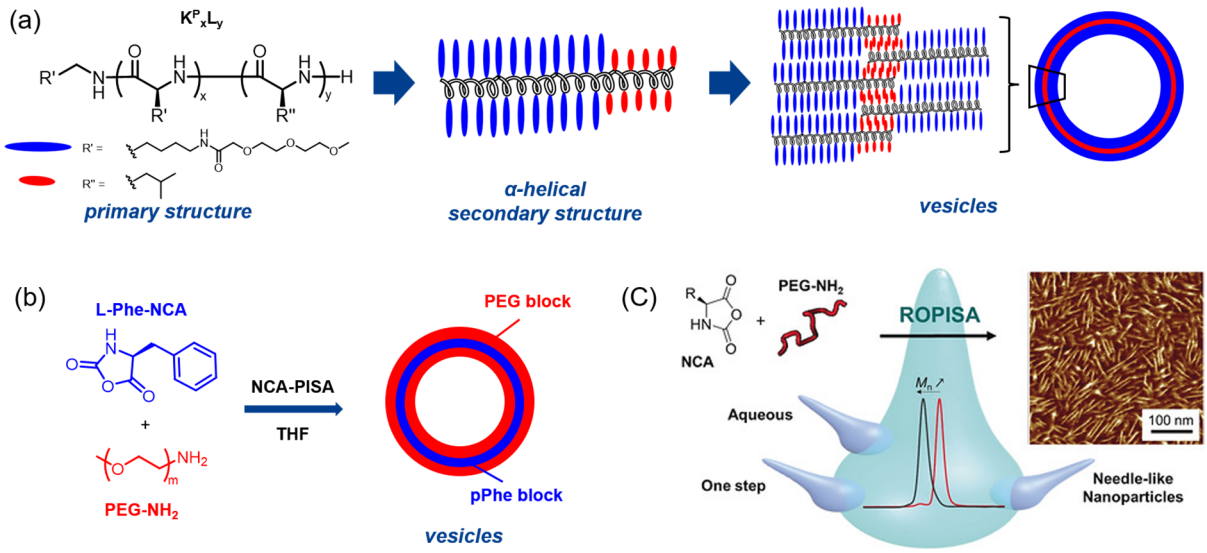


Figure 4. Solution assemblies of polypeptides. (**a**) Schematic showing the formation of polypeptide vesicles by conformation-specific assembly. (**b**) Schematic overview of NCA-PISA system developed by Du et al. using L-phenylalanine NCA as the monomer and polyethylene glycol amine (PEG-NH_2) as the initiator. (**c**) Schematic of ROPISA developed by Bonduelle/Lecommandoux research group. Reproduced with permission [55]. Copyright 2020, Wiley-VCH.

3.2. Discrete Chiral Nano- and Microstructures

In addition to conventional micelles and vesicles, NCA-derived polypeptides can form discrete nano- and microstructures with pronounced anisotropy, curvature, or chiral shape expression [32]. These structures are often generated in solution or at interfaces, but they are different from ordinary amphiphilic aggregates because their morphologies include super-helices, spirals, fibers, rings, and toroids rather than simple core–corona objects.

Early examples were reported in 2009 using a binary system containing amphiphilic polypeptide block copolymers (PBLG-*b*-PEG) and polypeptide homopolymers (PBLG). Super-helical rods and rings were observed when the polymer solution in a mixed solvent of THF-DMF was precipitated by water, with the polypeptide chains forming the core and PEG chains forming the shell (Figure 5a) [58]. Mechanistic study suggested that PBLG-*b*-PEG and PBLG tended to co-assemble into rod-like structures in THF-DMF as a result of tendency of PBLG to adopt a liquid crystal alignment. When water-was added, interfacial tension of the surface of the hydrophobic PBLG rod core increased, causing the PBLG chains to shrink and twist to minimize the total free energy. This work demonstrated that multicomponent polypeptide systems can generate helical supramolecular objects through co-assembly, rather than only spherical or vesicular aggregates. A later study extended this strategy by combining experiments with computer simulations. Through simulation-assisted self-assembly of polypeptide-based block copolymers and homopolymers, hierarchical nanostructures with designed morphologies were developed, which could be tuned by adjusting parameters such as temperature, block rigidity, and component molar ratio [59,60].

A different class of discrete chiral structures was reported in 2018, which described the self-assembly of *α*-helical polypeptides into microscopic and enantiomorphic spirals by direct emulsification (Figure 5b) [61]. The final objects were micrometer-scale spiral particles with clear handedness, providing a direct morphological expression of chiral *α*-helical polypeptide assembly. A fiber-bundling-mediated mechanism was proposed for the transfer of helicity and chirality from *α*-helical chains to higher hierarchical levels. The *α*-helical polypeptides first assemble into fibers, which then bundle within a confined spherical geometry to generate micrometer-sized spiral particles, as supported by SEM analysis. Rather than treating the polypeptide simply as an amphiphilic block, this work highlighted the ability of *α*-helical chains to organize hierarchically into visible chiral shapes.

Recent studies have further connected discrete chiral morphology with the process of polymerization. A fast catalyst-free synthesis of stereoselective polypeptides was achieved through hierarchical chiral assembly in water (Figure 5c) [62]. In this system, ε-benzyloxycarbonyl-$_{L/D}$-lysine NCAs underwent ultrasonication-assisted ROPISA initiated by PEG-NH_2 in an aqueous medium. The polymerization of L- and D-enantiomers produced predominantly right- and left-handed superhelical assemblies, respectively, in a one-pot process. Racemic monomers could also give stereoselective polypeptide segments through assembly-driven polymerization. This example differs from post-polymerization self-assembly because chain growth and hierarchical chiral assembly are coupled during polymer formation.

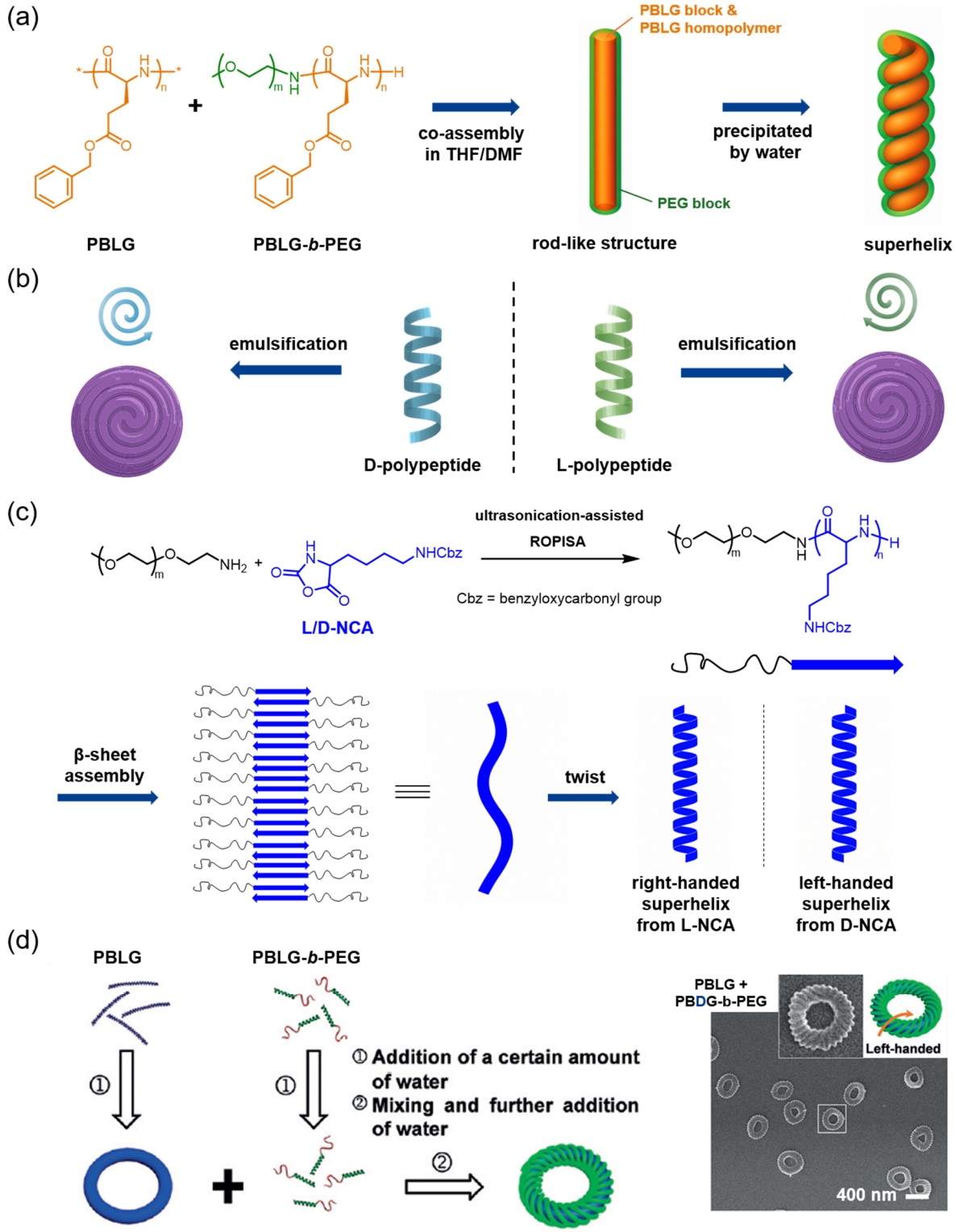


Figure 5. Discrete chiral nano-/microstructures of NCA-derived polypeptides. (**a**) Co-assembly of PBLG and PBLG-*b*-PEG into superhelices. (**b**) Fiber bundling into enantiomorphic spirals. (**c**) Polymerization-coupled superhelical assembly. (**d**) Toroids formed by a two-step self-assembly of PBLG and PBL(D)G-*b*-PEG. Reproduced with permission [17]. Copyright 2020, Wiley-VCH.

Toroidal nanostructures represent another distinctive class of chiral morphology in polypeptide hierarchical assembly. An early mechanistic example described toroid formation through a supramolecular "cyclization reaction" of rodlike micelles, showing how one-dimensional polypeptide-containing micellar precursors can bend and close into ring-shaped objects [63]. Helical toroids were later reported from a two-step self-assembly of the binary system of PBLG and PBLG-*b*-PEG, further demonstrating that co-assembly can transform rodlike packing into closed, twisted, and helically organized toroidal structures (Figure 5d) [17]. These works suggest that toroids

are not merely geometric rings; their formation involves anisotropic packing and curvature of chiral polypeptide segments, providing a pathway for amplifying molecular and conformational chirality into nanoscale morphology. Subsequent studies expanded this family to fluorescent homopolypeptide toroids [64], homochiral "8"-shaped nanotoroids [19], triangular nanotoroids [15], substrate-induced nanotoroids [14], and hierarchical helical toroids obtained through one-pot controllable assembly [16].

Together, these studies show that homopolypeptides and block copolypeptides can access discrete chiral nano- and microstructures beyond conventional amphiphilic packing. Super-helices, microscopic spirals, nanofibers, nanotoroids all illustrate how polypeptide secondary structure, rod-like packing, or multicomponent co-assembly can generate anisotropic and curved morphologies. Although not every report fully resolves the mechanism of chirality transfer, these discrete structures provide an important morphological bridge between molecular chirality and material-level chiroptical responses, which will be discussed in the next section.

3.3. Liquid-Crystalline and Bulk Assemblies

At higher concentrations, in the bulk state, or under film-forming conditions, polypeptide assembly can extend from discrete nanoobjects to continuous ordered materials. Classical *α*-helical polypeptides such as poly(γ-benzyl-$_L$-glutamate) (PBLG) are known to behave as rigid-rod-like macromolecules with macrodipoles rather than flexible polymer coils. Above certain concentrations, these rod-like chains can align with each other and form liquid-crystalline phases, including nematic and cholesteric phases (Figure 6a) [21–24,65–69]. The ability to form liquid crystal phase, again, emphasizes the importance of secondary structures of polypeptides for the construction of long-range ordered materials. As a processing-related example, PBLG nanofibers were prepared by electrospinning from isotropic and biphasic liquid-crystalline solutions, showing that liquid-crystalline order in *α*-helical polypeptides can be further transferred into solid anisotropic fibers [70].

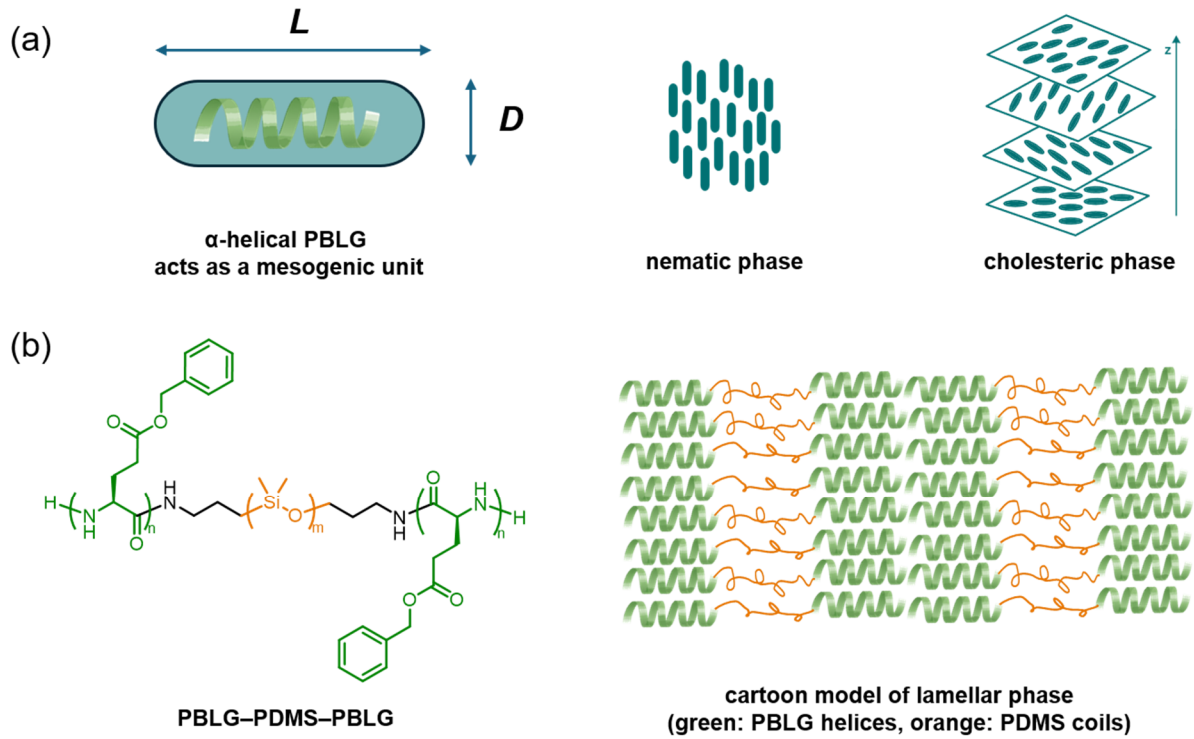


Figure 6. Liquid-crystalline and bulk assemblies of NCA-derived polypeptides. (**a**) *α*-Helical PBLG chains behave as chiral rigid rods to form liquid crystal phases. (**b**) Bulk assembly of PBLG-PDMS-PBLG.

This liquid-crystalline tendency also strongly affects the self-assembly of polypeptide-containing block copolymers. In ordinary flexible block copolymers, the final morphology is mainly controlled by block incompatibility and volume fraction [71]. In *α*-helical polypeptide-based block copolymers, however, the helical block introduces an additional factor: rod-like packing. Utilizing this property, a lot of rod-coil and rod-rod block copolymer assembly systems has been designed and investigated [72–75]. PBLG–PDMS–PBLG triblock copolymers provide a representative example: these materials combine two rigid PBLG blocks with a soft polydimethylsiloxane (PDMS) middle block, and their nano-organization depends strongly on the length and

conformation of the PBLG segments. PBLG chains with up to 23 repeating units adopt *β*-sheet while longer ones favor *α*-helical conformations, which in turn affects the supramolecular structure in the condensed state, leading to hexagonal and lamellar phase, respectively (Figure 6b) [76,77]. When the temperature changes, the block copolymers show reversible transitions relevant to the thermotropic liquid crystal behavior. These suggest that block copolypeptide assembly should be understood as a balance between two effects: the usual phase separation of block copolymers and the intrinsic ordering tendency of *α*-helical polypeptides.

Taken together, the hierarchical assembly of NCA-derived polypeptides spans from solution nanoobjects to discrete chiral nano-/microstructures and liquid-crystalline or bulk ordered phases. In these systems, secondary structures are not passive conformations; they influence chain stiffness, packing directionality, interchain association, and long-range ordering. While conventional amphiphilic packing often dominates simple micelles and vesicles, more complex morphologies such as spirals, helical toroids, nanotoroids, liquid-crystalline phases, and ordered block copolymer domains more clearly reflect the role of polypeptide conformation and chirality. These hierarchical structures provide the physical basis for chiroptical behavior, because optical activity depends not only on molecular stereochemistry but also on how chains, domains, and chromophores are arranged across length scales. The following section therefore discusses how these assembled polypeptide architectures are translated into chiroptical properties.

4. Chiroptical Properties of Polypeptide Materials

4.1. Circular Dichroism and Vibrational Circular Dichroism

Circular dichroism (CD) is the most basic chiroptical signal of polypeptides. In dilute solution, CD is commonly used to identify secondary structures such as *α*-helices, *β*-sheets, and random coils [78]. Representative CD curves are shown in Figure 7 [8]. However, CD spectra of polypeptide materials should not always be interpreted only as single-chain conformational signals. Once polypeptide chains aggregate, align, or form liquid-crystalline phases, the CD response can also be influenced by interchain packing and mesoscale order. For example, in lyotropic cholesteric polyglutamate solutions, Tsuchihashi and co-workers showed that CD signals at around 800 nm can arise from selective reflection of circularly polarized light by the cholesteric pitch [79].

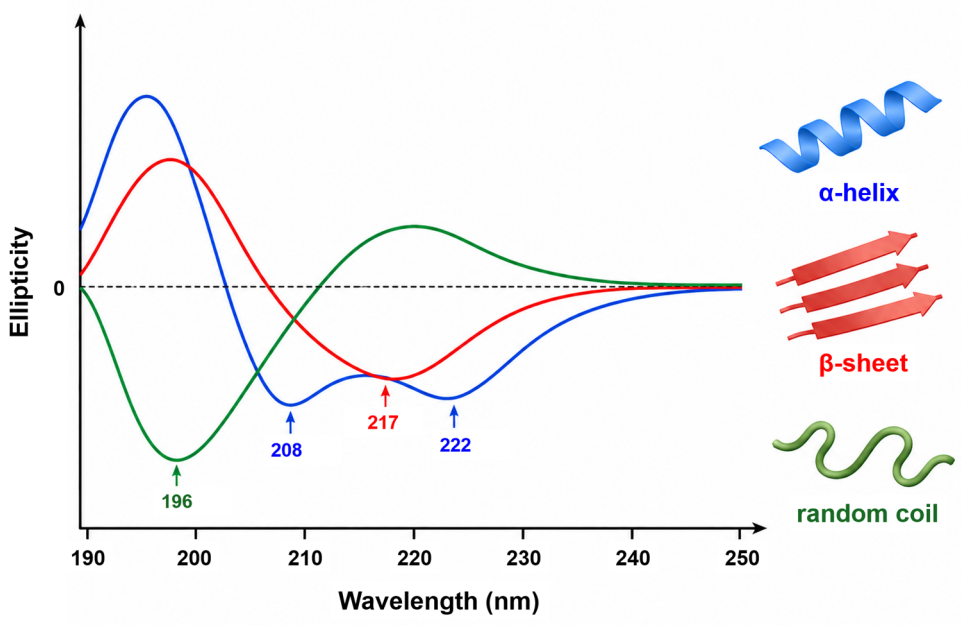


Figure 7. Representative CD responses of different conformations of polypeptides.

Vibrational circular dichroism (VCD) provides complementary chiroptical information by measuring the differential absorption of left- and right-circularly polarized infrared light. While electronic CD probes backbone and side-chain electronic transitions in the UV region, VCD is sensitive to vibrational modes such as the amide I and amide II bands, making it a useful tool for distinguishing *α*-helices, *β*-sheets, and disordered conformations in the infrared region [80]. For NCA-derived polypeptides, VCD has been used to study how solvent composition, temperature, and aggregation state affect secondary structure, as demonstrated by works on PBLG, poly(L-glutamic acid), and poly(L-lysine) [44,81,82].

4.2. Induced Circular Dichroism through Chromophore Organization

Achiral molecules can display induced circular dichroism (ICD) within their absorption bands when interacting with chiral inducing molecules [83]. ICD signals, in turn, provide evidence for interaction or chiral transfer between interested chiral-achiral pairs. For polypeptide systems, far-UV CD mainly reflects the peptide secondary structure. By contrast, when a CD signal appears in the absorption region of a chromophore, it indicates that the chromophore has been placed in a chiral electronic environment or arranged in a chiral manner. Therefore, ICD is particularly useful for evaluating whether the chirality of a polypeptide scaffold has been transferred to side-chain, terminal, or noncovalently incorporated chromophores (Table 1).

For chromophores attached to the side chains of polypeptides, the α-helical backbone can transfer its chirality to the pendant groups by providing a stereoregular environment. For example, in 1975, achiral side-chain chromophores in helical polypeptides were shown to exhibit extrinsic chiroptical activities in dilute solutions or liquid crystalline phases. Poly-β-benzyl-$_L$-aspartate, poly-β-p-nitrobenzyl-$_L$-aspartate, and poly-γ-p-nitrobenzyl-$_L$-glutamate gave ICD signals in the absorption regions of the benzyl or p-nitrobenzyl chromophores, which resulted from the loss of rotational freedom of the chromophores after connecting to the helical backbone [84]. Similarly, helically arranged azobenzene chromophores with distinct ICD signals were prepared by attaching azobenzene to the side chain of NCA monomers and then polymerization [85–87]. Other side-chain chromophores studied include naphthalene, anthracene, and pyrene [88–93].

Terminal chromophore functionalization provides another useful approach. Compared with side-chain modification, end-group labeling introduces fewer chromophores and usually perturbs the polypeptide secondary structure less strongly. In 1980, the ICD signals of α-helical PBLG with covalently attached terminal chromophores were utilized to probe the local conformation of peptide units near the chain ends. The terminal chromophores were shown to sense both local helical conformation and interchain assembly, giving responses in ICD signals when external stimuli were applied [94].

A third route is to place achiral chromophores into chiral polypeptide assemblies through noncovalent interactions. In this case, the chromophore does not need to be chemically attached to the polymer. Instead, it can be organized by confinement within a chiral liquid-crystalline or supramolecular environment [95]. Sisido and co-workers provided several important examples of this strategy. Poly(α-amino acid)s bearing amphiphilic side chains were shown to bind hydrophobic guests and induce CD in the guest absorption region [96], while dye-doped PBLG gels enabled reversible cholesteric ordering of guest molecules [97,98]. In cholesteric polypeptide films doped with azobenzene derivatives, induced CD arose from the organization of the achiral dye within the chiral PBLG matrix [99]. Related liquid-crystalline gels and films further showed that dye orientation could be controlled by light, indicating that noncovalent chromophore loading can lead to dynamic and stimuli-responsive chiroptical behavior [100]. These studies establish chiral polypeptide assemblies as host matrices capable of transferring chirality to guest chromophores without covalent modification.

Table 1. Strategies for ICD in polypeptide–chromophore systems.

Strategy	Chromophore Organization	Representative Examples	Origin of ICD	Design Value
Side-chain attachment	Chromophores are covalently installed along the polypeptide side chains	Benzyl-, p-nitrobenzyl-, azobenzene-, naphthalene-, and pyrene-containing polypeptides	The α-helical backbone restricts chromophore motion and arranges pendant groups in a stereoregular environment	Provides high chromophore density and can generate strong chromophore-region CD, but may perturb secondary structure
Terminal functionalization	Chromophores are attached to one or both chain ends	Terminal chromophore-functionalized PBLG	Chain-end chromophores sense local helical conformation and interchain association	Offers a clean probe of local chirality with minimal modification of the backbone
Noncovalent guest incorporation	Achiral dyes are embedded in polypeptide assemblies, gels, or liquid-crystalline phases	Hydrophobic guests in amphiphilic poly(α-amino acid)s, dye-doped PBLG gels, azobenzene-doped cholesteric films	Chiral supramolecular or liquid-crystalline environments orient guest chromophores and induce CD in their absorption bands	Enables modular, reversible, and stimuli-responsive chiroptical materials without covalent dye attachment

From a materials-design viewpoint, these examples suggest three levels of chirality transfer. At the molecular level, the local secondary structure of the polypeptide controls the conformation and electronic environment of covalently attached chromophores. At the supramolecular level, interchain packing and ordered domains can

organize multiple chromophores into chiral arrangements. At the mesoscopic level, liquid-crystalline or other hierarchical assemblies can provide chiral fields that induce optical activity in guest dyes. The ICD signal therefore serves as a bridge between structural chirality and optical function. For the development of chiroptical polypeptide materials, ICD is also an important design criterion, which is especially relevant for emissive systems as chromophore-level chirality is often a prerequisite for circularly polarized luminescence.

4.3. Circularly Polarized Luminescence from Emissive Polypeptide Assemblies

Circularly polarized luminescence (CPL) represents a higher level of chiroptical function than CD or ICD because it requires the emissive excited state to possess chiral asymmetry. For systems without significant interchromophoric coupling, CPL generally arises when the individual emissive chromophore is intrinsically chiral or located in a chiral local environment. For systems involving coupled chromophores or aggregate/excimer emission, CPL requires a chiral spatial arrangement of the emissive units, which gives rise to chiral excitonic or aggregate excited states [101,102]. For polypeptide-based materials, this is challenging but attractive. The polypeptide backbone provides intrinsic chirality and secondary structures, but most polypeptides themselves are not strong luminophores. Therefore, emissive polypeptide CPL systems usually rely on one of three strategies: introducing luminescent side chains or terminal groups, organizing emissive chromophores in a chiral polypeptide assembly, or using liquid-crystalline or aggregated structures to amplify the dissymmetry of emission.

An early representative example is the circularly polarized fluorescence (CPF) of polypeptides with side-chain aromatic rings. Developed by Sisido and coworkers in 1980s, aromatic polypeptides, such as poly(L-1- and 2-naphthylalanine) (poly(1- and 2-NapAla), poly(anthrylmethyl L-aspartate) (poly[Asp(OCH_2-9-Ant)]), and poly(L-1-pyrenylalanine) (poly(L-1-PyrAla), showed different levels of CPF signals in their solution states [91,93,103]. With the highest luminescent dissymmetry factor (g_{lum}) values recorded at the level of 10^{-3}, these early studies undoubtedly supported the chirality transfer from backbone amino acids to the excited states of side-chain fluorophores.

In 2020, luminescent liquid-crystal polyglutamates bearing cyanostilbene-based mesogenic emissive side chains (named as PGAC-m) showed a more recent example of CPL-active polypeptide materials (Figure 8a) [25]. In PGACs, the polypeptide backbone supplied the chiral scaffold, while the side-chain liquid-crystalline units acted as the emissive components with aggregation-induced emission enhancement (AIEE) characteristics. The authors showed that the PGACs can form a lamellar-ordered chiral smectic C phase (Figure 8b) and the properties could be tuned by manipulating the spacer length between the backbone and cyanostilbene. In glassy liquid crystal film state, the samples exhibited striking ICD signals at around 350 nm, indicating successful chiral transfer from polypeptide backbone to cyanostilbene. The system finally showed peaked CPL signals at 458 nm, as well as a maximum solid fluorescence quantum yield and the g_{lum} of PGAC-m of 34.1% and 4.5×10^{-2}, respectively. This work therefore provides a useful example of how side-chain engineering and liquid-crystalline ordering can be combined in polypeptides to produce efficient CPL-active materials.

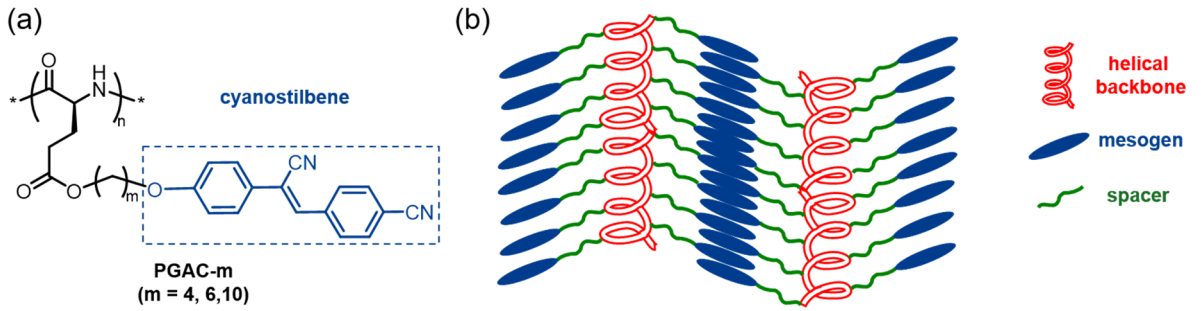


Figure 8. Luminescent liquid-crystal polyglutamates bearing emissive side chains. (**a**) Chemical structure of PGAC-m. (**b**) Proposed molecular stacking of PGAC-m.

In 2023, aqueous CPL of polypeptide materials was achieved by the chiral self-assembly of end group-functionalized α-helical PBLG (Figure 9) [104]. By attaching an aggregation induced emission (AIE) luminogen, named TNB, at the terminal group of linear PBLG homopolypeptides (the conjugate is named as TN-PBLG), the chirality of PBLG chains efficiently transferred into an emissive chiral aggregate state through hierarchical assembly (Figure 9). Specifically, the TN-PBLG was first dissolved in good solvents including tetrahydrofuran (THF) and dioxane (DOA), after which water as a poor solvent was added to give the nanotoroid or nanorod-dispersed aqueous solutions, respectively. CD measurements revealed distinct CD signals of the nanotoroid assemblies in the range of 240–480 nm, supporting the chiral arrangement of pendant phenyl groups. Typical mirror-image CPL profiles were observed for L-

and D-type nanotoroid samples with g_{lum} values at 5×10^{-4}. By contrast, the DOA-resulted nanorod control group gave no CPL response, indicating a morphology dependence. Further hierarchical co-assembly of TN-PBLG and the free TNB luminogen gave nanotoroids with much higher g_{lum} of 7×10^{-3}.

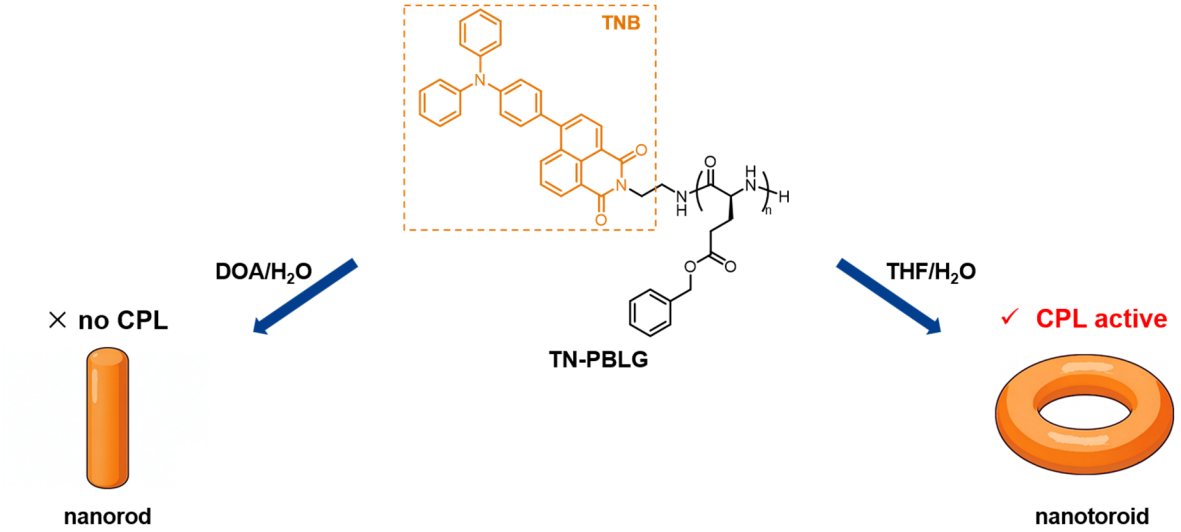


Figure 9. Aqueous CPL from α-helical homopolypeptide nanotoroids.

The role of α-helical structure was further clarified in a follow-up research by correlating the CPL behavior with parameters such as degree of polymerization, self-assembly temperature, and α-helix stability [105]. By directly linking polypeptide secondary structure to CPL performance, it is indicated that the α-helix is not only a structural motif observed by CD but also actively regulates how chirality is transferred to the emissive aggregate. Longer or more stable helical segments can strengthen the chiral environment, while changes in assembly conditions can alter the final CPL response. This work therefore provides a useful framework for designing future homopolypeptide CPL systems: control over chain length and helical stability should be considered as important as the choice of luminophore.

Another system of aqueously dispersed homopolypeptide nanotoroids with CPL properties was from the non-covalent co-assembly of helical polypeptides (PBLGs) with achiral triphenylamine (TPA) derivatives (Figure 10) [18]. This work is different from the above studies as the chiral transfer between luminogens all relies on non-covalent interactions and luminogens do not need to be pre-installed covalently at the chain end of polypeptides. This advantage allows the facile introduction of several luminogens with different structures and colors, including blue, yellow, and red. Notably, a deep-red CPL can be achieved with a record g_{lum} of 1.1×10^{-2} among aqueously polypeptide-based nanoparticles by tuning the doping content. The strong CPL from achiral luminophores, again, indicates that the nanotoroidal homopolypeptide assembly can efficiently induce chiral organization of guest chromophores. This work therefore expands homopolypeptide nanotoroids from a single emissive assembly motif to a more modular platform for color-tunable aqueous CPL.

More recently, the scope of polypeptide chiroptical emission has been extended from fluorescence to room-temperature phosphorescence (RTP). Poly(glutamic acid) aggregates with circularly polarized room-temperature phosphorescence (CPRTP) were reported with highlighted roles of poly(vinyl alcohol) (PVA) in chirality inversion and amplification (Figure 11) [106]. Specifically, poly(L-glutamic acid)s (PLGAs) with achiral phosphorescent end groups were first synthesized and assembled into vesicular architectures that showed weak CPRTP (Figure 11a). When a second polymer matrix, PVA, was added, however, the authors observed both inversion and amplification of the CPRTP signal, with the g_{lum} improved from 10^{-4} to 10^{-2} level (Figure 11b–d). Mechanism study reveals the extensive hydrogen bonding networks between polypeptide and PVA contributes to the stronger chiral transfer and inversed chiral packing pattern of the chromophores. The scope of phosphorescent end groups was finally extended to achieve multicolor afterglow from blue to red (Figure 11e). This work suggests that polypeptide CPL materials do not need to rely only on the primary polypeptide scaffold; secondary matrices and hydrogen-bonding networks may provide additional handles for tuning emission handedness and intensity.

Above research works share two common features: they all employ a polyglutamic acid-based backbone, and they all rely on organic chromophores. In principle, the chiral environment of polyglutamic acid could also induce chiral absorption and/or emission from metal complexes. In this regard, the CPL of lanthanide complexes induced by PLGA reported in 2019 showed a representative example [107]. Detailly, the europium compounds, $EuCl_3$ or $Na_3[Eu(DPA)_3]$ (DPA = pyridine-2,6-dicarboxylic acid), were mixed with fibrils of PLGA in aqueous solutions

and incubated, leading to strong CPL signals at ~590 nm and g_{lum} values up to 2×10^{-2}. With higher sensitivity than VCD, the induced CPL was proposed as a new method for probing protein fibrils.

In addition to polyglutamic acid, poly($_L$-lysine) (PLL) represents another powerful backbone in the design of CPL-active polypeptide materials. In neutral state, PLL also favors the formation of α-helical conformation, while the side-chain free amines provide handrails for hydrogen bonding or forming ion pairs. Utilizing this property, chirality was transferred from PLL templates to disulfonic fluorescent dyes, such as NK 2571, giving large Stokes shift of 230 nm and g_{lum} of 2×10^{-3} (Figure 12a) [108]. Moreover, CPL from clusterization-triggered emission (CTE) was achieved by solid phase co-assembly of PLL and oleate ion (OL) (Figure 12b). Under mechanical pressure, PLL aligned well on the interface of self-assembled oleate bilayers, giving transparent films with ordered multilayer structures. Without the addition of external luminophores, the film generated significant CPL signals at 462 nm with the g_{lum} of 1.6×10^{-2} via the CTE mechanism [109].

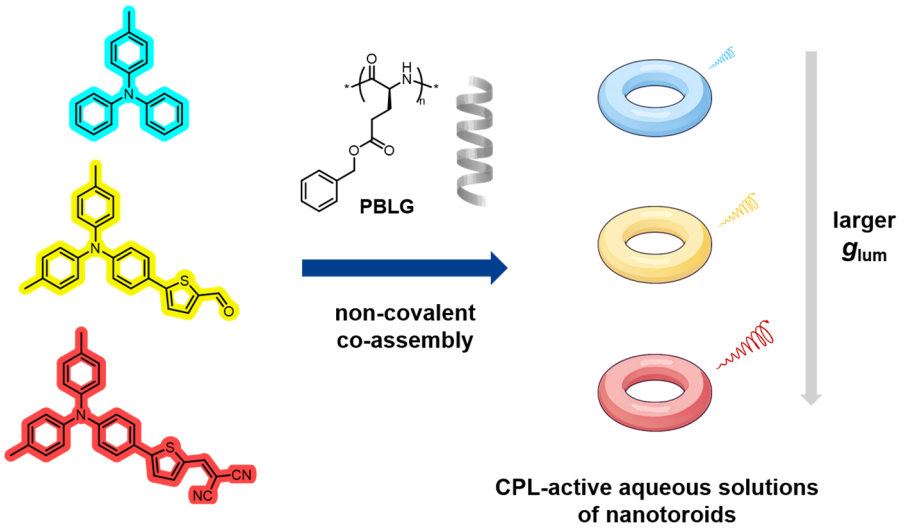


Figure 10. Noncovalent co-assembly of PBLG with achiral triphenylamine derivatives.

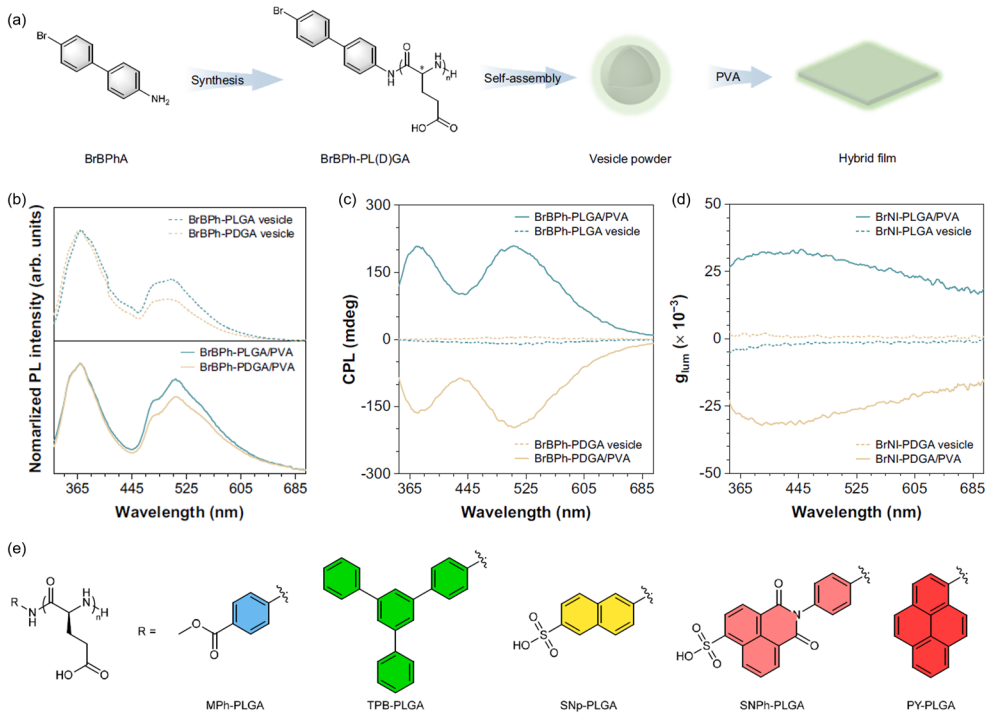


Figure 11. PVA matrix-induced chirality inversion and amplification of CPRTP. (**a**) Representative synthesis of 4-bromobiphenyl (BrBPh)-functionalized PLGA or PDGA and their co-assembly with PVA. (**b**–**d**) Photoluminescence (PL) spectra, CPRTP spectra, and g_{lum} curves for BrBPh-PL(D)GA samples with or without the co-assembly of PVA. (**e**) Scope of phosphorescent end groups studied. (**a**–**e**) Reproduced with permission [106]. Copyright 2026, Springer Nature.

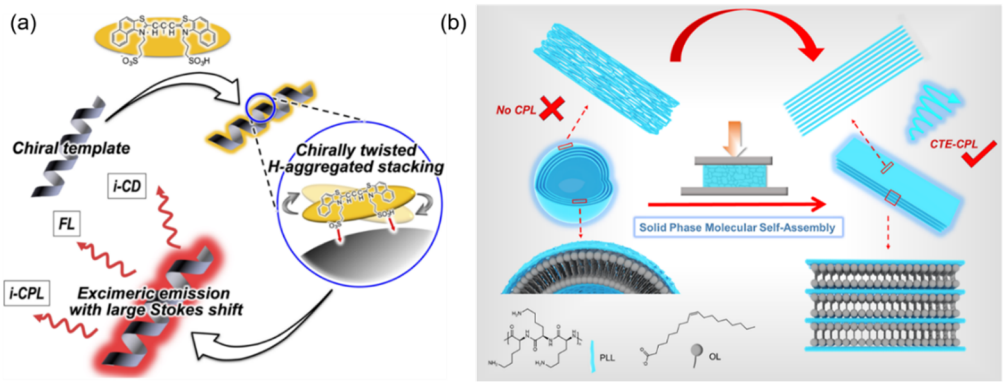


Figure 12. PLL-based CPL-active polypeptide systems. (**a**) Co-assembly of NK 2571 with PLL for CPL and large Stokes shift. Reproduced with permission [108]. Copyright 2023, Wiley-VCH. (**b**) CPL-active films formed by the co-assembly of PLL and sodium oleate. Reproduced with permission [109]. Copyright 2021, Springer Nature.

Taken together, these studies reveal several design principles in common (Table 2). First, chromophore-level chirality is essential. Whether the emissive unit is covalently attached, terminally introduced, or noncovalently co-assembled, it must experience a chiral environment that can be detected by ICD or translated into CPL. Second, *α*-helical secondary structure is a recurring structural origin of chirality transfer. It provides chain stiffness, stereoregularity, and a persistent chiral field. Third, hierarchical assembly is usually required to amplify the optical response. Liquid-crystalline ordering, aqueous aggregation, nanotoroid formation, and polymer-matrix confinement all help convert local chirality into an emissive chiral arrangement.

Table 2. Representative CPL-active NCA-derived polypeptide materials in recent years and their design principles.

System	Scaffold	Luminophore	Incorporation Mode	Assembly/Phase	Key CPL Feature	g_{lum}	Design Principle	Refs.
PGAC	Polyglutamate	Cyanostilbene	Side chain	Chiral smectic C liquid-crystal phase	High solid-state CPL	4.5×10^{-2} (458 nm)	Liquid-crystal organization of emissive mesogens	[25]
TN-PBLG (+TNB)	PBLG	TNB	Terminal (+co-assembly)	Nanotoroids	Aqueous CPL; morphology-dependent	7×10^{-3} (~600 nm)	Terminal AIEgen organized by PBLG nanotoroid (hierarchical co-assembly)	[104,105]
PBLG + TPA	PBLG	TPA derivatives	Noncovalent	Nanotoroids	Multicolor/deep-red CPL	up to 1×10^{-2} (multicolor)	Achiral luminophores organized by PBLG nanotoroid	[18]
PLGA + PVA	PLGA	Phosphorescent unit	Terminal	Aggregates	CPRTP; inversion/amplification; multicolor	up to 3×10^{-2} (multicolor)	Polymer matrix regulates chiral transfer	[106]
PLGA + Eu(III)	PLGA	Eu(III) complex	Coordination	Fibril assembly In aqueous solution	CPL of Lanthanide metal ion	2×10^{-2} (~590 nm)	Chirality transfer from fibril to Eu(III) by coordination	[107]
PLL + disulfonic dyes	PLL	disulfonic dyes	Noncovalent (electrostatic interaction)	Methanol solution	Large Stokes shift	2×10^{-3} (~700 nm)	Dyes organized by *α*-helical PLL	[108]
PLL + OL	PLL	PLL-OL	Noncovalent (electrostatic interaction)	Film	Clusterization-triggered emission	1.6×10^{-2} (462 nm)	Mechanical pressure-driven solid phase co-assembly	[109]

5. Conclusions and Outlook

NCA-derived polypeptides provide a unique polymer platform for hierarchical chiral assembly and chiroptical materials. Their value comes from the combination of synthetic programmability and biomolecule-inspired conformational order. Through NCA ROP, the stereochemistry, chain length, block sequence, topology, side-chain functionality, and terminal groups of polypeptides can be adjusted. These molecular parameters further determine secondary structures such as *α*-helices, *β*-sheets, and coil-like conformations, which serve as the first level of chiral organization. From there, polypeptides can assemble into micelles, vesicles, fibers, spirals, nanotoroids, liquid-crystalline phases, and bulk ordered structures. These hierarchical assemblies provide the structural basis for transferring molecular chirality into optical asymmetry [32].

In chiroptical materials, CD and VCD remain essential tools for probing polypeptide secondary structures, aggregation, and higher-order ordering. ICD further shows whether chirality has been transferred from the

polypeptide scaffold to side-chain, terminal, or noncovalently incorporated chromophores. CPL represents a more demanding function, because emissive chromophores must be arranged in a chiral excited-state environment. Recent examples, including liquid-crystalline polyglutamates, aqueous homopolypeptide nanotoroids, and circularly polarized room-temperature phosphorescent aggregates, demonstrate that NCA-derived polypeptides can indeed serve as programmable scaffolds for emissive chiroptical materials.

Despite these advances, the field of chiroptical NCA-derived polypeptide materials remains at an early stage. Synthetic polypeptides have a long history [33], and chromophore-functionalized, or even CPL-active polypeptides have been studied for decades [85,93]. Nevertheless, the reported systems still rely on a relatively limited set of polypeptide scaffolds, luminophores, and assembly motifs, and general structure–property relationships remain difficult to establish. A particular challenge is that the polypeptide scaffold primarily provides conformational and supramolecular chirality rather than strong emission itself. Efficient chiroptical emission therefore requires the simultaneous optimization of chirality transfer, chromophore organization, photoluminescence quantum yield, and luminescence dissymmetry, which do not necessarily improve in parallel. In addition, hierarchical polypeptide assemblies can be sensitive to concentration, solvent composition, pH, ionic strength, temperature, and processing history. Such responsiveness is attractive for sensing and adaptive materials, but it also presents challenges for long-term structural stability and reproducibility.

Further development is therefore highly desired in both chiroptical performance and material format. Current polypeptide-based CPL materials still have room for improvement in brightness, dissymmetry factor, processability, long-term stability, and batch-to-batch reproducibility. Future studies would benefit from reporting g_{lum} together with quantum yield, lifetime, morphology distribution, concentration dependence, and preparation reproducibility, thereby enabling more meaningful comparison between different material platforms. In addition, most examples are based on solution assemblies, aqueous dispersions, liquid-crystalline phases, or polymer aggregates, whereas processable films, coatings, fibers, elastomers, and device-compatible solid materials remain less developed.

The structural toolbox can be expanded beyond α-helical PBLG-derived systems. β-Sheet-forming polypeptides are comparatively underexplored for CPL materials, even though peptide and amyloid-like assemblies often form twisted ribbons, fibrils, and helical nanostructures. Extending these concepts to NCA-derived β-sheet-rich polypeptides may provide new routes to chromophore organization and CPL generation. Block copolypeptides are another promising direction, because they can couple secondary-structure chirality with nanoscale phase separation and polymer processability. Topology is also an interesting variant to study with. By designing polypeptide materials with topology beyond linear, we may benefit from the unique connectivity of cyclic, star-like, or bottlebrush-like polymers and achieve unrevealed self-assembly structures and chiroptical properties.

Importantly, the most compelling applications of NCA-derived chiroptical materials may not necessarily lie in competing directly with established inorganic, organic small-molecule, or liquid-crystalline materials in conventional optoelectronic devices. Instead, the distinctive combination of molecular chirality, chemical programmability, self-assembly, biodegradability, and potential biocompatibility may create opportunities where the material itself interacts with biological environments or disappear after completing its function. Water-dispersible CPL-active polypeptide nanoparticles, for example, could potentially provide a basis for polarization-resolved bioimaging and chiral biosensing, in which circularly polarized emission offers an additional optical dimension beyond fluorescence intensity or wavelength [110–112]. Environment-responsive changes in polypeptide conformation and assembly could further be translated into changes in CD, CPL intensity, handedness, or emission wavelength, enabling optical reporting of local chemical or biological environments [113,114].

One particularly attractive direction is the development of transient chiroptical materials. Biodegradable CPL-active nanoparticles, fibers, or coatings could potentially serve as temporary optical probes, implantable or wearable sensors, degradable optical tags, or polarization-encoded information materials that function for a defined period and subsequently undergo degradation [115]. In such applications, biocompatibility and biodegradability may distinguish polypeptide-based systems from many persistent inorganic or organic chiroptical materials, especially when direct contact with cells and tissues is necessary. At the same time, these advantages should not be assumed solely from the polypeptide backbone: the toxicity and degradation products of incorporated chromophores and other components must also be evaluated. Moreover, the degradability that is desirable for biomedical or transient applications may conflict with the long-term photochemical and mechanical stability required for displays and conventional optoelectronic devices. Application-specific control over degradation and stability will therefore be essential.

Looking forward, progress will require moving from the demonstration of chiroptical activity toward application-oriented molecular and materials design. Combining NCA polymerization with post-polymerization chromophore installation can broaden the accessible emissive structures, while noncovalent co-assembly with

achiral dyes can enable modular tuning of emission color and excited-state organization. Block copolypeptides and topological polypeptides may provide routes to robust, hierarchically ordered CPL-active materials, whereas hybrid matrices and responsive environments could allow dynamic control over handedness, intensity, lifetime, and emission wavelength. Ultimately, establishing quantitative connections among polymer sequence and topology, secondary structure, hierarchical assembly, chromophore organization, and chiroptical output will be necessary to transform NCA-derived polypeptides from model systems into functional chiroptical materials. Their strongest future opportunities may lie where this structural programmability is combined with properties that conventional chiroptical materials do not readily provide—particularly aqueous compatibility, biodegradability, and transient functionality.

Author Contributions: S.W.: Conceptualization, writing—original draft preparation; M.Z., M.K. and W.W.: Writing—review and editing; Z.L.: Conceptualization, supervision, writing—review and editing. All authors have read and agreed to the published version of the manuscript.

Funding: This research received no external funding.

Institutional Review Board Statement: Not applicable.

Informed Consent Statement: Not applicable.

Data Availability Statement: Not applicable.

Conflicts of Interest: The authors declare no conflict of interest.

Use of AI and AI-Assisted Technologies: During the preparation of this work, the authors used ChatGPT to polish the language and help with literature search. After using this tool/service, the authors reviewed and edited the content as needed and take full responsibility for the content of the published article.

References

1. Zhong, H.; Zhao, B.; Deng, J. Polymer-Based Circularly Polarized Luminescent Materials. *Adv. Opt. Mater.* **2023**, *11*, 2202787. https://doi.org/10.1002/adom.202202787.
2. Puneet, P.; Shao, S.W.; Ho, R.M. Induced Circular Dichroism and Circularly Polarized Luminescence for Block Copolymers with Chiral Communications. *Macromol. Rapid Commun.* **2023**, *44*, 2200369. https://doi.org/10.1002/marc.202200369.
3. Yang, S.; Zhang, S.; Hu, F.; Han, J.; Li, F. Circularly polarized luminescence polymers: From design to applications. *Coord. Chem. Rev.* **2023**, *485*, 215116. https://doi.org/10.1016/j.ccr.2023.215116.
4. Kim, M.; Zhang, M.; Zhu, Y.L.; Yan, Y.; Pu, X.; Choi, W.; Chung, S.; Cho, K.; Kim, J.; Tsukruk, V.; et al. Hierarchical chiral supramolecular assemblies with strong and invertible chiroptical properties. *Science* **2025**, *389*, eadu0296. https://doi.org/10.1126/science.adu0296.
5. Zheng, H.; Li, W.; Li, W.; Wang, X.; Tang, Z.; Zhang, S.X.A.; Xu, Y. Uncovering the Circular Polarization Potential of Chiral Photonic Cellulose Films for Photonic Applications. *Adv. Mater.* **2018**, *30*, 1705948. https://doi.org/10.1002/adma.201705948.
6. Rasines Mazo, A.; Allison-Logan, S.; Karimi, F.; Chan, N.J.A.; Qiu, W.; Duan, W.; O'Brien-Simpson, N.M.; Qiao, G.G. Ring opening polymerization of α-amino acids: Advances in synthesis, architecture and applications of polypeptides and their hybrids. *Chem. Soc. Rev.* **2020**, *49*, 4737–4834. https://doi.org/10.1039/c9cs00738e.
7. Song, Z.; Fu, H.; Wang, R.; Pacheco, L.A.; Wang, X.; Lin, Y.; Cheng, J. Secondary structures in synthetic polypeptides from N-carboxyanhydrides: Design, modulation, association, and material applications. *Chem. Soc. Rev.* **2018**, *47*, 7401–7425. https://doi.org/10.1039/c8cs00095f.
8. Bonduelle, C. Secondary structures of synthetic polypeptide polymers. *Polym. Chem.* **2018**, *9*, 1517–1529. https://doi.org/10.1039/c7py01725a.
9. Skoulas, D.; Christakopoulos, P.; Stavroulaki, D.; Santorinaios, K.; Athanasiou, V.; Iatrou, H. Micelles Formed by Polypeptide Containing Polymers Synthesized Via N-Carboxy Anhydrides and Their Application for Cancer Treatment. *Polymers* **2017**, *9*, 208. https://doi.org/10.3390/polym9060208.
10. Tian, B.; Tao, X.; Ren, T.; Weng, Y.; Lin, X.; Zhang, Y.; Tang, X. Polypeptide-based vesicles: Formation, properties and application for drug delivery. *J. Mater. Chem.* **2012**, *22*, 17404–17414. https://doi.org/10.1039/c2jm31806g.
11. Rathore, O.; Sogah, D.Y. Self-Assembly of β-Sheets into Nanostructures by Poly(alanine) Segments Incorporated in Multiblock Copolymers Inspired by Spider Silk. *J. Am. Chem. Soc.* **2001**, *123*, 5231–5239. https://doi.org/10.1021/ja004030d.
12. Salas-Ambrosio, P.; Morales-Patlan, E.; Cedillo-Servin, G.; Tronnet, A.; Villavicencio, K.P.; Gómez-Lizárraga, K.; Benítez-Martínez, J.A.; Sanchez-Arevalo, F.M.; Velasquillo, C.; Ceapă, C.D.; et al. Electrospinning Lysine-Polypeptide Copolymers: Creating Microfiber Meshes for Biomedical Applications. *ACS Appl. Polym. Mater.* **2024**, *6*, 8733–8744. https://doi.org/10.1021/acsapm.4c00344.

13. Aggeli, A.; Nyrkova, I.A.; Bell, M.; Harding, R.; Carrick, L.; McLeish, T.C.B.; Semenov, A.N.; Boden, N. Hierarchical self-assembly of chiral rod-like molecules as a model for peptide β-sheet tapes, ribbons, fibrils, and fibers. *Proc. Natl. Acad. Sci. USA* **2001**, *98*, 11857–11862. https://doi.org/10.1073/pnas.191250198.
14. Guo, Q.; Fang, R.; Lin, J.; Cai, C. Polypeptide Nanotoroids Formed on Substrate via Solvent Evaporation-Induced Self-Assembly. *Adv. Mater. Interfaces* **2025**, *12*, e00722. https://doi.org/10.1002/admi.202500722.
15. Du, Y.; Li, Y.; Jin, R.; Lin, J.; Cai, C. Triangular Nanotoroids Self-Assembled from Polypeptide Homopolymers: The Formation Route and Mechanisms. *Angew. Chem. Int. Ed.* **2025**, *64*, e202508525. https://doi.org/10.1002/anie.202508525.
16. Gao, W.; Wang, S.; Gao, L.; Lin, J.; Cai, C. Hierarchical Helical Toroids Constructed from One-pot Controllable Self-Assembly of Polypeptides. *Angew. Chem. Int. Ed.* **2026**, *65*, e24375. https://doi.org/10.1002/anie.202524375.
17. Xu, P.; Gao, L.; Cai, C.; Lin, J.; Wang, L.; Tian, X. Helical Toroids Self-Assembled from a Binary System of Polypeptide Homopolymer and its Block Copolymer. *Angew. Chem. Int. Ed.* **2020**, *59*, 14281–14285. https://doi.org/10.1002/anie.202004102.
18. Ye, Y.; Hu, X.; Yang, D.; Gu, Q.; Liu, S.; Jiang, J.; Liu, G.; Du, J. Aqueously dispersed homopolypeptide nanotoroids with tunable circularly polarized luminescence. *Chin. Chem. Lett.* **2026**, *37*, 111844. https://doi.org/10.1016/j.cclet.2025.111844.
19. Jin, R.; Du, Y.; Lin, J.; Cai, C. Homochiral "8"-shaped nanotoroids assembled from polypeptides. *Giant* **2024**, *20*, 100343. https://doi.org/10.1016/j.giant.2024.100343.
20. Jin, R.; Liu, J.; Du, Y.; Wang, L.; Lin, J.; Cai, C. Regulating the Topology of Polypeptide Nanotoroids through Solvent-Triggered Nanofiber Twisting. *Macromolecules* **2026**, *59*, 7595–7604. https://doi.org/10.1021/acs.macromol.6c00499.
21. Robinson, C. Liquid-crystalline structures in solutions of a polypeptide. *Trans. Faraday Soc.* **1956**, *52*, 571–592. https://doi.org/10.1039/tf9565200571.
22. Samulski, E.T.; Tobolsky, A.V. Solid "Liquid Crystal" Films of Poly-γ-benzyl-L-glutamate. *Nature* **1967**, *216*, 997. https://doi.org/10.1038/216997a0.
23. Uematsu, I.; Uematsu, Y. Polypeptide liquid crystals. In *Liquid Crystal Polymers I*; Advances in Polymer Science*;* Platé, N.A., Ed.; Springer-Verlag: Berlin, Heidelberg, Germany, 1984; vol. 59, pp. 37–73.
24. Lin, J.; Abe, A.; Furuya, H.; Okamoto, S. Liquid Crystal Formation Coupled with the Coil−Helix Transition in the Ternary System Poly(γ-benzyl L-glutamate)/Dichloroacetic Acid/Dichloroethane. *Macromolecules* **1996**, *29*, 2584–2589. https://doi.org/10.1021/ma951026r.
25. Chen, Y.; Lu, P.; Yuan, Y.; Zhang, H. Preparation and property manipulation of high efficiency circularly polarized luminescent liquid crystal polypeptides. *J. Mater. Chem. C* **2020**, *8*, 13632–13641. https://doi.org/10.1039/d0tc03276j.
26. Song, Z.; Han, Z.; Lv, S.; Chen, C.; Chen, L.; Yin, L.; Cheng, J. Synthetic polypeptides: From polymer design to supramolecular assembly and biomedical application. *Chem. Soc. Rev.* **2017**, *46*, 6570–6599. https://doi.org/10.1039/c7cs00460e.
27. Ahn, B.; Kwon, W.; Kim, H.; Ree, M. Cooperative and selective self-assembly behaviors of diblock copolypeptides in nanoscale thin films. *Polym. Chem.* **2014**, *5*, 1912–1922. https://doi.org/10.1039/c3py01214j.
28. Ekatan, S.R.; Xue, T.; Song, Z.; Yang, T.; Ndaya, D.; Shaw, M.T.; Cheng, J.; Lin, Y. Thermomechanical Properties of Solid "Liquid Crystalline" Films from Hot-Pressed Synthetic Polypeptides of Various Macromolecular Architectures. *Macromolecules* **2024**, *57*, 2008–2018. https://doi.org/10.1021/acs.macromol.3c02005.
29. Cai, C.; Lin, J.; Lu, Y.; Zhang, Q.; Wang, L. Polypeptide self-assemblies: Nanostructures and bioapplications. *Chem. Soc. Rev.* **2016**, *45*, 5985–6012. https://doi.org/10.1039/c6cs00013d.
30. Hadjichristidis, N.; Iatrou, H.; Pitsikalis, M.; Sakellariou, G. Synthesis of Well-Defined Polypeptide-Based Materials via the Ring-Opening Polymerization of α-Amino Acid *N*-Carboxyanhydrides. *Chem. Rev.* **2009**, *109*, 5528–5578. https://doi.org/10.1021/cr900049t.
31. Deming, T.J. Synthesis of side-chain modified polypeptides. *Chem. Rev.* **2016**, *116*, 786–808. https://doi.org/10.1021/acs.chemrev.5b00292.
32. Song, P.; Lv, J.; Yang, C.; Gu, Q.; Liu, S.; Zhang, Y.; Wang, W.; Zhu, Y.; Du, J. Ring-opening polymerization of N-carboxyanhydrides: An efficient approach toward peptides, peptoids, and functional materials. *Prog. Polym. Sci.* **2025**, *169*, 102013. https://doi.org/10.1016/j.progpolymsci.2025.102013.
33. Kricheldorf, H.R. Polypeptides and 100 Years of Chemistry of α-Amino Acid *N*-Carboxyanhydrides. *Angew. Chem. Int. Ed.* **2006**, *45*, 5752–5784. https://doi.org/10.1002/anie.200600693.
34. Wu, Y.; Chen, K.; Wang, J.; Chen, M.; Dai, W.; Liu, R. Recent Advances and Future Developments in the Preparation of Polypeptides via *N*-Carboxyanhydride (NCA) Ring-Opening Polymerization. *J. Am. Chem. Soc.* **2024**, *146*, 24189–24208. https://doi.org/10.1021/jacs.4c05382.
35. Lu, H.; Wang, J.; Song, Z.; Yin, L.; Zhang, Y.; Tang, H.; Tu, C.; Lin, Y.; Cheng, J. Recent advances in amino acid N-carboxyanhydrides and synthetic polypeptides: Chemistry, self-assembly and biological applications. *Chem. Commun.* **2014**, *50*, 139–155. https://doi.org/10.1039/c3cc46317f.
36. Wang, S.; Lu, H. Unveiling Proton Transfer as the Key Process to Understand and Promote the Ring-Opening Polymerization of *N*-Carboxyanhydrides. *Polym. Sci. Technol.* **2025**, *1*, 76–81. https://doi.org/10.1021/polymscitech.4c00040.

37. Tian, Z.Y.; Zhang, Z.; Wang, S.; Lu, H. A moisture-tolerant route to unprotected α/β-amino acid *N*-carboxyanhydrides and facile synthesis of hyperbranched polypeptides. *Nat. Commun.* **2021**, *12*, 5810. https://doi.org/10.1038/s41467-021-25689-y.
38. Ruggiero, M.T.; Sibik, J.; Orlando, R.; Zeitler, J.A.; Korter, T.M. Measuring the Elasticity of Poly-l-Proline Helices with Terahertz Spectroscopy. *Angew. Chem. Int. Ed.* **2016**, *128*, 6991–6995. https://doi.org/10.1002/ange.201602268.
39. Tsuji, Y.; Yasunaga, T.; Sano, T.; Ushio, H. Kinetic studies of the helix-coil transition in aqueous solutions of poly(α-L-glutamic acid) using the electric field pulse method. *J. Am. Chem. Soc.* **1976**, *98*, 813–818. https://doi.org/10.1021/ja00419a031.
40. Wu, X.; Yang, S.; Njus, J.M.; Nagarajan, R.; Cholli, A.L.; Samuelson, L.A.; Kumar, J. Solvent Specified Conformation in Poly(α-l-glutamic acid) Thin Films. *Biomacromolecules* **2004**, *5*, 1214–1218. https://doi.org/10.1021/bm034540a.
41. Tiffany, M.L.; Krimm, S. New chain conformations of poly(glutamic acid) and polylysine. *Biopolymers* **1968**, *6*, 1379–1382. https://doi.org/10.1002/bip.1968.360060911.
42. Myer, Y.P. The pH-Induced Helix-Coil Transition of Poly-L-lysine and Poly-L-glutamic Acid and the 238-mμ Dichroic Band. *Macromolecules* **1969**, *2*, 624–628. https://doi.org/10.1021/ma60012a012.
43. Bellesia, G.; Shea, J.E. Self-assembly of β-sheet forming peptides into chiral fibrillar aggregates. *J. Chem. Phys.* **2007**, *126*, 245104. https://doi.org/10.1063/1.2739547.
44. Fulara, A.; Lakhani, A.; Wójcik, S.; Nieznańska, H.; Keiderling, T.A.; Dzwolak, W. Spiral Superstructures of Amyloid-Like Fibrils of Polyglutamic Acid: An Infrared Absorption and Vibrational Circular Dichroism Study. *J. Phys. Chem. B* **2011**, *115*, 11010–11016. https://doi.org/10.1021/jp206271e.
45. Park, S.B.; Sung, M.H.; Uyama, H.; Han, D.K. Poly(glutamic acid): Production, composites, and medical applications of the next-generation biopolymer. *Prog. Polym. Sci.* **2021**, *113*, 101341. https://doi.org/10.1016/j.progpolymsci.2020.101341.
46. Carlsen, A.; Lecommandoux, S. Self-assembly of polypeptide-based block copolymer amphiphiles. *Curr. Opin. Colloid Interface Sci.* **2009**, *14*, 329–339. https://doi.org/10.1016/j.cocis.2009.04.007.
47. Dongmo Foumthuim, C.J.; Giacometti, A. Solvent quality and solvent polarity in polypeptides. *Phys. Chem. Chem. Phys.* **2023**, *25*, 4839–4853. https://doi.org/10.1039/d2cp05214h.
48. Cai, C.; Wang, L.; Lin, J. Self-assembly of polypeptide-based copolymers into diverse aggregates. *Chem. Commun.* **2011**, *47*, 11189–11203. https://doi.org/10.1039/c1cc12683k.
49. Chécot, F.; Brûlet, A.; Oberdisse, J.; Gnanou, Y.; Mondain-Monval, O.; Lecommandoux, S. Structure of Polypeptide-Based Diblock Copolymers in Solution: Stimuli-Responsive Vesicles and Micelles. *Langmuir* **2005**, *21*, 4308–4315. https://doi.org/10.1021/la0468500.
50. Xu, W.; Ding, J.; Chen, X. Reduction-Responsive Polypeptide Micelles for Intracellular Delivery of Antineoplastic Agent. *Biomacromolecules* **2017**, *18*, 3291–3301. https://doi.org/10.1021/acs.biomac.7b00950.
51. Bellomo, E.G.; Wyrsta, M.D.; Pakstis, L.; Pochan, D.J.; Deming, T.J. Stimuli-responsive polypeptide vesicles by conformation-specific assembly. *Nat. Mater.* **2004**, *3*, 244–248. https://doi.org/10.1038/nmat1093.
52. Holowka, E.P.; Pochan, D.J.; Deming, T.J. Charged Polypeptide Vesicles with Controllable Diameter. *J. Am. Chem. Soc.* **2005**, *127*, 12423–12428. https://doi.org/10.1021/ja053557t.
53. Jiang, J.; Zhang, X.; Fan, Z.; Du, J. Ring-Opening Polymerization of *N*-Carboxyanhydride-Induced Self-Assembly for Fabricating Biodegradable Polymer Vesicles. *ACS Macro Lett.* **2019**, *8*, 1216–1221. https://doi.org/10.1021/acsmacrolett.9b00606.
54. Li, H.; Cornel, E.J.; Fan, Z.; Du, J. Chirality-controlled polymerization-induced self-assembly. *Chem. Sci.* **2022**, *13*, 14179–14190. https://doi.org/10.1039/d2sc05695j.
55. Grazon, C.; Salas-Ambrosio, P.; Ibarboure, E.; Buol, A.; Garanger, E.; Grinstaff, M.W.; Lecommandoux, S.; Bonduelle, C. Aqueous ring-opening polymerization-induced self-assembly (ROPISA) of N-carboxyanhydrides. *Angew. Chem. Int. Ed.* **2020**, *59*, 622–626. https://doi.org/10.1002/anie.201912028.
56. Grazon, C.; Salas-Ambrosio, P.; Antoine, S.; Ibarboure, E.; Sandre, O.; Clulow, A.J.; Boyd, B.J.; Grinstaff, M.W.; Lecommandoux, S.; Bonduelle, C. Aqueous ROPISA of α-amino acid *N*-carboxyanhydrides: Polypeptide block secondary structure controls nanoparticle shape anisotropy. *Polym. Chem.* **2021**, *12*, 6242–6251. https://doi.org/10.1039/d1py00995h.
57. Tinajero-Díaz, E.; Judge, N.; Li, B.; Leigh, T.; Murphy, R.D.; Topham, P.D.; Derry, M.J.; Heise, A. Poly(l-proline)-Stabilized Polypeptide Nanostructures via Ring-Opening Polymerization-Induced Self-Assembly (ROPISA). *ACS Macro Lett.* **2024**, *13*, 1031–1036. https://doi.org/10.1021/acsmacrolett.4c00400.
58. Cai, C.; Lin, J.; Chen, T.; Wang, X.S.; Lin, S. Super-helices self-assembled from a binary system of amphiphilic polypeptide block copolymers and polypeptide homopolymers. *Chem. Commun.* **2009**, *45*, 2709–2711. https://doi.org/10.1039/b823367e.
59. Cai, C.; Li, Y.; Lin, J.; Wang, L.; Lin, S.; Wang, X.S.; Jiang, T. Simulation-Assisted Self-Assembly of Multicomponent Polymers into Hierarchical Assemblies with Varied Morphologies. *Angew. Chem. Int. Ed.* **2013**, *52*, 7732–7736. https://doi.org/10.1002/anie.201210024.
60. Cao, K.; Du, Y.; Lin, J.; Cai, C. Regulating the Chirality of the Superhelices Self-Assembled from Block Copolymer/Homopolymer Binary Systems by the Mixing Ratio of the Polymers. *Macromolecules* **2024**, *57*, 6514–6521. https://doi.org/10.1021/acs.macromol.4c00474.

61. Vacogne, C.D.; Wei, C.; Tauer, K.; Schlaad, H. Self-Assembly of α-Helical Polypeptides into Microscopic and Enantiomorphic Spirals. *J. Am. Chem. Soc.* **2018**, *140*, 11387–11394. https://doi.org/10.1021/jacs.8b06503.
62. Liu, B.; Fang, R.; Li, W.; Wu, X.; Liu, T.; Lin, M.; Sun, J.; Chen, X. Fast Catalyst-Free Synthesis of Stereoselective Polypeptides via Hierarchical Chiral Assembly. *J. Am. Chem. Soc.* **2024**, *146*, 16558–16566. https://doi.org/10.1021/jacs.4c03281.
63. Yang, C.; Gao, L.; Lin, J.; Wang, L.; Cai, C.; Wei, Y.; Li, Z. Toroid Formation through a Supramolecular "Cyclization Reaction" of Rodlike Micelles. *Angew. Chem. Int. Ed.* **2017**, *56*, 5546–5550. https://doi.org/10.1002/anie.201701978.
64. Fan, L.; Jiang, J.; Sun, Q.; Hong, K.; Cornel, E.J.; Zhu, Y.; Du, J. Fluorescent homopolypeptide toroids. *Polym. Chem.* **2022**, *13*, 1495–1501. https://doi.org/10.1039/d1py01691a.
65. Duke, R.W.; Du Pre, D.B.; Hines, W.A.; Samulski, E.T. Poly(γ-benzyl L-glutamate) helix-coil transition. Pretransition phenomena in the liquid crystal phase. *J. Am. Chem. Soc.* **1976**, *98*, 3094–3101. https://doi.org/10.1021/ja00427a006.
66. Miller, W.G.; Wee, E.L. Liquid crystal-isotropic phase equilibriums in the system poly(γ-benzyl α-L-glutamate)-methylformamide. *J. Phys. Chem.* **1971**, *75*, 1446–1452. https://doi.org/10.1021/j100680a014.
67. Mori, T. Thermally Induced Cholesteric-to-Nematic-to-Cholesteric Transition of Poly(L-glutamic acid) Liquid Crystals. *Polym. J.* **1985**, *17*, 1145–1147. https://doi.org/10.1295/polymj.17.1145.
68. Toriumi, H.; Kusumi, Y.; Uematsu, I.; Uematsu, Y. Thermally Induced Inversion of the Cholesteric Sense in Lyotropic Polypeptide Liquid Crystals. *Polym. J.* **1979**, *11*, 863–869. https://doi.org/10.1295/polymj.11.863.
69. Wu, L.; Müller, E.A.; Jackson, G. Understanding and Describing the Liquid-Crystalline States of Polypeptide Solutions: A Coarse-Grained Model of PBLG in DMF. *Macromolecules* **2014**, *47*, 1482–1493. https://doi.org/10.1021/ma401230x.
70. Tsuboi, K.; Marcelletti, E.; Matsumoto, H.; Ashizawa, M.; Minagawa, M.; Furuya, H.; Tanioka, A.; Abe, A. Preparation of poly(γ-benzyl-L-glutamate) nanofibers by electrospinning from isotropic and biphasic liquid crystal solutions. *Polym. J.* **2012**, *44*, 360–365. https://doi.org/10.1038/pj.2011.137.
71. Mai, Y.; Eisenberg, A. Self-assembly of block copolymers. *Chem. Soc. Rev.* **2012**, *41*, 5969–5985. https://doi.org/10.1039/c2cs35115c.
72. Olsen, B.D.; Segalman, R.A. Self-assembly of rod–coil block copolymers. *Mater. Sci. Eng. R Rep.* **2008**, *62*, 37–66. https://doi.org/10.1016/j.mser.2008.04.001.
73. Fu, X.; Park, J.M.; Liang, R.; Xue, Y.; Zhong, M. Hierarchically structured materials derived from synthetic polymers: Design and bulk self-assembly strategies. *Prog. Polym. Sci.* **2025**, *170*, 102027. https://doi.org/10.1016/j.progpolymsci.2025.102027.
74. Zhou, F.; Ye, T.; Shi, L.; Xie, C.; Chang, S.; Fan, X.; Shen, Z. Synthesis and Self-Assembly of Rod–Rod Block Copolymers with Different Rod Diameters. *Macromolecules* **2013**, *46*, 8253–8263. https://doi.org/10.1021/ma4014687.
75. Rubatat, L.; Kong, X.; Jenekhe, S.A.; Ruokolainen, J.; Hojeij, M.; Mezzenga, R. Self-Assembly of Polypeptide/π-Conjugated Polymer/Polypeptide Triblock Copolymers in Rod−Rod−Rod and Coil−Rod−Coil Conformations. *Macromolecules* **2008**, *41*, 1846–1852. https://doi.org/10.1021/ma702278a.
76. Ibarboure, E.; Papon, E.; Rodríguez-Hernández, J. Nanostructured thermotropic PBLG–PDMS–PBLG block copolymers. *Polymer* **2007**, *48*, 3717–3725. https://doi.org/10.1016/j.polymer.2007.04.046.
77. Ibarboure, E.; Rodríguez-Hernández, J. Supramolecular structures from self-assembled poly(γ-benzyl-l-glutamate)–polydimethylsiloxane–poly(γ-benzyl-l-glutamate) triblock copolypeptides in thin films. *Eur. Polym. J.* **2010**, *46*, 891–899. https://doi.org/10.1016/j.eurpolymj.2010.02.006.
78. Bulheller, B.M.; Rodger, A.; Hirst, J.D. Circular and linear dichroism of proteins. *Phys. Chem. Chem. Phys.* **2007**, *9*, 2020–2035. https://doi.org/10.1039/b615870f.
79. Tsuchihashi, N.; Nomori, H.; Hatano, M.; Mori, S. Circular Dichroism in Lyotropic Liquid Crystals of Polyglutamate Solutions. *Bull. Chem. Soc. Jpn.* **1975**, *48*, 29–32. https://doi.org/10.1246/bcsj.48.29.
80. Keiderling, T.A. Structure of Condensed Phase Peptides: Insights from Vibrational Circular Dichroism and Raman Optical Activity Techniques. *Chem. Rev.* **2020**, *120*, 3381–3419. https://doi.org/10.1021/acs.chemrev.9b00636.
81. Singh, R.D.; Keiderling, T.A. Vibrational circular dichroism of poly(γ-benzyl-L-glutamate). *Biopolymers* **1981**, *20*, 237–240. https://doi.org/10.1002/bip.1981.360200117.
82. Paterlini, M.G.; Freedman, T.B.; Nafie, L.A. Vibrational circular dichroism spectra of three conformationally distinct states and an unordered state of poly(L-lysine) in deuterated aqueous solution. *Biopolymers* **1986**, *25*, 1751–1765. https://doi.org/10.1002/bip.360250915.
83. Gawroński, J.; Grajewski, J. The Significance of Induced Circular Dichroism. *Org. Lett.* **2003**, *5*, 3301–3303. https://doi.org/10.1021/ol0352456.
84. Nomori, H.; Tsuchihashi, N.; Takagi, S.; Hatano, M. Induced Circular Dichroism of Benzyl Chromophores Bound to Helical Polypeptides. *Bull. Chem. Soc. Jpn.* **1975**, *48*, 2522–2526. https://doi.org/10.1246/bcsj.48.2522.
85. Goodman, M.; Kossoy, A. Conformational Aspects of Polypeptide Structure. XIX. Azoaromatic Side-Chain Effects. *J. Am. Chem. Soc.* **1966**, *88*, 5010–5015. https://doi.org/10.1021/ja00973a042.
86. Sisido, M.; Ishikawa, Y.; Itoh, K.; Tazuke, S. Helically arranged azobenzene chromophores along a polypeptide chain. 1. Synthesis and circular dichroism. *Macromolecules* **1991**, *24*, 3993–3998. https://doi.org/10.1021/ma00014a004.

87. Sisido, M.; Ishikawa, Y.; Harada, M.; Itoh, K. Helically arranged azobenzene chromophores along a polypeptide chain. 2. Prediction of conformations and calculation of theoretical circular dichroism. *Macromolecules* **1991**, *24*, 3999–4003. https://doi.org/10.1021/ma00014a005.
88. Ueno, A.; Nohara, M.; Toda, F.; Uno, K.; Iwakura, Y. Synthesis of poly-L-naphthylalanine and its secondary structure. *J. Polym. Sci. Polym. Chem. Ed.* **1975**, *13*, 2751–2762. https://doi.org/10.1002/pol.1975.170131210.
89. Sato, M.; Morikawa, H.; Yoshimoto, M.; Nakahira, T.; Iwaruchi, S. Secondary Structure and Side-Chain Orientation of Poly(L-glutamines) Having Naphthalene Chromophores. *Nippon Kagaku Kaishi* **1992**, *1992*, 1368–1373. https://doi.org/10.1246/nikkashi.1992.1368.
90. Shoji, O.; Nakajima, D.; Annaka, M.; Yoshikuni, M.; Nakahira, T. Highly controlled side-chain chromophore orientation in poly[N5-1-(1-pyrenyl)ethyl-l-glutamines]. *Polymer* **2002**, *43*, 1711–1714. https://doi.org/10.1016/s0032-3861(01)00740-6.
91. Egusa, S.; Sisido, M.; Imanishi, Y. One-dimensional aromatic crystals in solution. 4. Ground- and excited-state interactions of poly(L-1-pyrenylalanine) studied by chiroptical spectroscopy including circularly polarized fluorescence and fluorescence-detected circular dichroism. *Macromolecules* **1985**, *18*, 882–889. https://doi.org/10.1021/ma00147a011.
92. Sisido, M.; Egusa, S.; Imanishi, Y. One-dimensional aromatic crystal in solution. 1. Synthesis, conformation, and spectroscopic properties of poly(L-1-naphthylalanine). *J. Am. Chem. Soc.* **1983**, *105*, 1041–1049. https://doi.org/10.1021/ja00342a065.
93. Sisido, M.; Egusa, S.; Okamoto, A.; Imanishi, Y. Circularly polarized fluorescence of aromatic poly(α-amino acids). *J. Am. Chem. Soc.* **1983**, *105*, 3351–3352. https://doi.org/10.1021/ja00348a074.
94. Shimizu, T.; Sisido, M.; Imanishi, Y.; Higashimura, T. Local conformations of ends of α-helical poly[Glu(OBzl)] studied by circular dichroism of terminal chromophores. *Biopolymers* **1980**, *19*, 1271–1279. https://doi.org/10.1002/bip.1980.360190703.
95. Stryer, L.; Blout, E.R. Optical Rotatory Dispersion of Dyes Bound to Macromolecules. Cationic Dyes: Polyglutamic Acid Complexes. *J. Am. Chem. Soc.* **1961**, *83*, 1411–1418. https://doi.org/10.1021/ja01467a036.
96. Sisido, M.; Akiyama, K.; Imanishi, Y. Poly(α-amino acids) carrying amphiphilic side chains. Synthesis, conformation, hydrophobic binding, and induced circular dichroism. *Macromolecules* **1984**, *17*, 1773–1778. https://doi.org/10.1021/ma00139a025.
97. Sisido, M.; Kishi, R. Liquid-crystalline polymer gels. 3. Facile and reversible cholesteric ordering of dye molecules doped in poly(γ-benzyl L-glutamate) gels. *Macromolecules* **1991**, *24*, 4110–4114. https://doi.org/10.1021/ma00014a023.
98. Kishi, R.; Sisido, M. Liquid-crystalline polymer gels, 4. Photocontrol of dye orientation in a polymer gel having a cholesteric liquid-crystalline order. *Makromol. Chem.* **1991**, *192*, 2723–2732. https://doi.org/10.1002/macp.1991.021921117.
99. Sisido, M.; Narisawa, H.; Kishi, R.; Watanabe, J. Induced circular dichroism from cholesteric polypeptide films doped with an azobenzene derivative. *Macromolecules* **1993**, *26*, 1424–1428. https://doi.org/10.1021/ma00058a036.
100. Narisawa, H.; Kishi, R.; Sisido, M. Photocontrol of orientation of photochromic dichroic dyes in cholesteric polymer films. *Macromol. Chem. Phys.* **1995**, *196*, 1419–1430. https://doi.org/10.1002/macp.1995.021960505.
101. Sang, Y.; Han, J.; Zhao, T.; Duan, P.; Liu, M. Circularly Polarized Luminescence in Nanoassemblies: Generation, Amplification, and Application. *Adv. Mater.* **2020**, *32*, 1900110. https://doi.org/10.1002/adma.201900110.
102. Kumar, J.; Nakashima, T.; Kawai, T. Circularly Polarized Luminescence in Chiral Molecules and Supramolecular Assemblies. *J. Phys. Chem. Lett.* **2015**, *6*, 3445–3452. https://doi.org/10.1021/acs.jpclett.5b01452.
103. Sisido, M.; Okamoto, A.; Egusa, S.; Imanishi, Y. One-Dimensional Aromatic Crystals in Solution VI. Synthesis and Spectroscopic Characterization of Poly(β-9-anthrylmethyl L-aspartate). *Polym. J.* **1985**, *17*, 1253–1261. https://doi.org/10.1295/polymj.17.1253.
104. Jiang, J.; Ma, F.; Dong, R.; Zhang, S.; Zhang, Z.; Tan, H.; Cai, X.; Qiu, Z.; Xiong, Y.; Han, W.; et al. Aqueous Circularly Polarized Luminescence Induced by Homopolypeptide Self-Assembly. *J. Am. Chem. Soc.* **2023**, *145*, 27282–27294. https://doi.org/10.1021/jacs.3c06769.
105. Jiang, J.; Ye, Z.; Zhang, S.; Ma, F.; Lu, L.; Qiu, Z.; Sun, J.; Xiong, Y.; Zhao, Z.; Lam, J.W.Y.; et al. *α*-Helix-Driven Regulation of Aqueous Circularly Polarized Luminescence in Homopolypeptide Self-Assembly. *Aggregate* **2025**, *6*, e70123. https://doi.org/10.1002/agt2.70123.
106. Jiang, J.; Pan, Y.; Zhao, J.; Zhang, S.; Ma, F.; Zhang, Z.; Liu, M.; Qiu, Z.; Zhao, Z.; Sun, J.; et al. Poly(vinyl alcohol) induced chirality inversion and amplification of circularly polarized room-temperature phosphorescence in homopolypeptide aggregates. *Nat. Commun.* **2026**, *17*, 2915. https://doi.org/10.1038/s41467-026-69707-3.
107. Krupová, M.; Kapitán, J.; Bouř, P. Induced Lanthanide Circularly Polarized Luminescence as a Probe of Protein Fibrils. *ACS Omega* **2019**, *4*, 1265–1271. https://doi.org/10.1021/acsomega.8b03175.
108. Yoshida, K.; Kuwahara, Y.; Hano, N.; Horie, Y.; Takafuji, M.; Ryu, N.; Nagaoka, S.; Oda, R.; Ihara, H. Chiral *H*-aggregation-induced large Stokes shift with CPL generation assisted by α-helical poly(L-lysine) substructure. *Chirality* **2023**, *35*, 411–417. https://doi.org/10.1002/chir.23553.

109. Liao, P.; Zang, S.; Wu, T.; Jin, H.; Wang, W.; Huang, J.; Tang, B.Z.; Yan, Y. Generating circularly polarized luminescence from clusterization-triggered emission using solid phase molecular self-assembly. *Nat. Commun.* **2021**, *12*, 5496. https://doi.org/10.1038/s41467-021-25789-9.
110. Li, D.; Jiang, Z.; Liu, X.; Cheng, Y. Recent Advances in Application of Circularly Polarized Luminescence Probes toward Bioimaging Technology. *Chem. Biomed. Imaging* **2026**, *4*, 144–166. https://doi.org/10.1021/cbmi.5c00091.
111. Dai, Y.; Chen, J.; Zhao, C.; Feng, L.; Qu, X. Biomolecule-Based Circularly Polarized Luminescent Materials: Construction, Progress, and Applications. *Angew. Chem. Int. Ed.* **2022**, *61*, e202211822. https://doi.org/10.1002/anie.202211822.
112. Stachelek, P.; MacKenzie, L.; Parker, D.; Pal, R. Circularly polarised luminescence laser scanning confocal microscopy to study live cell chiral molecular interactions. *Nat. Commun.* **2022**, *13*, 553. https://doi.org/10.1038/s41467-022-28220-z.
113. Chen, P.; Fan, H.; Du, S.; Wen, X.; Zhang, L.; Liu, M. Supramolecular chiroptical sensing of chiral species based on circularly polarized luminescence. *Soft Matter* **2024**, *20*, 8937–8946. https://doi.org/10.1039/d4sm00960f.
114. Jhun, B.H.; Park, S.Y.; You, Y. Molecular sensors producing circularly polarized luminescence responses. *Dyes Pigm.* **2023**, *208*, 110786. https://doi.org/10.1016/j.dyepig.2022.110786.
115. Bai, W.; Shin, J.; Fu, R.; Kandela, I.; Lu, D.; Ni, X.; Park, Y.; Liu, Z.; Hang, T.; Wu, D.; et al. Bioresorbable photonic devices for the spectroscopic characterization of physiological status and neural activity. *Nat. Biomed. Eng.* **2019**, *3*, 644–654. https://doi.org/10.1038/s41551-019-0435-y.

Materials and Interfaces

Scilight

Article

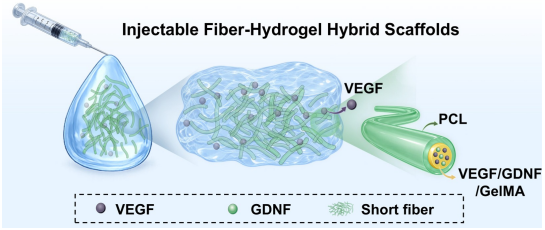
Check for updates

Injectable Fiber-Hydrogel Hybrid Scaffolds for Localized Growth Factor Delivery and Modulation of Vascular and Neuronal Cell Responses

Li Ruan [1], Kaiqin Mo [1], Wenzhe Du [1], Kang Huo [2], Jianfeng Han [2], Jichuan Qiu [3], Feng Tian [1,*], and Jiajia Xue [1,*]

[1] State Key Laboratory of Organic-Inorganic Composites, Beijing Laboratory of Biomedical Materials, Beijing University of Chemical Technology, Beijing 100029, China
[2] Department of Neurology, The First Affiliated Hospital of Xi'an Jiaotong University, Xi'an 710061, China
[3] State Key Laboratory of Crystal Materials, Shandong University, Jinan 250100, China
* Correspondence: fengtian@buct.edu.cn (F.T.); jiajiaxue@mail.buct.edu.cn (J.X.)
Received: 3 July 2026; Revised: 23 September 2026; Accepted: 28 September 2026; Published: 30 September 2026

Abstract: Ischemic stroke is a leading cause of mortality and long-term disability worldwide and is characterized by neuronal loss, vascular impairment, and limited endogenous repair. Recovery after ischemic injury requires coordinated vascular and neural responses. However, the unfavorable post-stroke microenvironment, rapid loss of trophic factors, and poor retention of therapeutic proteins remain major barriers to tissue regeneration. Here, we developed an injectable hierarchical fiber-hydrogel hybrid scaffold for localized delivery of angiogenic and neurotrophic factors. Core-shell gelatin methacryloyl/polycaprolactone (GelMA/PCL) electrospun nanofibers were fabricated by coaxial electrospinning, in which vascular endothelial growth factor (VEGF) and glial cell line-derived neurotrophic factor (GDNF) were encapsulated within the GelMA core, while PCL served as the outer shell. The growth factor-loaded nanofibers were then processed into short fibers and incorporated into a VEGF-containing hydrogel matrix composed of thiol-modified hyaluronic acid/heparin and gelatin. The resulting hybrid scaffold combined an injectable hydrogel network with embedded fibrous components and provided localized release of VEGF and GDNF. *In vitro* studies showed that the hybrid scaffold promoted endothelial cell migration, supported endothelial cell growth, and maintained angiogenic activity under oxygen-glucose deprivation (OGD) conditions. In addition, the scaffold enhanced SH-SY5Y cell growth and supported PC12 neurite outgrowth. By integrating hydrogel-based injectable support, and localized trophic factor delivery, this scaffold provides a biomaterial platform for modulating vascular and neuronal cell responses under ischemia-mimicking conditions, which is promising for recovery after ischemic injury.



Keywords: Ischemic stroke; trophic factors; localized release; core-shell short nanofibers; hybrid scaffold

1. Introduction

Ischemic stroke remains one of the leading causes of mortality and long-term disability worldwide [1,2]. The abrupt interruption of cerebral blood flow induces severe neuronal death, vascular damage, blood-brain barrier disruption, and persistent neuroinflammatory responses, ultimately leading to long-term neurological deficits [3,4]. Although thrombolytic therapy and mechanical thrombectomy have substantially improved acute stroke management, their clinical benefits are limited by narrow therapeutic windows and their inability to rebuild damaged neural tissue [5,6]. Therefore, developing regenerative strategies that promote structural and functional recovery of the injured brain is an important objective in stroke therapy.

Increasing evidence suggests that post-stroke recovery depends on coordinated reconstruction of the neurovascular unit, a dynamic microenvironment composed of neurons, endothelial cells, glial cells, and extracellular matrix components [5,7]. Within the neurovascular unit, vascular remodeling and neuronal regeneration are highly

Copyright: © 2026 by the authors. This is an open access article under the terms and conditions of the Creative Commons Attribution (CC BY) license (https://creativecommons.org/licenses/by/4.0/).
Publisher's Note: Scilight stays neutral with regard to jurisdictional claims in published maps and institutional affiliations.

interdependent. Newly formed blood vessels supply oxygen, nutrients, and trophic cues that support neuronal survival and differentiation, while regenerating neural cells contribute to vascular stabilization and functional integration [8]. Accordingly, simultaneous promotion of angiogenesis and neurogenesis has emerged as a promising strategy for enhancing neurovascular repair after ischemic injury.

Growth factor-based therapies have attracted considerable attention because of their ability to regulate multiple regenerative processes. Among them, vascular endothelial growth factor (VEGF) is a potent angiogenic factor that promotes endothelial cell proliferation, migration, and vascular network formation, while glial cell line-derived neurotrophic factor (GDNF) plays a critical role in neuronal survival, neurite extension, and neural differentiation [9–15]. Despite their therapeutic potential, direct administration of growth factors is limited by rapid degradation, short biological half-life, and poor retention at the injury site [5,16]. Biomaterial-based delivery systems that protect bioactive proteins and enable localized release over a defined period are therefore highly desirable for improving therapeutic efficacy [17–19].

Hydrogels have been widely investigated for neural tissue engineering owing to their high water content, tissue-like mechanical properties, and potential for minimally invasive delivery. In particular, injectable hydrogel precursors with flowable characteristics can be readily administered into irregular defect, enabling conformal filling of the lesion site and rapid in situ gelation to establish a three-dimensional regenerative microenvironment [20–22]. However, hydrogels alone generally provide limited structural guidance for tissue regeneration and may show limited retention of encapsulated bioactive agents because of relatively rapid diffusion [20–22].

Electrospun fibrous materials offer tunable morphology, orientation, and composition for tissue-engineering applications. Polymeric electrospun fibers and microfibers provide versatile platforms for structural design, functionalization, and biomedical applications [23–25]. Beyond structural support, electrospun nanofibers can also be used for biomolecule delivery and release regulation [26–28]. In particular, core-shell nanofibers fabricated by coaxial electrospinning can physically isolate sensitive biomolecules within the fiber core, thereby protecting their bioactivity during fabrication and regulating release through the surrounding shell layer [29–31]. This compartmentalized structure separates the bioactive core from the protective shell and can improve protein preservation and delivery performance [32,33]. However, the continuous morphology of electrospun nanofibers limits their suitability for minimally invasive injection and their ability to conform to irregular lesion cavities. Processing nanofibers into short fibers can improve their injectability, dispersibility, and integration within hydrogel matrices [23,34,35]. Recent studies have demonstrated that incorporating short electrospun fibers into hydrogels enables hierarchical fiber-hydrogel composites that combine biomimetic fibrous architecture, structural support, and tissue-like microenvironments [36–40]. Such hybrid systems have shown promise in musculoskeletal and other soft-tissue regeneration, whereas their application in ischemic brain repair remains largely unexplored. Ischemic brain injury presents additional challenges, including irregular lesion cavities, the extremely soft mechanical properties of brain tissue, and the need for coordinated neurovascular regeneration and appropriately timed therapeutic delivery.

In this study, we developed an injectable fiber-hydrogel hybrid scaffold by incorporating VEGF/GDNF-loaded gelatin methacryloyl/polycaprolactone (GelMA/PCL) core-shell short electrospun fibers into a VEGF-containing hydrogel matrix composed of thiol-modified hyaluronic acid/heparin and gelatin. The hierarchical architecture combines an injectable hydrogel matrix with embedded short fibrous components to enable localized delivery of VEGF and GDNF. The scaffold was evaluated under oxygen-glucose deprivation (OGD) conditions for its effects on endothelial cell migration, angiogenic activity, SH-SY5Y cell metabolic activity, and PC12 neurite outgrowth. This study aimed to establish a fiber-hydrogel platform for localized delivery of angiogenic and neurotrophic factors and coordinated modulation of vascular and neuronal cellular responses under ischemia-mimicking conditions.

2. Experimental Section

2.1. Materials

PCL (M_n = 80,000) was purchased from Aladdin Biochemical Technology Co., Ltd. (Shanghai, China). GelMA was obtained from EFL Biotechnology Co., Ltd. (Suzhou, China). VEGF and GDNF were purchased from Abcam (Cambridge, UK) and Wuhan Huamei Bioengineering Co., Ltd. (Wuhan, China), respectively. Human VEGF and GDNF enzyme-linked immunosorbent assay (ELISA) kits were supplied by Wuhan Huamei Bioengineering Co., Ltd. Cell Counting Kit-8 (CCK-8) and Live/Dead Cell Viability/Cytotoxicity Assay Kit were purchased from Solarbio Life Sciences (Beijing, China). Alexa Fluo 555 phalloidin, 4′,6-diamidino-2-phenylindole (DAPI), and Alexa Fluor 488-conjugated secondary antibody were obtained from Thermo Fisher Scientific (Waltham, MA, USA). Anti-neurofilament 200 (NF200) antibody (1:500) was purchased from Sigma-Aldrich.

The injectable hydrogel precursor, HyStem-HP, composed of thiol-modified hyaluronic acid/heparin, gelatin, and a polyethylene glycol diacrylate (PEGDA) crosslinker, was obtained from Advanced BioMatrix (Carlsbad, CA, USA). All other reagents were of analytical grade and used as received unless otherwise stated.

2.2. Fabrication of Hybrid Scaffolds

Growth factor-loaded GelMA@PCL core-shell nanofibers were fabricated by coaxial electrospinning. Briefly, PCL and GelMA were separately dissolved in trifluoroethanol at concentrations of 10% *w*/*v*. Lithium phenyl-2,4,6-trimethylbenzoylphosphinate (0.25% *w*/*v*) was added to the GelMA solution as a photoinitiator. For the preparation of VEGF/GDNF-loaded nanofibers, VEGF and GDNF were added to the GelMA core solution at a final concentration of 10 μg/mL immediately before electrospinning. During coaxial electrospinning, the GelMA solution containing VEGF and GDNF was used as the core phase, while the PCL solution was used as the shell phase. Coaxial electrospinning was performed at an applied voltage of 15 kV, with the core and shell flow rates set at 0.3 and 1.0 mL/h, respectively. The nanofibers were collected on a rotating drum collector at 1300 rpm to obtain aligned nanofibrous membranes. During the 6 h electrospinning process, the GelMA core solution containing VEGF and GDNF was freshly prepared every hour to minimize prolonged exposure to trifluoroethanol and preserve the bioactivity of the encapsulated growth factors. The collected membranes were then exposed to 405 nm light (10 mW/cm^2) for 30 s to photocrosslink the GelMA core. Oxygen plasma treatment was subsequently performed at 30 W for 20 s to improve the surface hydrophilicity of the nanofibers. To visualize the separate core and shell streams during coaxial electrospinning, rhodamine B and indocyanine green (ICG) were separately incorporated into the GelMA core and PCL shell solutions, respectively, before electrospinning.

The aligned core-shell nanofibrous membranes were processed into short fiber fragments by cryosectioning. Briefly, the membranes were cut into 1.5 × 1.5 cm^2 pieces, embedded in optimal cutting temperature compound, and frozen at −20 °C. The frozen fiber blocks were cryosectioned into short fiber fragments with approximate dimensions of 100 × 50 μm^2. Residual compound was removed by repeated washing with deionized water, followed by ultrasonic dispersion for 30 min. The dispersed short fibers were then lyophilized and stored for subsequent use.

For the fabrication of the injectable growth factor-loaded hybrid scaffold, two flowable precursor solutions were prepared according to the manufacturer's protocol. The first precursor consisted of thiol-modified hyaluronic acid/heparin (10 mg) and gelatin (10 mg) dissolved in 2 mL of phosphate-buffered saline (PBS), into which soluble VEGF and VEGF/GDNF-loaded GelMA@PCL short fibers were uniformly dispersed. The second precursor contained the PEGDA crosslinker (5 mg in 0.5 mL). Upon co-injection, the two precursor solutions rapidly mixed and initiated thiol-mediated crosslinking, enabling in situ hydrogel formation after incubation at 37 °C for 20 min. The final concentrations of free VEGF and VEGF/GDNF-loaded short fibers in the hybrid hydrogel precursor were 100 ng/mL and 5 mg/mL, respectively. Pristine hybrid scaffolds containing 5 mg/mL pristine GelMA@PCL short fibers without growth factors were prepared as controls.

2.3. Characterization of Hybrid Scaffolds

The core-shell architecture of the electrospun nanofibers was characterized using transmission electron microscopy (TEM, HT7700, Hitachi, Japan). The morphology of the electrospun nanofibers, short fibers, hydrogels, and hybrid scaffolds was examined by scanning electron microscopy (SEM, S-4800, Hitachi, Japan). The fiber diameter was quantified using ImageJ by measuring 30 randomly selected fibers per sample from representative SEM images, and the results were presented as mean ± SD. Fiber alignment was independently evaluated using a fast Fourier transform-based image analysis in ImageJ. Briefly, selected regions of the SEM images were subjected to 2D fast Fourier transform to generate the corresponding Fourier spectra. The angular distribution of the Fourier intensity was subsequently analyzed to obtain the fiber orientation distribution, which was used to characterize the overall alignment of the fibrous membranes. For hydrogel-based samples, freeze-dried specimens were used to examine scaffold morphology and the distribution of short fibers within the dried matrix. The surface hydrophilicity of the nanofibers before and after plasma treatment was evaluated by water contact angle measurements using an OCA20 contact angle analyzer (Krüss, Germany).

To evaluate injectability at different gelation times, the two precursor solutions were mixed and incubated at 37 °C for 0, 10, and 20 min. At each time point, the hybrid hydrogel was loaded into a syringe and manually extruded through a 26 G needle, and the injection process was photographed. The rheological properties of the gelled hybrid hydrogel (d = 5 mm) were characterized using a rotational rheometer.

The degradation behavior of the nanofibers and hybrid scaffolds was evaluated in PBS at 37 °C under gentle shaking. PCL nanofibers and growth factor-loaded core-shell nanofibers (Fiber-GF) were prepared as circular

samples with a diameter of 15.6 mm. Pristine hydrogels and hybrid scaffolds were prepared with a volume of 350 μL. Each sample was immersed in 500 μL PBS and collected at predetermined time points. After washing with deionized water, the samples were lyophilized and weighed. The remaining mass was calculated as the percentage of dry weight relative to the initial dry weight.

To investigate the release of VEGF and GDNF, hybrid scaffolds with a volume of 100 μL were incubated in 100 μL PBS at 37 °C. At predetermined time points (2, 4, 6, 8, 10, 12, and 14 days), the release medium was completely collected and replaced with an equal volume of fresh PBS. The concentrations of VEGF and GDNF in the collected media were quantified using ELISA kits according to the manufacturers' instructions, and cumulative release was calculated by summing the amounts measured at each time point. The final cumulative released amount was considered the total releasable amount of each growth factor from the scaffold and was used to determine the corresponding dose for the free growth factor control groups.

2.4. In Vitro Evaluation of Angiogenic Activity under OGD Conditions

An OGD model was established to simulate ischemic injury *in vitro*. Briefly, human umbilical vein endothelial cells (HUVECs) were cultured in glucose-free medium and placed in an anaerobic chamber with less than 1% O_2 for 1 h before subsequent experiments. After OGD treatment, cells were assigned to four groups: untreated control group (Blank), free VEGF group (Free-VEGF), scaffold without growth factors group (Scaffold), and growth factor-loaded hybrid scaffold group (Scaffold-GF). The Free-VEGF group was treated with free VEGF at a dose equivalent to the total releasable amount from 100 μL of the Scaffold-GF scaffold (19.6 ± 3.2 ng per 100 μL scaffold). Scaffold extracts were prepared by incubating scaffolds with a volume of 100 μL in 500 μL serum-free DMEM for 24 h, followed by filtration through a 0.22 μm membrane. For the scratch assay, OGD-treated HUVECs were seeded into 24-well plates at a density of 1×10^4 cells per well and cultured until a confluent monolayer formed. A linear wound was generated using a sterile 200 μL pipette tip, and different scaffold extracts were then added. After 24 h of incubation, cells were fixed with 3% glutaraldehyde, permeabilized with 0.1% Triton X-100, blocked with 1% bovine serum albumin, and stained with Alexa Fluor 555 phalloidin and DAPI. The remaining wound area was quantified using ImageJ.

For cell growth analysis, sterilized scaffolds (100 μL) were placed in 24-well plates, and OGD-treated HUVECs were seeded at a density of 1×10^4 cells per well. Cell growth was evaluated on days 1, 3, 5, and 7 using the CCK-8 assay. Cell viability and cytocompatibility were further assessed by Live/Dead staining on day 7 using calcein-AM and propidium iodide, followed by fluorescence microscopy.

For the tube formation assay, Matrigel was diluted with serum-free DMEM at a volume ratio of 1:1 on ice and added to 24-well plates. After 45 min at 37 °C, OGD-treated HUVECs were seeded onto Matrigel at a density of 3×10^4 cells per well and then incubated with different scaffold extracts prepared as described in the scratch assay. After 4 h, capillary-like networks were imaged using optical microscopy. Total number of junctions, total vessel length, and vessel percentage area were quantified using ImageJ.

2.5. In Vitro Evaluation of Neural Cell Growth and Differentiation under OGD Conditions

SH-SY5Y and PC12 cells were used to evaluate the neuroprotective and neuroregenerative effects of the hybrid scaffold under ischemia-mimicking conditions. Briefly, cells were cultured in glucose-free medium and placed in an anaerobic chamber with less than 1% O_2 for 1 h before subsequent experiments. After OGD treatment, cells were assigned to four groups: untreated control group (Blank), free GDNF group (Free-GDNF), scaffold without growth factors group (Scaffold), and growth factor-loaded hybrid scaffold group (Scaffold-GF). The Free-GDNF group was treated with free GDNF at a dose equivalent to the total releasable amount from 100 μL of the Scaffold-GF scaffold (9.9 ± 1.8 ng).

For cell growth analysis, SH-SY5Y neuroblastoma cells were cultured in DMEM supplemented with 10% fetal bovine serum at 37 °C. After OGD treatment, scaffolds (100 μL) were placed in 24-well plates, and SH-SY5Y cells were seeded at 1×10^4 cells per well. Cell growth was assessed on days 1, 3, and 5 using the CCK-8 assay. Cell viability and cytocompatibility was evaluated by Live/Dead staining on day 5 and observed using fluorescence microscopy.

For neuronal differentiation, OGD-treated PC12 cells were seeded into 24-well plates and cultured in differentiation medium containing nerve growth factor (NGF) at 50 ng/mL. To evaluate the effects of growth factors released from the scaffolds while minimizing direct physical contact between the scaffolds and PC12 cells, 200 μL of the hybrid scaffold was placed in the upper chamber of each Transwell insert. After 10 days of co-culture, cells were fixed and immunostained with anti-NF200 antibody, followed by Alexa Fluor 488-conjugated

secondary antibody. Cell nuclei were counterstained with DAPI. Neurite outgrowth was visualized using confocal laser scanning microscopy and quantitatively analyzed using ImageJ.

2.6. Statistica Analysis

All experiments included at least three parallel samples, and data are presented as mean ± standard deviation (SD). Statistical analyses were performed using GraphPad Prism 10. Comparisons between two groups were performed using Student's t-test. Comparisons among more than two groups were performed using one-way analysis of variance (ANOVA), followed by Tukey's multiple-comparisons test. Statistical significance was defined as $p < 0.05$.

3. Results and Discussion

3.1. Fabrication and Characterization of Injectable Fiber-Hydrogel Hybrid Scaffolds

VEGF/GDNF-loaded GelMA@PCL core-shell nanofibers were fabricated by coaxial electrospinning, using the VEGF/GDNF-containing GelMA solution as the core phase and the PCL solution as the shell phase. In this configuration, the hydrophilic GelMA core provided a compartment for protein encapsulation, while the PCL shell maintained the fibrous morphology and was expected to retard the outward diffusion of the loaded proteins. As shown in the inset of Figure 1a, rhodamine B and ICG were used to visualize the core and shell streams within the coaxial needle, respectively, illustrating their spatially separated configuration during electrospinning. The TEM image further showed the core-shell structure of the resulting nanofibers (Figure 1a). SEM observation further confirmed the formation of continuous and uniform nanofibers, with an average diameter of 940 ± 180 nm (Figures 1b and S1). The as-spun nanofibers exhibited a water contact angle of 120.5°, reflecting the hydrophobic nature of the PCL-rich surface. After oxygen plasma treatment, the water contact angle decreased to 53.4°, indicating improved surface wettability (Figure S2).

The electrospun nanofiber membranes were then processed into short fibers by cryosectioning followed by ultrasonic dispersion. Optical microscopy confirmed that the resulting GelMA@PCL short fibers had an average length of 58.5 ± 20.2 μm, allowing their homogeneous dispersion within the thiol-modified hyaluronic acid/heparin and gelatin precursor (Figure 1c). The injectable system comprised two precursors: a thiol-modified hyaluronic acid/heparin and gelatin solution containing soluble VEGF and short fibers, and PEGDA crosslinker solution. Upon co-injection, the two flowable precursor solutions rapidly mixed and underwent thiol-mediated crosslinking, enabling rapid in situ gelation to form a stable fiber-hydrogel hybrid scaffold. The morphology of the hydrogel-based scaffolds was examined by SEM after freeze-drying. The pristine HyStem-HP hydrogel exhibited a porous interconnected morphology (Figure 1d). After incorporation of short fibers, the hybrid scaffold maintained a similar porous architecture, with short fibers distributed throughout the hydrogel matrix (Figure 1e).

The injectability of the hybrid hydrogel was evaluated at 0, 10, and 20 min after mixing the two precursor solutions (Figure S3a). The hydrogel could be injected through a 26 G needle at all tested time points, including after gelation at 37 °C for 20 min. Rheological analysis of the gelled hydrogel further showed shear-thinning behavior, with viscosity decreasing as the shear rate increased (Figure S3b). These results demonstrate that the hybrid hydrogel remained injectable through a 26 G needle under the tested conditions.

The mass retention of different scaffold components was evaluated in PBS at 37 °C. PCL nanofibers showed minimal mass loss over 30 days, whereas Fiber-GF showed approximately 24% mass loss during the same period (Figure 1f). This mass decrease was mainly associated with the hydrated GelMA core and the release or loss of encapsulated components, while the PCL shell remained relatively stable. For the hydrogel-based samples, the pristine HyStem-HP hydrogel retained 29.2 ± 6.0% of its initial mass after 30 days, whereas the hybrid scaffold retained 47.1 ± 12.9% due to slower degradation of the embedded nanofibers (Figure 1g).

Each 100 μL of hybrid scaffold contained 19.6 ± 3.2 ng of VEGF and 9.9 ± 1.8 ng of GDNF, confirming the successful incorporation of both types of growth factors in the scaffold. The release profiles of VEGF and GDNF from the hybrid scaffold were further quantified by ELISA. Both growth factors showed an early release phase during the initial incubation period, followed by a marked decrease in release rate at later time points (Figure 1h,i). VEGF release reached 19.6 ± 3.2 ng by day 8 and was no longer detectable at day 10, whereas GDNF release remained detectable through day 10, reaching 9.9 ± 1.8 ng, but was no longer detectable at day 12. The resulting release profile from the hydrogel matrix and embedded core-shell short fibers may provide locally available angiogenic and neurotrophic cues during the initial cellular response to ischemic injury.

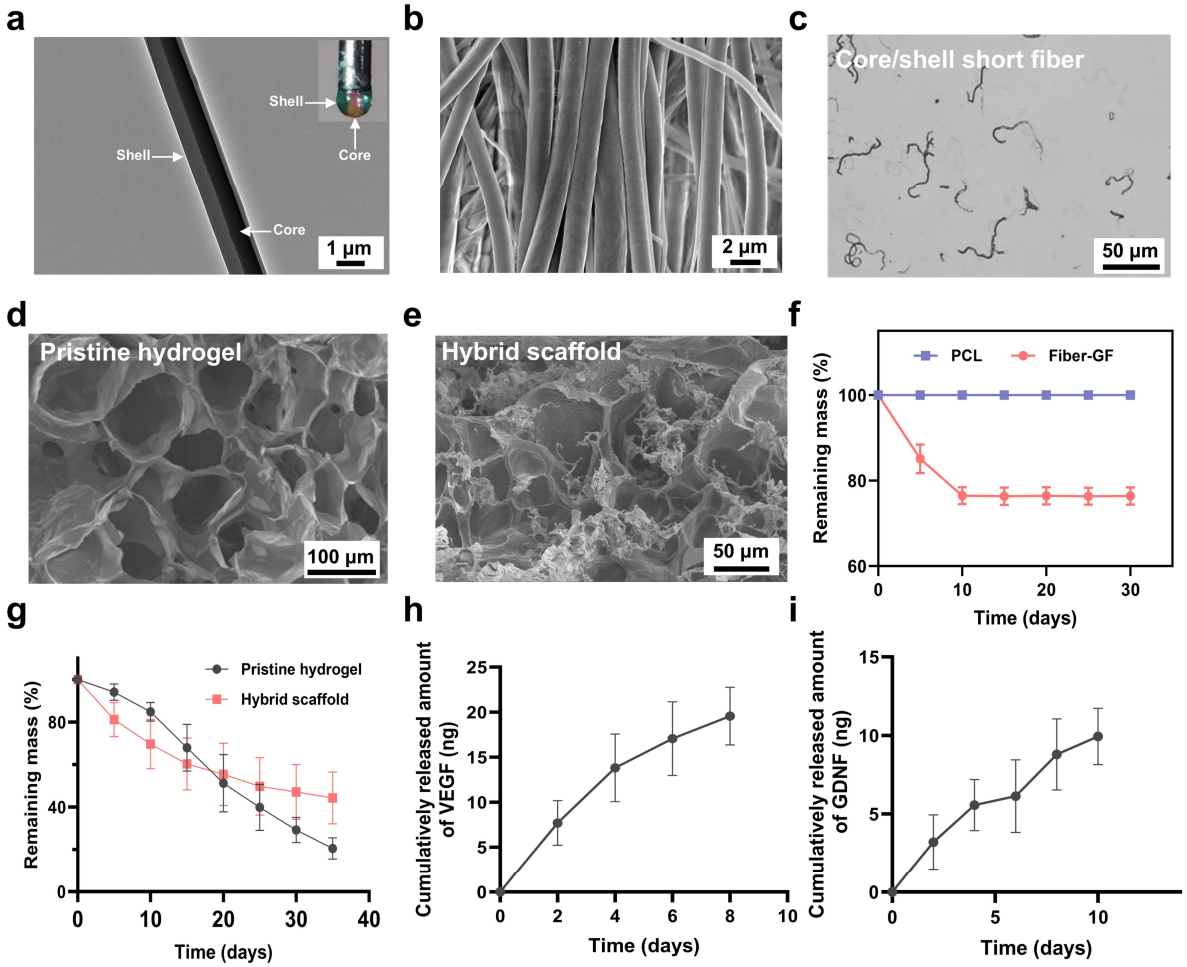


Figure 1. Characterization of GelMA@PCL short fibers and hybrid scaffolds. (**a**) TEM image of GelMA@PCL core-shell nanofibers, with the inset showing the spatially separated core and shell streams within the coaxial needle labeled with rhodamine B and ICG, respectively. (**b**) SEM image of GelMA@PCL core-shell nanofibers. (**c**) Optical microscopy image of GelMA@PCL short fibers. (**d**,**e**) SEM images of freeze-dried (**d**) pristine HyStem-HP hydrogel and (**e**) GelMA@PCL short fiber/HyStem-HP hybrid scaffold, respectively. (**f**) Mass retention profile of PCL nanofibers and Fiber-GF in PBS at 37 °C. (**g**) Mass retention profiles of pristine hydrogel and hybrid scaffold in PBS at 37 °C. (**h**,**i**) Cumulatively released profiles of (**h**) VEGF and (**i**) GDNF from the hybrid scaffold, respectively. Data are presented as mean ± SD (n = 3).

3.2. Regulation of Endothelial Cell Migration, Growth, and Tube Formation under OGD Conditions

Endothelial cell migration is an early event during angiogenesis and is important for vascular remodeling after ischemic injury. To evaluate the effect of the hybrid scaffold on endothelial migration under ischemic conditions, HUVECs were first subjected to OGD for 1 h and then assigned to the Blank, Free-VEGF, Scaffold, and Scaffold-GF groups. The cells were treated with basal culture medium, free VEGF-containing medium, scaffold extract, or Scaffold-GF extract, respectively, and their migratory response was evaluated using a scratch assay. After incubation for 24 h, HUVECs in the Blank group showed limited migration into the scratched area, indicating impaired endothelial cell motility after OGD treatment (Figure 2a). In contrast, the Free-VEGF, Scaffold, and Scaffold-GF groups showed reduced remaining wound areas, suggesting improved cell migration after treatment. The Scaffold group also reduced the remaining wound area compared with the Blank group, indicating that the scaffold extract itself provided a favorable environment for HUVECs migration. Quantitative analysis showed that the Scaffold-GF group exhibited the smallest remaining wound area, reaching 10.1 ± 0.6%, while the Free-VEGF group showed a comparable value of 11.4 ± 1.1% (Figure 2b). These results indicate that the VEGF-containing hybrid scaffold extract retained pro-migratory activity under OGD conditions.

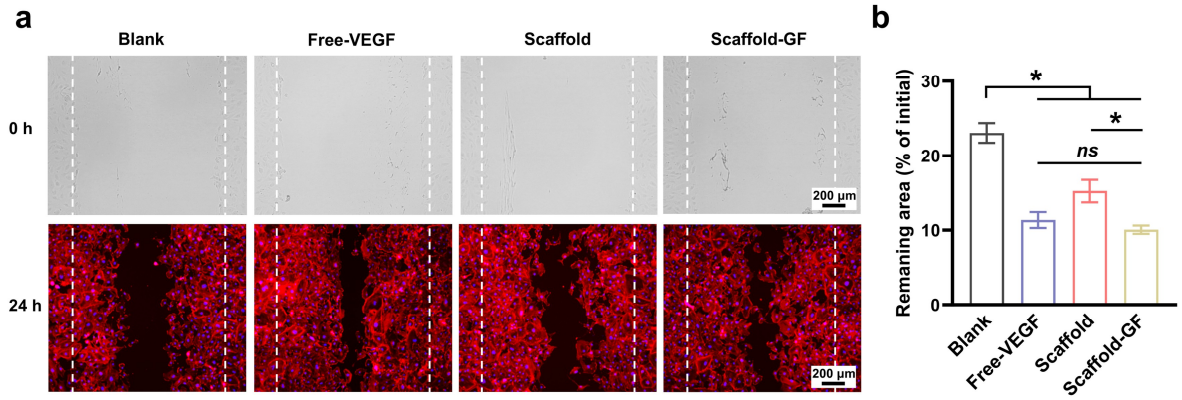


Figure 2. Effect of hybrid scaffolds on HUVECs migration under OGD conditions. (**a**) Representative images of the scratch assay by OGD-treated HUVECs after incubation with basal culture medium, free VEGF-containing medium, scaffold extract, or Scaffold-GF extract at 0 and 24 h. F-actin was stained with phalloidin, and nuclei were stained with DAPI. White dashed lines indicate the initial scratch boundaries. (**b**) Quantification of the remaining wound area after 24 h. Data are presented as mean ± SD (n = 3). Statistical significance was analyzed using one-way ANOVA followed by Tukey's multiple-comparisons test. * $p < 0.05$; n.s., not significant.

The effect of the scaffold on endothelial cell growth was further evaluated using the CCK-8 assay. As shown in Figure 3a, the optical density (OD) value increased gradually from day 1 to day 7 in all groups. On days 3, 5, and 7, the Free-VEGF, Scaffold, and Scaffold-GF groups showed higher OD values than the Blank group. The increased OD value in the Scaffold group suggests that the scaffold matrix itself may contribute to the cellular response. This effect may be associated with the presence of gelatin and hyaluronic acid/heparin, which have been reported to support cell–matrix interactions and cellular activity [41–43]. The Scaffold-GF group showed a further increase in the OD value compared with the Scaffold group, suggesting an additional effect of the released growth factors. Live/Dead staining at day 7 showed predominantly viable cells with few dead cells in all groups, indicating good cytocompatibility of the scaffolds (Figure 3b).

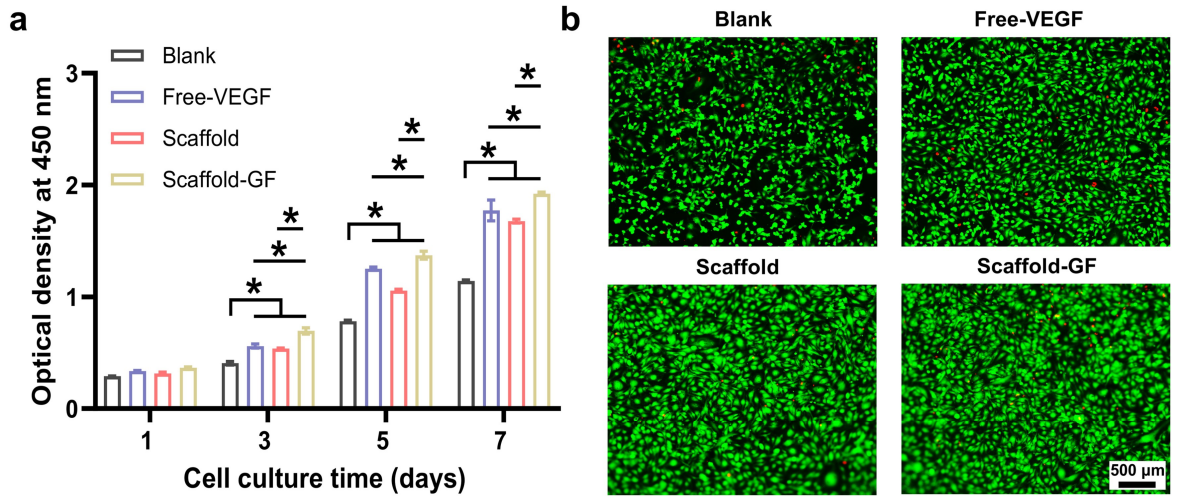


Figure 3. (**a**) OD values of HUVECs cultured with different scaffolds for 1, 3, 5, and 7 days, measured using the CCK-8 assay. (**b**) Live/Dead staining of HUVECs at day 7 (green: live; red: dead). Data are presented as mean ± SD (n = 3). At each time point, statistical significance among groups was analyzed using one-way ANOVA followed by Tukey's multiple-comparisons test. * $p < 0.05$.

Functional angiogenic activity was evaluated using a Matrigel tube formation assay. After OGD treatment, HUVECs were seeded on Matrigel and incubated with basal culture medium, free VEGF-containing medium, scaffold extract, or Scaffold-GF extract. After 4 h of incubation, HUVECs in the Free-VEGF and Scaffold-GF groups formed more evident capillary-like networks than those in the Blank and Scaffold groups (Figure 4a). Quantitative analysis showed that total number of junctions, total vessel length, and vessel percentage area were increased in the Free-VEGF and Scaffold-GF groups compared with the Blank and Scaffold groups (Figure 4b). No significant difference was observed between the Free-VEGF and Scaffold-GF groups, although Free-VEGF

showed a slight trend toward higher tube formation parameters. This result is reasonable because the tube formation assay is a short-term assay in which soluble VEGF can directly stimulate endothelial network formation. The comparable response in the Scaffold-GF group indicates that the scaffold-derived growth factors retained angiogenic bioactivity under OGD conditions.

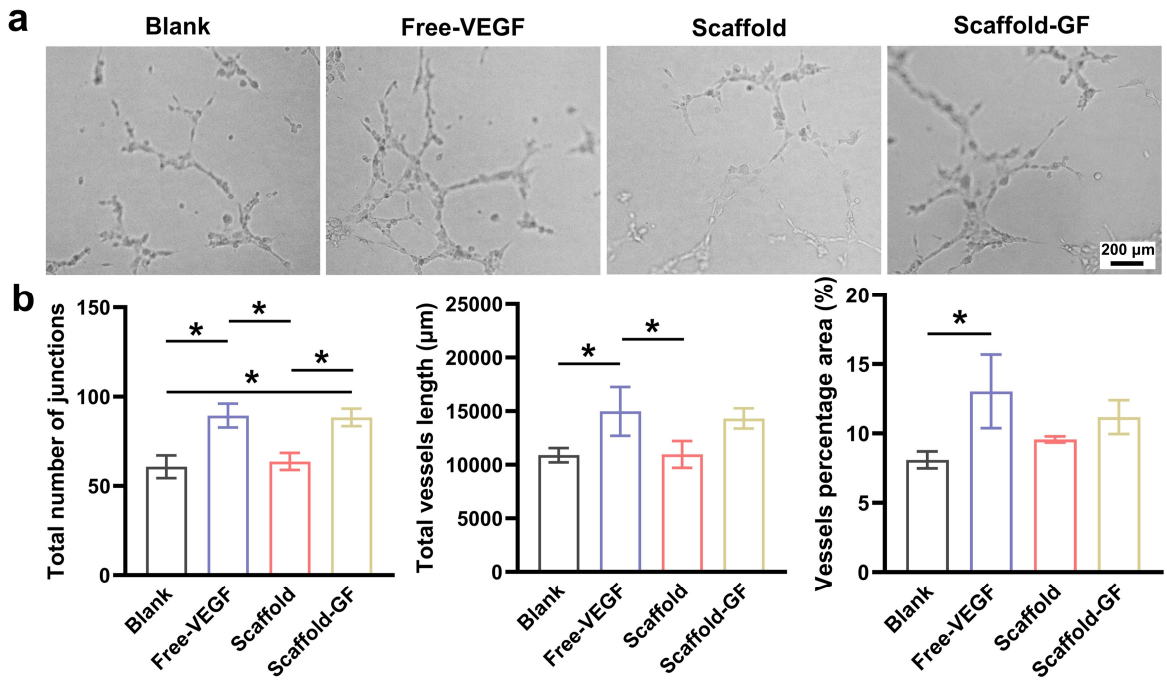


Figure 4. Effect of hybrid scaffolds on HUVECs tube formation under OGD conditions. (**a**) Representative images of capillary-like networks formed by OGD-treated HUVECs on Matrigel after incubation with basal culture medium, free VEGF-containing medium, scaffold extract, or Scaffold-GF extract for 4 h. (**b**) Quantitative analysis of total number of junctions, total vessel length, and vessel percentage area. Data are presented as mean ± SD (n = 3). Statistical significance was analyzed using one-way ANOVA followed by Tukey's multiple-comparisons test. * $p < 0.05$.

3.3. SH-SY5Y Cell Growth and PC12 Neurite Differentiation under OGD Conditions

Supporting neuronal cell survival and neurite outgrowth is important for neural repair after ischemic injury. To evaluate the effect of the hybrid scaffold on neuronal cell behavior, SH-SY5Y cells were subjected to OGD for 1 h and then treated with basal culture medium (Blank), free GDNF-containing medium (Free-GDNF), pristine scaffold (Scaffold), or growth factor containing scaffold (Scaffold-GF), respectively. Cell growth was evaluated on days 1, 3, and 5 using the CCK-8 assay. As shown in Figure 5a, the OD values increased over time in all groups. On days 3 and 5, the Free-GDNF group showed higher OD values than the Blank and Scaffold groups. The Scaffold-GF group exhibited the highest OD values among the tested groups, suggesting a favorable effect of the growth factor-loaded scaffold on SH-SY5Y cell growth under OGD conditions. Live/Dead staining on day 5 showed predominantly viable cells with few dead cells in all groups, indicating no obvious cytotoxicity toward SH-SY5Y cells (Figure 5b).

PC12 cells were used to evaluate neuronal differentiation and neurite outgrowth. After OGD treatment, PC12 cells were cultured in NGF-containing differentiation medium, while different scaffolds were placed in Transwell inserts to minimize direct scaffold–cell contact and assess the effects of released GDNF on neurite outgrowth. After 10 days of co-culture, NF200 immunostaining showed neurite extension in all groups, with more pronounced neurite outgrowth in the Free-GDNF and Scaffold-GF groups than in the Blank and Scaffold groups (Figure 6a). Quantitative analysis showed that the average neurite lengths in the Scaffold-GF and Free-GDNF groups were 181.7 ± 48.8 μm and 185.3 ± 58.5 μm, respectively, which were higher than those in the Blank group (123.8 ± 28.4 μm) and Scaffold group (137.0 ± 44.6 μm) (Figure 6b). No significant difference in average neurite length was observed between the Scaffold-GF and Free-GDNF groups. A similar trend was observed for the longest neurite length. These results indicate that GDNF-containing treatments supported neurite outgrowth of OGD-treated PC12 cells in the presence of NGF, and Scaffold-GF achieved a comparable effect to free GDNF treatment.

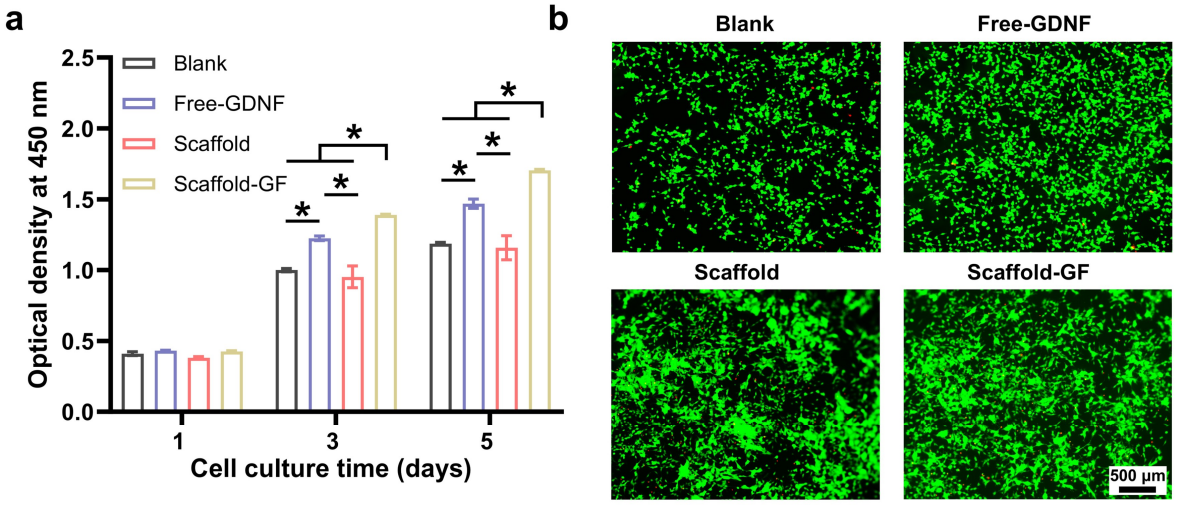


Figure 5. Effect of hybrid scaffolds on SH-SY5Y cell growth and viability under OGD conditions. (**a**) OD values of SH-SY5Y cells cultured with different treatments for 1, 3, and 5 days, measured using the CCK-8 assay. (**b**) Live/Dead staining of SH-SY5Y cells on day 5. Green fluorescence indicates live cells, and red fluorescence indicates dead cells. Data are presented as mean ± SD (n = 3). At each time point, statistical significance among groups was analyzed using one-way ANOVA followed by Tukey's multiple-comparisons test. * $p < 0.05$.

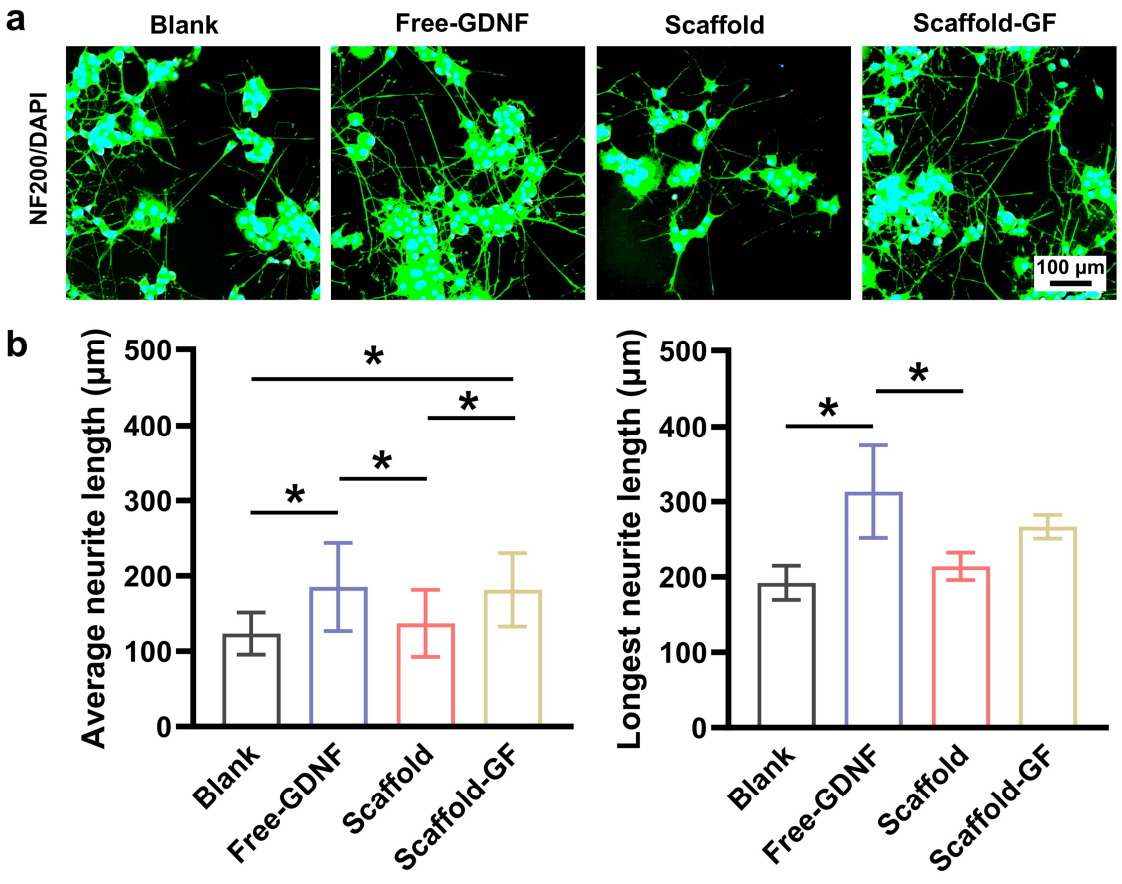


Figure 6. Effect of hybrid scaffolds on PC12 neurite outgrowth under OGD conditions. (**a**) Representative fluorescence images of PC12 cells showing neurite extension after co-culture with different scaffolds in a Transwell system. NF200, green; DAPI, blue. (**b**) Quantitative analysis of average neurite length and longest neurite length. Data are presented as mean ± SD (n = 3). Statistical significance was analyzed using one-way ANOVA followed by Tukey's multiple-comparisons test. * $p < 0.05$.

Taken together, these findings suggest that the hybrid scaffold can modulate endothelial and neuronal cell responses under ischemia-mimicking OGD conditions. Nevertheless, the present study is limited to an *in vitro*

OGD model and therefore does not fully capture the complex pathophysiological environment of ischemic brain injury. Further animal studies will be required to determine whether these cellular responses translate into therapeutic benefit and to assess scaffold retention, degradation, and biological performance *in vivo*.

4. Conclusions

In this study, we developed a hierarchical fiber-hydrogel hybrid scaffold by incorporating VEGF/GDNF-loaded GelMA@PCL short nanofibers into a VEGF-containing hyaluronic acid/heparin and gelatin hydrogel matrix. The scaffold combined a hydrogel network with embedded fibrous components and provided localized release of angiogenic and neurotrophic factors mainly during the early incubation period. The core-shell short fibers improved the structural retention of the hydrogel scaffold while serving as additional growth factor reservoirs. Under OGD conditions, the hybrid scaffold promoted HUVECs migration, supported endothelial cell responses, and maintained angiogenic activity in a tube formation assay. It also enhanced SH-SY5Y cell growth and supported PC12 neurite outgrowth in the presence of NGF. These results suggest that the hybrid scaffold can modulate vascular and neuronal cell responses in an ischemia-mimicking microenvironment. This work provides a biomaterial platform for the design of injectable materials aimed at neurovascular repair.

Supplementary Materials: The following supporting information can be downloaded at: https://media.sciltp.com/articles/others/2609301642414796/MI-26070026-SI.pdf. Figure S1. (a) Diameter distribution of GelMA@PCL core-shell nanofibers obtained from SEM images and (b) fiber orientation distribution determined by fast Fourier transform-based analysis of SEM images. Figure S2. Water contact angle measurements of Fiber-GF before and after plasma treatment. Figure S3. Injectability of the hybrid scaffold. (a) Representative images showing extrusion through a 26 G needle at 0, 10, and 20 min after precursor mixing. (b) Shear-thinning behavior of the hybrid hydrogel after gelation at 37 °C for 20 min.

Author Contributions: L.R., K.M., W.D., F.T., J.X.: conceptualization; L.R., K.M., W.D., K.H., J.H., J.Q.: methodology; K.H., J.H., J.Q.: software; F.T., J.X.: data curation; L.R., K.M.: writing—original draft preparation; L.R., K.M., W.D.: visualization, investigation; F.T., J.X.: supervision; J.Q., F.T., J.X.: validation; L.R., K.H., J.H., J.Q., F.T., J.X.: writing—reviewing and editing. All authors have read and agreed to the published version of the manuscript.

Funding: This work is supported by the Fundamental Research Funds for the Central Universities (buctrc202312), Interdisciplinary Research Center of Beijing University of Chemical Technology (No. XK2025-05), Talent Introduction Research Initiation Fund (2022-T-02), and the Opening Foundation of State Key Laboratory of Organic-Inorganic Composites (oic-202601002 and oic-202602035).

Institutional Review Board Statement: Not applicable.

Informed Consent Statement: Not applicable.

Data Availability Statement: The data presented in this study are available on request from the corresponding authors.

Conflicts of Interest: The authors declare no conflict of interest.

Use of AI and AI-Assisted Technologies: During the preparation of this work, the authors used ChatGPT to improve the language and readability of the manuscript. After using this tool, the authors reviewed and edited the content as needed and take full responsibility for the content of the published article.

References

1. Campbell, B.C.V.; De Silva, D.A.; Macleod, M.R.; Coutts, S.B.; Schwamm, L.H.; Davis, S.M.; Donnan, G.A. Ischaemic stroke. *Nat. Rev. Dis. Primers* **2019**, *5*, 70. https://doi.org/10.1038/s41572-019-0118-8.
2. Tuo, Q.Z.; Zhang, S.T.; Lei, P. Mechanisms of neuronal cell death in ischemic stroke and their therapeutic implications. *Med. Res. Rev.* **2022**, *42*, 259–305. https://doi.org/10.1002/med.21817.
3. Candelario-Jalil, E.; Dijkhuizen, R.M.; Magnus, T. Neuroinflammation, Stroke, Blood-Brain Barrier Dysfunction, and Imaging Modalities. *Stroke* **2022**, *53*, 1473–1486. https://doi.org/10.1161/strokeaha.122.036946.
4. Guan, X.; Zhu, S.; Song, J.; Liu, K.; Liu, M.; Xie, L.; Wang, Y.; Wu, J.; Xu, X.; Pang, T. Microglial CMPK2 promotes neuroinflammation and brain injury after ischemic stroke. *Cell Rep. Med.* **2024**, *5*, 101522. https://doi.org/10.1016/j.xcrm.2024.101522.
5. Xu, A.; Zhang, H.; Zhang, Y.; Wu, J.; Huang, Z. Ischemic stroke and intervention strategies based on the timeline of stroke progression: Review and prospects. *Acta Pharm. Sin. B* **2025**, *15*, 4543–4581. https://doi.org/10.1016/j.apsb.2025.07.026.
6. Günkan, A.; Ferreira, M.Y.; Vilardo, M.; Scarcia, L.; Bocanegra-Becerra, J.E.; Cardoso, L.J.C.; Fabrini Paleare, L.F.; de Oliveira Almeida, G.; Semione, G.; Ferreira, C.; et al. Thrombolysis for Ischemic Stroke Beyond the 4.5-Hour Window: A Meta-Analysis of Randomized Clinical Trials. *Stroke* **2025**, *56*, 580–590. https://doi.org/10.1161/strokeaha.124.048536.
7. Kanazawa, M.; Hatakeyama, M.; Ninomiya, I. Angiogenesis and neuronal remodeling after ischemic stroke. *Neural Regen. Res.* **2020**, *15*, 16–19. https://doi.org/10.4103/1673-5374.264442.

8. Ohab, J.J.; Fleming, S.; Blesch, A.; Carmichael, S.T. A Neurovascular Niche for Neurogenesis after Stroke. *J. Neurosci.* **2006**, *26*, 13007–13016. https://doi.org/10.1523/jneurosci.4323-06.2006.
9. Pérez-Gutiérrez, L.; Ferrara, N. Biology and therapeutic targeting of vascular endothelial growth factor A. *Nat. Rev. Mol. Cell Biol.* **2023**, *24*, 816–834. https://doi.org/10.1038/s41580-023-00631-w.
10. Lee, C.; Kim, M.J.; Kumar, A.; Lee, H.W.; Yang, Y.; Kim, Y. Vascular endothelial growth factor signaling in health and disease: From molecular mechanisms to therapeutic perspectives. *Signal Transduct. Target. Ther.* **2025**, *10*, 170. https://doi.org/10.1038/s41392-025-02249-0.
11. Shahriar, S.; Biswas, S.; Zhao, K.; Akcan, U.; Tuohy, M.C.; Glendinning, M.D.; Kurt, A.; Wayne, C.R.; Prochilo, G.; Price, M.Z.; et al. VEGF-A-mediated venous endothelial cell proliferation results in neoangiogenesis during neuroinflammation. *Nat. Neurosci.* **2024**, *27*, 1904–1917. https://doi.org/10.1038/s41593-024-01746-9.
12. Houghton, F.M.; Adams, S.E.; Ríos, A.S.; Masino, L.; Purkiss, A.G.; Briggs, D.C.; Ledda, F.; McDonald, N.Q. Architecture and regulation of a GDNF-GFRα1 synaptic adhesion assembly. *Nat. Commun.* **2023**, *14*, 7551. https://doi.org/10.1038/s41467-023-43148-8.
13. Yan, Q.; Matheson, C.; Lopez, O.T. *In vivo* neurotrophic effects of GDNF on neonatal and adult facial motor neurons. *Nature* **1995**, *373*, 341–344. https://doi.org/10.1038/373341a0.
14. Zhang, X.; Gong, B.; Rao, F.; Hu, H.; Tian, F.; Lu, Y.; Zhang, L.; Xia, Y.; Xue, J. Spatiotemporally controlled delivery of biological effectors from nanofiber scaffolds accelerates skin wound healing in porcine models. *Sci. Adv.* **2025**, *11*, eadz5302. https://doi.org/10.1126/sciadv.adz5302.
15. Liu, J.; Yao, Z.; Hu, Z.; Zhang, X.; Gong, B.; Dai, Y.; Weng, H.; Xiao, L.; Zhang, B.; Li, T.; et al. Spatiotemporal Delivery of Required Facilitators for Microenvironment Remodeling Propels Neural Regeneration after Spinal Cord Injury. *Adv. Mater.* **2026**, *38*, e03479. https://doi.org/10.1002/adma.202503479.
16. Cheah, E.; Wu, Z.; Thakur, S.S.; O'Carroll, S.J.; Svirskis, D. Externally triggered release of growth factors—A tissue regeneration approach. *J. Control. Release* **2021**, *332*, 74–95. https://doi.org/10.1016/j.jconrel.2021.02.015.
17. He, S.N.; Liu, S.N.; Zhang, T.T.; Shi, L.Q.; Ma, R.J. The research progress on dynamic covalent bonding-based nanocarriers for protein drug delivery. *Acta Polym. Sin.* **2025**, *56*, 1293–1312. (In Chinese)
18. Meng, R.; Lin, Y.T.; Yao, W.Q.; Zhang, S.M.; Chen, W.H.; Zhang, X.Z. Research on smart peptides for drug targeted delivery and immune activation. *Acta Polym. Sin.* **2025**, *56*, 1333–1344. (In Chinese)
19. Vermonden, T.; Censi, R.; Hennink, W.E. Hydrogels for Protein Delivery. *Chem. Rev.* **2012**, *112*, 2853–2888. https://doi.org/10.1021/cr200157d.
20. Li, J.; Weber, E.; Guth-Gundel, S.; Schuleit, M.; Kuttler, A.; Halleux, C.; Accart, N.; Doelemeyer, A.; Basler, A.; Tigani, B.; et al. Tough Composite Hydrogels with High Loading and Local Release of Biological Drugs. *Adv. Healthc. Mater.* **2018**, *7*, 1701393. https://doi.org/10.1002/adhm.201701393.
21. Hong, L.T.A.; Kim, Y.M.; Park, H.H.; Hwang, D.H.; Cui, Y.; Lee, E.M.; Yahn, S.; Lee, J.K.; Song, S.C.; Kim, B.G. An injectable hydrogel enhances tissue repair after spinal cord injury by promoting extracellular matrix remodeling. *Nat. Commun.* **2017**, *8*, 533. https://doi.org/10.1038/s41467-017-00583-8.
22. Ma, X.; Gao, F.; Su, W.; Ran, Y.; Bilalijiang, T.; Tuolhen, Y.; Tian, G.; Ye, L.; Feng, Z.; Xi, J.; et al. Multifunctional injectable hydrogel promotes functional recovery after stroke by modulating microglial polarization, angiogenesis and neuroplasticity. *Chem. Eng. J.* **2023**, *464*, 142520. https://doi.org/10.1016/j.cej.2023.142520.
23. Fu, X.; Wang, J.; Qian, D.; Chen, Z.; Chen, L.; Cui, W.; Wang, Y. Living Electrospun Short Fibrous Sponge via Engineered Nanofat for Wound Healing. *Adv. Fiber Mater.* **2023**, *5*, 979–993. https://doi.org/10.1007/s42765-022-00229-5.
24. Wan, X.; Zhao, Y.; Li, Z.; Li, L. Emerging polymeric electrospun fibers: From structural diversity to application in flexible bioelectronics and tissue engineering. *Exploration* **2022**, *2*, 20210029. https://doi.org/10.1002/exp.20210029.
25. Shahriar, S.M.S.; Mondal, B.; Andrabi, S.M.; Xie, J. Polymer Microfibers: Fabrication, Structural Design, Functionalization, and Biomedical Applications. *Mater. Interfaces* **2026**, *3*, 85–137. https://doi.org/10.53941/mi.2026.100009.
26. Zhang, X.; Guo, W.; Zhang, J.; Xiong, F.; Yao, Z.; Lin, J.; Hu, S.; Liu, Q.; Tian, F.; Zhao, N.; et al. Nanofibrous Guidance Conduits with Multiple Gradient Cues for Spinal Cord Repair. *Adv. Mater.* **2025**, *37*, 2503892. https://doi.org/10.1002/adma.202503892.
27. Gong, B.; Jin, B.; Qin, J.; Sun, Y.; Du, W.; Zhou, X.; Jiang, X.; Liu, W.; Tian, F.; Zhang, L.; et al. Synergistic Integration of Immune Regulation and Bioactive Guidance Cues in Multi-Channel Nanofibrous Nerve Guidance Conduits for Accelerated Peripheral Nerve Regeneration. *Adv. Fiber Mater.* **2025**, *7*, 1244–1259. https://doi.org/10.1007/s42765-025-00556-3.
28. Li, L.; Tian, F.; Li, Z.; Xu, M.L.; Fang, L.; Zhang, X.; Ruan, L.; Zhang, T.; Song, J.; Hu, X.; et al. Harnessing exogenous stimuli and functionally 3D aligned fibrous scaffolds for spatiotemporal modulation of bone regeneration. *Cell Press Blue* **2026**, *1*, 100006. https://doi.org/10.1016/j.cpblue.2026.100006.
29. Rahmati, M.; Mills, D.K.; Urbanska, A.M.; Saeb, M.R.; Venugopal, J.R.; Ramakrishna, S.; Mozafari, M. Electrospinning for tissue engineering applications. *Prog. Mater. Sci.* **2021**, *117*, 100721. https://doi.org/10.1016/j.pmatsci.2020.100721.

30. Chen, J.; Zhang, G.; Zhao, Y.; Zhou, M.; Zhong, A.; Sun, J. Promotion of skin regeneration through co-axial electrospun fibers loaded with basic fibroblast growth factor. *Adv. Compos. Hybrid Mater.* **2022**, *5*, 1111–1125. https://doi.org/10.1007/s42114-022-00439-w.
31. Cheng, X.; Xu, N.; Wu, H.; Pan, X.; Zhao, Y.; Chen, X.; Su, Y.; Wei, Y.; Jiang, Q.; Fan, J.; et al. A Coordinated Cascade Therapy-Based Janus Fibrous Membrane Drives Bone Regeneration through Mediating the Transformation of Energy Metabolism Pathway. *Adv. Funct. Mater.* **2025**, *35*, 2423212. https://doi.org/10.1002/adfm.202423212.
32. Yang, Q.; Li, J.; Meng, H.; Wang, Y.; Hu, L.; Su, W.; Xu, J.; Hou, J.; Zhao, R.; Wang, Z.; et al. Coaxial Electrospun Nanofibrous Membranes as Dual-Functional Biomimetic Tendon Sheath for Tendon Repair and Anti-Peritendinous Adhesion. *Adv. Healthc. Mater.* **2025**, *14*, 2402074. https://doi.org/10.1002/adhm.202402074.
33. Jian, D.; Ye, K.; Wang, L.; Jin, L.; Yang, H.; Ma, L.; Yi, C.; Mao, Z.; Wu, J. Enhance efferocytosis capacity of dendritic cells for diabetic wound healing by nanozyme-loaded nanofiber dressings. *Nano Today* **2025**, *64*, 102787. https://doi.org/10.1016/j.nantod.2025.102787.
34. Cheng, G.; Yin, C.; Tu, H.; Jiang, S.; Wang, Q.; Zhou, X.; Xing, X.; Xie, C.; Shi, X.; Du, Y.; et al. Controlled Co-delivery of Growth Factors through Layer-by-Layer Assembly of Core–Shell Nanofibers for Improving Bone Regeneration. *ACS Nano* **2019**, *13*, 6372–6382. https://doi.org/10.1021/acsnano.8b06032.
35. Tang, Y.; Wang, J.; Cai, Z.; Sarmento, B.; Du, Y.; Cui, W. Intestine-Settled Electrospun Short-Fibers Modulate Epithelial Transport Proteins to Reduce Purine and Glucose Uptake. *Adv. Fiber Mater.* **2025**, *7*, 186–203. https://doi.org/10.1007/s42765-024-00475-9.
36. Wang, H.; Zhang, Y.; Zhang, Y.; Li, C.; Zhang, M.; Wang, J.; Zhang, Y.; Du, Y.; Cui, W.; Chen, W. Activating Macrophage Continual Efferocytosis via Microenvironment Biomimetic Short Fibers for Reversing Inflammation in Bone Repair. *Adv. Mater.* **2024**, *36*, 2402968. https://doi.org/10.1002/adma.202402968.
37. Vinikoor, T.; Dzidotor, G.K.; Le, T.T.; Liu, Y.; Kan, H.-M.; Barui, S.; Chorsi, M.T.; Curry, E.J.; Reinhardt, E.; Wang, H.; et al. Injectable and Biodegradable Piezoelectric Hydrogel for Osteoarthritis Treatment. *Nat. Commun.* **2023**, *14*, 6257. https://doi.org/10.1038/s41467-023-41594-y.
38. Zhuo, H.; Dong, X.; Liu, Q.; Hong, L.; Zhang, Z.; Long, S.; Zhai, W. Bamboo-inspired ultra-strong nanofiber-reinforced composite hydrogels. *Nat. Commun.* **2025**, *16*, 980. https://doi.org/10.1038/s41467-025-56340-9.
39. Han, Z.; Bao, L.; Yu, Y.; Zhao, Y.; Wang, M.; Sun, Y.; Fu, M.; Zhou, Q.; Liu, W.; Cui, W.; et al. Injectable short-fiber hydrogel with fatigue resistance and antibacterial properties for synergistic periodontitis therapy. *Chem. Eng. J.* **2025**, *520*, 166298. https://doi.org/10.1016/j.cej.2025.166298.
40. Wang, Q.; Yang, J.; Meng, J.; Yu, J.; Li, X.; Ding, B. Bioinspired hierarchical fiber-hydrogel dressing with dual immunomodulatory and angiogenic functions for diabetic wound healing. *J. Control. Release* **2025**, *386*, 114063. https://doi.org/10.1016/j.jconrel.2025.114063.
41. Hu, Y.; Yu, B.; Jia, Y.; Lei, M.; Li, Z.; Liu, H.; Huang, H.; Xu, F.; Li, J.; Wei, Z. Hyaluronate- and gelatin-based hydrogels encapsulating doxycycline as a wound dressing for burn injury therapy. *Acta Biomater.* **2023**, *164*, 151–158. https://doi.org/10.1016/j.actbio.2023.04.021.
42. Xu, K.L.; Di Caprio, N.; Fallahi, H.; Dehghany, M.; Davidson, M.D.; Laforest, L.; Cheung, B.C.H.; Zhang, Y.; Wu, M.; Shenoy, V.; et al. Microinterfaces in biopolymer-based bicontinuous hydrogels guide rapid 3D cell migration. *Nat. Commun.* **2024**, *15*, 2766. https://doi.org/10.1038/s41467-024-46774-y.
43. Wang, M.; Li, W.; Hao, J.; Gonzales, A.; Zhao, Z.; Flores, R.S.; Kuang, X.; Mu, X.; Ching, T.; Tang, G.; et al. Molecularly cleavable bioinks facilitate high-performance digital light processing-based bioprinting of functional volumetric soft tissues. *Nat. Commun.* **2022**, *13*, 3317. https://doi.org/10.1038/s41467-022-31002-2.